Computationally Synthesised Inorganic and Organometallic Complexes

A thesis presented in partial fulfilment of the requirements of the degree of

Doctor of Philosophy
in
Chemistry

at Massey University, Albany, New Zealand

Muhammad Arif Sajjad
2017

Dedicate to my late father and brother

Abstract

Catalytic aromatic ring C–H bond functionalisations by transition metal cyclometallation reactions are important for organic transformation reactions. The cyclometallated product, which contains a new metal–carbon bond is formed as a consequence of different types of carbon–hydrogen····metal (C–H····M) interactions. These C–H···M interactions have been known as anagostic, preagostic and agostic interactions. By nature, the anagostic interaction has mainly electrostatic components, the preagostic interaction has electrostatic components with some back-bonding from metal to C–H antibonding orbital involved and the agostic interaction has mainly covalent components when the C–H bond donates electron density to the partially occupied metal centre. Prior to the current thesis work, an in-depth study that addresses the influence of steric and electronic factors on the anagostic, preagostic and agostic carbon–hydrogen····metal interaction was missing. In this thesis, the influence of both the steric and electronic factors on the anagostic, preagostic and agostic C–H···M interactions has been studied. It is seen that the electronic and steric influences play differently for different ligand systems as with the flexible tetralone ligand, a maximum of steric and electronic influence results into another type of anagostic interaction named as the 'C-anagostic' interaction. It is also seen that a stronger steric and electronic effect can trigger agostic covalency at the anagostic stage of the reaction. The inflexible ligand ensures the short anagostic approach, which has some back-bonding character and the nature of the interaction lies into the preagostic category. Finally, the aromatic ring agostic interactions have more complexity as new donations named as 'syndetic' from C–C pi bond to metal antibonding orbitals were recognised which shares the same antibonding acceptor orbitals as the agostic donation does. The recognition of new bonding situations in C–H····M interactions can have significant implications for C–H bond functionalisation reactions.

Acknowledgements

This thesis owes its existence by the inspiration and support of a large number of people. Firstly, I would like to express my sincere gratitude to Distinguished Professor Peter Schwerdtfeger for providing me this PhD opportunity and funding throughout my PhD studies. His continuous guidance, encouragement and support helped me in all the time of my PhD research.

I would also like to express my sincere gratitude to co-supervisors Professor Alastair J. Nielson and Associate professor John A. Harrison for their incredible guidance, sustained encouragement, constructive criticism, and sympathetic attitude throughout my PhD studies. I would not have imagined having better mentors for my PhD research.

I am very thankful to Centre of Theoretical Chemistry and Physics (CTCP) for providing me access to computer cluster and technical assistance in my computational work. I am also thankful to Institute of Natural and Mathematical Sciences (INMS) administration for their great assistance during the period of my PhD studies.

Special thanks to INMS Chemistry staff at Massey university Albany, especially Dr Marie-Anne Thelen, Dr Debbie Jordan, Dr Thomas Fallon and Erin Moffet for the support and encouragement during my PhD studies.

I owe my special regards and heartiest gratitude to my late father Hafiz Sajjad Hussain who made great devotion to my studies. Without his kindness, everlasting love, guidance, and encouraging passion it would have been a dream to complete my PhD studies. I am sorry he cannot see me graduate but his memories will be with me always. I also say my thanks to my late brother Atif Sajjad who was so kind and a symbol of love for me. I am also sad that he cannot see me graduate but I will miss him always. I remember the day last year he asked me ‘when you are going to complete your PhD’. I told him, in next 3-4 months but in the period he passed away. He was a great soul! I do admit that losing father (age 54 years) and brother (age 20 years) in final year of my PhD was extremely painful.

I am extremely thankful to my family especially my mother, brothers (Dr Tariq Sajjad and Asif Sajjad) and sisters (Summia Perveen and Shaista Perveen) for their full support, encouragement and sincere prayers during my stay in New Zealand. I would greatly appreciate the role of my elder brother Dr Tariq Sajjad who has always been a source of inspiration to me.

Last but not least, I thank to my beloved wife Atsha Nadeem and my sweet daughter Zainab Fatime for being patient with me. Finally, I thank all my friends for their help and support during my stay in New Zealand.

Abbreviations

DFT	density functional theory
PBE-D3	Perdew–Burke–Ernzerhof exchange-correlation functional with D3 version of Grimme's dispersion parameters
B3LYP	Becke's 3-parameter hybrid functional with the correlation functional of Lee, Yang, and Parr
BP86	Becke's 1988 exchange and Perdew 86 correlation functional
CAM-B3LYP	a new hybrid exchange-correlation functional B3LYP modified by Coulomb- attenuating method
CAM-B3LYPD3	CAM-B3LYP functional with D3 version of Grimme's dispersion parameters
Aug	augmented
cc-pVDZ	correlation-consistent polarised valence double-zeta
cc-pVTZ	correlation-consistent polarised valence triple-zeta
EHT	extended Hückel theory
QTAIM	quantum theory of atoms in molecules
NBO	natural bond orbital
LP	lone pair
NCI	non-covalent interaction
RDG	reduced density gradient
2D	two-dimensional
3D	three-dimensional
IR	infra-red
NMR	nuclear magnetic resonance
BCP	bond critical point
RCP	ring critical point

Reference Chart of C–H····M Interactions

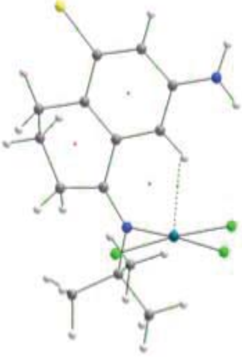

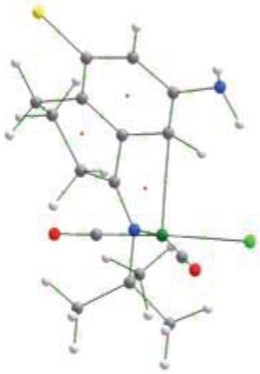

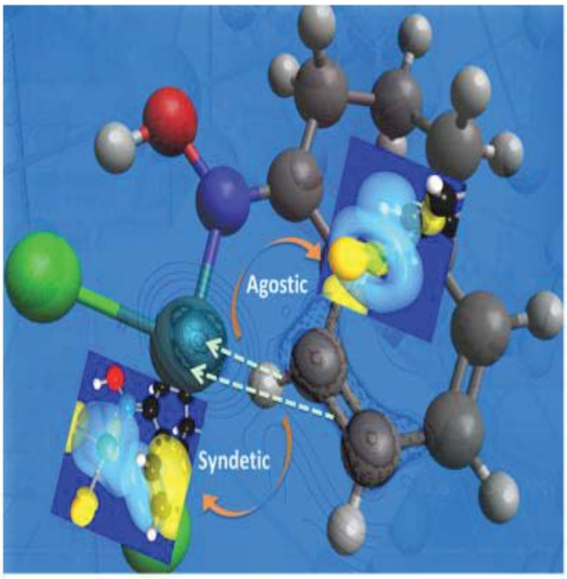

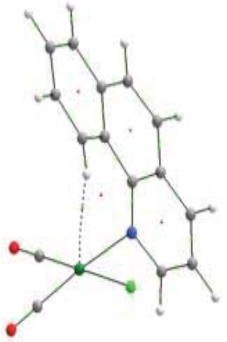

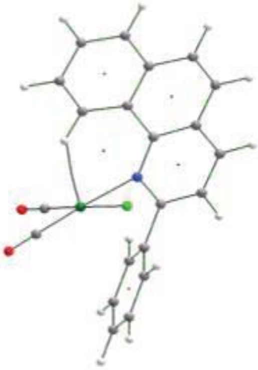

Publications and Thesis Structure

Publications relevant to this thesis

1. **M. A. Sajjad**, K. E. Christensen, N. H. Rees, P. Schwerdtfeger, J. A. Harrison, A. J. Nielson, *Chem. Comm.*, 2017, **53**, 4187–4190.

2. A. J. Nielson, J. A. Harrison, **M. A. Sajjad**, P. Schwerdtfeger, *Eur. J. Inorg. Chem.*, 2017, 2255–2264.

3. J. A. Harrison, A. J. Nielson, **M. A. Sajjad**, G. C. Saunders, P. Schwerdtfeger, *Eur. J. Inorg. Chem.*, 2016, 64–77.

Additional publications

4. J. A. Harrison, **M. A. Sajjad**, P. Schwerdtfeger, A. J. Nielson, *Cryst. Growth Des.*, 2016, **16**, 4934–4942.

Table of Contents

Chapter 1 Introduction: Carbon–Hydrogen···Metal Interactions in C–H Activation/Functionalisation reactions

Chapter 2 Computational Methodology for Carbon–Hydrogen···Metal Interactions

Chapter 3 Steric and Electronic Manipulation of Anagostic Interactions in Oximes and Imines Complexes of Rhodium (I)

Chapter 1

Introduction: Carbon–Hydrogen····Metal Interactions in C–H Activation/Functionalisation reactions

1.1 C–H Bond Activation

The synthesis of novel organic compounds containing new carbon–carbon (C–C) or carbon-heteroatom (C–Y) bonds is an attractive approach in organic chemistry. One of the best examples is the discovery of cross-coupling reactions where two pre-functionalised materials coupled together and form organic compounds with a new C–C or C–Y bond. In this regard, many cross-couplings reactions have been developed such as Suzuki, Sonogashira, Stille, Kumada, Hiyama or Negishi cross-couplings. The significance of cross-coupling reactions has been accepted by awarding the Noble prize 2010 to Richard F. Heck, Ei-ichi and Akira Suzuki. [1]

The utilisation of pre-functionalised substrates in cross-coupling reactions provides higher selectivity and reactivity compared to non-functionalised ones. But there are some complications associated with the use of pre-functionalised substrates. To make them pre-functionalised and then isolate them is a costly process. Hence, these complications led to efforts to find alternative ways to synthesise the identical final compounds with the same selectivity. The discovery of C–H bond activation is one of the best alternatives in this regard.[1]

The carbon–hydrogen (C–H) bonds are largely found in organic species but they are considered as non-reactive moieties in organic synthesis. Their usage as reactive points is very advantageous from the economical point of view. It also saves energy and time compared to the usage of pre-functionalised substrates. The conversion of nonfunctional CH groups into functional ones (C–C or C–Y) has now become a well-established phenomenon in organic synthesis. For this purpose, a large number of substrates such as alkyne, alkene, arenes and polymeric compounds etc. have been utilised. The inclusion use of transition metals for C–H bond activation field has evolved new opportunities in CH functionalisation reactions.[2]

The C–H bond activation process was first observed in 1936 in a hydrogen-deuterium exchange reaction in methane using a Ni catalyst.[3] A unique way of reactivity on the metal surface was observed which caused the cleavage of alkane C–H bonds.[3] Later, Hodges and Garnett in the 1960s described the deuteration of arenes and alkanes catalysed by a homogeneous solution of platinum salts and that was a remarkable discovery in this field. The first catalytic system was introduced by Shilov in 1972, in which hydroxylation and chlorination reactions of methane were achieved using platinum (II) salts. The mechanistic details of this work demonstrated the formation of a methyl platinum (II) intermediate in the first step, followed by oxidation of platinum (II) intermediate to Pt (IV) in the second and then functionalisation process in the final step (Figure 1.1).[3] The smaller rate constants for oxidation of methanol compared with the oxidation of an unactivated methyl group indicated an uncommon chemo-selectivity of for the reactions. Therefore, a new term "activation of saturated hydrocarbons" was introduced.[2]

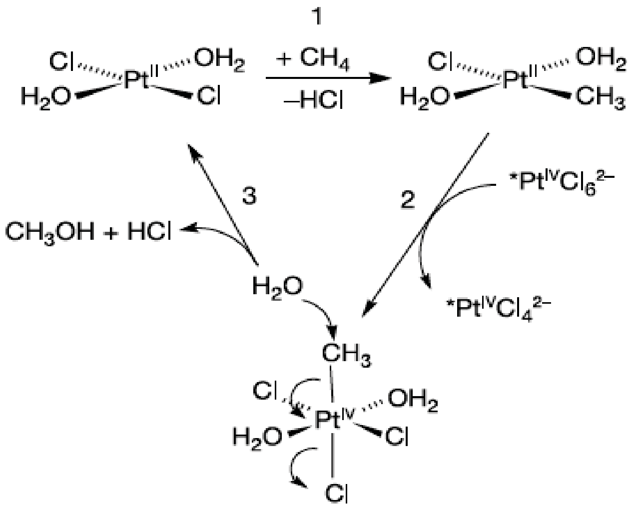

Figure 1.1 Catalytic system proposed by Shilov.[3]

The term "C–H bond activation" was proposed after the Parshall study on hydrogen-deuterium exchange reaction at the benzene nucleus using homogeneous metal hydride complexes. In the study, surprisingly, the fast rates for the labelling reaction were observed in the case of electron-deficient arenes which pointed out to a different mechanism for the cleavage of the C–H bond than the expected electrophilic substitution mechanism.[2,4] The term C–H activation was introduced to distinguish metal-catalysed C–H bond cleavage from the traditional radical and ionic substitution.[2] Thus, C–H bond activation is a process in which a specific CH group of a ligand interacts with the metal catalyst and forms an organometallic complex. The formed complex contains a new M–C bond and acts as an intermediate which is not an ionic or free-radical intermediate.[2]

Despite the fact that C–H activation is an advantageous approach in organic synthesis, it also has some complications also. For instance, the C–H bond is unreactive and has a high dissociation energy. Transition metals have proved to be excellent mediators in solving this problem as many of them are involved in activating and breaking the C–H bond. Another complication in the C–H activation process lies in the selectivity (regio-, enantio-, and chemo-) of the reaction when more than one CH group interacts with the transition metal.[1] Therefore, the activation of a particular CH group out of many CH groups of a ligand is a challenging but desirable goal.[5] For this purpose, different approaches have been adopted to achieve this goal. One of the most utilised approaches is the use of donor molecules with N, O, P, S, or other atoms for the coordination to the metal which directs certain C–H bonds into close proximity to with the metal. These donor molecules, known as directing groups, act as facilitators as they direct the metal to certain CH groups and assist in achieving CH activation. Obviously, the role of natural steric and electronic effects associated with the donor ligands cannot be neglected in this directing process. Both these steps; bonding of donor molecules to the metal and then intramolecular activation of a C–H bond after interacting with the metal, results in a new carbon–metal (C–M) bond and this process has been named as cyclometallation.[6] The complexes containing new C–M bonds are called cyclometallated complexes. Once the CH activation is achieved or formation of the C–M bond is done, a coupling partner such as alkene or aryl halide is used to functionalise the activated C–H bond and make new products.[7, 8, 9, 10]

1.1.1 Classification of C–H Bond Activation Reactions

The transition metal-mediated C–H activation process depends on some crucial factors which include the nature of the metal precursor, nature of ligands, substrate, solvent, and additives. Based on these factors, C–H bond activation reactions have been classified into oxidative addition, σ-bond metathesis, electrophilic activation, 1,2-addition, and metalloradical activation.[3, 11]

1.1.1.1 Oxidative Addition

Oxidative addition reactions occur for electron rich transition metal complexes such as Re, Fe, Os, Rh, Ir and Pt complexes. In this reaction, the oxidation state of metal changes from x to x+2 as two new ligands become attached to it (Figure 1.2). The reactive species [L_nM^x] are produced from the metal precursor by thermal or photochemical treatment.[3]

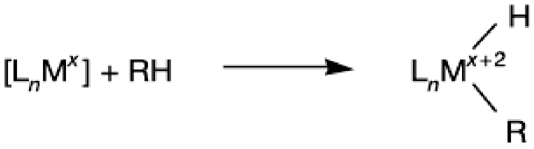

Figure 1.2 C–H bond activation via oxidative addition reaction.[3]

1.1.1.2 Sigma-Bond Metathesis

Early transition metal complexes with d^0 metal configuration undergo a concerted process which involves the transfer of a hydrogen from one ligand to another through a 4-membered transition state which forbids oxidation of the metal. This is an alternative mechanism for electron deficient metals, which cannot undergo oxidative addition (Figure 1.3).[3, 12]

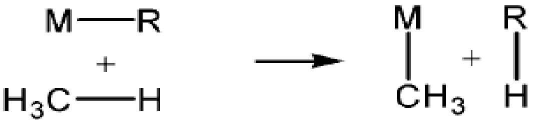

Figure 1.3 C–H bond activation via sigma-bond metathesis reaction.[12]

1.1.1.3 Electrophilic Activation

Electrophilic mechanism of C–H activation resembles sigma-bond metathesis. This reaction proceeds as the alkane C–H bond binds to an electrophilic metal centre, the strength of the C–H bond reduces. As a result the C–H bond length increases and finally loss of an H occurs and M–CH_3 type species are formed. The proton acceptor can be an external base or solvent or a basic group around the coordination sphere of the metal (Figure 1.4).[12]

Figure 1.4 C–H bond activation via electrophilic reaction.[12]

1.1.1.4 1, 2-Addition

C–H bond activation by the 1,2-addition reaction involves the addition of an alkane to a metal-nonmetal double bond (Figure 1.5). An example of such type of reaction involves the addition of methane into a Zr=N bond.[3,12]

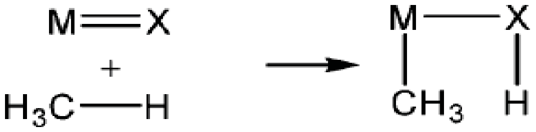

Figure 1.5 C–H bond activation via a 1,2-addition reaction.[12]

1.1.1.5 Metalloradical Activation

Complexes which exist in monomer-dimer equilibrium can reversibly cleave alkane C–H bonds (Figure 1.6). Examples of such complexes include rhodium (II) porphyrin complexes. Methane is the highly reactive hydrocarbon typically used for this type of reaction.[3,12]

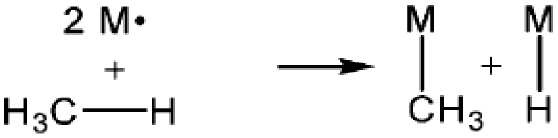

Figure 1.6 Metalloradical CH activation reaction.[12]

1.2 Cyclometallation Reactions

Cyclometallation, first introduced by Trofimenko[6], is an organometallic reaction in which a new carbon–metal σ-bond is formed by the interaction of a CH group and the metal atom. Cyclometallated intermediates are key components in the C–H functionalisation process. The formation of these cyclometallated intermediates usually proceeds in two steps: the first step is the initial coordination of the metal with a donor molecule; while the second step is the intramolecular interaction between a CH group and the metal. As a result of these steps, a metallacycle is formed after the removal of the CH hydrogen by a leaving group which is usually a base.[7,10] The obtained metallacycle has a chelate arrangement which enhances the stability of the organometallic compound. The metallacycle can be 4-, 5-, or 6-membered but 5-membered metallacycles are most common in C–H functionalisations. The greater use of 5-membered cyclometallated intermediates in synthetic organic chemistry arises as they ensure higher regio-selectivity.[8]

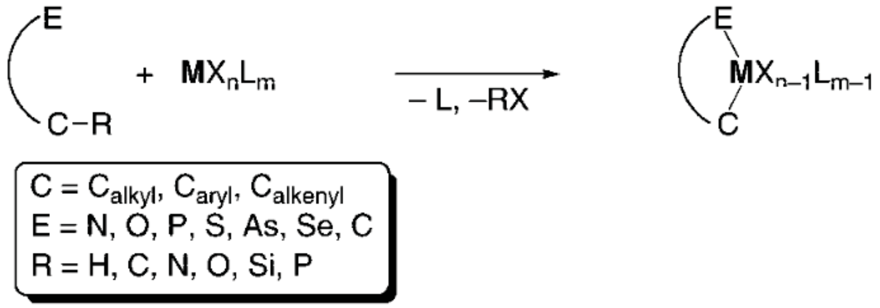

Figure 1.7 Cyclometallation reaction scheme.[10]

Cyclometallation reactions have been reported in a large number of transition metal complexes of platinum group metals such as rhodium, ruthenium, palladium, platinum and others. Among these, palladium has been widely studied and a large number of cyclopalladation reactions with a number of substrates are evident. Cyclometallated compounds have many applications in the fields of catalysis, photonics and material sciences.[8,10]

1.2.1 Elements of Cyclometallation Reactions

The key elements of cyclometallation reactions involve the nature of directing ligands, the metal, metal precursors including ancillary ligands, and nature of the C–H bonds. As the cyclometallated intermediates are a key part of the C–H functionalisations so these intermediates can also affect the overall C–H activation/functionalisation process. Optimal choice of these intermediates can improve the C–H functionalisation process.[10]

1.2.1.1 Nature and Structure of Directing Ligands

The first step of the cyclometallation reaction is the exchange of a weakly coordinating ligand in the metal precursor with a potentially favourable directing ligand. The nature and structure of the initial ligand become crucial for the pre-coordination step. Binding of a donor ligand to the metal changes its electron density and the steric effects associated with the ligand structure assist in the bond activation process as well as the cyclometallation reaction.[7,10] The pre-coordination of neutral donor molecules such as phosphine, amine or imine ligands can be carried out by a thermodynamically controlled mechanism or by a dimer cleavage process. For anionic ligands, such as amide (NR_2), or neutral carbon ligands, such as *N*-heterocyclic carbenes, pre-coordination to the metal centre is complicated.[10]

The basicity of donor ligands can affect the pre-coordination step. In most cases, the hard-soft acid-base principle is followed.[13] Successful cyclometallation is carried out with the combination of hard-donor ligands (alkoxides, aryl oxides, or amines) along with high-valent transition metals. In the same way, the soft transition metals like the platinum group metals favour binding to soft Lewis bases such as phosphines and sulfides. [7,10] There are also some examples where the soft donor ligands along with hard metals i.e., pyridine ligands with zirconium (IV) metal, have been used.[14] The mismatch of the hard-soft combination can affect the regio-selectivity of the cyclometallation reactions.[15]

The steric bulk associated with the structure of donor ligands can influence the pre-coordination to the metal centre. It has been shown that the NMe_2 ligand coordinates well to metal centres while the NEt_2 ligand weakens the coordination and similarly the $NiPr_2$ ligand does not coordinate to the metal centre.[16] On the other hand, steric bulk of the softer donor ligands such as phosphine and sulphides favours metal coordination. For example, the bulky ligand $P(t\text{-}Bu)_3$ provides stability to coordinatively unsaturated metal complexes and favours metallacycle formation.[17]

Despite the fact that a large number of directing groups have been utilised there are some limitations in selecting directing groups. Earlier studies showed that some directing groups i.e., pyridine, oxazoline, sulfide, and phosphine containing nitrogen, oxygen, sulfur and phosphorous heteroatoms favour the formation of thermodynamically stable five- or six-membered metallacycles. These stable cyclometallated intermediates are either difficult to isolate or they prevent further functionalisation reactions.[18] These conventional directing groups have been replaced with directing ligands with multifunctional ligands such as oxidising directing groups. The oxidising directing groups are beneficial as they oxidise the metal and limit the use of external oxidants.[19]

The electronic effects associated with the directing groups are also crucial for cyclometallation reactions. For example, the cyclopalladation is disfavoured in the case of aromatic aldehydes due to the greater electron withdrawing effect of the carbonyl group compared to imines which are poorer electron withdrawing ligands.[20]

1.2.1.2 Nature of Metal Precursors and Ancillary Ligands

The nature of the metal precursor is one of the crucial elements in cyclometallation. Because the ligand coordinates to the metal centre via a heteroatom in the primary step, there is a need for a vacant site to be created on the metal atom.[10] In this regard, various types of metal precursors have been used: including dimeric or monomeric complexes, e.g.

$[RuCl_2(CO)_2]$ and $[MCl(Cod)]_2$ (M = Ir, Rh, Cod=1,5cyclooctadiene); precursors containing weakly coordinating ligands, e.g., $[PdCl_2(NCMe)_2]$ $[PdCl_2(SEt_2)_2]$ $[Os(PR_3)_2H_5]$, or $[Ir(PPh_3)_2H_5]$ and complexes where one of the anionic ligands can be replaced by a neutral ligand, e.g., K_2PdCl_4 or K_2PdCl_4.[21, 22]

The next step associated with the metal precursors is the choice of ancillary ligands around the metal centre as the elimination of the proton from a CH group is necessary in order to make a cyclometallated product.[7,8,10] It has been found that strongly basic ligands enhance the formation of metallacycles by removing the proton easily.[22] Therefore, ancillary ligands such as alkoxides, an alkyl group, or a hydride, facilitate the deprotonation from the C–H group and thus makes C–H bond activation faster.[22] Acetate (AcO^-) has been proven as the best ancillary ligand for cyclometallation reactions due to its multiple binding modes (mono-, chelate-, and bridge) to metals. One of the oxygen atoms of the acetate ligands can weakly coordinate to the CH group and reorganises the structure. The weak C–H···O interaction between the CH group and the oxygen of the acetate group causes an increase in C–H bond length and hence, the C–H bond cleaves and a new C–M bond forms.[23]

1.2.1.3 Nature of C–H bond

The carbon hybridisation is an important factor as aromatic $C(sp^2)$–H bond activation dominates over $C(sp^3)$–H in most of the C–H functionalisation reactions.[10] The dominance of the C_{aryl}–H bond can be attributed to the higher kinetic lability of the aromatic protons compared to aliphatic hydrocarbons. The lability of the C–H bond can be influenced by using electronic substituents. The acidity of aliphatic C–H bonds can be influenced by electron withdrawing substituents; in the same way, donor substituents on the aromatic ring enhance cyclometallation through an electrophilic C_{aryl}–H bond activation process.[24]

1.2.2 Mechanisms of Cyclometallation Reactions

Based on the nature of the C–H bond and the electronic configuration of the metal, three cyclometallation mechanisms have been reported. The cyclometallated intermediates can be formed via sigma bond metathesis, electrophilic activation, and oxidative addition reactions. The mechanistic debate on cyclometallated processes is still on-going.[10]

1.2.2.1 σ-Bond Metathesis

The mechanism for cyclometallated intermediate formation via *σ*-bond metathesis C–H bond activation is different for early and late transition metals. For instance, in the case of early high-valent transition metals, the metallacycle is formed via a 4-membered transition state between the CH group and the metal.[10]

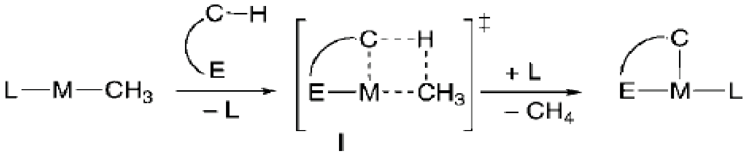

Figure 1.8 Metallacycle formtation via a 4-membered transition state.[10]

In the case of late transition metals there is formation of a stabilised σ-complex. A σ-complex is formed between metal and carbon and hydrogen by the donation of electron density from the metal to the CH bond.[25]

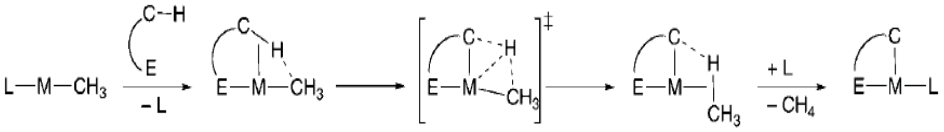

Figure 1.9 Metallacycle formation via *σ*-complex.[10]

1.2.2.2 Electrophilic Cyclometallation

Electrophilic C–H bond activation occurs with electron-poor late transition metals. A well-known example is the C_{aryl}–H bond activation mediated by palladium (II) which has electrophilic character. The early studies demonstrate that electron donating substituents on the aromatic ring enhance C–H activation, similar to organic electrophilic aromatic substitutions.[10] However, contrary to the organic model of electrophilic aromatic substitutions where a π-complex is followed by a σ-complex (arenium intermediate), in organometallic electrophilic C–H bond activation there is no evidence for formation of a π-complex. Instead, there is only evidence for the formation of a σ-complex.[10]

A π-bound intermediates also become insignificant if the metal complex contains ancillary ligands such as acetate or carbonate which perform multiple functions. These templating ligands participate in the transition state simultaneously as ligand to metal donors and as hydrogen bond acceptors and also act as proton scavengers to complete the C–H bond activation process.[10] Thus, these multifunctioning ligands favour the direct formation of σ-complexes without involvement of a π-complex.[10]

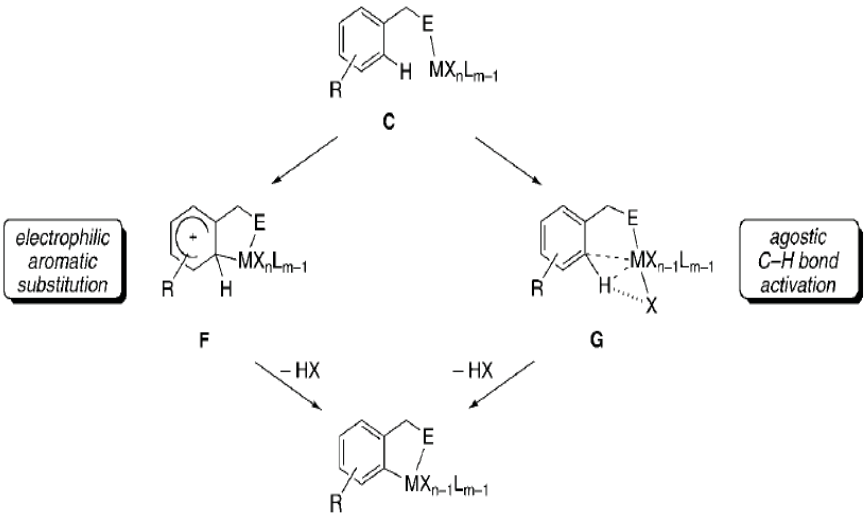

Figure 1.10 Mechanism showing the C–H activation via an electrophilic cyclometallation reaction.[10]

A theoretical study of this model indicates formation of an agostic interaction at the early stage of the bond activation. The corresponding intermediate G represents the metal-hydrogen interaction and only weak metal carbon interaction, and this step of the reaction is the rate-determining the AcO···H interaction provides stability to the intermediate.[26]

1.2.2.3 Oxidative Addition

C–H or C–R bond activation occurs via oxidative addition when the electron rich metal donates electron density to the antibonding C–H bond orbital. The oxidative addition is commonly found in cyclometallation reactions using electron-rich transition metals.[27]

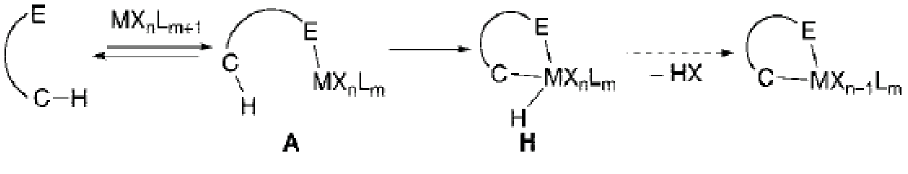

Figure 1.11 C–H activation via an oxidative addition reaction.[10]

In the above figure, the product **H** is an oxidative addition product. Oxidative addition is different from electrophilic cyclometallation where the C–H bond is an electron donor. In contrast to electrophilic C–H activation, the C_{aryl}–H bond-activation rate via oxidative addition correlates with the electron-withdrawing ability of aromatic substituents.[10]

1.3 Carbon–Hydrogen····Metal Interactions in Transition Metal Complexes

Carbon–hydrogen···metal (C–H····M) interactions are crucial because of their involvement in catalytic transformation of organic compounds by the C–H activation/functionalisation process. They play a vital role in the formation of cyclometallated products which are then used to synthesise a large number of novel organic compounds in further functionalisation reactions. There are now two well-defined terms used to differentiate C–H···M interactions; the well-known agostic interactions and the less well-known anagostic or preagostic interactions.[28]

Agostic interactions have been recognised as 3-centre 2-electron systems; three centres being carbon, hydrogen, and metal, while two electrons correspond to those from the C–H bond. They are known as partially covalent type interactions, and an agostic bond is formed when a CH group is in close vicinity to the metal centre, and a significant donation of electron density from the C–H sigma bond to the partially occupied metal centred orbital occurs. [29, 30]

On the other hand, for some complexes it was found that despite the close distance between the CH group and metal, there was no exchange of electron density between the C–H bond and metal centre. This type of interaction has been categorised as anagostic[31] or pseudo-agostic[32] or preagostic.[33] Anagostic interactions have largely been observed in d^8 transition metal complexes which have a square planar metal coordination sphere. The complete understanding of both agostic and anagostic interactions is essential in order to avoid mis-characterisation of interactions.[28]

Both agostic and anagostic interactions are different from hydrogen bonding interactions X–H···M (where X is mostly an electronegative atom and sometimes X=C) interactions which are known as 3-centre 4-electron systems. The three centres are the carbon, hydrogen and metal atoms and the four electrons correspond to the 2-electrons from the X–H bond, and another two electrons from donation by the electron-rich metal into the X–H antibonding orbital. The hydrogen bonding interactions are stronger when X is more electronegative.[34, 35]

The structural and spectroscopic properties of agostic and anagostic C–H···M interactions are different from X–H···M hydrogen-bonding interactions. The metal-hydrogen distance is 1.8–2.2 Å and 2.3–2.9 Å in the case of agostic and anagostic interactions respectively, while the metal-hydrogen distance is 2.65–3.5 Å for hydrogen-bonding interactions. The C–H···M angle in anagostic and agostic interactions is 90–130^o and 130–170 ^{o} respectively, whereas the X–H···M angle tends to be linear (160–180^o).[36]

Regarding spectroscopic properties, NMR spectra show upfield chemical shifts for the proton of the CH group and a significant decrease in coupling constant ^{1}JC–H in agostic interactions; whereas, in the case of anagostic and hydrogen bonding interactions the interacting proton of the CH group shows a downfield chemical shift and the coupling constant remains unchanged.[28] The decrease in ^{1}JC–H in agostic interactions is due to reduced bond order after C–Hσ donation to the metal antibonding orbital. The CH stretching frequency (cm^{-1}) in the IR spectrum decreases compared to the corresponding free ligands in the case of an agostic interaction. The reason for this decrease is the donation of electron density from the C–Hσ bond to a partially occupied metal centred orbital and building of a weak covalent interaction.[35]

1.3.1 Agostic Carbon–Hydrogen···Metal Interactions

The close proximity between the CH group hydrogen and the metal led Green and co-workers[28-30] to discover this new type of attractive interaction where the C–H bond donates electron density to an electron deficient transition metal. This new type of attractive interaction was named as the agostic interaction (agostic means ‘to draw towards’ from Greek word αγοστος) Since then a large number of organometallic complexes have been reported with evidence of agostic interactions.[28-30] These agostic interactions are key intermediates in C–H activation processes.[28]

Scherer and McGrady proposed a definition for the agostic interaction, as an interaction which occurs by the distortion in the geometry of organometallic complex which brings a C–H bond into close proximity with the metal centre.[37] Based on the connectivity of the interacting CH group, agostic interactions have been categorised as α, β, γ, δ or others. The position of the hydrogen atom close to the metal provides a clue for this interaction. X-ray crystallography gives structural evidence but locating hydrogen atoms accurately can be problematic because hydrogen atom contains only one electron that has almost no effect on the diffraction pattern. In this regard, NMR spectroscopy provides reliable evidence for the presence of an agostic interaction by measuring the agostic proton chemical shift and CH coupling constant ^{1}JC–H. On forming the close approach, the agostic proton shows an upfield chemical shift and the coupling constant ^{1}JC–H is significantly reduced.[35]

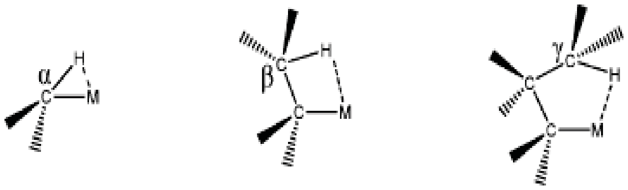

Figure 1.12 α, β, and γ agostic interactions.[35]

The first theoretical study on α-agostic alkylidene complexes, based on extended Hückel theory, was reported by Hoffman and co-workers.[38] It was found that the α-agostic interaction was not a direct orbital interaction between sigma CH and a vacant metal orbital in the tantalum complex, $[H_2TaCH_2]^{3-}$ with the distorted geometry. It was found that orbital overlap between σCH_2 bonding orbital and the LUMO orbital of the metal was not strong, instead significant orbital overlap was found between carbene CH_2 HOMO (sp^2 lone pair orbital) and the metal LUMO+1. The closer energies of the HOMO CH_2 and LUMO+1 metal as well as the strong hybridisation of the LUMO+1 metal orbital were the main driving forces for this interaction.[38] Another extended Hückel theory on titanium complexes indicated that the α-agostic interaction is the result of the best orbital overlap between metal and CH_2 orbitals. The distortion of the ligand can facilitate this interaction as it influences the shape and energy of the participating orbitals. Distortion of the methyl ligand in $[Ti(dmpe)Cl_3(CH_3)]$ (dmpe = bis(dimethylphosphino)ethane) favoured an α-agostic interaction compared to $[TiCl_3(CH_3)]$ where there was no distortion observed. The distortion of the methyl group can be attributed to the steric effect of the dmpe ligand.[39]

EHT (extended Hückel theory) calculations have been performed to analyse the β-agostic interactions in $[Ti(dmpe)Cl_3(C_2H_5)]$.[40] It was found that a β-agostic interaction results from the reorganisation of the M-C_α bond and not from the direct interaction of C_β–H and metal. The X-ray structure showed a Ti···C_β distance of 2.501 Å which confirms the formation of the β-agostic interaction.[40]

Desiraju et al[41] performed DFT theoretical studies along with AIM (atoms in molecules theory) and NBO (natural bond orbital) analyses to investigate agostic interactions in different transition metal complexes. The constructive orbital overlap between the donor C–Hσ bonding orbital with the antibonding metal orbital is favored in α-agostic interactions compared to β-agostic interactions. For β-agostic interactions, the distortion of the ligand facilitates the close approach of C_β–H group towards the metal centre. The donation of electron density from C_α–C_β to metal antibonding orbitals contributes in stabilising the β-agostic interaction.[41]

Scherer et al[42] performed an extensive DFT study to understand the nature of β-agostic interactions by varying the metal (Ti, Zr, V, and Nb) and the chloro ligand in d^0 and d^1 complexes with 3-coordination and 4-coordination metal spheres. They described that the β-agostic interaction occurs when the metal affords less than or equal to 16*e* in the coordination sphere and these interactions are favoured when the metal is three-coordinated and very rare when four-or six coordinated.[42]

Boncella et al[43] synthesised the alkylidene tantalum complexes containing different π-donor ligands. X-ray crystallographic and spectroscopic studies showed the presence of α-agostic interactions between the alkylidene C–H bond and tantalum metal. It was concluded that weak π-donor ligands, such as Cl and Br, and a donor with one electron pair, like NMe_2, strengthen the α-agostic interactions whereas the alkoxides with two electron pairs and stronger π donors weaken the α-agostic interaction.[43]

The strength of the agostic interaction varies from very weak to 10 kcal mol^{-1}.[44] The energy of agostic interactions depends on the nature of the metal and coordinated ligands. For instance, DFT study of β-hydride and methyl migratory insertion reactions in complexes $[CpM(PH_3)(CH_2CH_3)R]^+$ (M = Co, Rh, Ir; R=H, CH_3) indicates that the binding energy of the β-agostic interaction is greater than the α-agostic interaction in cobalt complexes. As the agostic interaction is the result of a donation from C–Hσ to an empty d-orbital of the metal, according to ligand field effects, the destabilisation energy increases from 3d to 5d. Thus cobalt accepts electron density and makes the agostic interaction stronger.[45]

Increased steric effects associated with ligand structure favour the agostic interaction. Bulky substituents restrict the alkyl chain on the metal coordination sphere and therefore favour the agostic interaction.[46] For instance, there were agostic interactions observed in $[IrH_2L_2]^+$ complex (L=P(tBu)$_2$(Ph) or P(H)$_2$(CH_2CH_3)) but not in the complex where L=PH_3.[45] Another study based on X-ray and theoretical models also claims the presence of an agostic interaction in the complex $[Ir(H)_2(PR_2Ph)_3]^+$ [R = cyclohexane], whereas no agostic interaction was observed with R=isopropyl.[46]

Milstein et al[47] demonstrated the role of *tert*-butyl substituents in facilitating agostic interactions in a combined experimental and DFT study of ruthenium complexes. The agostic interaction was favoured in a complex when in the ancillary ligand, an extra *tert*-butyl group was placed on phosphorous.[47]

Baratta et al[48] carried out an experimental and DFT based study to illustrate the structural and electronic properties of 14*e* ruthenium complexes. Their study revealed that the intermolecular interaction between the hydrogen of xylyl substituents with the ruthenium metal form the non-classical agostic interaction of the type (Ru···η^3–H_2C).

NMR spectra showed an upfield shift for the agostic carbon but downfield shift for agostic hydrogens. Bonding of this non-classical mode of agostic interaction showed the major donation of electron density from carbon p orbital to metal σ and dπ antibonding orbitals.[48]

Bullock et al[49] isolated two agostic isomers (γ and β) of molybdenum complex [η-$C_5H_5Mo(CO_2)(PiPr_3)$] experimentally and then further characterised them by DFT calculations. The distance of Mo⋯H was shorter in the β-agostic isomer [1.971 Å] compared to the γ-agostic isomer ([2.114 Å] and C–H bond elongation for β- and γ-agostic isomers were 0.07 Å and 0.03 Å respectively. The overall stabilisation energy for these agostic isomers was 12 kcalmol^{-1} obtained by comparing the energy of a single point calculation with the fully optimised structure as shown in Figure 1.13. The β-agostic isomer was less stable than the γ-agostic isomer.[49]

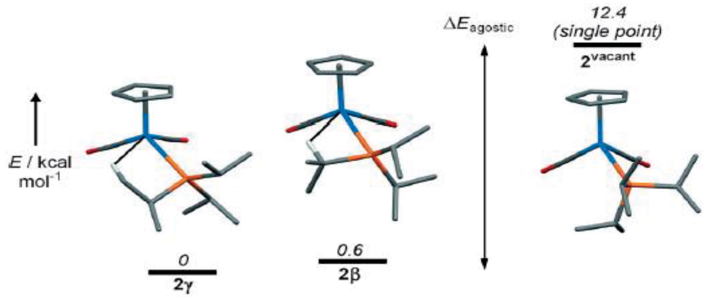

Figure 1.13 Theoretical energy diagram for *cis* and *trans*-agostic isomers. Atom colour: Blue for Mo; Orange for P, grey for C; red for O and white for H.[49]

Ortuño et al. studied the role of solution dynamics on the agostic interaction in Pt(II) complexes. They described that the solution dynamics of agostic interactions depends on the ligand structure and also the stability of the agostic interaction. They described that agostic interactions could be switched on and off depending on the strength of the interaction.[50]

To analyse the agostic interactions, the NBO approach[36,42] is a very useful tool as it describes the donor-acceptor interactions. However, to further explore the nature of the agostic interactions, QTAIM (the quantum theory of atoms in molecules) approach developed by Bader[51], which is based on the topological analysis of the electron density, will also be utilised. [35]

Popelier and Logothetis applied the QTAIM approach for the first time to investigate the agostic interaction in titanium complexes: $[Cl_2Ti–CH_3]^+$ (**1**), $[Cl_2Ti–CH_2CH_3]^+$ (**2**) and $[Cl_2Ti–CH_2CH_2CH_3]^+$ (**3**). Though the structural parameters of **1** lie in the range of an α-agostic interaction there was no bond critical point (bcp) observed. Whereas, in complexes

2 and **3** there were bcps and bond paths present between Ti···H_β and Ti···H_γ, respectively, which was evidence of agostic interactions (Figure 1.14)**.** In both latter cases the ring critical point (rcp) was close to the bond critical point (bcp) which indicates bcp instability and due to this instability bcps may not exist in some compounds.[52]

They further differentiated agostic interactions from hydrogen bonding based on QTAIM parameters. In the QTAIM approach the bcp, bond path and interatomic surface between the metal and agostic hydrogen confirm the presence of agostic interactions. The charge density of agostic interactions is 0.04–0.05 a.u. while the hydrogen bonding range is 0.002–0.035 a.u. The Laplacian of the electron density lies between 0.15–0.25 a.u. which is outside the range of hydrogen bonding [0.024–0.14 a.u.]. The QTAIM charge of agostic hydrogens has a negative value compared to non-agostic hydrogens. The atomic basin energy values of agostic hydrogens decrease significantly compared to non-agostic hydrogens. On the other hand, in case of hydrogen bonding, the QTAIM charge on the interacting hydrogen has a positive value and the atomic basin energy value increases compared to other hydrogens.[52]

The dipolar polarisation value of the agostic hydrogen was found to be 15–30 percent larger compared to other hydrogens. This means the proximity of the metal to the agostic hydrogen extends the electron cloud further away from the nucleus. In case of hydrogen bonding interactions, the dipolar polarisation value for the interacting hydrogen decreases.[52]

Scherer et al[53] performed a topological study using QTAIM (quantum theory of atoms in molecules) approach for β-agostic interactions in a complex [$EtTiCl_3$(dmpe)] using experimental and theoretical charge densities. They found a similar number of bond critical and ring critical points between the calculated and measured structures. QTAIM properties confirmed the β-agostic interaction between Ti···H_β which was facilitated by the Ti–Cα bond as there was a notable change in curvature found for this bond (Figure 1.15).[53]

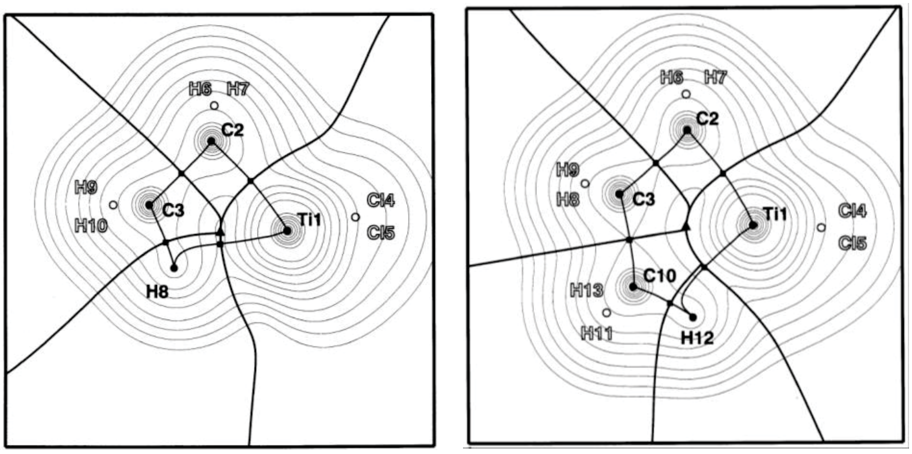

Figure 1.14 AIM pictures of $TiCl_2H_5Cl_2^+$ (left) and $TiC_3H_7Cl_2^+$ (right) complexes showing electron density, molecular graph, and interatomic surfaces. Bond critical points are represented by squares and ring critical point by a triangle.[53]

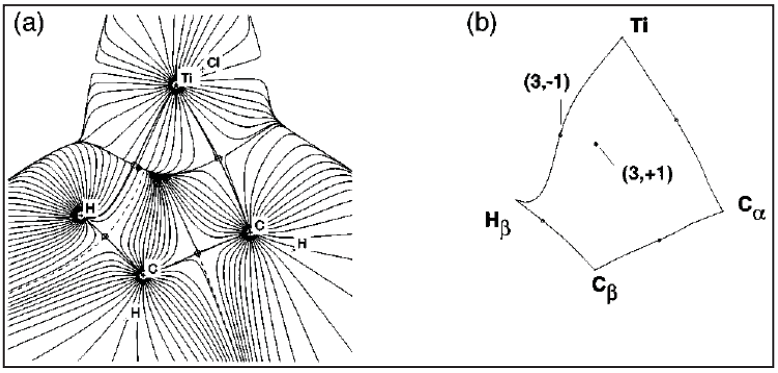

Figure 1.15 Calculated gradient vector field showing bond critical points for Ti···H_β.[54]

Nielson et al[54] revealed the presence of the linear agostic M···H-C interaction in a number of early and late transition metal complexes by using DFT studies along with NBO and QTAIM approaches. The interesting thing about this work was the involvement of back bonding from the metal to a CH antibonding orbital in these linear agostic interactions (Figure 1.16).[54]

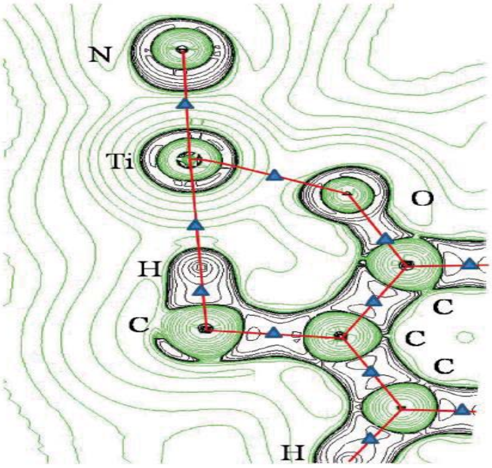

Figure 1.16. QTAIM contour plot of the laplacian of the electron density showing a bcp between Ti and H in a linear orientation.[54]

1.3.2 Preagostic or Anagostic C–H···M Interactions

Preagostic or anagostic interactions are mostly found in d^8 transition metal square planar complexes and are of interest due to their involvement in C–H bond activation processes. These interactions have been differentiated by various structural, spectroscopic and bonding properties compared to agostic interactions.[28,34,35]

The presence of these interactions has been reported in many X-ray and spectroscopic studies on organometallic complexes.[55] The weak anagostic interactions can affect the reactivity of the metal centre.[55b] Also, they have been observed in catalysts responsible for Ullman homocoupling reactions of simple aryl bromides.[55a] Anagostic intermediates have also been reported in the reaction mechanism of dehydrogenative coupling of primary alcohols and amines.[56] Anagostic interactions can provide stability to the structure of organometallic complexes[57] and are also involved in the formation of supramolecular networks.[55f]Anagostic interactions have also been found in catalysts used in Suzuki-Miyaura cross-coupling reactions[58] and facilitate cyclometallation of telluroethers.[59] Sometimes the anagostic interaction has been observed to cause distortion of the structure of organometallic complexes so their role on influencing geometry and properties of complexes can not be ignored.[55k]

Elias et al[60] reported the presence of anagostic interactions in a palladacycle based on structural and spectroscopic evidence. On further analysis, they found that anagostic interactions in a palladacycle increased the temperature range which activated the catalysts.[60]

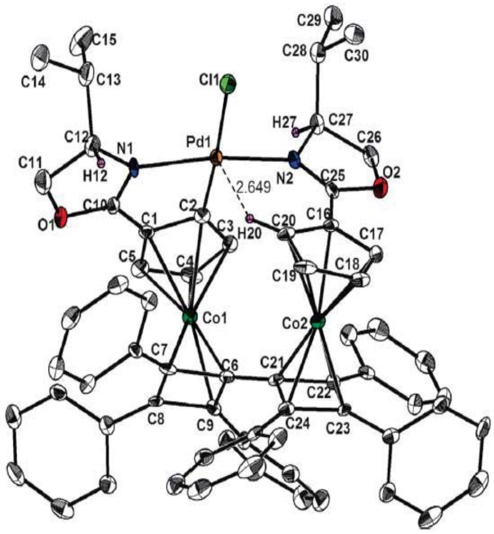

Figure 1.17 Cyclopalladated complex showing the anagostic interaction between Pd and H.[60]

Ellman et al. using DFT calculations provided evidence of the involvement of preagostic interactions in the mechanistic pathway for cyclometallation. They have shown that the cyclometallated product was formed as a result of preagostic and agostic interactions. The energy profile of the mechanism shows that the agostic intermediate is more stable than the preagostic intermediate.[61]

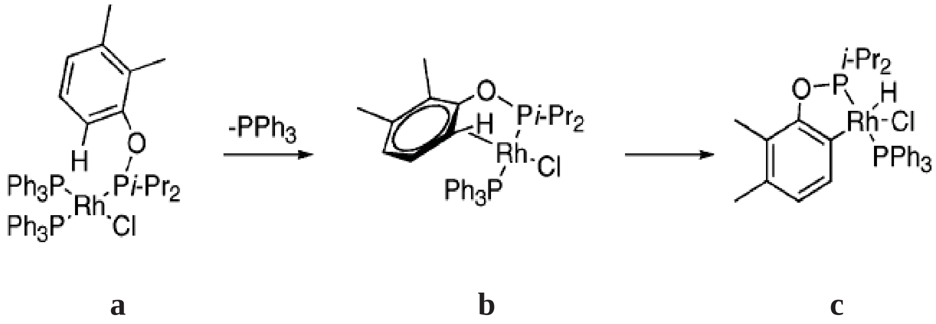

Figure 1.18 Proposed pathway for cyclometallation by Ellman et al.[61] **a**) Preagostic; **b**) Agostic; **c**) Cyclometallated product.

The nature and strength of anagostic interactions have not been extensively studied compared to agostic interactions. SciFinder scholar shows more than two thousand citations for the word ‘agostic’ and less than one hundred citations for the word ‘anagostic’. There is little work done on the mechanistic understanding of these interactions.[62]

Jarvis et al[63] reported anagostic interactions in Pt (II) complex with a di-benzylidene acetone diphosphine chelating ligand. An interesting feature of this anagostic interaction was that two protons showed a similar downfield shift in the NMR spectrum as result of proton exchange. X-ray structure analysis showed the distance between Pt⋯H_a of 2.624 Å and the DFT optimised structure showed 2.595 Å. NBO calculations showed the second-order perturbation energy value of 1.59 kcal mol^{-1} for a donation of electron density from Pt dz^2 to C–Hσ*.[63]

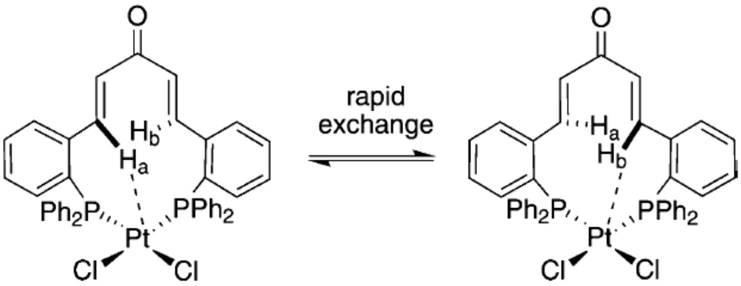

Figure 1.19 Complexes indicating exchange of Pt⋯H interactions.[63]

Dyker et al[64] reported two anagostic interactions from aliphatic and the aromatic hydrogens to palladium (II). The distance between Pd⋯$H_{aromatic}$ was 2.723 Å and Pd⋯$H_{aliphatic}$ was 2.447 Å. The NMR spectrum showed a downfield shift for both anagostic hydrogens. The aromatic proton showed a chemical shift of 11.17 ppm and the aliphatic hydrogen 24b showed a doublet signal at 8.55 ppm. The QTAIM calculations showed the charge density of 0.019 a.u. for Pd⋯H^3 and 0.027 a.u. for Pd⋯H^{24} and Laplacian values 0.05 a.u. and 0.08 a.u. for Pd⋯H^3 and Pd⋯H^{24} respectively.[64]

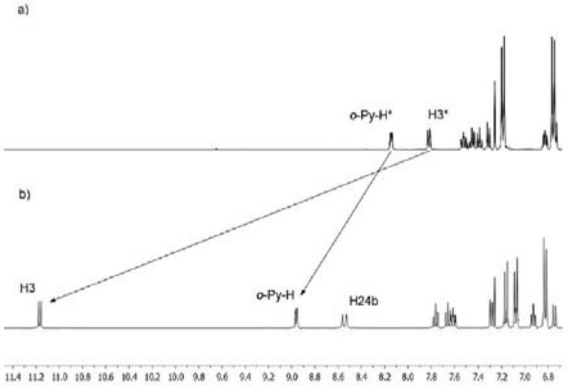

Figure 1.20 Diagram showing aliphatic and aromatic Pd⋯H interactions.[64] The NMR spectrum (right) indicates the downfield chemical shift for the interacting hydrogens in the complex (b) compared to the free ligand (a).

Scherer et al studied the C–H····M interaction using structural, orbital, NMR and topological characterisation. They categorised the anagostic interactions as repulsive and hydrogen bonding, whereas the preagostic and agostic interactions were attractive interactions. Anagostic and hydrogen bonding interactions have electrostatic dominance with the former being a repulsive interaction as the hydrogen is negatively charged while in hydrogen bonding the metal acts as hydrogen bond acceptor. Preagostic interactions are considered as being a precursor to the formation of agostic interactions. The preagostic interaction is formed when the metal dxy/yz orbital donates electron density to the C–Hσ* orbital. The anagostic and hydrogen bond interactions are 3c–4*e* systems while the preagostic and agostic interactions are both are 3c–2*e* systems.[65]

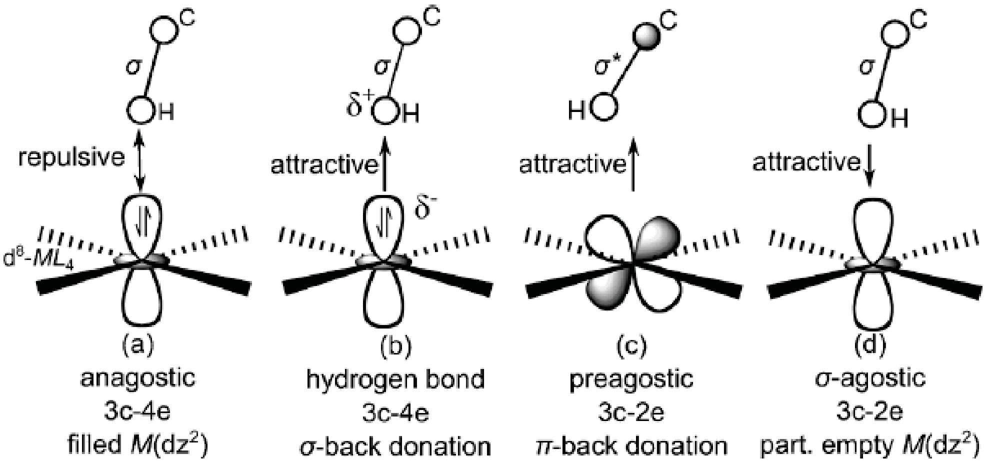

Figure 1.21 Classification of different types of C–H····M interactions proposed by Scherer et al.[65]

A recent paper[66] on anagostic interactions by Lepetit and co-workers introduced C–anagostic interaction in a combined experimental and theoretical investigation of Rh-pincer complexes. The geometrical parameters indicated significant bending of the C–H bond which facilitates the C-anagostic interaction (Figure 1.22). Non-covalent interaction (NCI) analysis showed an attractive (blue) interaction between carbon and metal and the NBO analysis supported this stabilising interaction by indicating donation from the C^1–C^2 π orbital to Rh 5s* orbital (5.5 kcalmol^{-1}).[66]

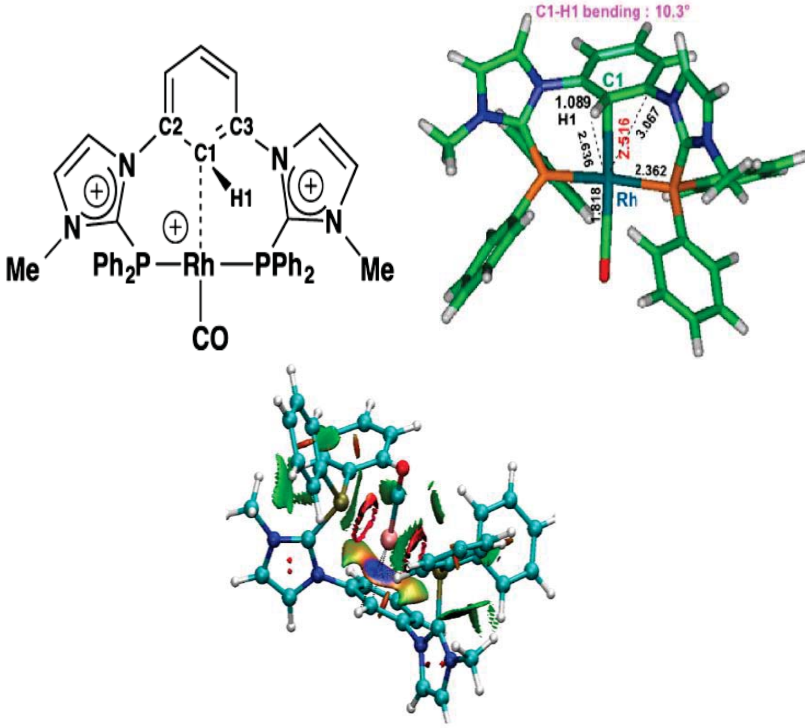

Figure 1.22 Diagram showing the role of C–H bending in formation of the C-anagostic interaction. The blue spot in NCI 3D plot shows the attractive anagostic interaction between Rh and the anagostic carbon.[66]

1.4 Summary

The literature is dominated by the agostic interaction out of the four categories of carbon–hydrogen···metal interactions. The agostic interaction is a partially covalent interaction where the C–H bond donates electron density to the metal; the preagostic interaction is one where a back-bonding component from the metal to C–H antibonding orbitals is involved; and the anagostic interaction is known as a weakly repulsive interaction. There are two different types of anagostic interactions described in the literature where the H-anagostic interaction is thought of as a repulsive interaction as both the metal and the anagostic H have positive charges. The second type of anagostic interaction, which has recently been introduced, is known as a C-anagostic interaction, which is an attractive interaction between carbon and metal. However, in the past the preagostic and anagostic interactions have been thought of as a single interaction but recent published work describes them as two separate interactions. The literature shows that there is only a small amount of work done on the mechanistic understanding of the preagostic and anagostic interactions. Therefore, a more detailed mechanistic understanding of anagostic and preagostic interactions is a needed at this time.

Chapter 2

Computational Methodology for Carbon–Hydrogen····Metal Interactions

2.1 Introduction

In the last few decades, computer simulations have attracted significant attention compared to experimental studies because of cost- and time-effective methodology. Now a day of complex problems in chemistry can be easily solved using computer simulations and many interesting and crucial molecular properties such as structural (bond lengths and angles), electrochemical (reduction potentials) and thermodynamic values (enthalpy, Gibbs free energy, entropy) can be easily determined. Furthermore, accurate spectroscopic properties such as NMR, IR and UV-Vis spectra of molecules can also be calculated using these simulations. The basis of the computational simulations is the Schrödinger equation 2.1 given below:

$$\hat{\mathrm{H}}\Psi = \mathrm{E}\Psi \qquad (2.1)$$

Where Ψ is a many body-electron wavefunction and is based on all the coordinates of electrons and the nuclei, $\hat{\mathrm{H}}$ is the Hamiltonian operator which has two terms for the kinetic energy (K.E) of electrons and nuclei and three terms for potential energy (P.E) of electron-nuclear attraction, electron-electron repulsion, and nuclear-nuclear attraction (equation 2.2). Equation 2.1 shows that the Hamiltonian of the wavefunction Ψ gives the total electronic energy E corresponding to that wavefunction.

$$\hat{\mathrm{H}} = -\sum_{\mathrm{i}} \frac{\hbar^2}{2m_e}\nabla_{\mathrm{i}}^2 - \sum_{\mathrm{k}} \frac{\hbar^2}{2m_k}\nabla_{\mathrm{k}}^2 - \sum_{i}\sum_{\mathrm{k}} \frac{e^2 Z_k}{r_{ik}} + \sum_{\mathrm{i}<j} \frac{e^2}{r_{ij}} + \sum_{k<l} \frac{e^2 Z_k Z_l}{r_{kl}} \qquad (2.2)$$

However, the many-electron Schrödinger equation 2.1 cannot be solved exactly even for two-electron systems. Therefore, approximations have been introduced in order to solve the Schrödinger equation 2.1. One way to solve the equation is to ignore the movement of the nuclei as they are heavier (larger mass) objects than electrons, which make their movements much slower than the electrons. This approximation is known as Born-Oppenheimer approximation, which leads to the formation of an electronic Schrödinger equation 2.3.

$$\hat{H}^{el}\Psi^{el} = E^{el}\Psi^{el} \qquad (2.3)$$

The Hamiltonian, $\hat{H}^{el}$, has now one term for kinetic energy of electrons and two terms for potential energy of electrons-nuclei attraction and electron-electron repulsion (equation 2.4).

$$\hat{H}^{el} = -\sum_{i}\frac{\hbar^2}{2m_e}\nabla_i^2 - \sum_{i}\sum_{k}\frac{e^2 Z_k}{r_{ik}} + \sum_{i<j}\frac{e^2}{r_{ij}} \qquad (2.4)$$

However, the nuclear-nuclear attraction term, which is a constant, is added into the electron energy, E^{el}, to produce the total energy of the system (equation 2.5).

$$E = E^{el} + \sum_{k<l}\frac{e^2 Z_k Z_l}{r_{kl}} \qquad (2.5)$$

The square of the wavefunction, Ψ, is used to describe the probability density of finding the electrons. To solve the Schrödinger equation in a physically relevant manner, it is necessary that Ψ must be continuous, single-valued, and antisymmetric with the interchange of electrons. After the wavefunction is determined, the expectation value of the operator can be calculated to determine any property of the molecule. For example, the expectation value of the Hamiltonian operator can be used to determine the molecular energy of a chemical system following equation 2.2:

$$\frac{\int \Psi_i^* \hat{H} \Psi_i}{\int \Psi_i^* \Psi_i} = E \qquad (2.6)$$

There is no straightforward way to determine Ψ and often it is approximated using a linear combination of atomic orbitals, Φ. This is done by assuming that every molecule has a ground state with E_0 and Ψ_0 and according to the variational principle, every Φ approximation related to energy E is either equal or greater than the ground sate energy E_0:

$$\frac{\int \Phi^* \hat{H} \Phi}{\int \Phi^* \Phi} = E \geq E_0 \qquad (2.7)$$

This relation shows that the Φ approximation meets the lowest energy wavefunction Ψ_0 when the value of the energy, E, approaches to the limiting value of the ground state energy E_0.[67, 68]

2.2 Basis Sets

The determination of the wavefunction is based on the linear combination of atomic orbitals (LCAO) approach (equation 2.8) which requires sets of one-particle functions (or atomic orbitals). These sets of one-particle functions are called basis sets whose selection requires some kind of expertise because of their direct influence on the accuracy of computations. Therefore, in order to obtain chemically meaningful results, it is recommended that the actual wavefunction must be well enough approximated by the chosen basis set. Generally, molecular orbitals are more accurately determined by a larger basis set compared to a smaller basis set.

$$\varphi_i = \sum_{\mu=1}^{K} c_{\mu i} f_\mu \qquad (2.8)$$

where φ_i shows molecular orbitals, $c_{\mu i}$ are numerical coefficients, f_μ are atomic orbitals, and K for the number of atomic orbital functions (or basis functions). [69, 70]

2.2.1 Types of Basis Functions

Two types of basis functions (or atomic orbitals) named as Slater type orbitals (STO) and Gaussian type orbitals (GTO) are employed to form a complete basis set.

2.2.1.1 Slater Type Orbitals (STOs)

Because of their resemblance with the hydrogen atom, Slater type orbitals (STOs) were used as basis functions and are generally defined as:

$$\phi_{abc}^{STO}(x,y,z) = N x^a y^b z^c e^{-\zeta r} \qquad (2.9)$$

Where N is a normalisation constant; a, b, c are related to the angular momentum: $L=a+b+c$. The radial extension is controlled by ζ (zeta); for example small ζ gives diffuse functions and large ζ gives tight functions. The exact orbitals for the hydrogen atom are reflected by the exponential dependence on the distance between the nucleus and the electron. Slater type orbitals (STOs) are not purely spherical harmonic functions because they do not have radial nodes. However, the nodes in the radial part can be introduced by the linear combination of STOs. The STOs are mostly used for atomic or diatomic systems where the high accuracy is required and in semi-empirical methods where all three- and four-centre integrals are ignored.[68,69]

2.2.1.2 Gaussian Type Orbitals (GTOs)

Cartesian coordinates are used to define Gaussian type orbital (GTOs) as:

$$\phi_{abc}^{GTO}(x,y,z) = Nx^a y^b z^c e^{-\alpha r^2} \qquad (2.10)$$

Where N is used for normalisation constant, a, b, c are used to define the angular momentum L = a+b+c and the width of the orbital is controlled by α for example small α gives diffuse functions whereas large α gives tight functions. The comparison of STOs and GTOs shows that STOs have advantageous over GTOs because exponentials in STOs depend on r whereas exponentials in GTO depend on r^2 value. Therefore, the STOs not only represent the proper behaviour near to the nucleus but also away from the nucleus compared to the GTOs where they fall off very quickly and define the “tail” of the wavefunction poorly. In order to get the same level of accuracy of the STOs, more GTOs are required. However in the calculation of the electronic properties of molecules, the GTOs are preferred as basis functions because they are better than STOs in terms of computational efficiency.[68,69]

2.2.2 Types of Basis Sets

Depending on the number of functions, different types of basis sets have been developed. Detail of these basis sets is given below.

2.2.2.1 Minimal Basis Set

In minimal or single–zeta basis set, one basis function is considered for each type of orbital occupied in the atom. For example, for hydrogen and helium atoms only single s-basis functions are used. Similarly two s-functions and one set of p-functions are used for the second row of the periodic table. As the minimal basis set contains very few functions, therefore, the quality of basis functions must be good. The Slater type orbitals ensure good quality but due to complexity in calculating integrals with STOs, GTOs are contracted to approximate the STOs. In this strategy, the contraction parameters are chosen by fitting the contracted GTOs to STOs. One of the best examples is STO-3G where three primitive GTOs are contracted for each basis function in order to approximate Slater functions.[68,69]

2.2.2.2 Split-Valence Basis Set

A minimal basis set has a limited flexibility and is not a viable option for highly accurate molecular calculations. However, the efficiency of a basis set can be enhanced by increasing the number of basis functions. The contraction parameters can be determined by variational optimisation where adding more basis functions brings the electronic energy closer to the variational energy. Therefore, split-valence basis sets have been introduced with the concept that the chemical bonding is mainly concerned with the valence orbitals and thus, the valence orbitals should have more basis functions than the core ones. For instance, a double zeta (DZ) valence basis set is represented with two contracted basis functions for the valence orbitals and only one contracted basis function for the core orbitals. Similarly, a triple-zeta split valence basis set is one where three contracted basis functions are used for each valence orbital while one contracted basis function is used for each of the core orbitals.[68,69]

The popular split-valence basis sets used in most of the computational calculations are the Pople basis sets such as 3-21G, 6-31G and 6-311G etc[68,69] where the first two basis sets belong to double-zeta valence basis sets while the third one is known as a triple-zeta valence basis set. In the 3-21G basis set, the 3 indicates the number of primitive GTOs involved – 3 GTOs for the core orbitals and 21 means the two primitive GTOs are involved in making the contracted GTOs for the inner part of the valence orbitals and one primitive GTOs involved in making the contracted GTOs for the outer part of the valence orbitals. Similarly in 6-311G, the core orbitals are represented by the contraction of six primitive GTOs and the valence orbitals are defined by three functions where three, one and one primitive GTOs are involved to form the contracted GTOs. [68,69]

2.2.2.3 Dunning's Correlation-Consistent Basis sets

In the case of a split-valence basis set, there is a disadvantage in using large numbers of primitive GTOs in order to converge towards the infinite basis set limit. Dunning and co-workers developed correlation consistent basis sets by optimising with correlated CISD wavefunctions where comparatively smaller number of primitives is required. These basis sets have been designed to converge systematically towards the infinite basis set limit and also have been geared to recover the correlation energy of valence electrons. The name correlation-consistent refers to functions which contribute the same amounts of correlation energy are included at the same stage; no matter what function type they belong to. For instance: the first d-function provides a large energy lowering; the energy decrease from a second d-function and first f function is similar; as is the contribution to lowering of the energy from the third d-function, second f-function and the first g-function. The addition of the polarisation functions should therefore be done in the order: 1d, 2d1f, and 3d2f1g. Several types of Dunning's correlation consistent basis sets have been described depending on the final number of contracted functions such as cc-pVDZ, cc-pVTZ, cc-pVQZ, cc-pV5Z (correlation-consistent polarised valence double/triple/quadruple/quintuple zeta etc). These cc-basis sets can be further augmented by adding diffuse functions and the prefix aug- is used before the cc to indicate these diffuse functions. For example, the aug-cc-pVDZ has additional 1s-, 1p-, 1d-functions and the aug-cc-pVTZ has 1s-, 1p-, 1d-, and 1f functions extra for non-hydrogen atoms. [68,69]

2.2.2.4 Polarisation Basis Functions

The inclusion of polarisation functions in a basis set further increases the size of a basis set and refers to any higher angular momentum orbital which is not occupied in the ground state atom. For example, for an s-type orbital like the hydrogen atom, p-type polarisation functions are the only orbital type that can be added. Similarly d-polarisation functions are used for p-type orbitals and f-type or higher functions are considered as polarisation basis functions for transition metals with occupied d-type orbitals. The polarisation functions help the calculated electronic energy to get closer to the exact energy. Furthermore, the inclusion of polarisation functions improves the description of the electron density in the bonding region because its inclusion provides flexibility to the basis set. Adding a single set of polarisation functions for example, p-functions on hydrogens and d-functions on heavy atoms, to the DZ basis are known as *Double Zeta plus polarisation* (DZP).[68,69]

2.2.2.5 Diffuse Basis Functions

Diffuse basis functions (usually s- and p-type) are added for the systems with broad electron distributions. The electron density is extended over a large spatial region in these systems. Diffuse basis functions are especially used for anionic systems or in intermolecular complexes where the electron density is extended over a large region.[68,69]

2.2.2.6 Pseudopotentials

Pseudopotentials are also known as effective core potentials and are used to define the core electrons of transition metals, and heavy elements generally. The reason for the use of these potentials in heavy elements is to overcome the problems associated with the use of large amount of basis functions in order to define the core electrons. In transition metals, the speed of core electrons near the nucleus becomes a significant fraction of the speed of light and therefore relativistic effects cannot be ignored. These pseudopotentials describe these relativistic effects. Thus an ECP defines the atomic core and associated relativistic effects very well. The popular pseudopotentials in modern use are LANL (Los Alamos

National Laboratory), LANL2DZ (Los Alamos National Laboratory double-zeta) basis set and the Stuttgart-Dresden Pseudopotentials.[69,70]

2.3 Density Functional Theory and its Functionals

Density functional theory (DFT) is a computational method which determines the properties of molecules based on their electron density. Contrary to the approaches based on wavefunctions, which is not a physical property, electron density is a physical property of all molecules. Also the wavefunction becomes more complicated as the number of electrons increases but the difficulty in determination of electron density is largely independent of the number of electrons. The basis of DFT is the Hohenberg-Kohn-Sham theorem which states that the ground-state electronic energy can be fully determined by the electronic density (ρ). The 'functional' means that the energy of the molecule is a function of the electron density E[ρ(x,y,z)] and electron density is a function of the positional coordinates of the electrons ρ(x,y,z).

The exact ground state electronic energy $E_{DFT}[\rho]$ is the sum of the kinetic energy of electrons $T[\rho]$, the electron-nuclear interaction energy $E_{ne}[\rho]$, the electron-electron repulsion energy or coulomb energy $J[\rho]$ and electron exchange-correlation energy $E_{xc}[\rho]$:

$$E_{DFT}[\rho] = T[\rho] + E_{ne}[\rho] + J[\rho] + E_{xc}[\rho] \qquad (2.11)$$

Each of the above terms is a functional because each of the energy terms is a function of electron density ρ, which is a function of position of electrons (x,y,z). The values for the first three energy functionals can be determined by *ab-initio* or semi-empirical methods. The challenge comes in determining the value for the fourth term, $E_{xc}[\rho]$. The electron correlation in the fourth term, $E_{xc}[\rho]$, originates from electron spin related effects due to the Pauli-exclusion principle.[69]

In order to determine an accurate expression for the exchange-correlation energy, different approximations can be used. The first approximation, known as the local density approximation, assumes uniform distribution of electron density in a gaseous state. This approximation works well for electronic band structures for solids where the energy gap is associated with electrical conductivity. Outside of this, the scope of this approximation is very limited. The first exchange-correlation energy functional ($E_{xc} = E_S + E_{VWN}$) based on the local density approximation consists of the exchange functional of Slater, Es, and the correlation functional of Vosko, Wilk, and Nusair. Both of these functionals (E_S and E_{VWN}) are based on uniform electron density.

The second type of approximation is known as the gradient-corrected approximation in which a gradient-corrected factor is included along with electron density calculations. In this approximation, the gradient factor takes into account the non-homogenous behaviour of the electron density and thus has been named as gradient-corrected. The inclusion of gradient corrected-factors in functionals improves the calculations. For example, by combing two gradient functionals as in the BLYP approximation[71], $E_{XC} = E_B + E_{LYP}$ where E_B is from the Becke correlation functional and E_{LYP} is the Lee, Yang, and Parr electron exchange functional, reduces the average energy difference between the computed and experimental values to less than 3 kcal mol^{-1} for acetylene, ethylene, and ethane. The most popular functional based on the gradient-corrected approximation is BP86[72] which consists of the Becke 1988 exchange functional and Perdew 86 correlation functional.

The third approximation is known as the hybrid approximation, which contains both Hartree-Fock and DFT exchange plus DFT correlation approximations. In the recipe for the hybrid approximation, the HF and DFT exchange approximations is used for calculating the exchange energy while the DFT approximation is considered for the electron correlation energy. The weight factor for each of the components (HF and DFT functionals) is approximated empirically. The hybrid functionals perform well in calculating many molecular properties compared to Gradient-corrected functionals. Therefore, they are widely used in computational chemistry and have become a very popular choice. For example, the hybrid GGA functional B3LYP [73] which contains Becke’s 3-term correlation functional and the Lee, Yang, and Parr exchange functional has widely been employed by computational chemists. Another popular hybrid functional PBE1PBE (or PBE0)[74], which has been formed by combining 25% HF exchange, 75% PBE exchange and 100% PBE correlation is also foremost choice in computational chemistry.[69, 75]

In recent developments, DFT functionals with dispersion corrected factors have been introduced which account for the dispersion forces between atoms in intra- or intermolecular interactions. The most popular functional in this regard is the third generation DFT-D3 functional developed by Stefan Grimme and co-workers[76] for calculating the dispersion energy using higher order dispersion coefficients. The calculated dispersion energy is the combination of dispersion energies of a two-body term and a three-body term. Some of the famous functionals in this category are PBE-D3[76, 77], B3LYP-D3[73,76], and B97-D3[76, 78] etc.[79]

2.4 Computational Methods & Basis Sets for Transition Metal Complexes

The choice of a reliable computational method and basis set in order to attain a good level of accuracy is a vital step in computational chemistry. The level of accuracy in computational chemistry is proportional to the time of computation. Therefore, it is always necessary to choose a reasonable computational time without compromising the desired computational accuracy. Thus, for many-electron systems such as organometallic complexes, it is impractical to use coupled cluster (CC) methods. Although CC methods ensure a very high level of accuracy they take too long to compute, which is the main obstacle to the use of these methods in large systems. Hence, the density functional methods (DFT) have been found best alternatives for computations, especially geometry optimisations of transition metal complexes of Ni, Rh, Pd and Ir. The major advantage of DFT methods is that they ensure a good compromise between accuracy and computational time of the calculations for organometallic complexes.[80]

2.4.1 DFT Functionals and Basis sets for Geometry Optimisation of Transition Metal Complexes

Calculation of the minimum energy molecular geometry is an important step in obtaining other chemical information such as thermochemical data, NMR, IR and other spectral properties. Therefore accurate geometry optimisation of molecules is a key first stage in any computational analysis. In the context of DFT, different kinds of functionals have been developed. In the case of species containing transition metals like Pd, Ni, Rh and Ir, there is no universal DFT functional for calculational use. However, the hybrid functionals have been the most popular choice for the calculation of organometallic complexes containing these transition metals. In particular for geometry optimisation of these transition metal complexes, B3LYP[73] has been extensively used. Statistical data shown in Figure 2.1 shows dominance of the B3LYP functional in quantum chemical calculations during the period 2002–2006.[79] Regarding transition metal complexes Figure 2.2 shows that B3LYP dominated in the 2008–2009[80] but the use of dispersion corrected functionals such as ωB97X-D[81] etc. has reduced the use of B3LYP functional in 2013–2014.[80]

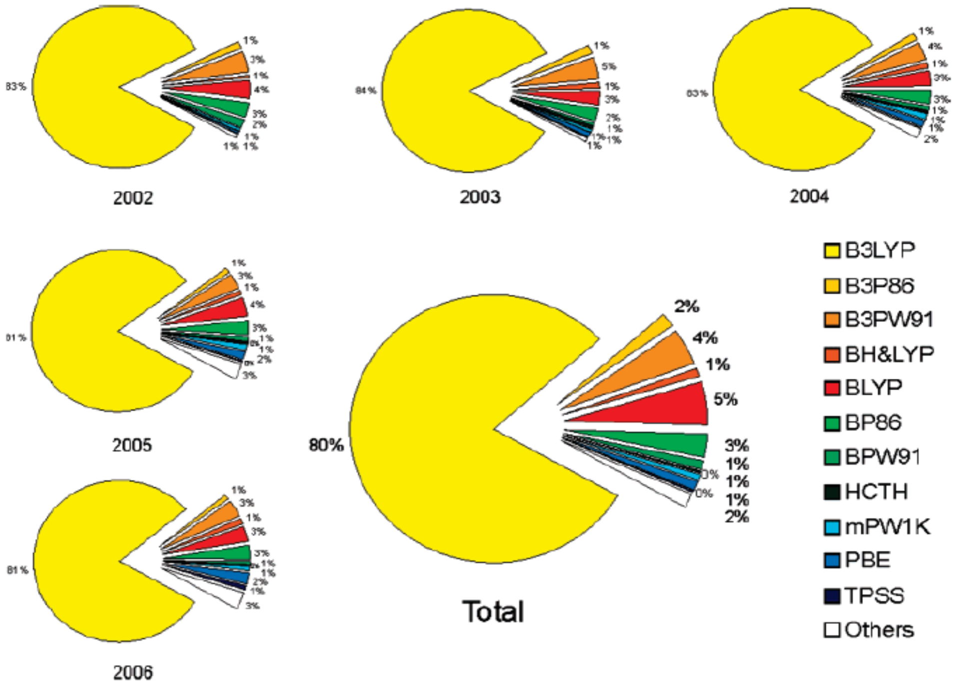

Figure 2.1 General use of some popular DFT functionals used in quantum chemical calculations in year 2002–2006.[79]

The use of B3LYP in a large number of studies is due to its overall good accuracy in reproducing the crystal structures. For instance, the geometry optimised structure of Pd (II) chloride using the B3LYP functional shows an error within 5% compared to the X-ray structure. In another case, the B3LYP optimised structures of reactants and intermediates in alkyl coupling reactions show a good agreement compared with CCSD(T)[82] reference data.[83] Consequently, B3LYP also performs well in structure optimisation of alkene-Ir(Cp) complexes compared to the X-ray structure.[80]

In addition to B3LYP, the other functionals such as BP86[72], B3PW91[84], and PBE0[74] also perform well in some cases. For example, the B3PW91 functional performs better than B3LYP in geometry optimisation of second-row transition metal complexes such as [Rh(NO)(PF_3)$_3$] and [RhCp(C_2H_4)$_2$].[85]

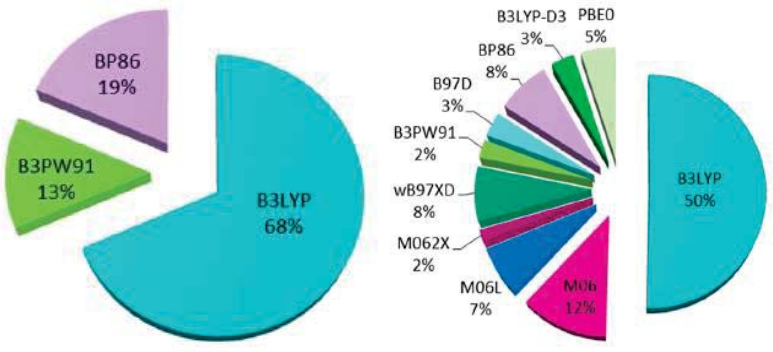

a **b**

Figure 2.2 Use of some popular DFT methods for geometry optimisation of transition metal complexes (Pd, Ni, Rh and Ir) in 2008–2009 (a) and 2013–2014 (b).[80]

In fact, none of the functionals mentioned above contain dispersion correction factors and thus for the study of intramolecular interactions where dispersion forces cannot be ignored, these functionals are not the best choice. Therefore, the choice of DFT functionals should be made according to the nature of intramolecular interactions. In this context a comparison of the performance of different functionals in the structure optimisation of a cationic Cp-Ru-allyl complex show better performance when dispersion corrected functionals are used when compared to the experimental x-ray structure. The other functionals as shown in Figure 2.3 overestimate the bond distance of Ru–C(3) e.g. PBE/4-31G(d) (SDD+f for Ru) and B3LYP/4-31G(d) (SDD+f for Ru) show 0.3 Å and 0.4 Å longer bond lengths respectively.[86] However, by the use of dispersion-corrected BP86 (BP86-D2) with a triple zeta quality basis set the bond length was reduced to now be within 0.1 Å[87] The error was reduced to within 0.01 Å of the experimental value by using PBE-D3/def2/TZVP calculations[88].[80]

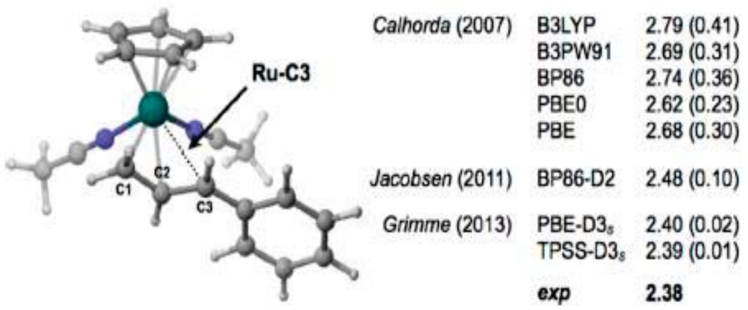

Figure 2.3 Comparison of Ru–C^3 bond length in Cp-Ru-allyl complex optimised by various DFT functionals.[80]

Another benchmark study on a number of phosphine complexes containing the metals Pd, Rh, Ir and Ni shows that the dispersion-corrected DFT ωB97X-D functional gives better agreement with x-ray structure compared to B3LYP.[89] However, it is also essential to not rely on dispersion corrected factors while comparing solely with x-ray structures as dispersion interactions would be different in x-ray structures than in solution. Therefore, in the case of homogeneous catalysis where intramolecular dispersion forces in the catalyst are very weak, the inclusion of dispersion-corrected factors may result in formation of intramolecular interactions which may be absent in solution.[80]

In the context of the choice of basis sets and effective core potentials in geometry optimisation of transition metal complexes, conversely to the rapid development of a number of DFT methods, the selection of basis sets and pseudopotentials has not changed significantly in recent years. The statistical data presented by Schoenebeck et al[80] show still the dominance of the effective core potential (ECP) LANL2DZ[90]for the transition metal along with Pople basis sets 6-31G(d) or 6-31G(d, p) for the main group atoms (Figure 2.4). The Stuttgart-Dresden (SDD)[91] as ECP with polarisation or without polarisation functions has also been employed as a good choice because of greater flexibility in the valence shell compared to LANL2DZ.[81]

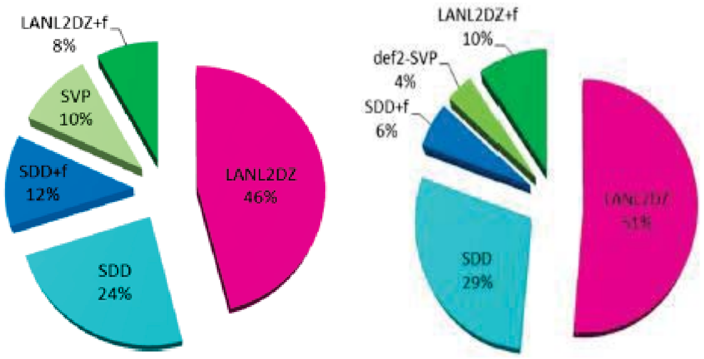

a **b**

Figure 2.4 Use of some popular basis sets for geometry optimisation of transition metal complexes (Pd, Ni, Rh and Ir) in 2008–2009 (a) and 2013–2014 (b).[80]

2.4.2 DFT Functionals and Basis Sets for Theoretical Investigation of C–H···M Interactions

Since geometrical parameters are crucial for structural characterisation of C–H····M interactions, good choices of DFT functional and basis set are always necessary for geometry optimisation of metal complexes. It is obvious that detailed characterisation of C–H···M bonding interactions is closely related to geometry optimisation of the complexes. It is a matter of the fact that B3LYP is the most widely used functional in order to reproduce the x-ray structures, so that most of the theoretical studies on C–H···M interactions have also been based on the B3LYP functional.[92] However, other theoretical studies on C–X (X=H, C, Cl) bond activation by metal catalysts performed by Grimme and co-workers[93] reveals that the dispersion-corrected DFT functionals give activation energies more accurately (better agreement with the CCSD(T) method). The best agreement was found in the case of PBE-D3 and PW6B95-D3[94] functionals.[80]

According to the DFT functional data provided by the Schoenebeck and co-workers[80], the trend of the use of DFT functionals has shifted slightly towards functionals containing dispersion corrected factors such as DFT-D3. In the case of availability of x-ray structures of transition metal complexes, the testing of DFT functionals is highly recommended. In this sense, a greater similarity between the structural parameters of the theoretically optimised and X-ray structures gives better confidence for further orbital and interaction analysis.[80]

Regarding the choice of basis set, it has been shown that a high level basis set is a prerequisite for the study of C–H···M interactions. A large triple-zeta quality basis set, with or without polarisation functions, in combination with a Stuttgart-type effective core potential is suitable for the metal atom, and aug-cc-pVTZ basis set[95] for the atoms bonded to the metal centres and proximate to the metal centres; the rest of the atoms can be treated by correlation consistent double-zeta basis with or without augmented functions, as appropriate.[92]

2.5 Approaches to Bonding Characterisations of C–H····M Interactions

2.5.1 Quantum Theory of Atoms in Molecules (QTAIM)

The QTAIM method developed by Richard Bader[51] is a well-known approach to describe bonding through the topological analysis of electron density. TThe basic principle of QTAIM is to look at the electron density and its gradient and from these establish the critical points of the electron density (ρ). The critical points are the certain points where the gradient of the electron density ($\nabla\rho$) vanishes. Critical points are classified by their rank and signature and are denoted by (rank, signature). By definition, the rank is the number of non-zero diagonal eigenvalues of the Hessian matrix of the Laplacian of the electron density and signature is the algebraic sum of the signs of the diagonal eigen values of the Hessian matrix of the Laplacian of electron density. A critical point with rank less than three is mathematically unstable and can disappear with smaller changes in the electron density by the nuclear movement. Therefore, the critical points with rank values less than 3 are generally not found in equilibrium charge distributions. Generally, there are four types of stable critical points: nuclear attractor (NA) or (3, –3) CP, bond critical point (bcp) or (3, –1) cp, ring critical point (rcp) or (3, +1) cp, and cage or (3, +3) cp. The nuclear attractor or (3, –3) cp arises because the electron density is maximum at atomic nucleus in all three directions (x, y, z). The cage critical point or (3, +3) cp is the point where the electron density is minimum with respect to all three directions. The bcp or (3, –1) cp is a saddle point where the electron density is minimum along the bond path between two atomic nuclei (where they share a bond or connect two (3, -3) CPs) and maximum at the atomic nuclei. Finally, the ring critical point (rcp) or (3, +1) cp is a saddle point on the surface where the maximum electron density lies between the two atomic nuclei but minimum at the atomic nuclei.[51]

In the QTAIM approach, an atomic centre behaves as an attractor and corresponds to a local maximum of the electron density. The gradient lines around an atom define its atomic basin and two atomic basins are separated by zero-flux surfaces. A zero-flux surface divides the charge density of two atoms and it is a surface where the gradient of the charge density is a minimum perpendicular to the surface. Thus, in a molecular system the charge density would be minimum between two atoms and this separates them from each other. The point where the shared charge density of two atoms reaches minimum corresponds to the bond critical point. The line of maximum electron density connecting two atomic nuclei in a bonding situation is known as bond path. In QTAIM topological analysis, two atoms would be considered as bonded if they are connected by a bond path and have a corresponding bcp between their basins. To further elaborate the nature of interactions, QTAIM atomic basin properties of the bonded atoms play a vital role.[51]

2.5.1.1 QTAIM Descriptors for C–H···M Interactions

Popelier et al. characterised the nature of agostic C–H···M interactions using the QTAIM approach. There are two kinds of QTAIM properties used in order to unveil the nature of C–H···M interactions. Firstly, the QTAIM properties associated with the bond critical point, which include: electron density (ρ); Laplacian of electron density ($\nabla^2\rho$); energy density (H); and bond ellipticity (ε). Secondly, the QTAIM properties which are related to atomic basins separately i.e. charge (q), energy (E), dipolar polarisation (μ), and volume (v).[52]

The detailed analysis of C–H···M interactions using QTAIM and NBO approach described by Desiraju et al[41] showed that sometimes a BCP may not be present in the case of weak agostic interactions and here the NBO approach can be beneficial. But a huge amount of work based on QTAIM analysis on C–H···M interactions supports the use of the QTAIM approach to uncover the nature of weak or strong C–H···M interactions.

2.5.1.2 Bond Critical Point Properties:

(i) Electron density at the bcp, ρ(bcp): The strength of interaction between two atoms is proportional to the amount of electron density at the bond critical point. A greater electron density indicates a stronger interaction as it is closely associated with the bond order. Usually, a ρ(bcp) greater than 0.20 e/bohr^3 indicates a shared interaction whereas a ρ(bcp) less than 0.10 a.u. indicates a closed-shell type interaction.[96]

According to Popelier and Logothetis, the value for an agostic interaction lies in the range of 0.15–0.25 e/bohr^3 which is different from that observed for hydrogen bonding interactions (0.002–0.035 a.u.).[52]

(ii) Laplacian of electron density at bcp, $\nabla^2\rho$ (bcp): The Laplacian of electron density, $\nabla^2\rho$, or a second derivative of electron density is the sum of three eigenvalues (λ1+ λ2 + λ3) of the Hessian matrix of electron density, where the first two eigen values (λ1 and λ2) are perpendicular to the bond path and are negative, whereas the third eigen value (λ3) lies along the bond path and is positive. The Laplacian of electron density, $\nabla^2\rho$ (bcp), value measures the degree to which the electron density is accumulated or depleted along a bond path. The negative Laplacian, $\nabla^2\rho$ (bcp), value determines the extent to which the density is accumulated in the interatomic surface along the bond path (shared interactions) while the positive value measures the extent to which the electron density is depleted in interatomic surface and concentrated in the separated atomic basins (closed-shell interactions). 101] In the case of agostic interactions, the range of $\nabla^2\rho$(bcp) value lies between 0.15 and 0.25 e/bohr^5 whereas for hydrogen bonding interactions the range of $\nabla^2\rho$(bcp) value is from 0.024 to 0.139 a.u.[52]

(iii) Bond ellipticity, ε: Bond ellipticity determines the directional distribution of the electron density in the bond. It is defined as:

$$\varepsilon = \frac{\lambda_1}{\lambda_2} - 1 \quad (where\ |\lambda_1| \geq |\lambda_2|\ ) \qquad (2.12)$$

Where λ_1, λ_2 are eigenvalues, when λ_1 and λ_2 are equal then the ellipticity becomes zero and the electron density around the bond would be cylindrically symmetrical. In case of agostic interactions, the involved C–H bond has higher ellipticity upon interaction with the metal in the complex compared with the ligand. The reason for the higher ellipticity value is the donation of electron density to the metal centred orbitals which weakens the strength of the C–H bond.[96]

(iv) Energy densities at bcp (*H*, *G*, *V*): The energy densities contain information about the mechanics of a bonding interaction. There are two crucial parameters related to energy densities which have been used in analysing the nature of interactions. The first parameter is the total energy density which when integrated over all space produces the total electronic energy. It is a sum of potential energy (V) and kinetic energy (G) densities and gives useful information in analysing the nature of interactions. For example, a positive value of the total energy density H indicates closed-shell interactions whereas a negative value of H shows shared interactions. In combination with the Laplacian of the electron density having $\nabla^2\rho$(bcp) and H(bcp) both positive corresponds to purely closed shell interactions; a positive value of $\nabla^2\rho$(bcp) and a negative value of H(bcp) show a weak interaction with some covalency involved; while having both negative values for $\nabla^2\rho$(bcp) and H(bcp) defines a purely shared (covalent) interaction.[96]

A second parameter associated with energy densities is the ratio of absolute value of the potential energy density to the kinetic energy density, $|V|/G$. A $|V|/G$ value > 2 indicates purely shared interaction (covalent); 2 < $|V|/G$ value > 1 shows electrostatic interaction with some covalency; while $|V|/G$ value < 1 shows a purely electrostatic interaction.[97]

Table 2.1 Relationship between QTAIM descriptors and nature of the interaction.[96,97]

$\nabla^2\rho(\text{bcp}) > 0$, $H(\text{bcp}) > 0$	———————>	Pure closed shell
$\nabla^2\rho(\text{bcp}) < 0$, $H(\text{bcp}) < 0$	———————>	Pure shared shell
$\nabla^2\rho(\text{bcp}) > 0$, $H(\text{bcp}) < 0$	———————>	Transit closed shell
$\lvert V\rvert/G(\text{bcp}) < 1$	———————>	Closed shell
$\lvert V\rvert/G(\text{bcp}) > 1$	———————>	Shared
$\lvert V\rvert/G(\text{bcp}) > 1 < 2$	———————>	Intermediate between closed and shared

Oldfield and co-workers characterised the preagostic C–H···M interactions based on the QTAIM approach, where they found that one M···H bcp has a slightly negative H(bcp) value whereas another two preagostic interactions had slightly positive values. Because the Laplacian values were positive in all cases, they categorised the nature of the first interaction as partially covalent while the other two were included into the category of purely electrostatic interactions.[34]

2.5.1.3 Integrated Atomic Properties:

To explore the nature of atomic basins (Ω) before and after the interaction, atomic properties have been employed and investigated. The important properties used for the analysis of C–H···M interactions are described below:

(i) Atomic charge $q(\Omega)$: $q(\Omega)$ is the charge after subtracting the electronic population $N(\Omega)$ from the nuclear charge Z_{Ω}. In case of C–H···M interactions, the agostic hydrogen is slightly negative compared to non-agostic hydrogens and this criteria is opposite to a hydrogen bonding interaction.[52,96]

(ii) The atomic energy $E(\Omega)$: The atomic energy corresponds to the electron-nuclear, electron-electron, and nuclear-nuclear interactions associated with an individual atom. The total molecular energy E_{total} is the sum of the atomic energies, $E(\Omega)$, can be denoted as:

$$E_{total} = \sum_{\Omega} E(\Omega) \qquad (2.13)$$

It has been shown that the atomic energy of the agostic hydrogen involved in a C–H···M interaction is significantly smaller than the non-agostic hydrogens. This is opposite to that of hydrogen bonding interactions where the atomic energy of hydrogen rises upon interaction.[52,96]

(iii) Atomic dipolar polarisation $\mu(\Omega)$: The atomic dipolar polarisation $\mu(\Omega)$ defines the polarisability of the electron density which means the degree to which an atomic electron density is distorted from a spherical shape. The atomic dipolar polarisation value for an agostic interaction is 15–30% larger compared to normal hydrogen. Conversely, in a hydrogen bonding interaction, the dipolar polarisation value of hydrogen decreases.[52,96]

(iv) Atomic volume $V(\Omega)$: The atomic volume $V(\Omega)$ is the space bounded by the intersections of interatomic surfaces from the interior of molecule and a chosen isodensity value. The overall molecular volume consists of the volume of all constituent atoms. In the gas phase, a molecule extends to infinity so that an isodensity surface value is specified. Usually the outer isodensity surface value of 0.001 a.u. is used as it covers 99% of the electron population. In the case of agostic interactions, the interacting hydrogen volume increases significantly - up to 15% compared to non-agostic hydrogens.[52,96]

2.5.2 Natural Bond Orbital (NBO) Analysis

The natural bond orbital (NBO) approach developed by Weinhold and co-workers[98] is one of the most useful methods for studying the nature of orbital interactions based on the Lewis concept of chemical bonding. In this approach, natural atomic orbitals which are localised 1-centre orbitals combine in an optimised linear combination to form natural hybrid orbitals which then combine and form natural bonding orbitals. The main feature of natural orbitals is they contain maximum occupancy of electron density. A natural bonding orbital has the maximum occupancy character, which is close to 2.000 e, is ideal situation for a natural Lewis structure. The natural population analysis using the NBO approach is numerically more stable than other similar analyses, such as the Mulliken population analysis, which works poorly for larger basis sets.[98]

Regarding C–H···M interactions, and other similar types of reactions, the donor-acceptor relationships have been featured in NBO analysis. The second order stabilisation energy, $E(2)$, derived from perturbation theory is used to define the two electron stabilisation interaction from a donor or occupied orbital to an acceptor or electron deficient orbital. The $E(2)$ is expressed by the relation:

$$E(2) = \frac{qi\ (F(i,j)^2)}{\varepsilon_i - \varepsilon_j} \qquad (2.14)$$

Where q_i is the donor orbital occupancy; $F(i,j)$ is the off-diagonal Fock matrix element; and ε_i, ε_j are the orbital energies of the donor and acceptor natural bond orbitals. A higher $E(2)$ value indicates a larger donation of electron density from donor to acceptor atom and thus a stronger interaction.[98]

2.5.3 Non-Covalent Interaction (NCI) Index

In recent times, the NCI approach has been used to analyse C–H···M interactions. NCI analysis is based on the electron density and its reduced gradient S(ρ), and differentiates between various types of weak interactions such as attractive, repulsive and vander Waals dispersive interactions. The obtained two-dimensional and three-dimensional NCI plots between the reduced density gradient, s(ρ) versus $\mathrm{sign}(\lambda_2)*\rho$, where the λ_2 is the second density Hessian eigen value, indicate blue region for attractive, red for repulsive and green for van-der Waals dispersive interactions.[99] The depth of the colour is related to the strength of the interaction.[99b]

Although, the QTAIM approach gives a lot of information regarding the strength and nature of the interaction but sometimes, in the case of weak interactions a QTAIM bcp can vanish especially when the bcp and rcp get too close to each other. In this case, NCI analysis can be an alternative and some important features of the interaction can be studied by the two-dimensional and three-dimensional NCI plots. Hence, the NCI analysis not only verifies the QTAIM bcps (for which the $\nabla\rho(r) = 0$) but also explores the non-AIM bcps (for which the $\nabla^2\rho(r) > 0$). The non-AIM bcps are the points characterised by the following condition indicated in equation 2.15:

$$\frac{\nabla\rho^2(r)}{\rho(\mathrm{r})}-\frac{4}{3}\frac{(\nabla\rho(\mathrm{r}))^2}{\rho(\mathrm{r})^2}=0 \qquad (2.15)$$

Thus, the topological picture of reduced density gradient S(r) recovers all the QTAIM bcps as well as the critical points related to the shells such as one-electron potential and very weak intramolecular interactions.[99]

2.5.4 Spectroscopic Properties

2.5.4.1 NMR Properties

NMR properties such as the C–H bond coupling constant (^1JC–H) and the chemical shift of the interacting hydrogen are used to explore the nature of C–H···M interactions. In agostic interactions where the C–H bond donates electron density to a metal orbital, the C–H bond length becomes longer which results in lowering the ^1JC–H significantly. In the agostic case, the ^1JC–H can decrease more than 50% whereas in anagostic and hydrogen bonding interactions, the coupling constant remains almost unchanged as a consequence of having no change in the C–H bond order. The chemical shift value of the interacting hydrogen of the C–H group goes upfield in an agostic C–H···M interaction compared to anagostic and hydrogen bonding interactions where the interacting hydrogen shows downfield chemical shift.[35]

2.5.4.2 C–H Stretching Frequencies

The infrared stretching frequency of an interacting C–H group is also used to differentiate C–H····M interactions. As the C–H bond elongates in an agostic interaction, the stretching frequency significantly decreases. On the other hand, in the anagostic interaction where there is no such change in C–H bond length, the C–H stretching frequency changes only slightly.[35]

2.6 Summary

It has been shown that the DFT B3LYP functional, because of its good agreement with the experimental structure, has been utilised in most of the computational studies on transition metal complexes. However, recently the trend has shifted towards dispersion corrected DFT functionals (DFT-D) particularly in the case of weak interactions where the dispersion forces become very important. Regarding the choice of functionals for the C–H···M interactions, B3LYP, BP86 and PBE-D3 have been used. The most recent literature shows a greater use of the PBE-D3 functional for geometry optimisation of structures.

The C–H····M interactions vary in their nature and strength ranging from electrostatic to covalent, therefore computational approaches which account well for the electrostatic interactions such as QTAIM and NCI and the orbital interactions between C–H and metal, such as NBO have been used. The QTAIM properties associated with the bond critical point such as electron density, Laplacian of the electron density, ellipticity and QTAIM atomic basin properties such as atomic charge, volume and energy, are the main descriptors used for C–H···M interactions. The $E(2)$ value obtained from an NBO analysis accounts for donor-acceptor interactions as it contains terms for the driving forces: which are the spatial overlap and the energy resonance. Further information can be taken from the spectroscopic data, which include the ^1J C–H coupling constant, the proton chemical shift and the C–H vibrational frequency.

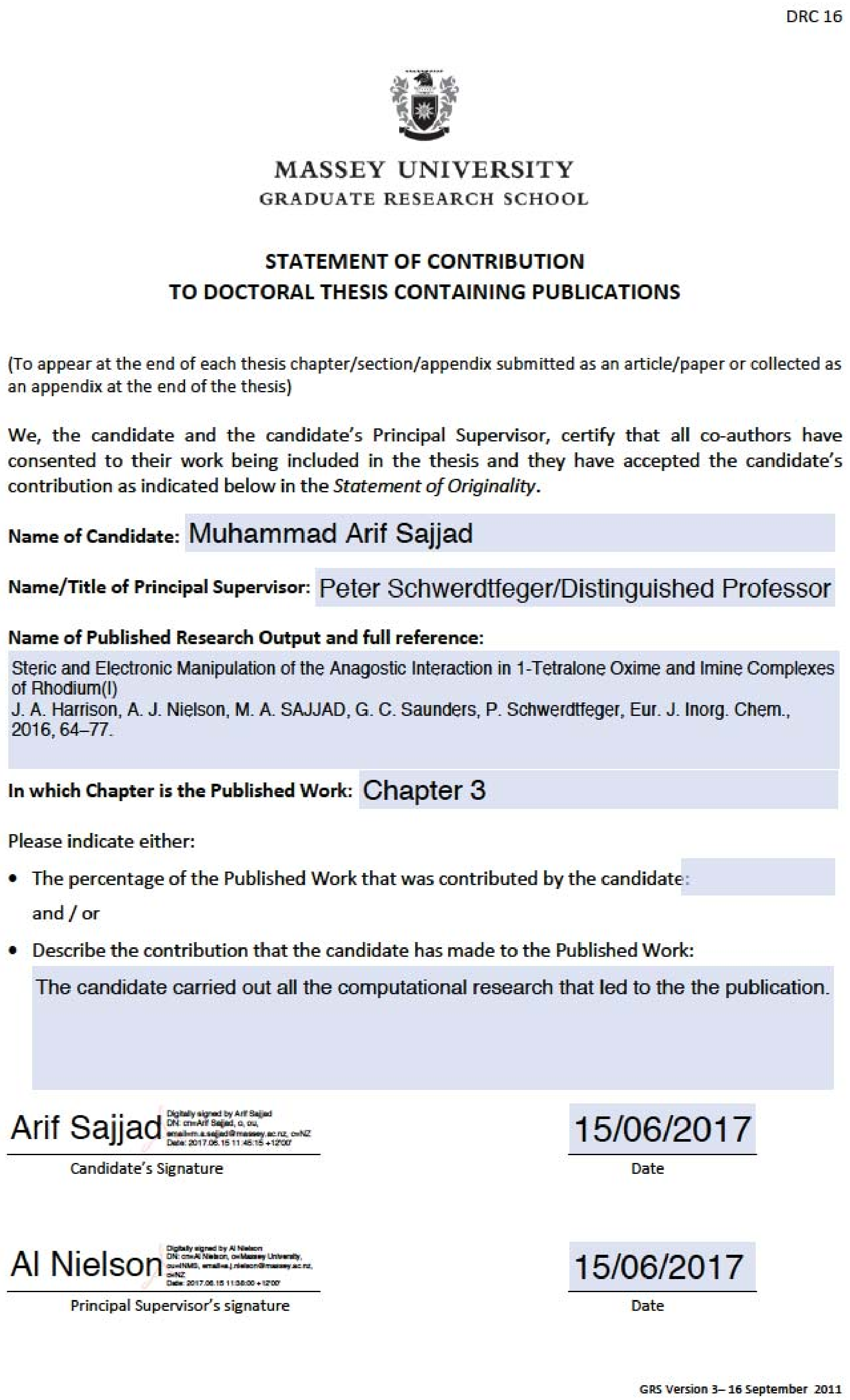

DRC 16

MASSEY UNIVERSITY
GRADUATE RESEARCH SCHOOL

STATEMENT OF CONTRIBUTION TO DOCTORAL THESIS CONTAINING PUBLICATIONS

(To appear at the end of each thesis chapter/section/appendix submitted as an article/paper or collected as an appendix at the end of the thesis)

We, the candidate and the candidate's Principal Supervisor, certify that all co-authors have consented to their work being included in the thesis and they have accepted the candidate's contribution as indicated below in the *Statement of Originality*.

Name of Candidate: Muhammad Arif Sajjad

Name/Title of Principal Supervisor: Peter Schwerdtfeger/Distinguished Professor

Name of Published Research Output and full reference:

Steric and Electronic Manipulation of the Anagostic Interaction in 1-Tetralone Oxime and Imine Complexes of Rhodium(I)
J. A. Harrison, A. J. Nielson, M. A. SAJJAD, G. C. Saunders, P. Schwerdtfeger, Eur. J. Inorg. Chem., 2016, 64–77.

In which Chapter is the Published Work: Chapter 3

Please indicate either:

- The percentage of the Published Work that was contributed by the candidate:

  and / or

- Describe the contribution that the candidate has made to the Published Work:

  The candidate carried out all the computational research that led to the the publication.

Arif Sajjad Digitally signed by Arif Sajjad
DN: cn=Arif Sajjad, o, ou,
email=m.a.sajjad@massey.ac.nz, c=NZ
Date: 2017.06.15 11:46:15 +12'00'

Candidate's Signature

15/06/2017

Date

Al Nielson Digitally signed by Al Nielson
DN: cn=Al Nielson, o=Massey University,
ou=INMS, email=a.j.nielson@massey.ac.nz,
c=NZ
Date: 2017.06.15 11:38:00 +12'00'

Principal Supervisor's signature

15/06/2017

Date

GRS Version 3– 16 September 2011

Chapter 3

Steric and Electronic Manipulation of Anagostic interactions in Oxime and Imine Complexes of Rhodium (I)

3.1 Introduction

The transformation of a C–H bond into a new C–C or C–Y bond has become an attractive strategy in many industrial processes which are involved in the production of pharmaceuticals, natural products, and luminescent materials.[100] One of the useful reactions in this area is the ligand-directed cyclometallation reaction where a metal-carbon (M–C) bond is formed after the activation of C–H bond in a transition-metal catalysed process.[101] However, the M–C bond formation is not a straightforward reaction and involves several different intermediates.[10,101] These intermediates have been termed as the well-known agostic intermediate and the less well-known anagostic,[28,31] pseudoagostic[32] or preagostic[33-34,102]intermediates. The agostic interactions have been described as partial-covalent type interactions in which a C–Hσ bond donates electron density to the metal centre,[28] whereas the anagostic interactions are electrostatic type interactions.[28] The literature shows that an investigation of these C–H····M interactions by varying the properties of the ligands has not been fully explored. A detailed understanding of the anagostic interaction can be advantageous for designing the ligands for the ligand-directed C–H bond activation process.[103]

X-ray studies indicate that there is an above-plane orientation of a ligand for the anagostic interaction, whereby a C–H bond hydrogen makes a close approach to metal centre. The close approach is identified in the ^{1}H NMR spectrum by a downfield shift for the interacting hydrogen compared to the free ligand.[104] Until now, two close approaches for the anagostic interactions have been recognised. The first type is the long M····H approach where the M····H distance is usually in the range of 2.5 to 2.80 Å whereas the other type is the short M···H approach where the distance between metal and aromatic hydrogen is usually below 2.5 Å.[34] Previous studies indicate that the increase in steric congestion at the coordinating atom forces the C–H hydrogen close to the metal and this increases the chances of the cyclometallation reaction to occur.[105] Whereas the literature gives experimental and theoretical evidence for these categorised approaches,[34–36] a rational systematic study of steric and electronic influences for both of these anagostic approaches is lacking.[104] In the present work, various electron donating and withdrawing substituents are used at appropriate positions on the ligand to study electronic influences and steric effects.

3.2 Aim

- To manipulate by electronic and steric effects the anagostic interactions in 1-tetralone oxime and imine complexes of rhodium (I).

3.3 Choice of Steric and Electronic Substituents

^{1}H NMR studies have shown that the complex [Rh(CO)$_2$Cl(1-tetralone oxime)] exhibits a downfield chemical shift for an above-plane hydrogen compared to the free ligand.[104a]A molecular model shows that for the [Rh(CO)$_2$Cl(1-tetralone oxime)] complex (Figure 3.1) the C^8–H hydrogen would lie above the coordination plane and make a close approach to the metal when the nitrogen atom of the ligand coordinates to the rhodium centre.

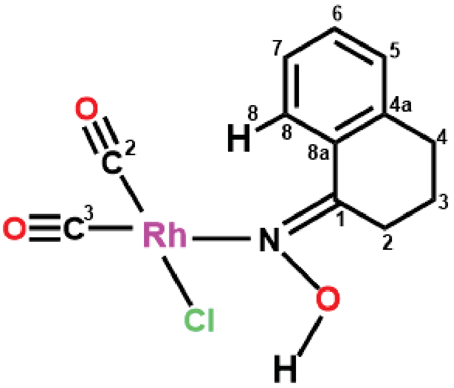

Figure 3.1 Molecular model showing the structure and numbering for [Rh(CO)$_2$Cl(1-tetralone oxime]).

The complexes for which calculated structures were obtained are shown in scheme 3.1. The structure of [Rh(CO)$_2$Cl(1-tetralone oxime] complex **1** was initially obtained and then a variety of N-substituents were used to change the steric size at the coordinating atom, i.e. complexes **2**–**5** where the OH (**1**) has been replaced by OMe (**2**), OCMe$_3$ (**3**), Me (**4**) and CMe$_3$ (**5**) groups respectively.

To see the electronic effects on the metal···H^8 separations, the strongest electron donating and withdrawing groups available were used to influence either the σ or π-systems of the aromatic ring but not both at the same time.[106] The choice of the *para* substituents was based on the stronger electronic influence at the *para* position compared to the *meta* position (complexes **7–10)**, but not the *ortho* position to the C–H^8 group as it can involve a combination of steric (complexes **11–13**) and electronic effects (complexes **14–16**).[107] The effects were then compared with the unsubstituted ligand complex **1** similar to the Hammet protocol.[106] The substituents used for σ and π-electron withdrawing effects were SO_2Cl (F value: 1.16; R value: –0.05)[106], complex **7**, and N=NPO(OEt)$_2$ (F value: –0.05; R value: 0.79)[106], complex **8**, respectively. The substituents used for σ and π-electron withdrawing effects were $B(OH)_3^-$ (F value: –0.42; R value: –0.02)[106], complex **9** and S^- (F value: –0.03; R value: –1.24)[106], complex **10**. To further influence the metal···H^8 close approach, a combined electronic and steric effect was used in **17** where NH_2 (F value: –0.08; R value: –0.74)[106] at R^1 or C^7 and S^- at R^2 or C^5 position along with (N)–CMe$_3$ was placed.

Scheme:

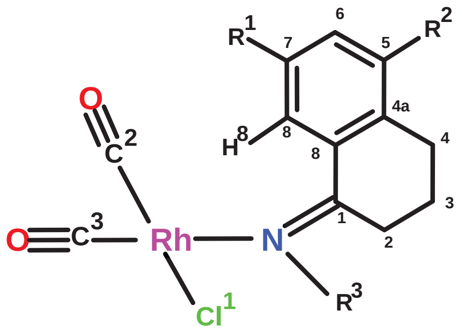

(**1**) R^1, R^2 = H, R^3 = OH
(**2**) R^1, R^2 = H, R^3 = OMe
(**3**) R^1, R^2 = H, R^3 = OCMe$_3$
(**4**) R^1, R^2 = H, R^3 = Me
(**5**) R^1, R^2 = H, R^3 = CMe$_3$
(**7**) R^1 = H, R^2 = N$_2$PO(OEt)$_2$, R^3 = OMe
(**8**) R^1 = H, R^2 = SO$_2$Cl, R^3 = OMe
(**9**) R^1 = H, R^2 = B(OH)$_3^-$, R^3 = OMe
(**10**) R^1 = H, R^2 = S$^-$, R^3 = OMe
(**11**) R^1 = Me, R^2, R^3 = H, R^3 = OH
(**12**) R^1 = Me$_2$CH, R^2 = H, R^3 = OH
(**13**) R^1 = CMe$_3$, R^2 = H, R^3 = OH
(**14**) R^1 = NO$_2$, R^2 = H, R^3 = OH
(**15**) R^1 = OMe, R^2 = H, R^3 = OH
(**16**) R^1 = F, R^2 = H, R^3 = OH
(**17**) R^1 = NH$_2$, R^2 = S$^-$, R^3 = CMe$_3$

Complex (6)

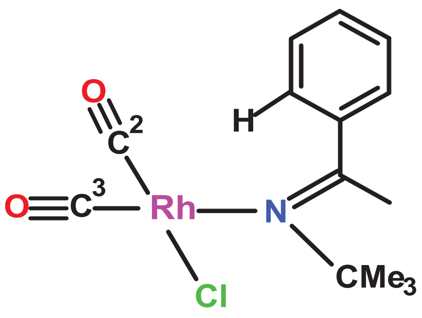

Scheme 3.1 Computed rhodium (I) complexes.

3.4 Computation Approach

DFT calculations using the dispersion-corrected Grimme PBE-D3 functional[76,77] were used to optimise the structures of the coordination complexes **1**–**17** using Gaussian09 software[108]. The choice of PBE-D3 was based on dispersion factors which are necessary for weak interactions. However, a comparison with some other popular DFT functionals for transition metal complexes such as B3LYP[73], BP86[72], CAM-B3LYP[109] and CAM-B3LYPD3[110] was made for complex **2**. A triple-zeta quality basis set (aug-cc-pVTZ-PP)[111] for rhodium metal; aug-cc-pVTZ[95] for attached ancillary ligands (Cl and CO) and the anagostic hydrogen atom and a double-zeta quality basis set (aug-cc-pVDZ)[95] for remainder of the atoms were employed. All the optimised structures were energy minimised and were verified by vibrational analysis, which showed no imaginary frequency for any of the complexes. The wavefunction files (.wfx or .wfn) for QTAIM analysis were obtained from the Gaussian calculations and the QTAIM calculations were performed by the AIMALL software[112]. The NBO calculations were carried out using the NBO 6.0 software[113] and NBOVIEW 2.0 was used to visualise the NBO overlaps.[113] The NCI calculations were performed using NCIPLOT 2.0[99] and the VMD 1.9.2[114] was used to visualise the 3D iso-surfaces.

The same basis sets were used to calculate the NMR spectral properties. However, for the ^1JC–H calculation, the basis set was decontracted for the C and H to allow for a more accurate determination of the electron density at the nucleus. The similar methodology was used for the ligands calculations.

3.5 Results and Discussion

3.5.1 DFT Computed Structure and Properties of [Rh(CO)$_2$Cl(1-tetralone oxime)], Complex 1

Computational calculations using the density functional theory (DFT) based PBE-D3 hybrid functional were carried out to optimise the geometries for the oxime and imine complexes [RhCl(CO)$_2$(L)] (L = 1-tetralone oxime and imine derivatives) shown in (Scheme 1). For the analysis of [RhCl(CO)$_2$(1-tetralone oxime)] (**1**), for which the crystal structure is not available,[104a] two configurations for **1** were computed (Figure 3.1). It was found that the structure **1**, where the H^8 sits out towards the chloro ligand, is 5.4 kcal mol^{-1} more stable compared to structure **1a** where H^8 sits out over the *cis*-CO ligand. The reason for the greater stability of structure **1** is expected to be related to hydrogen bonding between Cl and the OH group of the ligand [distance: 2.071 Å]. Also, the structure **1** is the more relevant configuration to proceed with cyclometallation reaction, as hydrogen is inclined towards the proton acceptor Cl$^-$ ligand.[9-10] Hence, in the present work, the structure **1** was chosen as a reference complex for further analysis.

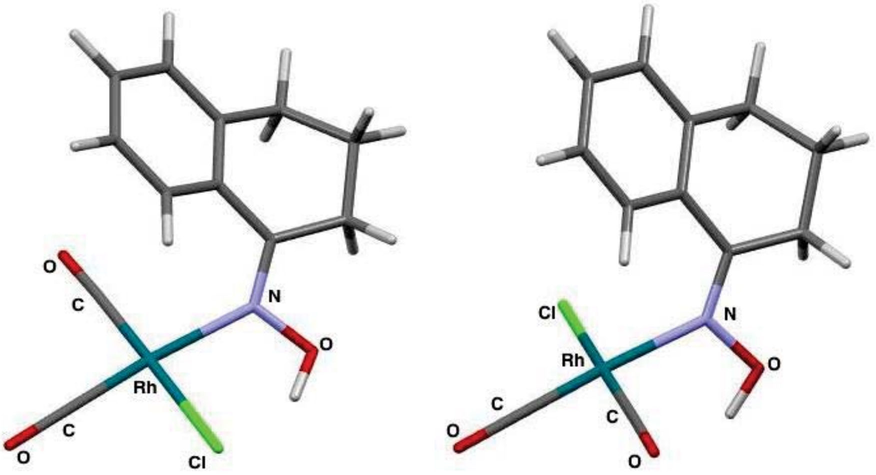

1 **1a**

Figure 3.1 DFT structures of **1** and **1a**.

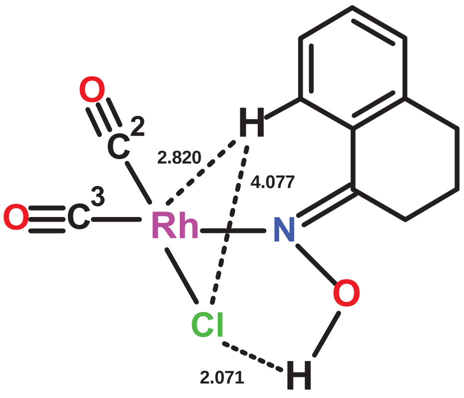

Figure 3.2 Important separations in complex **1**.

In the preferred configuration, the structure of complex **1** shows that upon coordination, the chair-like form of the free ligand changes to a boat-like form. Due to this conformational change, the benzene ring tilts away from the metal centre such that H^8 points out towards the chloro ligand with a large separation [H^8···Cl distance: 4.077 Å]. H^8 lies over the metal coordination plane where the Rh···H^8 separation is 2.820 Å and the Rh···H^8–C angle is 110^o (Table 3.2). As mentioned earlier, below the coordination plane the OH group of the oxime ligand makes a very close approach to Cl [OH····Cl distance: 2.071 Å] which is well inside the van der Waals separation [2.95 Å][115] and indicates a strong M–Cl···HO interaction.[116] However, the M–Cl····HO angle [value: 74.6^o] is smaller than the range of angles [80–140^o] found for most M–Cl····HO interactions.[116] The presence of this interaction essentially 'locks' the ligand rotation about the Rh–N bond leading to the OC^2–Rh–N=C (the dihedral angle between the C=N bond on the Rh coordination plane) of 30.6^o which assists in pointing the C–H^8 hydrogen out towards Cl (Figure 3.1 for molecular structures; Figure 3.2 for the separations).

Comparing the free ligand and coordinated ligand for complex **1**, there are some notable torsional changes seen in the later. For instance, the N=C^1–C^{8a}–C^8 dihedral angle changes from –14.5^o (free ligand) to 32.8^o (complex) and the C^1–C^{8a}–C^8–H^8 changes from –1.50^o (free ligand) to 2.3^o (complex). These torsional differences indicate a large conformational change associated with the alicyclic ring in the complex where the chair-like form of the free ligand changes into a boat-like form on complexation. The Rh–carbonyl ligand metrics [Rh–C^{2}O and Rh–C^{3}O bond distances: 1.843 and 1.841 Å respectively], Rh–Cl bond length [value: 2.356 Å] and the corresponding angles are very similar to the non-anagostic structures in the rhodium complexes [Rh(CO)$_2$Cl(NH$_3$)][117] and [Rh(CO)$_2$Cl(pyridine)].[118] Comparisons of the complex **1** with these two structures, indicates that the Rh–N bond length [value for **1**: 2.134 Å] is intermediate between the DFT optimised structures for [Rh(CO)$_2$Cl(NH$_3$)] [Rh–N value: 2.187 Å][117] and [Rh(CO)$_2$Cl(pyridine)] [Rh–N value: 2.122(7) Å][118] but there are no significant differences in the other structural parameters about the coordination plane, so it appears that the oxime ligand aromatic ring does not exert a steric effect on the overall coordination geometry.

To determine the nature of the interactions of the close separations in **1**, especially for the Rh···H^8 separation, computational approaches which have been successful for evaluating the C–H····M interactions were employed.[35,66] QTAIM analysis which gives a topological description of bonding based on the electron density, shows a bond path and associated bond critical points between interacting atoms in a molecule.[51] However, in some cases, a bcp can be obliterated as it is known that when a ring critical point (rcp) is very close to the bond critical point (bcp), the two can coalesce and form a degenerate critical point. Therefore, care should be taken in interpreting the absence of bcp data in QTAIM analysis.[119] To resolve this problem recently developed NCI index method can be used whereby the reduced density gradient indicates an iso-surface between the atoms which lack a bcp.[99]

Turning to the calculated spectroscopic data, the ^{1}H NMR spectrum for **1** shows a downfield chemical shift of 0.52 ppm for H^8 compared with the free ligand and a small increase in the ^1JC–H coupling constant [154.1 and 139.4 Hz for **1** and free ligand, respectively] (Table 3.1) and both of these NMR spectroscopic features indicate the presence of the anagostic interactions.[28] The calculated C–H stretching frequency, νC–H, for complex **1** is 3105.2 cm^{-1}, which is 28.2 cm^{-1} lower compared to the free ligand which has a value of 3133.4 cm^{-1} (Table 3.1). The change in vibrational frequency reflects the admixture of other masses into the normal vibrational mode of formation of the complex as there is almost no change in the C–H bond length in the complex compared with the free ligand [bond lengths in complex **1** and the ligand: 1.091 and 1.090 Å, respectively). To see the strength of the C–H interaction, a more meaningful comparison between the elements in the second derivative matrix values in the free ligand and the complex indicates an insignificant difference (0.1 %). This is in full accord with the almost negligible changes in the parameters of the C–H bond length.

The QTAIM analysis [51] (Table 3.2) shows a bond path and bond critical point (bcp) between the metal and H^8. A smaller value for the electron density, ρ(bcp) and Laplacian of the electron density, $\nabla^2\rho$(bcp) [values: 0.0122 *e*/Bohr^3 and 0.0309 *e*/Bohr^5, respectively] indicate a weak electrostatic interaction which is similar to that found for other anagostic interactions.[34] The small positive value for the energy density [*H*(bcp): 0.0004 Hartree/Bohr^3] and a value close to 1 for |V|/G (|V| = absolute potential energy density, G = kinetic energy density) [value: 0.9460] also indicates the electrostatic dominance of the interaction. The QTAIM charges for both Rh and H^8 hydrogen are positive [values: 0.626 and 0.038 *e*, respectively] which would suggest the presence of an electrostatic repulsive interaction. For the Cl···HO separation, the QTAIM molecular graph (Figure 3.3a) shows a bond path with bcp properties [ρ(bcp): 0.0369 *e*/Bohr^3; $\nabla^2\rho$(bcp): 0.0650 *e*/Bohr^5 and *H*(bcp): -0.0060 Hartree/Bohr^3] indicating an electrostatic interaction with some covalency involved which is a feature of weak hydrogen bonding interactions. The QTAIM charges for Cl and H(–O) bond hydrogen [–0.554 and 0.592 *e*, respectively] also indicate an attractive situation (refer to Table 3.6 in Appendix A.2).

The recently reported non-covalent interaction index (NCI)[99] which is based on the reduced density gradient (RDG), s(r), is a useful tool to visualise the intramolecular or intermolecular interactions in a qualitative (3D picture) as well as a quantitative way (2D picture). The RDG, *s*(r), is a dimensionless quantity that specifies the behaviour of charge density, *ρ*(r), in the context of its local deviation from homogeneous electron gas. The lower bound of RDG reaches to zero when the gradient of electron density vanishes (e.g., at bond critical points). Hence, the low-value RDG iso-surfaces provide a simple and easy presentation of those regions of the electron density distribution that are dominated by specific non-covalent interactions. In addition, by using the sign of second largest eigen value, λ_2, of the electron density Hessian matrix, the nature of interactions can be distinguished in the sense that $\lambda_2 < 0$ indicate attractive and $\lambda_2 > 0$ repulsive interaction. In NCI analysis, when the quantity *ρ*(r).sign(λ_2) is mapped onto the RDG isosurface, both the nature and strength of the interactions can be determined. The RDG has similarities with the QTAIM electron density topology, as a low-RDG iso-surface will appear at any critical point where a stabilising interaction occurs. However, the RDG-based NCI descriptor can also indicate other than stabilising interactions, which do not appear in QTAIM bond paths.[99]

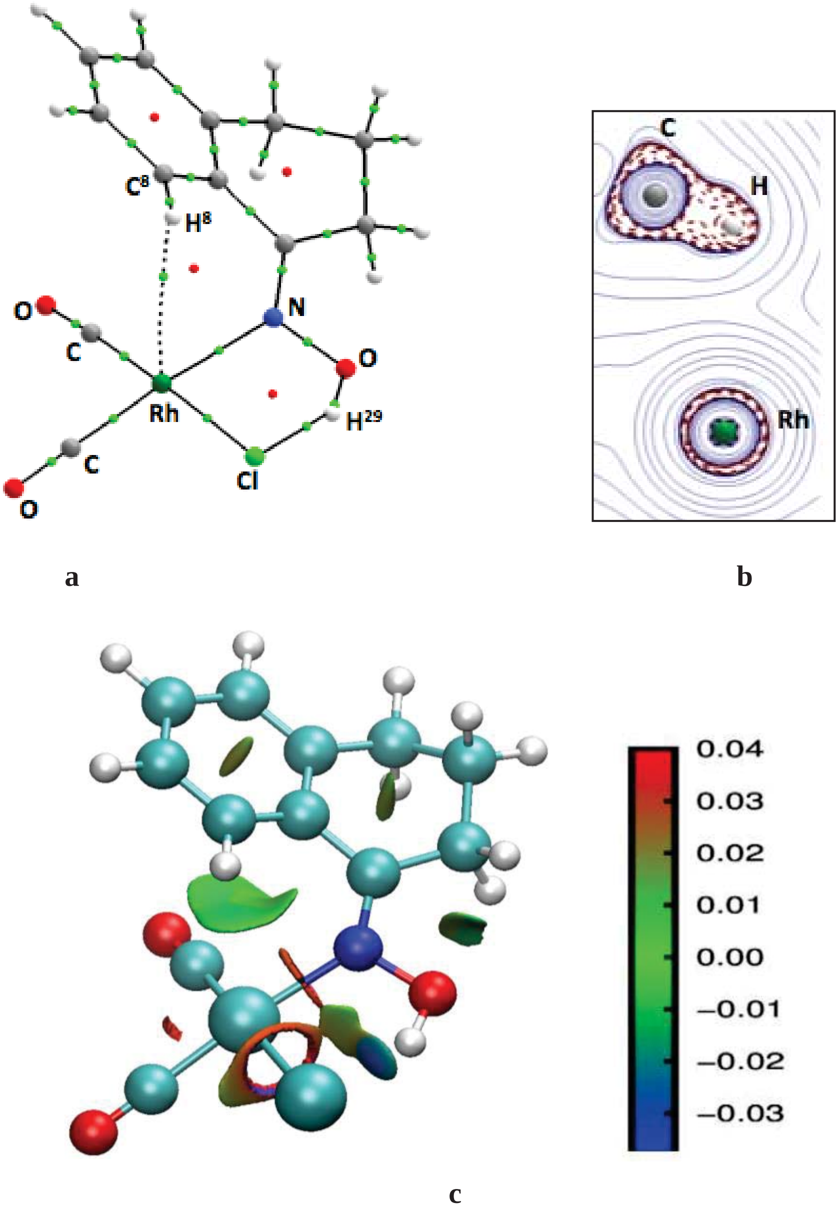

a

b

c

Figure 3.3 a) QTAIM molecular graph; b) Laplacian of electron density contour plot for C–H····M interaction; c) 3D NCI RDG iso-surface for **1**. The sign of the second Hessian eigenvalue (λ_2) times the electron density is shown by the colour map.

Based on a colour scheme, the NCI 3D RDG iso-surface describes the interaction as the attractive, repulsive or delocalised type when the surfaces appear as blue, red and green respectively. Also, the depth of the colour is associated with the interaction strength.[120] For complex **1**, 3D NCI RDG iso-surface (Figure 3.3c) verifies the interactions which were seen in the QTAIM molecular graph as there is a green surface present between the metal and C–H bond which indicates a weak delocalised interaction but in an attractive situation. The small donation between the C–H^8σ electron density and the metal orbitals are responsible for the green colour even though the QTAIM charges indicate a repulsive electrostatic interaction. There is a blue spot between OH and Cl atoms which indicates a much stronger bonding interaction for the H····Cl separation.

The NBO analysis[98]which demonstrates a Lewis picture of chemical bonding, shows little donation associated with Rh and C–H orbitals in complex **1**. The respective donations include LP (1) Rh to C–Hσ* orbital [*E*(2) value: 0.73 kcal mol^{-1}], LP (1) Rh to C^8–C^{8a}π* orbital [*E*(2) value: 0.56 kcal mol^{-1}] and C–Hσ to Rh–Cσ* orbital [*E*(2*)* values for Rh–C^2σ* and Rh–C^2σ*: 0.32 and 0.67 kcal mol^{-1}, respectively] being consistent with the QTAIM analysis which indicated the presence of minimal covalency. It is apparent from the energies and occupancies of the corresponding C–H and rhodium orbitals that the large difference in NBO energies between donor and acceptor NBOs is the major obstacle to efficient NBO overlap (refer to Table 3.4). Regarding the Cl····HO interaction, the NBO analysis verifies the covalency involved as there is a donation from LP(3) Cl to the O–Hσ* orbital with *E*(2) value of 15.9 $kcalmol^{-1}$. Other studies on the C–H····M interactions have shown that in square planar transition metal complexes, some covalency can develop when the H to metal distance is less than 2.35 Å.[34] which is much shorter than the C–H····Rh separation in **1** [2.820 Å].

3.5.2 Steric Effects at Nitrogen, Complexes 2–6

In cyclometallation reactions, it has been postulated that an increase in steric influence at the coordinating atom can shorten the C–H hydrogen and metal distance and consequently enhance the possibility of the reaction occurring.[105] Therefore, to ascertain the steric influence on the metal···hydrogen approach, complexes with various (N)–substituents were calculated.

The structural features of complex **2** (Table 3.1), where the OH group attached to N in **1** has been replaced with OMe, indicate significant changes in the structural parameters. With respect to distances, the Rh–N bond length in **2** increases to 2.150 Å in comparison to 2.134 Å in **1**, the Rh····H^8 separation is shorter than in **1** [2.624 and 2.820 Å values, respectively], the Cl····H^8 separation is significantly decreased in **2** [4.077 and 2.753 Å, respectively] and the Rh···C^8 separation is also reduced in **2** [3.354 and 3.104 Å, respectively] (Figure 3.4b). However, the variations in angles are more significant. For instance, the dihedral angle, (O)–C^2–Rh–N=C (refer to Figure 3.4b for the numbering) is larger in **2** than in **1** [69.2 and 30.6°, respectively] and this increase in dihedral angle shifts the H^8 hydrogen over the coordination plane more towards Cl as indicated by the Cl····H^8–

C^{8} angle which is more linear compared to **1** [values: 156.3 and 137.5^{o}, respectively]. The plane angle between the ligand aromatic ring and metal coordination sphere is increased to 65.4^{o} [c.f. 51.2^{o} in **1**] (Figure 3.5) whereas the Rh–N=C push-back angle (defined by the C=N bond with respect to the Rh coordination plane) is decreased in **2** [127.2^{o}; c.f. 132.9^{o} in **1**].

Further structural features indicate there are close approaches below the metal coordination plane between Rh and H^{32}–C with a distance of 2.721 Å, along with the corresponding angle of 101.3^{o} and also for the Cl····H^{30}–C separation with a distance of 2.762 Å and a corresponding angle of 124.3^{o} (Figure 3.4b).

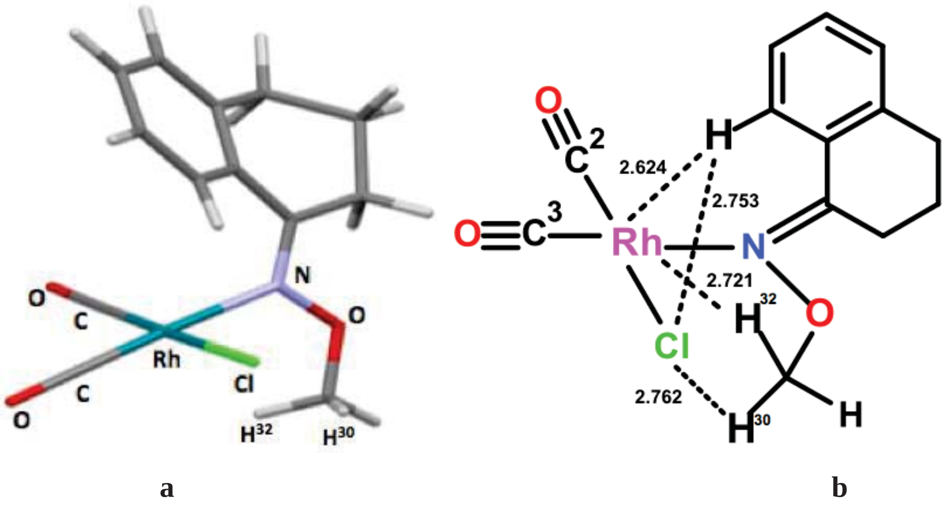

Figure 3.4 a) Optimised structure; b) Important separations for complex **2**.

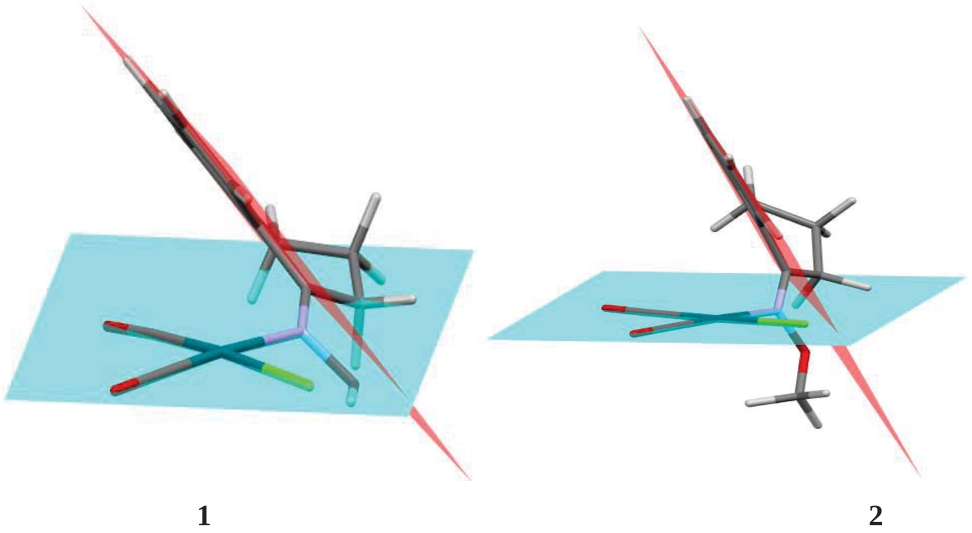

Figure 3.5 Optimised structures with aromatic and coordination planes for **1** and **2**.

The QTAIM analysis of **2** indicates three bcps (Figure 3.6a) where the two bcps below the plane belong to approaches for Rh···H^{30} [distance: 2.721 Å] and Cl···H^{32} [distance:

2.762 Å] separations, whereas the third one corresponds to the above plane $Rh\cdots H^8$ separation [distance: 2.624 Å]. The QTAIM properties for the $Rh\cdots\cdot H^8$ close approach in **2** show a small increase in the electron density compared with **1** as indicated by the Laplacian values [$\nabla^2\rho$: 0.0446 and 0.0309 *e*/Bohr^5 in **2** and **1**, respectively] (Table 3.3) but the total energy density is almost unchanged [*H*(bcp): 0.0003 and 0.0004 Hartree/Bohr^3 for **2** and **1**, respectively]. The atomic basin charges [*q*(Rh) and *q*(H^8): 0.635 and 0.061 *e*, respectively] again suggest a repulsive nature for the $Rh\cdots H^8$ interaction in **2**. Looking at the C–H^8 bcp properties, only very small differences between the complex and the free ligand are observed (Table 3.3). Comparison of the atomic basin properties for **2** and **1** shows a significant increase in the H^8-atomic charge in **2** [0.061 and 0.038 *e*, respectively for **2** and **1**] and in comparisons with the free ligands, the H^8 atomic charge in **2** is significantly increased [*q*(H) for complex and free ligand: 0.061 and 0.040 *e* in **2**, respectively; c.f. 0.038 and 0.040 *e* in **1**, respectively]. The other atomic basin properties such as the total energy (*E*), dipolar polarisation (*M*) and atomic volume (*V*) for H^8 only differ slightly in both **2** and **1** while for the free ligands for **2** and **1**, these properties are nearly identical (Table 3.3). Interestingly, no bcp was found for the above-plane $Cl\cdots\cdot H^8$–C^8 separation in **2** where the distance is 2.753 Å and the associated angle is 156.3°.

Regarding the below plane bond paths, the QTAIM analysis (refer to Table 3.6 in Appendix A.2) indicates a weakly electrostatic repulsive interaction for the the $Rh\cdots H^{32}$ separation as shown by the bcp properties, for which the Laplacian of electron density, energy density and QTAIM charges *q* for Rh and H^{32} are all positive [$\nabla^2\rho$ and *H*(bcp) values: 0.0446 *e*/Bohr^5 and 0.0004 Hartree/Bohr^3, respectively; *q*(Rh) and *q*(H^{32}) values: 0.635 and 0.045 *e*, respectively]. However, the second bcp below the coordination plane, $Cl\cdots H^{30}$, shows an attractive electrostatic interaction as the QTAIM charges for Cl and H^{30} are negative and positive [*q* values: –0.563 and 0.081 *e*, respectively] and the values for Laplacian of electron density and energy density are both positive [$\nabla^2\rho$: 0.0327 *e*/Bohr^5; *H*(bcp): 0.0013 Hartree/Bohr^3].

As there was no bcp was found for the $Cl\cdots H^8$ close approach [distance: 2.753 Å], an NCI analysis[99] was performed to see whether the interaction is present or not. The 3D NCI iso-surface picture (Figure 3.6b) shows a light blue spot between Cl and H^8 which reveals the presence of an attractive interaction which was not shown in QTAIM analysis.

The spectroscopic properties of the $Rh\cdots\cdot H^8$ interaction in complex **2** (Table 3.1), show there is a negligible change in C–H^8 stretching frequency and ^1JC–H coupling constant from the respective ligand compared with complex **1** [$\Delta\nu$C–H^8 and Δ^1JC–H values: 29.8 cm^{-1} and 3.8 Hz, respectively; c.f. 28.1 cm^{-1} and 3.8 Hz, respectively for **1**]. The smaller ^1JC–H increase in **2** correlates with the QTAIM parameters which disfavour the electron density donation from the C–H bond to the metal centred orbitals. However, there is a more downfield chemical shift for H^8 in **2** compared to **1** in the ^{1}H NMR spectrum [Δδ: 1.24 and 0.52 ppm, respectively]. As H^8 in **2** has a closer approach with the Rh and Cl atoms, it appears that the large downfield chemical shift can be attributed to anisotropy contributions[121] from both the metal and Cl so that the extent of the downfield shift would appear to be related to this aspect.

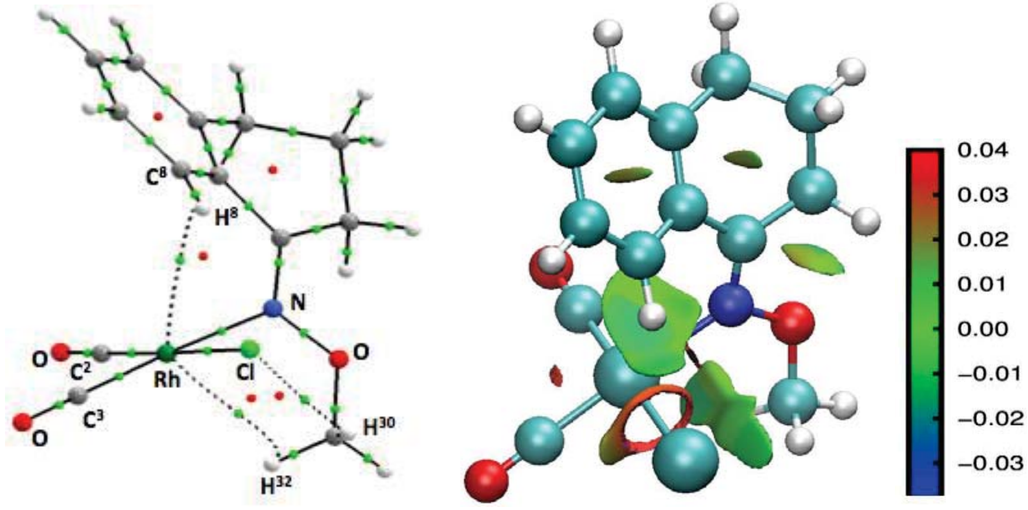

a **b**

Figure 3.6 a) QTAIM molecular graph; b) 3D NCI RDG iso-surface for **2**. The sign of the second Hessian eigenvalue (λ_2) times the electron density is shown by the colour map.

The NBO analysis for **2** (Table 3.4), as for **1**, identifies very small donations associated with C–H^8 and metal orbitals. It is seen that replacing OH by OMe has little meaningful influence on the Rh or C–H^8 energies in the way of developing efficient overlap, with a negligible change in the *E*(2) values from the C–Hσ to Rh–Cσ* orbitals being found [*E*(2) values for the donation from C–Hσ to the Rh–C^{2}σ* and to the Rh–C^{3}σ*: 0.90 and 1.01 kcal mol^{-1}, respectively for **2**; c.f. 0.32 and 0.67 kcal mol^{-1}, respectively for **1**]. However, with respect to structural changes, where the C^8 and H^8 atoms become closer to the Rh centre [distance values: 3.104 and 2.624 Å, respectively] comparatively larger donations are seen from the Rh lone pair to the C^8–C^{8a}π* orbital, in **2** compared to **1** [*E*(2) values: 2.14 and 0.56 kcal mol^{-1}, respectively]. In the same way, as the Cl ligand becomes closer to H^8, the donations from Cl lone pairs to the C–H^{8}σ*orbital become large [*E*(2) values: 0.25 and 1.11 kcal mol^{-1}; c.f. 0.0 kcal mol^{-1} for **1**] (Table 3.4). As the QTAIM analysis showed the Rh···H^8 interaction (Figure 3.6a; Table 3.3) is dominated by electrostatics, the absence of meaningful donations shown by the NBO analysis confirms that the anagostic interaction is purely electrostatic type interaction without noticeable orbital overlap between metal and C–H orbitals. Another structural parameter (Table 3.1) associated with the C–H^8···Rh separation that does not point to an overlap between the orbitals in **2** as the C–H^8···Rh bond angle which at 105.8^o is far from the linearity to give efficient Rh to C–Hσ* overlap.[41]

One of the most important aspects in computational chemistry is to check the suitability of the DFT functional.[80] In the present work, testing of DFT functionals was done by optimising the structure of complex **2** by the DFT functionals used by other workers for transition metal complexes such as BP86[72], B3LYP[73], CAM-B3LYP[109] and CAM-B3LYP-D3[110]. A structural feature comparison for **2** (Table 3.2) shows the similarity for most of the structural parameters obtained from functionals that include dispersion such as, PBE-D3 and CAM-B3LYP-D3. However, the Rh···H^8 separations are comparatively shorter in PBE-D3 compared with BP86 [Rh···H^8 distance: 2.624 and 2.683 Å, respectively; Rh····H^{32}, 2.721 and 2.732 Å, respectively]. In comparison with other functionals, PBE-D3 gives the shortest separations for the Rh···H^8 and Rh····C^8 separations compared to other functionals, and out of BP86 and B3LYP, BP86 is closer to PBE-D3 for these separations [Rh···H^8 distance: 2.624, 2.607 and 2.684 Å; Rh···C^8: 3.104, 3.150 and 3.207 Å for PBE-D3, BP86, and B3LYP, respectively].

Comparing the B3LYP and CAM-B3LYP structural features, CAM-B3LYP gives relatively shorter bond lengths and smaller bond angles. Overall, BP86, CAM-B3LYP, and CAM-B3LYPD3 perform similar to PBE-D3 but as the separations are shortest with PBE-D3, and includes the dispersion factors essential for weak interactions,[76] therefore, it justifies the use of PBE-D3 functional. A recent computational study based upon DFT shows the PBE-D3 functional is a reliable method for the study of anagostic interactions.[66] Thus, the PBE-D3 functional is used for all further calculations.

Replacing the (N)–OMe group in **2** by (N)–OCMe$_3$, complex **3**, the ligand moves slightly more upright as shown by a small increase in the C^2–Rh–N=C^1 dihedral angle [73.6^o compared with 69.2^o in **2**] (Figure 3.7a; Table 3.1) but more particularly by a noticeable increase in the angle between the aromatic ring and metal coordination planes which is almost 10^o larger [values: 74.9^o; c.f. 65.4^o in **2**]. Torsional changes in the ligand are seen in the N=C^1–C^{8a}–C^8 dihedral angles [31.9^o and 34.4^o in **3** and **2**, respectively] and the C^1–C^{8a}–C^8–H^8 dihedral angles [3.9^o and 6.3^o in **3** and **2**, respectively].

Table 3.1 Selected structural parameters and spectral data for complexes **1–17**.[a]

Complex	**1**	**2**	**3**	**4**	**5**	**6**	**7**	**8**	**9**
Bond Length									
Rh–N	2.134	2.150	2.166	2.124	2.182	2.161	2.136	2.150	2.146
Rh–Cl	2.356	2.351	2.366	2.348	2.382	2.367	2.335	2.349	2.371
C–H^8	1.091	1.092	1.090	1.092	1.091	1.090	1.090	1.092	1.092
(Ligand)	**1.090**	**1.090**	**1.090**	**1.090**	**1.090**	**1.090**	**1.090**	**1.090**	**1.091**
Separation									
Rh····H^8	2.820	2.624	2.764	2.586	2.548	3.030	2.651	2.632	2.584
Rh····C^8	3.354	3.104	3.211	3.105	2.861	3.131	3.116	3.061	3.035
Cl····H^8	4.077	2.753	2.534	2.919	2.542	2.736	4.020	2.698	2.863
Angles (^{o})									
Rh–N=C^1	132.9	127.2	125.4	127.6	118.7	117.4	128.6	126.7	126.6
Rh····H–C^8	110.1	105.8	104.3	108.2	95.2	85.1	105.0	102.6	103.8
Rh··· C–H^8	52.2	51.2	56.5	52.3	62.5	74.6	55.3	57.1	55.8
Cl····H–C^8	137.5	156.3	156.2	154.9	150.7	133.0	71.4	154.6	154.2
Dihedrals (^{o})									
(O)C^2–Rh–N=C	30.6	69.2	73.6	64.6	70.4	79.7	115.0	69.1	66.9
Ar-Plane/CP^b	51.2	65.4	74.9	62.7	58.7	54.1	59.7	62.5	60.9
N=C^1–C^{8a}–C^8	32.8	34.4	31.9	33.7	37.4	67.9	-36.8	36.3	32.4
(Ligand)	**-14.5**	**-14.4**	**-14.6**	**-11.5**	**2.2**	**0.0**	**-13.4**	**-14.4**	**-15.7**
C^1–C^{8a}–C^8–H^8	2.3	6.3	3.9	5.7	9.3	-1.1	-6.6	7.5	10.4
(Ligand)	**-1.5**	**-1.4**	**-1.5**	**-1.1**	**-0.7**	**-0.0**	**-1.9**	**-2.0**	**-2.9**
H^7–C^7–C^8–H^8	-1.0	-2.9	-1.5	-2.2	-4.5	0.4	1.4	-3.0	-3.7
(Ligand)	**-0.0**	**-0.1**	**-0.0**	**-0.6**	**-0.1**	**0.0**	**-0.6**	**-0.2**	**-0.6**
Spectral data									
νC–H^8 (cm^{-1})	3105.2	3103.1	3108.6	3093.4	3103.5	3127.6	3116.4	3104.5	3080.0
(Ligand)	**3133.3**	**3132.9**	**3131.7**	**3131.3**	**3130.8**	**3131.7**	**3130.8**	**3138.4**	**3112.2**
δH^8 (complex)	8.65	9.46	10.11	9.66	10.10	8.47	9.09	9.80	8.37
(Ligand)	**8.13**	**8.22**	**8.27**	**8.55**	**8.76**	**8.87**	**8.47**	**8.44**	**7.67**
Δδ = δC–δL	0.52	1.24	1.84	1.11	1.34	-0.40	0.62	1.36	0.76
^1JC–H^8 (Hz)	142.9	143.3	143.9	143.6	144.4	145.5	140.1	146.0	**136.6**
(Ligand)	**139.4**	**139.5**	**138.9**	**140.9**	**140.8**	**141.2**	**140.9**	**141.7**	**133.7**

Complex	**10**	**11**	**12**	**13**	**14**	**15**	**16**	**17**
Bond Length								
Rh–N	2.157	2.135	2.135	2.136	2.135	2.135	2.136	2.236
Rh–Cl	2.378	2.357	2.356	2.356	2.354	2.358	2.356	2.422
C–H^8	1.091	1.092	1.092	1.090	1.089	1.090	1.090	1.090
(Ligands)	**1.096**	**1.091**	**1.091**	**1.090**	**1.088**	1.089	1.089	1.090
Separation								
Rh····H^8	2.542	2.794	2.808	2.750	2.806	2.818	2.825	2.544
Rh····C^8	2.929	3.335	3.327	3.302	3.325	3.343	3.350	2.583
Cl····H^8	2.813	4.058	4.047	4.011	4.109	4.099	4.097	2.565
Angles (^{o})								
Rh–N=C^1	125.6	132.9	132.5	132.8	132.9	133.1	133.1	115.0
Rh····H–C^8	99.6	110.4	108.9	111.1	109.1	109.5	109.5	79.7
Rh··· C–H^8	58.8	51.7	53.0	51.0	52.9	52.6	52.7	75.8
Cl····H–C^8	151.7	138.1	137.5	139.6	135.1	136.1	135.9	133.7
Dihedrals (^{o})								
C^2–Rh–N=C	65.8	30.8	30.9	31.9	31.0	30.1	30.1	70.3
Ar-Plane/CP^b	58.8	50.1	50.1	48.3	48.8	50.0	50.9	53.6
N=C^1–C^{8a}–C^8	30.8	32.3	33.1	31.6	32.7	32.5	32.3	33.2
(Ligand)	**-13.4**	**-13.8**	**-13.7**	**-14.5**	**-13.3**	**-14.2**	**-13.0**	**6.2**
(N=)C–C–C^8–H^8	15.8	3.1	3.6	4.4	3.0	3.0	2.2	26.2
(Ligand)	**-2.6**	**-1.4**	**-1.5**	**-1.5**	**-1.3**	**-1.3**	**-1.2**	**-2.5**
H^7–C^7–C^8–H^8	-7.4	-2.1^c	-3.9^c	-3.6^c	-1.3^c	-1.3^c	-0.7^c	-12.6^c
(Ligand)	**-1.0**	**-0.0**^{c}	**-0.1**^{c}	**0.2**^{c}	**-0.1**^{c}	**-0.0**^{c}	**-0.2**^{c}	**-3.4**^{c}
Spectral data								
νC–H^8 (cm^{-1})	3105.2	3091.1	3085.2	3121.0	3133.2	3115.3	3123.7	3106.5
(Ligand)	**3131.6**	**3114.1**	**3109.4**	**3120.5**	**3160.5**	**3137.1**	**3146.8**	**3112.3**
δH^8 (complex)	7.72	8.48	8.51	8.75	9.70	8.20	8.31	6.85
(Ligand)	**6.92**	**7.96**	**7.96**	**8.40**	**9.11**	**7.69**	**7.70**	**6.79**
Δδ = δC–δL	0.80	0.52	0.55	0.35	0.59	0.51	0.60	0.06
^1JC–H^8 (Hz)	141.0	138.6	137.1	138.2	148.2	141.3	143.6	138.7
(Ligand)	**136.8**	**137.5**	**137.1**	**134.8**	**147.3**	**140.1**	**142.6**	**135.1**

[a] Values in bold correspond to ligands.

[b] Angle between aromatic ring and metal coordination planes. [c] H^7 replaced by C, N, and O.

Along with these differences there are also changes in some bond lengths with both the Rh–N and Rh–Cl bonds being slightly longer in **3** [Rh–N bond length: 2.166 and 2.150 Å in **3** and **2**, respectively; Rh–Cl bond length: 2.366 and 2.351 Å in **3** and **2**, respectively]. In **3**, changes in torsions allow H^8 to adopt a similar positioning to **2** but slightly closer to Cl [Cl····H^8 distance: 2.534 Å; c.f. 2.753 Å in **2**]. However, there is an insignificant change in the Cl····H^8–C^8 bond angle [156.3° and 156.2° in **3** and **2**, respectively]. With the H^8 sitting more over towards Cl, the Rh····H^8 separation becomes slightly longer [2.764 Å] compared with the **2** [2.624 Å] (Figure 3.7b). Therefore, it would appear from the Rh···H^8 and Cl···H^8 separations that the increase in the steric size on going from (N)–OMe to (N)–$OCMe_3$, pushes H^8 towards the Cl ligand in **3** which results in the Cl···H^8 separation closing up and lengthening of the Rh···H^8 separation.

The spectroscopic properties (Table 3.1) show a small increase in the νC–H for **3** compared to **2** [3108.6 and 3103.1 cm^{-1}, respectively] [the corresponding free ligand values are almost same for both]. However, but there is a larger downfield chemical shift for H^8 in the ^1H NMR spectrum [Δδ values: 1.84 and 1.24 ppm in **3** and **2**, respectively]. The larger downfield shift shows that the overall anisotropic environment for the hydrogen H^8 is important and not the metal····hydrogen separation as the Rh···H^8 separation is longer in **3** [2.764 Å; c.f. 2.624 Å in **2**].

The QTAIM properties for the above-plane close approaches in **3** (Figure 3.7c; Table 3.3) reveal that the electron density and the Laplacian values for Rh···H^8 separation are slightly smaller in comparison to **2** [$\nabla^2\rho$: 0.0358 and 0.0413 *e*/$Bohr^5$, respectively]. The QTAIM atomic basin property values in **3** are also slightly smaller compared to **2** and from the atomic charges [*q*(Rh) and *q*(H) values: 0.637 and 0.074 *e*, respectively], the interaction is again electrostatically repulsive similar to **1** and **2**. Despite the close Cl····H^8 separation in **2** [2.753 Å], no bcp was present, but now in **3**, a bcp is present for Cl···H^8 separation [distance: 2.534 Å]. The QTAIM properties for bcp Cl····H^8 indicate a weakly attractive electrostatic interaction as both the Laplacian and energy density values are positive [$\nabla^2\rho$(bcp): 0.0358 *e*/$Bohr^5$; *H*(bcp): 0.0005 Hartree/$Bohr^3$] and the QTAIM charges, *q*, for Cl and H^8 are negative and positive [values: –0.569 and 0.074 *e*, respectively] (refer to Table 3.6 in Appendix A.2).

The NBO analysis for **3** (Table 3.4) indicates a small decrease in the stabilisation energy, *E*(2), for the donations relevant to the Rh····H^8 separation compared with **2**. For instance, the *E*(2) value for the donation from the Rh to C–H^8σ* orbitals is 0.12 kcal mol^{-1} in **3** [c.f. 0.30 kcal mol^{-1} for **2**], the Rh to C^8–C^{8a}π* donation [1.41 kcal mol^{-1}; c.f. 2.14 kcal mol^{-1} in **2**] and the C–H to Rh–Cσ* donation [*E*(2) value for Rh–C^2σ*: 0.76 and 0.90 kcal mol^{-1} in **3** and **2**, respectively; for Rh–C^{3}σ*: 0.68 and 1.01 kcal mol^{-1} in **3** and **2**, respectively]. However, these changes are mainly insignificant. There is a small increase in the donation from Cl to the C–Hσ* orbital in **3** compared with **2** [*E*(2) value for Cl LP(2) to C–H^{8}σ*: 0.25 and 0.94 kcal mol^{-1} in **2** and **3**, respectively; Cl LP(3) to C–H^{8}σ*: 1.11 and 2.11 kcal mol^{-1} in **2** and **3**, respectively] and this increase in the donations correlates well with the closer Cl···H^{8} distance in **3** [distance values: 2.534; c.f . 2.753 Å in **2**].

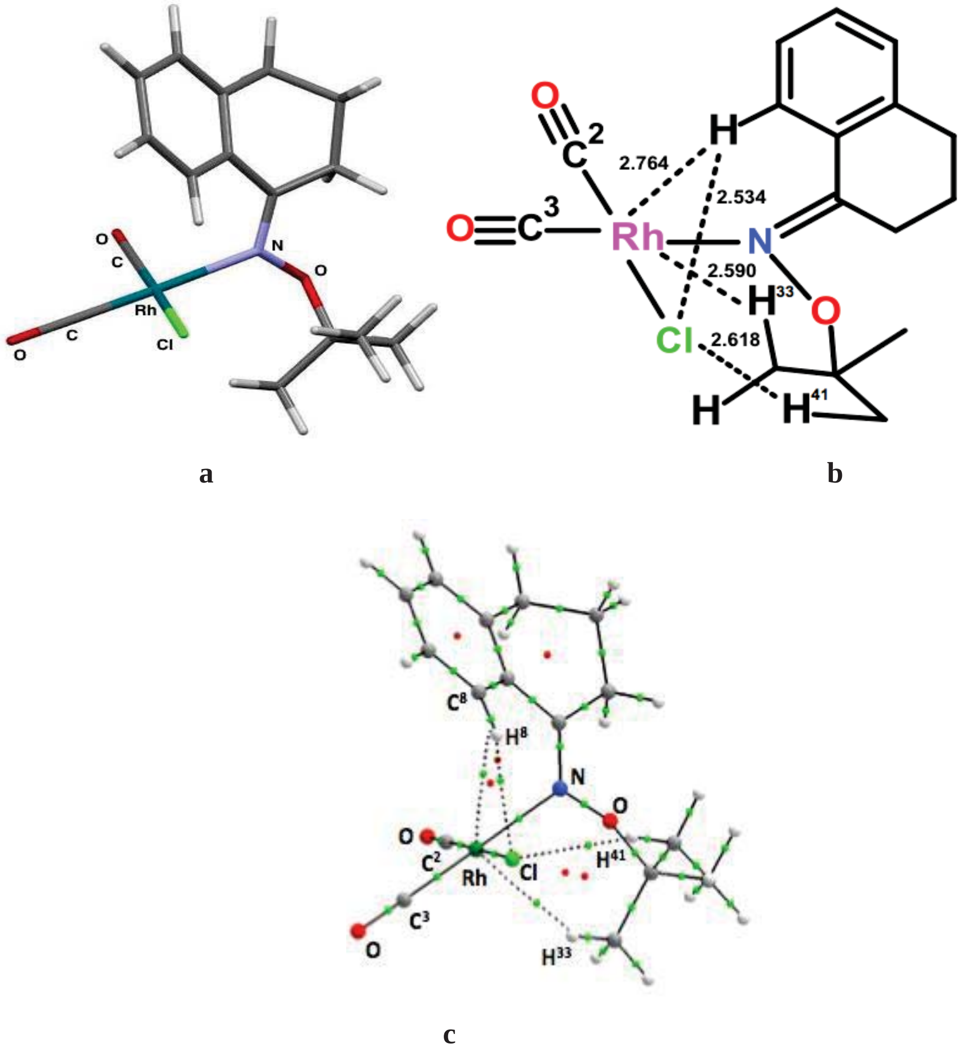

a

b

c

Figure 3.7 a) DFT optimised structure; b) Important separations **(**Å**)**; c) QTAIM graph for complex **3**.

Underneath the coordination plane in **3**, there is a significant change in the Rh–N–O–C (*tert*-butyl group) dihedral angle compared to **2** [values: –68.9^{o} and –11.1^{o}, respectively] which allows two of the methyl hydrogens to become close to the Rh centre [Rh····H^{33} distance: 2.590 Å; Rh····H^{33}–C angle: 126.1^{o}] as well as Cl [Cl····H^{41}–C distance: 2.618 Å; Cl····H^{33}–C distance: 2.819 Å] (Figure 3.7b). The close Rh····H^{33} separation gives an indication for a second anagostic approach and QTAIM analysis (refer to Table 3.6 in

Appendix A.2) indicates a small negative energy density [*H*(bcp) value: –0.0005 Hartree/Bohr^3] contrary to the Rh$\cdots$H^8 where the energy density is positive [*H*(bcp): 0.0004 Hartree/Bohr^3]. The NBO analysis for the Rh$\cdots$H^{33} interaction reveals little donation from Rh to the C^{32}–H^{33}σ^*orbital [*E*(2) value: 1.11 kcal mol^{-1}] and the C^{32}–H^{33} to Rh–C^2σ^* and Rh–C^3σ^* orbitals are also small [*E*(2) values: 0.78 and 0.67 kcal mol^{-1}, respectively], indicating that the interactions have some covalency components involved but they are very minor and cannot be regarded as significant. For the Cl approaches, QTAIM analysis shows only one bond path which is for the Rh$\cdots$H^{41} separation the QTAIM properties of which indicate a weak electrostatic attractive interaction [$\nabla^2\rho$: 0.0338 *e*/Bohr^5; *H*(bcp): 0.0008 Hartree/Bohr^3; *q*(Cl) and *q*(H^{41}): –0.569 and 0.049 *e*, respectively] (refer to Table 3.6 in Appendix A.2).

Table 3.2 Comparison of geometrical parameters for **2** using various DFT functionals.

Functional	**PBE-D3**	**B3LYP**	**BP86**	**CAM-B3LYP**	**CAM-B3LYP-D3**
Bond Length (Å)					
Rh–N	2.150	2.171	2.149	2.150	2.150
Rh–Cl	2.351	2.369	2.356	2.354	2.351
Rh–C^2	1.841	1.858	1.847	1.853	1.854
Rh–C^3	1.841	1.858	1.847	1.859	1.860
C–H^8	1.092	1.080	1.091	1.081	1.080
Separation (Å)					
Rh$\cdots$H^8	2.624	2.684	2.607	2.666	2.683
Rh$\cdots$C^8	3.104	3.207	3.150	3.184	3.161
Cl$\cdots$H^8	2.753	2.727	2.741	2.692	2.703
Angles (°)					
Rh–N=C^1	127.2	129.0	128.7	128.9	128.0
Cl–Rh–N	89.6	90.2	89.6	90.2	89.8
Rh$\cdots$H–C^8	105.8	109.3	109.9	108.9	106.3
Rh$\cdots$ C–H^8	51.2	52.2	51.1	52.4	54.5
Cl$\cdots$H–C^8	156.3	159.7	159.3	159.5	157.2
Dihedrals (°)					
(O)C^2–Rh–N=C	69.2	73.8	73.1	74.3	71.7
Ar-Plane/CP[a]	65.4	72.2	69.6	71.9	69.0
N=C^1–C^{8a}–C^8	34.4	33.8	32.7	34.7	35.7
C^1–C^{8a}–C^8–H^8	6.3	3.6	5.3	3.6	4.3
H^7–C^7–C^8–H^8	-2.9	-2.1	-2.7	-2.0	-1.9

[a] CP corresponds to coordination plane.

Moving further in assessing the influence of (N)–substituents on the C–H^8$\cdots$M anagostic approach, the (N)–R group on the ligand, were changed to complexes **4** and **5** with the (N)–Me and (N)–CMe$_3$ groups, respectively. The optimised structures of both complexes indicate that the (N)–substituents position behind the coordination plane contrary to the rotatable OMe and OCMe$_3$ substituents in **2** and **3**, which position below the coordination plane (Figure 3.8a; Figure 3.9a). The structural features for **4** show that the Rh–N bond length in **4** is now shorter than in (N)–OR complexes **2** and **3** [values: 2.124, 2.150 and 2.166 Å, respectively] but close to that in complex **1** [2.134 Å] (Figure 3.8b; Table 3.1). Similarly, the Rh–Cl bond length is also shorter in **4** [2.348 Å] compared to other complexes so far. There are no significant changes in the Rh–N=C push-back angle [127.6^{o}] and alicyclic ring torsion angles compared with the other complexes. The rotation about the Rh–N bond [(O)–C^{2}–Rh–N=C dihedral angle of 64.6^{o}] positions the C–H^{8} hydrogen above the coordination plane slightly more towards the metal than Cl compared with that in complexes **2**, (N)–OMe and **3**, (N)–OCMe$_{3}$ and this positioning results in shorter Rh····H^{8} separation [2.586 and 2.624 Å in **4** and **2**, respectively; c.f. 2.764 Å in **3**]. As the position of (N)–Me group is now more behind the coordination plane, the below-plane separations are longer compared to that found in complex **2**, and only H^{31} in **4** makes close approaches with Rh and Cl with the distances of 2.842 and 2.895 Å, respectively (Figure 3.8b).

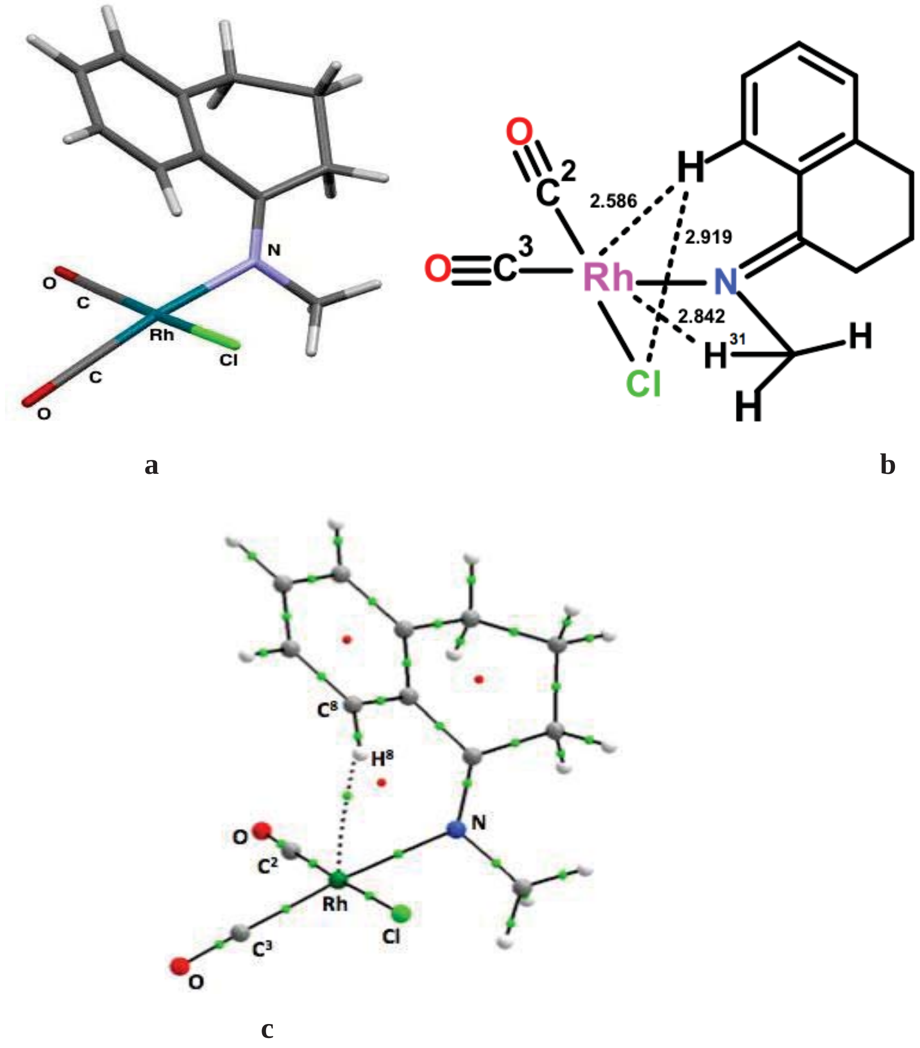

Figure 3.8 a) DFT structure; b) Important separations (Å); c) QTAIM molecular graph for complex **4**.

QTAIM analysis for **4** (Table 3.3) indicates a bcp for the Rh····H^8 close approach (Figure 3.8c) with little increase in the Laplacian of electron density [$\nabla^2\rho$: 0.0459 *e*/Bohr^5] and a little decrease in the energy density, [*H*(bcp): 0.0001 Hartree/Bohr^3] compared to **2**, (N)–OMe [$\nabla^2\rho$: 0.0446 *e*/Bohr^5; *H*(bcp): 0.0003 Hartree/Bohr^3]. The NBO analysis for **4** (Table 3.4) shows almost similar *E*(2) values of donor-acceptor interactions compared to **2**, which has (N)–OMe instead of (N)–Me. The spectroscopic properties for **4** (Table 3.1) are also quite similar to **2** except for the νC–H, which is slightly decreased [3093.4; c.f. 3103.1 cm^{-1} in **2**].

In (N)–CMe$_3$ complex **5**, the Rh–N bond further lengthens to 2.182 Å [c.f. 2.124 Å in case of (N)–Me complex **4**] and consequently, the Rh–N=C push-back angle reduces to 118.7^o [c.f. 127.6^o in **4**] (Table 3.1). However, the angle between the aromatic ring and coordination plane changes very little [58.7^o and 62.7^o in **5** and **4**, respectively]. Regarding the ligand dihedral angles, there are also small changes seen in **5** with the N=C^1–C^{8a}–C^8 dihedral increasing to 37.4 [c.f. 33.4^o in **4**] and C^1–C^{8a}–C^8–H^8 dihedral increasing to 9.3^o [c.f. 5.7^o in the case of **4**]. These torsional changes bring H^8 almost in the middle of the Rh–Cl bond over the coordination plane, and the relevant separations are shorter than in **4** [Rh····H^8 and Cl····H^8 separations: 2.548 and 2.542 Å; c.f. 2.586 and 2.919 Å in **4**] (Figure 3.9a,b). Interestingly in **5**, C^8 makes a very close approach to Rh with a distance of 2.861 Å [c.f. 3.105 Å in **4**]. Also in **5**, the Rh–Cl bond increases significantly to 2.382 Å [c.f. 2.348 Å in **4**] and this increase is an important feature for cyclometallation reactions as this lengthening can ease the removal of Cl and facilitates agostic interaction to develop.[10]

Underneath the coordination plane in **5**, the rotation about the Rh–N bond is such that one methyl group hydrogen (H^{39}) makes a close contact with both the Rh and Cl atoms with the distances of 2.672 and 2.627 Å respectively and another hydrogen (H^{40}) with Rh at distance 2.958 Å (Figure 3.9a,b). Another methyl group positions more in the coordination plane and one of its hydrogens (H^{34}) makes an approach with Cl at the distance of 2.912 Å.

The QTAIM analysis of **5** shows no bcp for the Rh····H^8 approach but there is for the Rh····C^8 approach (Figure 3.9c; Table 3.1)). The QTAIM properties for the Rh···C^8 bcp shows that the energy density is now negative [*H*(bcp)]: –0.0002 Hartree/Bohr^3] which indicates along with an electrostatic component there is some covalency also involved in the interaction. The QTAIM charges show that the C^8 negative charge is significantly increased [*q*(C^8) for **5** and **4**: –0.020 and –0.006 *e*, respectively] while the hydrogen charge is decreased compared to **4** and almost similar to **3**, containing (N)–OCMe$_3$ group [*q*(H^8) for **5**, **4** and **3**: 0.0075, 0.0061 and 0.0074 *e*, respectively]. The NBO analysis unveils covalency for the Rh···C^8 interaction as the Rh to C^8–$C^{8a}\pi^*$ and C–H to Rh–Cσ^* donations are stronger than the other complexes so far [E(2) values: 4.33 kcal mol^{-1} for Rh to C^8–$C^{8a}\pi^*$; 1.91 kcal mol^{-1} for C–H to the Rh–$C^2\sigma^*$ and 1.72 kcalmol^{-1} for C–H to the Rh–$C^3\sigma^*$] (Table 3.4). It is also noteworthy that the bond path for the Rh····C^8 separation is curved near to the C^8 carbon, (Figure 3.9c) which suggests strain in the system.[122] Interestingly, for the Cl····H^8 separation in **5** [distance: 2.542 Å] there is no bond path and bcp found whereas, for the similar separation in the complex **2** [distance: 2.534 Å], a bcp is present. However, the NCI index (Figure 3.9d) shows an attractive interaction between Cl and H^8 atoms as indicated by a light blue region between these atoms.[99]

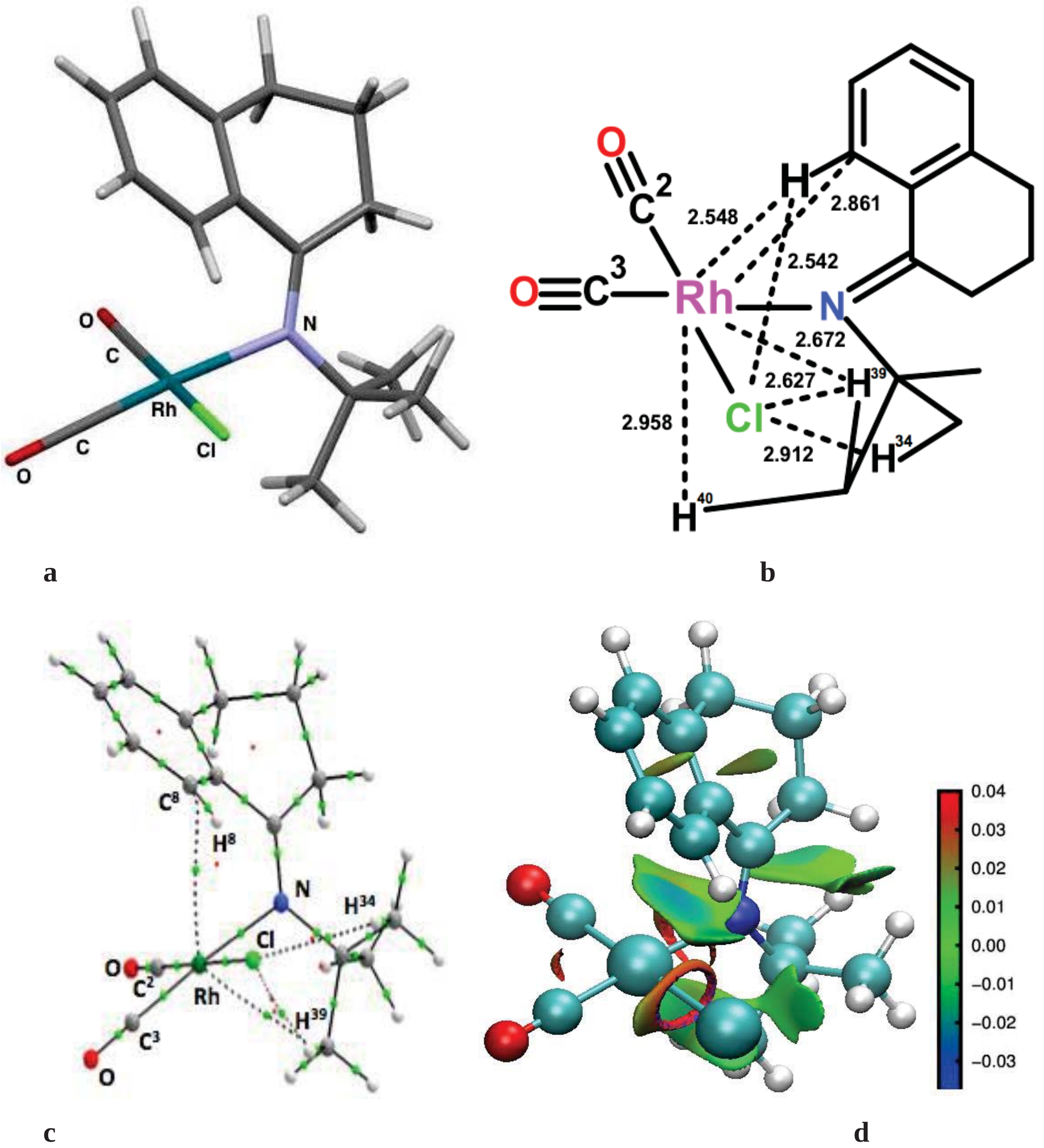

Figure 3.9 a) DFT structure; b) separations; c) QTAIM molecular graph; d) 3D NCI RDG iso-surface diagram for **5**. The sign of the second Hessian eigenvalue (λ_2) times the electron density is shown by the colour map.

Table 3.3 Selected QTAIM parameters for complexes **1–17**.

Complex	**1**	**2**	**3**	**4**	**5**[b]	**6**	**7**	**8**	**9**
Rh····X bond path	Rh····H	Rh····H	Rh····H	Rh····H	Rh····C	Absent	Rh····H	Rh····H	Rh····H
ρ(bcp)	0.0122	0.0169	0.0132	0.0177	0.0234	–	0.0171	0.0175	0.0188
$\nabla^2\rho$(bcp)	0.0309	0.0446	0.0358	0.0459	0.0630	–	0.0437	0.0466	0.0493
H(bcp)	0.0004	0.0003	0.0004	0.0001	-0.0002	–	0.0002	0.0003	0.0001
–V/G	0.9460	0.9770	0.9472	0.9869	1.0151	–	0.9812	0.9711	0.9900
ε(bcp)	0.6919	0.8143	1.7773	0.5616	0.8960	–	0.7502	0.9917	0.8445
C–H^8 bond critical point									
ρ(bcp)	0.2803	0.2815	0.2833	0.2810	0.2827	0.2822	0.2815	0.2828	0.2779
	0.2810	**0.2810**	**0.2807**	**0.2815**	**0.2819**	**0.2820**	**0.2823**	**0.2826**	0.2779
$\nabla^2\rho$(bcp)	-0.9435	-0.9566	-0.9708	-0.9537	-0.9655	0.9598	-0.9529	-0.9695	-0.9237
	-0.9459	**-0.9460**	**-0.9437**	**-0.9521**	**-0.9557**	**-0.9564**	**-0.9575**	**-0.9604**	**-0.9194**
ε(bcp)	0.0105	0.0111	0.0087	0.0098	0.0118	0.0099	0.0089	0.0084	0.0186
	0.0126	**0.0126**	**0.0132**	**0.0114**	**0.0118**	**0.0121**	**0.0092**	**0.0087**	**0.0181**
Atomic basin properties:									
H^8-atomic basin									
Charge, *q*(H)	0.038	0.061	0.074	0.061	0.075	0.064	0.039	0.078	0.023
	0.040	**0.040**	**0.035**	**0.051**	**0.054**	**0.054**	**0.052**	**0.057**	**0.003**
Total energy, *E*(H)	-0.642	-0.634	-0.627	-0.635	-0.630	-0.632	-0.631	-0.612	-0.643
	-0.609	**-0.609**	**-0.611**	**-0.604**	**-0.604**	**-0.604**	**-0.605**	**-0.602**	**-0.622**
Dipolar polarisation, *M*(H)	0.128	0.111	0.105	0.114	0.107	0.119	0.120	0.109	0.118
	0.129	**0.130**	**0.130**	**0.131**	**0.132**	**0.131**	**0.127**	**0.125**	**0.143**
Volume, *V*(H)^c	44.9	40.4	38.8	41.1	38.0	43.3	42.6	39.4	42.8
	46.5	**46.5**	**47.0**	**45.6**	**45.1**	**45.1**	**45.2**	**45.0**	**49.1**
C^8-atomic basin									
Charge, *q*(C)	-0.001	-0.011	-0.009	-0.006	-0.020	-0.008	0.002	-0.002	-0.037
	0.001	**0.001**	**0.000**	**0.001**	**0.001**	**0.000**	**0.008**	**0.015**	**-0.025**
Rh-atomic basin									
Charge, *q*(Rh)	0.626	0.635	0.637	0.633	0.654	0.644	0.634	0.632	0.644

Complex	**10**[b]	**11**	**12**	**13**	**14**	**15**	**16**	**17**[b]
Rh····X bond path	Rh····C	Rh····H	Rh····H	Rh····H	Rh····H	Absent	Rh····H	Rh····C
ρ(bcp)	0.0222	0.0127	0.0126	0.0137	0.0126	0.0123	0.0121	0.0401
$\nabla^2\rho$(bcp)	0.0563	0.0323	0.0322	0.0346	0.0331	0.0324	0.0311	0.0843
H(bcp)	-0.0003	0.0004	0.0005	0.0004	0.0006	0.0006	0.0005	-0.0055
–V/G	1.0210	0.9464	0.9405	0.9577	0.9187	0.9227	0.9316	1.2068
ε(bcp)	0.9507	0.7142	0.8207	0.6377	0.9199	0.9180	0.8797	0.1906
C–H^8 bond critical point								
ρ(bcp)	0.2774	0.2791	0.2786	0.2819	0.2829	0.2795	0.2798	0.2772
	0.2704	**0.2797**	**0.2795**	**0.2806**	**0.2841**	**0.2801**	**0.2804**	**0.2758**
$\nabla^2\rho$(bcp)	-0.9169	-0.9331	-0.9295	-0.9510	-0.9730	-0.9287	-0.9445	-0.9086
	-0.9532	**-0.9354**	**-0.9339**	**-0.9398**	**-0.9791**	**-0.9410**	**-0.9469**	**-0.9012**
ε(bcp)	0.0305	0.0135	0.0121	0.0137	0.0094	0.0162	0.0145	0.0399
	0.0266	**0.0157**	**0.0158**	**0.0137**	**0.0114**	**0.0185**	**0.0166**	**0.0350**
Atomic basin properties:								
H^8-atomic basin								
Charge, *q*(H)	0.026	0.029	0.027	0.033	0.094	0.054	0.064	0.046
	0.000	**0.032**	**0.031**	**0.029**	**0.099**	**0.056**	**0.067**	**0.006**
Total energy, *E*(H)	-0.639	-0.645	-0.643	-0.646	-0.614	-0.631	-0.626	-0.632
	-0.608	**-0.612**	**-0.612**	**-0.616**	**-0.586**	**-0.601**	**-0.595**	**-0.616**
Dipolar polarisation, *M*(H)	0.120	0.131	0.130	0.120	0.118	0.127	0.125	0.125
	0.147	**0.132**	**0.133**	**0.124**	**0.115**	**0.128**	**0.126**	**0.153**
Volume, *V*(H)[c]	42.4	45.0	44.6	39.0	39.4	44.1	43.8	40.1
	49.7	**46.6**	**46.4**	**43.7**	**40.8**	**45.5**	**45.2**	**48.4**
C^8-atomic basin								
Charge, *q*(C)	-0.056	-0.009	-0.012	-0.014	0.022	-0.001	0.011	-0.092
	-0.045	**-0.006**	**-0.008**	**-0.009**	**0.030**	**0.004**	**0.016**	**-0.049**
Rh-atomic basin								
Charge, *q*(Rh)	0.636	0.626	0.627	0.630	0.619	0.617	0.625	0.642

[a] [ρ(bcp) = *e*/Bohr^3; $\nabla^2\rho$(bcp) = *e*/Bohr^5; *H* = Hartree/Bohr^3; ε(bcp) = dimensionless, *q* = *e*, *M* = *e**Bohr, *E* = Hartree; V = 1/Bohr^3]. [b] Rh···C bcp properties. [c] 0.001 iso-surface.

Table 3.4. Selected NBO analysis parameters for complexes **1**–**17**.

Complex	**1**	**2**	**3**	**4**	**5**	**6**	**7**	**8**	**9**
C–H^{8}σ bond									
Occupancy	1.9753	1.9734	1.9746	1.9733	1.9715	1.9760	1.9734	1.9709	1.9727
(Ligand)	**1.9768**	**1.9770**	1.9766	**1.9761**	**1.9754**	**1.9753**	**1.9770**	**1.9761**	**1.9781**
Energy (a.u.)	-0.4433	-0.4338	-0.4294	-0.4354	-0.4302	-0.4321	-0.4497	-0.3154	-0.3215
(Ligand)	**-0.4166**	**-0.4163**	**-0.4144**	**-0.4101**	**-0.4066**	**-0.4098**	**-0.4303**	**-0.4425**	**-0.2947**
C–H^{8}σ* bond									
Occupancy	0.0159	0.0202	0.0250	0.0191	0.0239	0.0177	0.0173	0.0181	0.0189
(Ligand)	**0.0154**	**0.0162**	**0.0155**	**0.0168**	**0.0177**	**0.0174**	**0.0154**	**0.0153**	**0.0165**
Energy (a.u.)	0.3880	0.4063	0.4158	0.4020	0.4150	0.4073	0.3792	0.5184	0.5090
(Ligand)	**0.4055**	**0.4205**	**0.4058**	**0.4124**	**0.4127**	**0.4114**	**0.3960**	**0.3832**	**0.5202**
Rh–C^{2}σ* bond									
Occupancy	0.3720	0.3866	0.3791	0.3899	0.3819	0.3825	0.3964	0.3741	0.3761
Energy (a.u.)	0.3434	0.3784	0.3488	0.3910	0.4346	0.3893	0.3949	0.5129	0.4784
Rh–C^{3}σ* bond									
Occupancy	0.3203	0.3186	0.3093	0.3206	0.3110	0.3103	0.3276	0.3199	0.3256
Energy (a.u.)	0.1994	0.2298	0.2169	0.2483	0.3088	0.2624	0.2264	0.3686	0.3376
C^8–C^{8a}π* bond									
Occupancy	0.3939	0.3082	0.2918	0.3016	0.3135	0.3603	0.3869	0.3769	0.3357
Energy (a.u.)	-0.0098	-0.0029	0.0007	-0.0051	-0.0013	-0.0062	-0.0115	-0.0283	0.1174
Rhodium Lone pairs:									
LP (1)									
Occupancy (n)	1.9762	1.9633	1.9719	1.9611	1.9458	1.9675	1.9573	1.9574	1.9632
Energy (a.u.)	-0.1782	-0.1817	-0.1810	-0.1686	-0.1764	-0.1714	-0.1822	-0.0616	-0.0922
LP (2)									
Occupancy (n)	1.8095	1.8082	1.8062	1.8065	1.8037	1.8046	1.8109	1.8022	1.8029
Energy (a.u.)	-0.2318	-0.2282	-0.2226	-0.2203	-0.2190	-0.2177	-0.2328	-0.1294	-0.1373
LP (3)									
Occupancy (n)	1.7543	1.7590	1.7531	1.7549	1.7509	1.7495	1.7548	1.7465	1.7497
Energy (a.u.)	-0.2357	-0.2294	-0.2238	-0.2221	-0.2205	-0.2188	-0.2334	-0.1277	-0.1372
Cl Lone pairs:									
LP (2)									
Occupancy (n)	1.9653	1.9731	1.9632	1.9738	1.9705	1.9726	1.9733	1.9764	1.9762
Energy (a.u.)	-0.2616	-0.2684	-0.2724	-0.2530	-0.2640	-0.2606	-0.2277	-0.1842	-0.1895
LP (3)									
Occupancy (n)	1.9080	1.9453	1.9453	1.9486	1.9490	1.9503	1.9453	1.9589	1.9547
Energy (a.u.)	-0.2730	-0.2335	-0.2319	-0.2277	-0.2263	-0.2283	-0.2339	-0.1392	-0.1464
Donor-Acceptor Interactions: [*E*(2) kcal mol^{-1}]									
LP (1) Rh to C–H^{8}σ*	0.73	0.30	0.12	0.59	<0.05	<0.05	0.32	0.19	0.30
LP (2) Rh to C–H^{8}σ*	<0.05	<0.05	<0.05	<0.05	<0.05	<0.05	0.05	<0.05	0.08
LP (3) Rh to C–H^{8}σ*	<0.05	0.12	<0.05	0.18	0.06	<0.05	<0.05	0.10	0.09
LP (1) Rh to C^8–C^{8a}π*	0.56	2.14	1.41	2.09	4.33	<0.05	2.24	2.28	2.11
C–Hσ to Rh–C^{2}σ*	0.32	0.90	0.76	0.88	1.91	0.33	0.56	0.97	1.25
C–Hσ to Rh–C^{3}σ*	0.67	1.01	0.68	1.10	1.72	0.27	1.09	1.04	1.47
LP(2) Cl to C–H^8 σ*	<0.05	0.25	0.94	0.11	0.68	0.38	<0.05	0.32	0.18
LP(3) Cl to C–H^8 σ*	<0.05	1.11	2.11	0.63	1.88	0.85	<0.05	1.31	0.63
LP(1) C^8 to Rh–C^{2}σ*	<0.05	<0.05	<0.05	<0.05	<0.05	<0.05	<0.05	<0.05	<0.05
LP(1) C^8 to Rh–C^{3}σ*	<0.05	<0.05	<0.05	<0.05	<0.05	<0.05	<0.05	<0.05	<0.05

Table 3.4 continued Selected NBO analysis parameters for complexes **1–17**.

Complex	**10**	**11**	**12**	**13**	**14**	**15**	**16**	**17**
C–H^{8}σ bond								
Occupancy	1.9709	1.9713	1.9734	1.9720	1.9698	1.9687	1.9716	1.9646
(Ligands)	**1.9784**	**1.9763**	**1.9746**	**1.9743**	**1.9653**	**1.9727**	**1.9724**	**1.9746**
Energy (a.u.)	-0.3154	-0.4362	-0.4375	-0.4364	-0.4619	-0.4377	-0.4556	-0.3109
(Ligands)	**-0.2854**	**-0.4122**	**-0.4110**	**-0.4129**	**-0.4353**	**-0.4136**	**-0.4299**	**-0.2802**
C–H^{8}σ* bond								
Occupancy	0.0181	0.0168	0.0178	0.0188	0.0171	0.0149	0.0155	0.0220
(Ligands)	**0.0162**	**0.0170**	**0.0175**	**0.0180**	**0.0143**	**0.0154**	**0.0146**	**0.0184**
Energy (a.u.)	0.5184	0.3941	0.3894	0.3999	0.3794	0.3974	0.3784	0.6632
(Ligands)	**0.5061**	**0.4025**	**0.4022**	**0.4061**	**0.4045**	**0.4038**	**0.3940**	**0.5279**
Rh–C^{2}σ* bond								
Occupancy	0.3741	0.3723	0.3736	0.3738	0.3730	0.3712	0.3721	0.3679
Energy (a.u.)	0.5129	0.3476	0.3611	0.3609	0.3278	0.3337	0.3442	0.5905
Rh–C^{3}σ* bond								
Occupancy	0.3199	0.3208	0.3213	0.3213	0.3145	0.3174	0.3186	0.3030
Energy (a.u.)	0.3686	0.2028	0.2083	0.2069	0.1960	0.2081	0.1964	0.4591
C^{8}–C^{8a}π* bond								
Occupancy	–	0.3195	0.3250	0.3119	0.3651	0.3878	0.3572	–
Energy (a.u.)	–	-0.0029	0.0057	0.0099	-0.0292	-0.0069	-0.0242	–
Rhodium Lone pairs:								
LP(1)								
Occupancy (n)	1.9574	1.9757	1.9752	1.9746	1.9728	1.9762	1.9761	1.9478
Energy (a.u.)	-0.0862	-0.1786	-0.1810	-0.1821	-0.1941	-0.1828	-0.1816	-0.0847
LP(2)								
Occupancy (n)	1.8022	1.8093	1.8088	1.8090	1.8100	1.8096	1.8099	1.8009
Energy (a.u)	-0.1294	-0.2308	-0.2308	-0.2309	-0.2399	-0.2289	-0.2347	-0.1197
LP(3)								
Occupancy (n)	1.7465	1.7531	1.7527	1.7525	1.7575	1.7550	1.7550	1.7261
Energy (a.u.)	-0.1277	-0.2346	-0.2352	-0.2355	-0.2458	-0.2341	-0.2388	-0.1380
Cl Lone pairs:								
LP(2)								
Occupancy (n)	1.9764	1.9656	1.9654	1.9655	1.9634	1.9657	1.9649	1.9739
Energy (a.u.)	-0.1842	-0.2608	-0.2608	-0.2605	-0.2673	-0.2588	-0.2639	-0.1769
LP(3)								
Occupancy (n)	1.9589	1.9090	1.9098	1.9101	1.9013	1.9075	1.9052	1.9697
Energy (a.u.)	-0.1392	-0.2721	-0.2720	-0.2719	-0.2814	0.2709	-0.2761	-0.1303
Donor-Acceptor Interactions:								
[*E*(2) kcal mol^{-1}]								
LP(1) Rh to C–H^{8}σ*	0.16	0.49	0.94	1.06	0.83	0.58	0.81	<0.05
LP(2) Rh to C–H^{8}σ*	0.11	<0.05	<0.05	<0.05	<0.05	<0.05	<0.05	<0.05
LP(3) Rh to C–H^{8}σ*	0.08	<0.05	<0.05	<0.05	<0.05	<0.05	<0.05	<0.05
LP(1) Rh to C^{8}–C^{7}π*	<0.05	0.79	0.49	0.41	0.56	0.70	0.55	<0.05
C–Hσ to Rh–C^{2}σ*	1.34	0.76	0.23	0.28	0.30	0.68	0.30	2.97
C–Hσ to Rh–C^{3}σ*	1.79	1.19	0.56	0.64	0.62	1.10	0.64	3.38
LP(2) Cl to C–H^{8}σ*	0.25	<0.05	<0.05	<0.05	<0.05	<0.05	<0.05	1.17
LP(3) Cl to C–H^{8}σ*	0.66	<0.05	<0.05	<0.05	<0.05	<0.05	<0.05	0.70
LP(1) C^{8} to Rh–C^{2}σ*	<0.05	<0.05	<0.05	<0.05	<0.05	<0.05	<0.05	13.38
LP(1) C^{8} to Rh–C^{3}σ*	<0.05	<0.05	<0.05	<0.05	<0.05	<0.05	<0.05	17.59

The QTAIM molecular graph for **5** also shows three more bond paths for close approaches underneath the coordination plane. The QTAIM properties for all of them indicate weak electrostatic type interactions (refer to Table 3.6 in Appendix A.2). The bond paths associated with Cl, Cl···H^{34} and Cl···H^{39} indicate an attractive situation as indicated by the charges [*q*(Cl) and *q*(H^{39}): –0.582 and 0.037 *e*, respectively; *q*(H^{34}): 0.036 *e*] whereas the Rh···H^{39} is a repulsive interaction [*q*(Rh): 0.654 *e*; *q*(H^{39}): 0.037 *e*].

The spectroscopic analysis (Table 3.1) for complex **5** and the free ligand is not very different to the other complexes and ligands. The νC–H and ^1JC–H spectroscopic properties for **5** are slightly different to (N)–OMe complex **3** [ΔνC–H and Δ^1JC–H value for **5**: 27.3 cm^{-1} and 3.6 Hz, respectively; c.f. 23.1 cm^{-1} and 5.0 Hz, respectively in **3**]. However, in comparison with **3**, despite the closer Rh···H^8 separation in **5** [Rh···H^8: 2.764 Å and 2.548 Å, respectivley] the H^8 downfield shift is lower in **5** than **3** [Δδ: 1.34 and 1.84 ppm in **5** and **3**, respectively] which again strengthens the point that the closeness of the hydrogen H^8 to metal is not the influential factor in change in the proton chemical shift.

It can be seen from the complexes studied so far, especially in **5,** that when substituting a bulky group at the (N)–R position the Rh···H^8 distance becomes closer. One of the main factors involved in positioning H^8 over the metal coordination sphere in a back-and-forth manner was the flexibility of the alicyclic ring. In all the complexes so far, the (N)–CMe_3 group (**5**) produced the closest Rh····H^8 separation [2.548 Å], and it was thus of interest to remove the conformational effects associated with the ligand alicyclic ring to ascertain the Rh···H^8 approach for an aromatic ring that could potentially rotate, as acetophenone complex **6**. For this complex, there is also no crystal structure available to compare with the computational structure despite that the complex is a stable product after isolation.[123]

The optimised structure of complex **6** (Figure 3.10a) shows significant rotation of the aromatic ring and H^8 is now placed over the top of the Cl ligand. Now the Rh···H^8 distance becomes significantly longer than in **5** [3.030 and 2.548 Å, respectively] (Figure 3.10b) and lies out of the range for anagostic interactions [2.3–2.9Å].[34,65] Though H^8 inclines towards Cl, still it is not as close as was seen in **5** [Cl···H^8 distance: 2.736 and 2.542 Å, respectively]. The Rh–N bond length is now a little shorter compared to **5** [2.161 and 2.182 Å, respectively], however, the Rh–N=C push-back angle is essentially the same in both complexes [117.4 and 118.7 ^{o} in **6** and **5**, respectively]. The other significant structural changes in **6** are seen in the dihedral angles as the C^2–Rh–N=C^1 dihedral angle increases to 79.7^o [c.f. 70.4^o in **5**], the N=C^1–C^{8a}–C^8 dihedral angle increases significantly to 67.9^o compared to 37.4^o in **5** and the C^1–C^{8a}–C^8–H^8 dihedral angle is reduced to –1.1^o [c.f. 9.3^o in **5**]. Interestingly, despite the significant rotations associated with the benzene ring in **6**, the angle between the aromatic and coordination planes is only affected slightly [54.1^o and

58.7^{o} in **6** and **5**, respectively]. It is also noteworthy that the Rh–Cl bond length decreases to 2.367 Å from 2.382 Å in **5**. This decrease in Rh–Cl bond length suggests that the length of this bond is related to the electronic properties of the ligand.

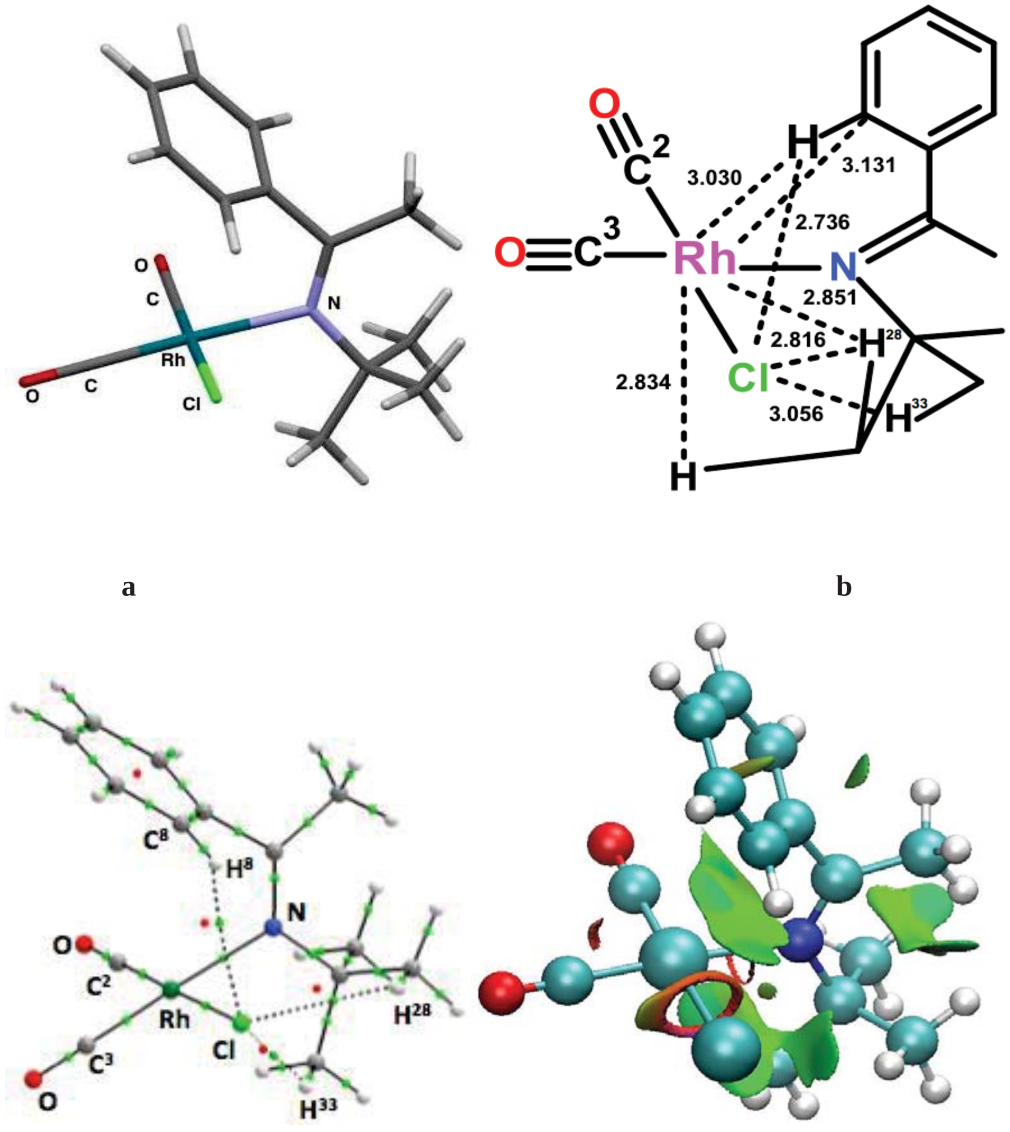

a **b**

c **d**

Figure 3.10 a) DFT structure; b) Separations (Å); c) QTAIM molecular graph; d) 3D NCI reduced density gradient (RDG) iso-surface diagram for **6**.

QTAIM analysis for **6** shows no bcp for the Rh····H^{8} separation as expected for a separation of 3.030 Å. However, there is a bond path and bcp present for the Cl····H^{8} separation, with properties [$\nabla^2\rho$: 0.0305 *e*/Bohr^{5}; *H*(bcp): 0.0011 Hartree/Bohr^{3}] showing a weak electrostatic type interactions (Figure 3.10c; Table 3.3). For the below-plane approaches, there are bond paths present for the Cl····H^{28} [distance: 2.816 Å] and Cl····H^{33} [distance: 3.056 Å] (Figure 3.10c) separations and their properties also lie in the weak electrostatic attractive interaction arena (refer to Table 3.6 in Appendix A.2). QTAIM atomic basin properties indicate a small decrease in the positive and negative charges on the H^8 and C^8, respectively, which shows that the electronics of the system is also affected by the removal of the alicyclic ring [$q(H^8)$ value in **6** and **5**: 0.064 *e* and 0.075 *e*; $q(C^8)$ value in **6** and **5**: –0.008 and –0.020 *e*, respectively]. Although there was no bond path seen for the above plane approaches in QTAIM analysis of **6**, a 3D NCI RDG iso-surface diagram (Figure 3.10d) shows a light blue spotted iso-surface between the C^8 and Rh indicating a weakly attractive interaction.

The NBO analysis for **6** (Table 3.4) also correlates with the QTAIM results as no donation is found from Rh to $C–H^8\sigma^*$ or $C^8–C^{8a}\pi^*$ orbitals. However, small donations from Cl to the C–Hσ*orbital are present, but these are of small magnitudes compared to **5** [*E*(2) values for Cl to $C–H^8\sigma^*$ in **6**: 0.38 and 0.85 kcal mol^{-1}, respectively; 0.68 and 1.88 kcal mol^{-1}, respectively in **5**].

The spectroscopic data for **6** (Table 3.1) indicate little change in $\nu C–H^8$ and $^1JC–H^8$ between the complex and free ligand. However, despite the longer $Rh\cdots H^8$ separation in **6**, [distance: 3.030 Å], H^8 shows an upfield chemical shift [Δδ: –0.040 ppm] which indicates that the H^8 is now not affected by the rhodium current density.[121]

3.5.3 Electronic Effects on the Aromatic Ring, Complexes 7–10

To ascertain the electronic effects in the [$Rh(CO)_2Cl$(1-tetralone oxime and imine] complexes, different electronic substituents based upon their electron donating or withdrawing ability as mentioned at the beginning of the chapter (Scheme 3.1) were placed on the aromatic ring of the (N)–OMe ligand. The reason behind the use of the (N)–OMe group instead of (N)–OH, was to avoid the (N)–OH····Cl hydrogen bonding effect seen in complex **1** which effectively reduced rotation about the Rh–N bond and thus flexibility in the complex. In the first instance, it was determined whether the *para* substituent could cause any structural change in the way that ligand sits over the metal. It was seen in complex **7** that the size of the $N=NPO(OCH_2CH_3)_2$ substituent (π-electron withdrawing group with F value: –0.05; R value: 0.79)[106] (Figure 3.11a) forces the alicyclic ring towards a chair-like conformation which results in significant tilting of H^8 towards the CO ligand that lies *trans* to Cl. Even after a significant change in the orientation of the ligand, H^8 still forms a close approach with Rh at a distance of 2.651 Å but with a $Rh\cdots H–C^8$ angle of 105.0° (Figure 3.11b; Table 3.2) that would suggest poor overlap of orbitals. The $Cl\cdots H^8$ separation is now the second longest after **1** [separation distances: 4.020 and 4.077 Å in **7** and **1**, respectively]. Comparing the other structural features found for **7** with those for **1**, the Rh–N bond length is almost same [2.134 and 2.136 Å in **1** and **7**, respectively] but Rh–Cl is slightly decreased [2.356 and 2.335 Å in **1** and **7**, respectively]. As there is a large twisting in the aromatic ring in **7**, the dihedral angle OC^2–Rh–N=C is significantly increased to 115.0^o compared to **1** [30.6^o]. These significant structural changes in **7** suggest that the N=NPO(OCH_2CH_3)$_2$ substituent is not a viable option for this study. Unfortunately, for π-bond electron withdrawal, all the other substituents of this type also have a significant σ-electron withdrawing component as the next π-donor, CH=NSO_2CF_3, has an R value of 0.37 but an F value of 0.63)[106]. Therefore, no other π-bond electron withdrawal substituent was used in the present work.

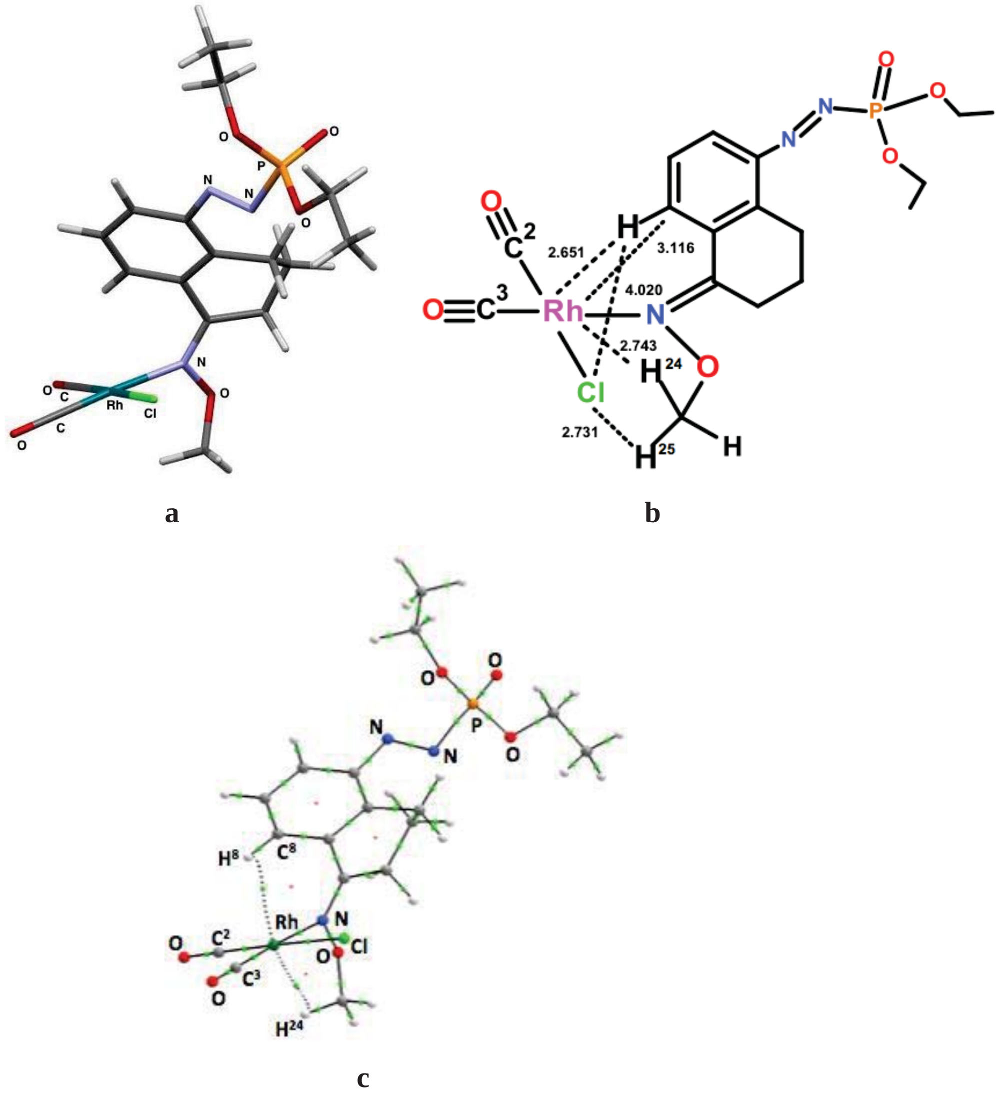

a b

c

Figure 3.11 a) DFT structure; b) Important separations (Å); c) QTAIM molecular graph for complex **7**.

Although it appears that the N=NPO(OEt)$_2$ substituent is not a suitable substituent, nevertheless a QTAIM analysis for **7** (Table 3.3) shows the carbon, C^8, charge now positive as expected from the electron withdrawing effect associated with the N=NPO(OEt)$_2$ substituent [q(C^8): 0.002 e; c.f. –0.011 e in **2**]. Despite the dramatic changes in the structure of **7**, there is still a bcp present with smaller positive Laplacian and energy density values [values for $\nabla^2\rho$ and H(bcp): 0.0437 e/Bohr^5 and 0.0002 Hartree/Bohr^3, respectively] (Table 3.3). The NBO analysis (Table 3.4) shows almost similar donations as were found in **2** for Rh to C^8–C$^{8a}\pi^*$ [E(2) value in **7** and **2**: 2.24 and 2.14 kcal mol^{-1}, respectively]. The spectroscopic properties indicate a small decrease in the νC–H and a slightly larger downfield chemical shift in in the ^{1}H NMR spectrum for H^8 in **7** compared with the free ligand.

The structural features (Table 3.1) for the remaining three complexes **8–10** with electron withdrawing SO$_2$Cl (complex **8**) and donating substituents B(OH)$_3^-$ (complex **9**) and S$^-$ (complex **10**), indicate a small but insignificant change in the Rh–N bond lengths [2.150, 2.146 and 2.157 Å in **8**, **9** and **10**, respectively] compared to **2** [2.150 Å]. As was seen in the previous complexes, the Rh–N bond length was one of the factors affecting the positioning of the H^8 over metal coordination plane but with the insignificant changes in the these bond lengths in **8–10**, a meaningfull comparison can be made by evaluating the Rh···H^8 separations in the context of the substituent influence on each of the complexes. Here, it is noteworthy to mention that the SO$_2$Cl (σ-electron withdrawing group) (complex **8**) and S$^-$ (π-electron donating group) (complex **10**) have nearly similar magnitude of effects at the *para*-position on the aromatic ring [F value for SO$_2$Cl: 1.16; R value for S$^-$: –1.24].[106] Since the anagostic interaction is essentially electrostatic in nature, therefore, the charge associated with the C–H^8 group is expected to be an influential parameter in determining the extent of the Rh···H^8 interaction.

In the first instance, electronic effects in the free ligands were assessed to see the effect of σ- and π-donating or withdrawing groups in ligands were different or not. It was seen that both the σ and π-electron withdrawing substituents result in increase in the positive charge on H^8 [q(H) values in case of SO$_2$Cl (**8**) and N=NPO(OEt)$_2$ (**7**) substituents: 0.057 and 0.052; 0.040 e for H] while both σ- and π-electron donation cause a decrease in the H^8 positive charge [q(H) values for **9** (B(OH)$_3^-$) and **10** (**S**$^-$): 0.003 and 0.000 e, respectively; c.f. 0.040 e for **1**] (Table 3.3). Even though the transmission is slightly greater for the σ-system, there is no clear distinction between σ- and π-electronic substituents.

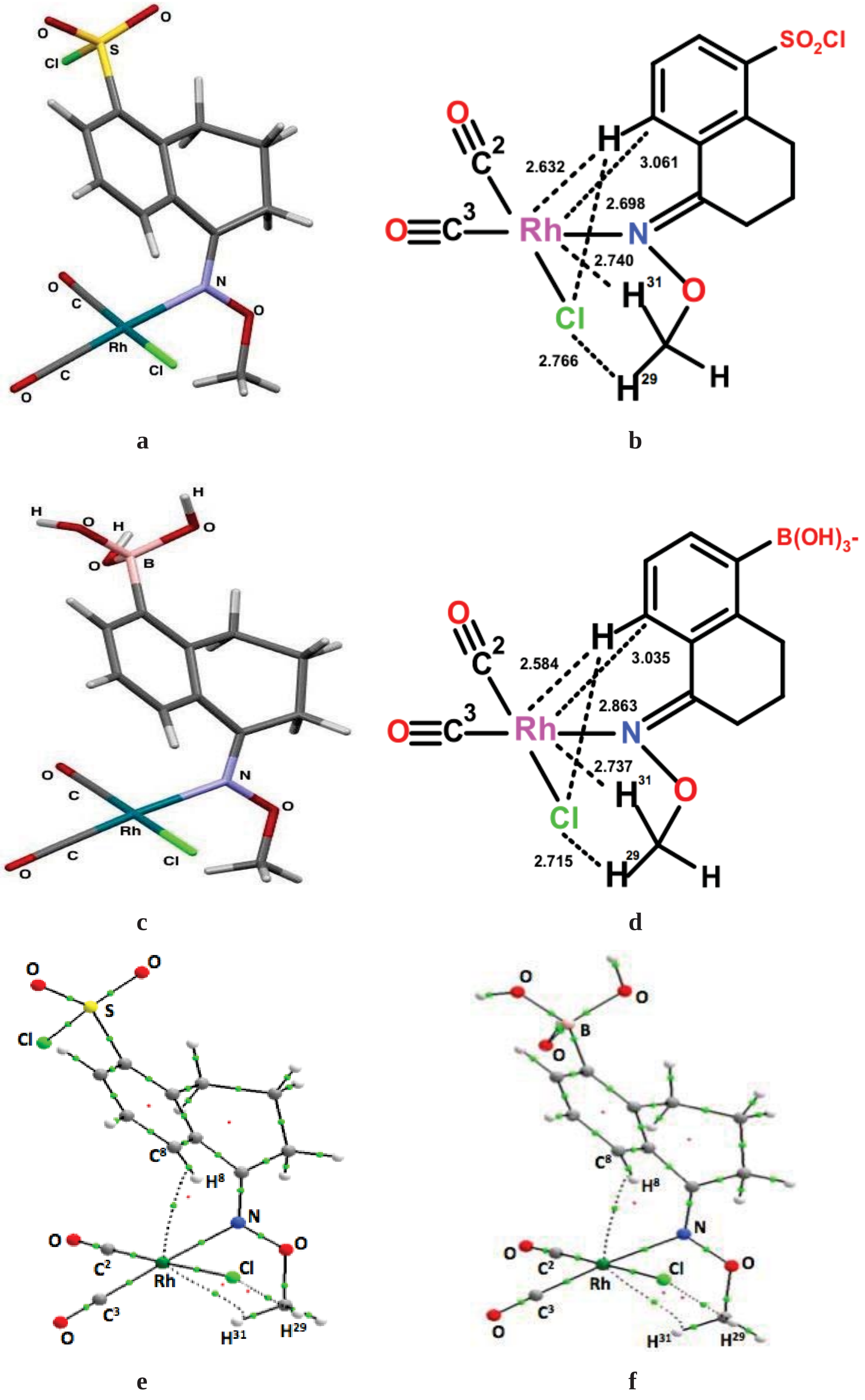

Figure 3.12 a,b) DFT structure and important separations (Å) for **8**, respectively; c,d) DFT structure and important separations (Å) for **9**, respectively; e,f) QTAIM molecular graphs for **8** and **9**, respectively.

Analysing the complexes, in complex **8**, with an SO_2Cl substituent (electron withdrawal through the σ-system) at C^5 of the tetralone system, the $Rh\cdots H^8$ separation increases slightly to 2.632 Å (Figure 3.12a,b) from 2.624 Å in complex **2** which has an H-substituent at C^5 (Table 3.1). This increase correlates with the slight increase in the H^8 atomic charge [$q(H^8)$ values in **8** and **2**: 0.078 and 0.061 *e*, respectively] (Table 3.3). As expected for the σ-donor $B(OH)_3^-$ substituent (**9**) and π-donor S^- complex (**10**), the H^8 atomic charge significantly decreases [$q(H)$ values: 0.023 and 0.026 in **9** and **10**, respectively; c.f. 0.061 *e* in **2**] which subsequently shortens the $Rh\cdots H^8$ separations [values: 2.584 and 2.542 Å in **9** and **10**, respectively; c.f. 2.624 Å for **2**] (Table 3.1). It is also noted that the increase in negative charge on C^8 [$q(C^8)$ in **9** and **10**: –0.037 and –0.056 *e*, respectively; c.f. –0.011 *e* in **2**] brings the $Rh\cdots C^8$ separation closer [values for **9** and **10**: 3.035 and 2.929, respectively; c.f. 3.104 Å for **2**], as a result of this closeness, the $Rh\cdots H^8$ distance also becomes shorter [values: 2.584 and 2.542 Å in **9** and **10**, respectively; c.f. 2.624 Å in **2**] (Figure 3.12c,d; Figure 3.13a,b). As the metal atomic charges are not very different for these complexes [0.644 and 0.637 *e* for **9** and **10**, respectively; c.f. 0.635 *e* for **2**], it appears that a decrease in the H^8 atomic charge reduces the electrostatic repulsion and allows H^8 to get closer to the metal. An increase in the positive charge also decreases the separation with negatively charged Cl. For instance, the increase in the positive charge on H^8 in the complex **8** shortens the $Cl\cdots H^8$ separation compared with **2** [$q(H^8)$: 0.078 *e* and 0.061 *e*; $Cl\cdots H^8$ separation: 2.698 and 2.753 Å, respectively]. Also, the increase in the negative charge at C^8 by the electron donating groups in case of σ-donor $B(OH)_3^-$ (**9**) and π-donor S^- (**10**) substituents, builds an attractive interaction with metal and as a result, the $Rh\cdots H^8$ separation becomes shorter. As the expected attraction between C^8 and Rh is greater in **10**, therefore, there is now a bond path for the $Rh\cdots C^8$ separation contrary to **8** and **9** where the $Rh\cdots H^8$ bond path exists. The negative value of *H*(bcp) in complex **10** [–0.0003 *e*] indicates a little covalency is involved, as revealed by NBO analysis which shows a comparatively larger donation for the C–H to $Rh–C^2σ^*$ and $Rh–C^3σ^*$ orbitals [*E*(2) values for **10**, 1.34 and 1.79 kcal mol^{-1}, respectively] (Table 3.4). However, these donations are not very different to complex **9** which has *E*(2) values: 1.25 and 1.47 kcal mol^{-1} respectively, therefore, the increase in the carbon C^8 negative charge appears to be the major driving force for building up the $Rh\cdots C^8$ interaction (Figure 3.12e,f; Figure 3.13c).

The other structural features (Table 3.1) show small decreases in the following dihedral angles: $OC^2–Rh–N=C$ [values: 69.1, 66.9 and 65.8° in **8**, **9** and **10**, respectively; c.f. 69.2° in **2**], $N=C^1–C^{8a}–C^8$ [36.3, 32.4 and 30.8 in **8**, **9** and **10**, respectively; c.f. 34.4° in **2**] and aromatic ring/coordination planes angle [62.5, 60.9° and 58.8° in **8**, **9** and **10**, respectively;

c.f. 65.4° in **2**]. Also, there is a significant change in the dihedral angle of C^1–C^{8a}–C^8–H^8 seen in **10** compared to **2** [15.8° and 6.3° for **10** and **2**, respectively]. The spectroscopic properties for complexes **8**, **9** and **10** change a little compared with **2** (Table 3.1).

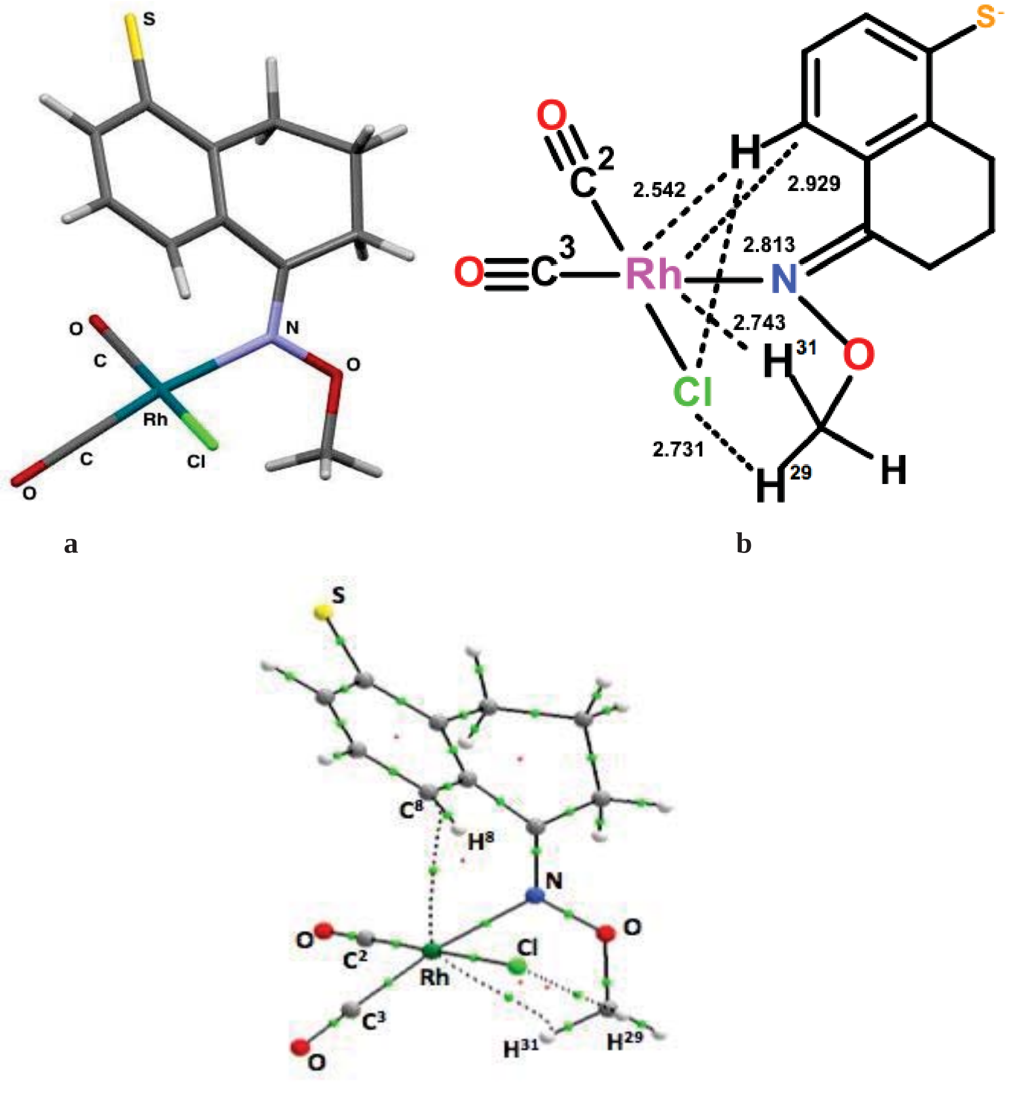

Figure 3.13 a) DFT structures; b) Important separations (Å); c) QTAIM molecular graph for **10**.

3.5.4 Steric and Electronic Effects at the C^7 Position, Complexes 11–16

The structural features for the complexes **11–16** (Table 3.2) with steric substituents at the C^7 position of the tetralone ring system indicate no significant changes in the separations, bond lengths as well as angles and torsions compared to complex **1**. The small decrease in the Rh···H^8 separation was seen in complexes **12** ($CHMe_2$ at C^7) and **13** (CMe_3 at C^7) [2.808 and 2.750 Å, respectively; c.f. 2.820 Å in **1**] (Figure 3.14). It is noted that the σ-donation ability of CMe_3 on an aromatic ring is slightly greater than for $CHMe_2$ (F values: –0.074 and –0.064, respectively)[106], which shows that the electronic effect may not be influencing the Rh···H^8 separations to any great extent.

With little significant change in the angles and torsions in complexes **11**–**13** (compare the values in Table 3.1) show that the increase in steric size at C^7 position does not appear to influence the Rh···H^8 interaction in these anagostic approaches. The other factor which prevents the angle changes near to coordinating N atom is the weak hydrogen bonding[119] between Cl and OH group in the coordination plane [Cl···HO distance in **11**–**13**: 2.076, 2.081 and 2.083 Å, respectively]. The strength of these interactions was revealed by the NBO analysis where the noticeable donations from the lone pair on Cl to the O–Hσ* orbital are present [the *E*(2) values: 15.67, 15.34 and 15.21 kcal mol^{-1} in **11**–**13**, respectively].

To assess electronic effects at the C^7 position, electronic substituents substituents were used which are relevant to experimentalnal studies.[104a] In particular, NO_2 (σ-withdrawing F value 0.65; π-withdrawing R value 0.13)[106], OMe (σ-withdrawing F value: 0.29; π-donating R value: –0.56)[106] and F (F value: 0.45; R value: –0.39)[106] substituents were placed at the C^7 position of complex **1** [complexes **14**, **15** and **16**, respectively in Scheme **1**].

Similar to the steric substituents in **11**–**13**, electronic substituents at the C^7 position in **14**–**16** do not have a noticeable influence on structural parameters (Table 3.1) (Figure 3.14; Figure 3.15). For instance, there is an insignificant increase in the Rh–N bond length, no change observed in the torsions of the alicyclic ring, push-back angles and plane angle (the angle between the ligand aromatic ring and metal coordition planes) compared with complex **1** (Table 3.1). In the same way, there are also no noticeable variations in the Rh····H^8, Rh····C^8 and Cl····H^8 separations in complexes **14**–**16** compared with **1** (Figure 3.15).

Interestingly, the QTAIM analysis (Table 3.3) reveals the electronic effects of the substituents at C^7 position as the charges for C^8 and H^8 are changed significantly in **14**–**16** complexes [*q*(H) values in **14**–**16**: 0.094, 0.054 and 0.064 *e*, respectively; *q*(C) values in **14**–**16**: 0.022, –0.001 and 0.011 *e*, respectively]. Despite the significant changes to the QTAIM charges, no significant change in the Rh···C^8 or Rh····H^8 separations was noticed [Rh····C^8 in **14**–**16**: 3.325, 3.343 and 3.350 Å, respectively; Rh····H^8 in **14**–**16**: 2.806, 2.818 and 2.825 Å, respectively] compared with **1** [Rh····C^8 and Rh····H^8 separations: 3.354 and 2.820 Å, respectively]. Thus, none of the substituents shows remarkable influence on the anagostic approaches as were seen earlier in *para* substituted complexes **8**, **9** and **10**.

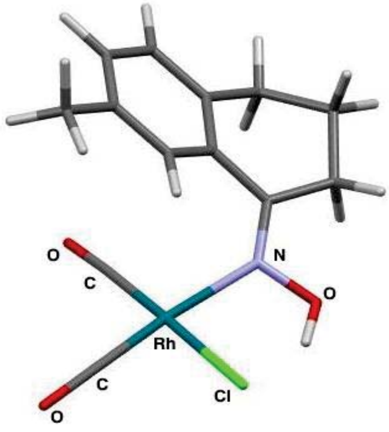

11

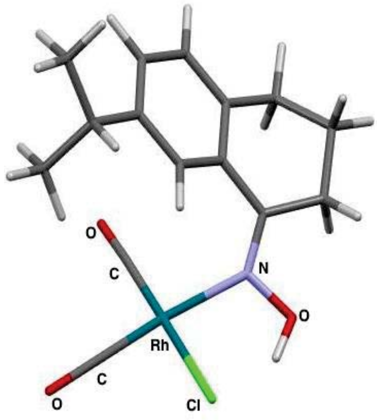

12

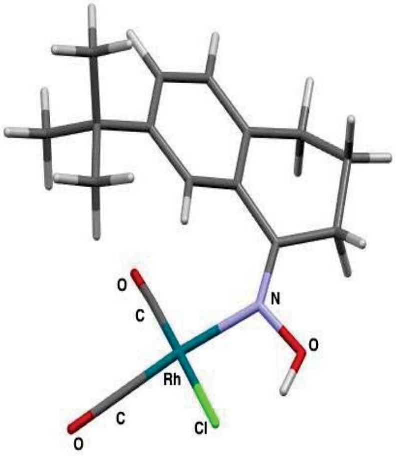

13

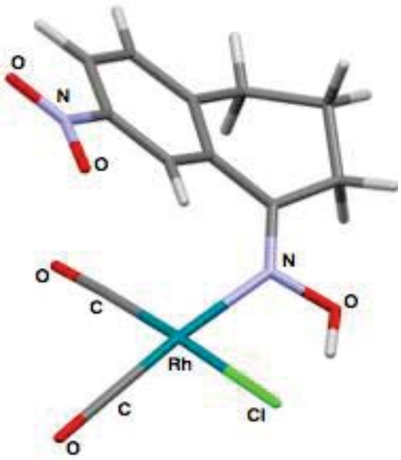

14

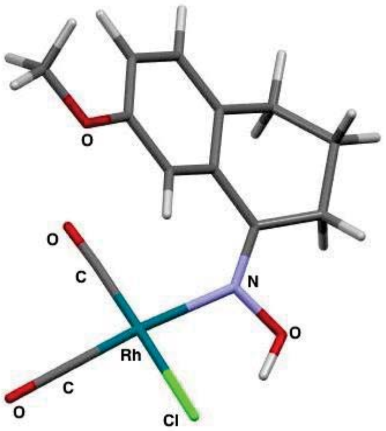

15

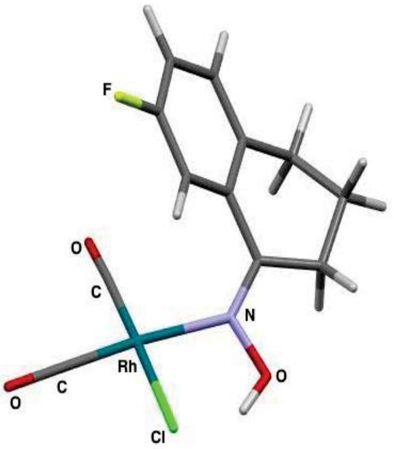

16

Figure 3.14 DFT optimised structures for **11–16**.

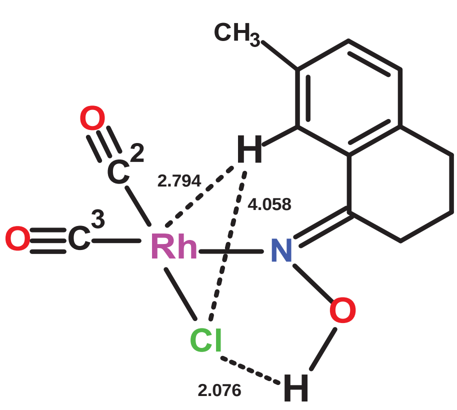

11

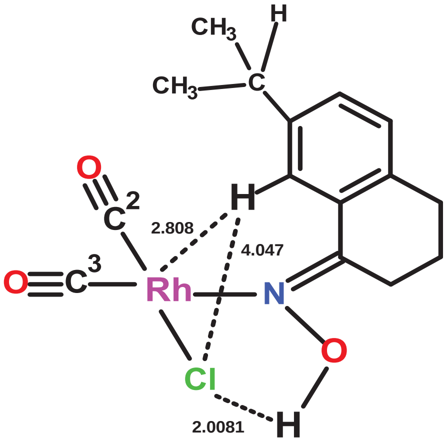

12

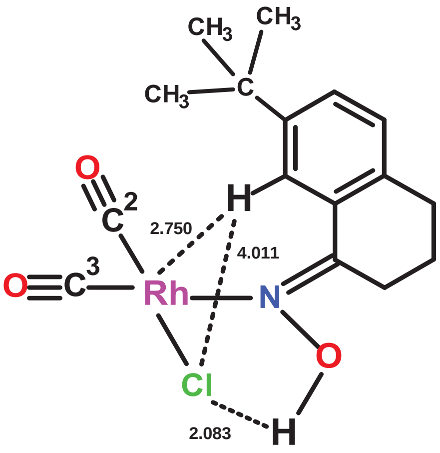

13

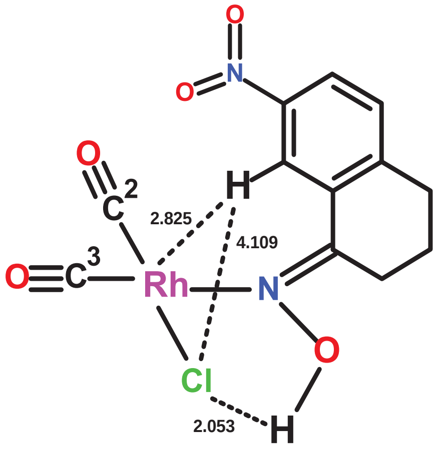

14

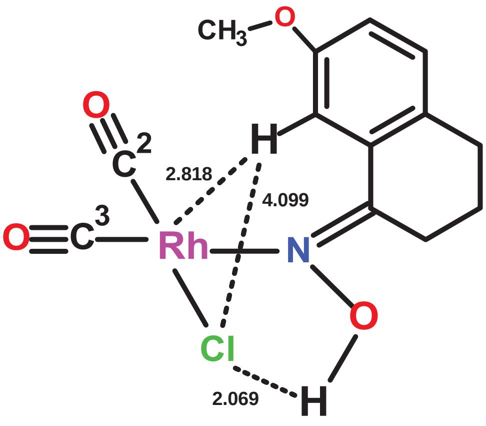

15

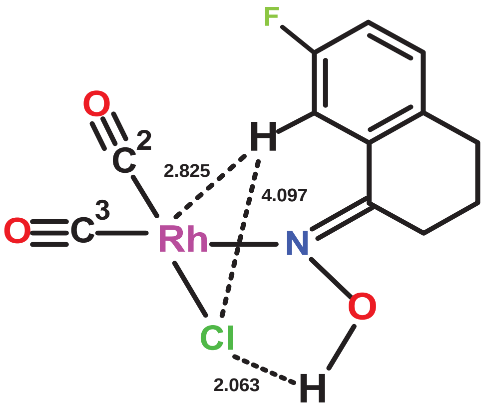

16

Figure 3.15 Important separations (Å) for **11**–**16**.

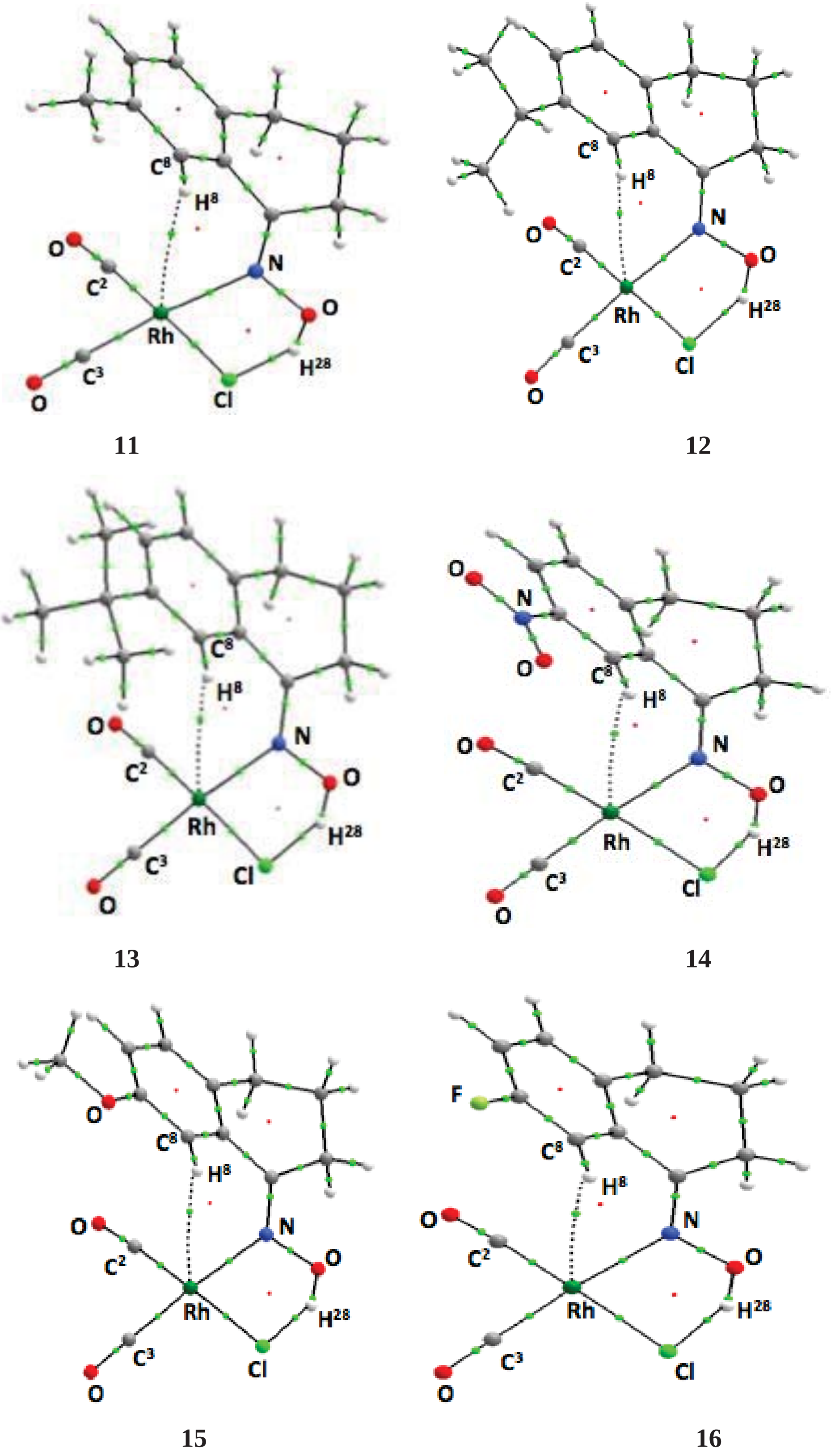

11 12

13 14

15 16

Figure 3.16 QTAIM molecular graphs for complexes **11–16**.

It should also be noted that the 7-substituted complexes are all (N)–OH oximes which have the OH····Cl hydrogen bonding component in the coordination plane whereas the **8**, **9** and **10** complexes [(N)–OMe complexes] do not have such a hydrogen bonding component. The Cl···HO distances are almost similar in **14** to **16** [2.053, 2.069 and 2.063 Å, respectively] and indicate the 'strong' weak M–Cl····H hydrogen bonding[116] similar to complex **1**. As an indication of the strength of this interaction, the QTAIM Cl and H^{28}(O) atomic charges for **14**, **15** and **16** show an attractive situation [q(Cl) and $q(H^{28})$ values for **14**: –0.545 and 0.594 e, respectively; q(Cl) and $q(H^{28})$ values for **15**: –0.554 and 0.592 e, respectively ; q(Cl) and $q(H^{28})$ values for **16**: –0.551 and 0.593 e, respectively], there is a bond path and associated bcp with a positive Laplacian value [$\nabla^2\rho$ for **14–16**: 0.0643, 0.0648 and 0.0649 e/Bohr^5, respectively] and negative energy density value [H(bcp) for **14–16**: –0.0069, –0.0062 and –0.0064 Hartree/Bohr^3, respectively] (Figure 3.16; refer to Table 3.6 in Appendix A.2). The negative energy density values indicate the involvement of some covalency for the donation from lone pair (LP) on Cl to the O–H^{28} antibonding orbital which is verified by the NBO analysis [E(2) values for the Cl to O–$H^{28}\sigma^*$ donation in **14–16**: 17.45, 16.18 and 16.54 kcal mol^{-1}, respectively] (Table 3.4).

Regarding QTAIM properties for the Rh····H^8 separation in **11–16** (Table 3.3), all complexes have a bond path for the Rh···H^8 separation, but the bcp properties are not very different as compared with **1**. The nature and strength of the interaction are also very similar. The NBO analysis also shows no noticeable changes in the donations compared with **1**. The spectroscopic properties (Table 3.1) also follow the same trend of no significant change compared with **1**.

3.5.5 Combined Steric and Electronic Effects, Complex 17

Earlier it was seen that a *tert*-butyl group attached to N (complex **5**) and an electron donating group S^- at the *para* position of the tetralone ring system (complex **10**) shortened the Rh···H^8 separations compared to other complexes [Rh···H^8 separation in **5** and **10**: 2.548 and 2.542 Å, respectively] (Figure 3.9a,b). Therefore, based on these results it was of interest to apply a combined steric and electronic influence which might lead to further closing up of the Rh···H^8 separation. For this purpose, an (N)–CMe_3 group was used to force an upright positioning of the tetralone system and two stronger electron-donating groups, S^- and NH_2 (for NH_2: F value –0.08; R value –0.74)[106] were placed at the C^5 and C^7 positions respectively as in complex **17** (Scheme 3.1).

The structural features of **17** (Table 3.1) show almost no change in the Rh···H^8 separation compared with **5** and **10** [distance: 2.544, 2.548 and 2.542 Å, respectively] (Figure 3.17a,b). However, the Cl···H^8 separation in **17** is more similar to **5** but not **10**

[Cl····H^8: 2.565, 2.542 and 2.813 Å, respectively]. The closer Cl····H^8 separation in **17** and **5** indicates that the (N)–CMe$_3$ group positions H^8 almost in the middle of the Rh–Cl bond. Interestingly, despite having similar positioning of H^8, both complexes **17** and **5** show some noticeable differences in separation angles: the Rh···H–C angle is almost 15^o smaller and the Cl····H–C^8 angle is 17^o smaller in **17** than in **5**. The Rh–N bond length in **17** has increased a little [Rh–N bond length in **17** and **5**: 2.236 and 2.182 Å, respectively but the Rh–N=C angle is slightly smaller in **17** [values: 115.0; c.f. 118.7^o in **5**]. Comparing the torsions in **17** and **5** indicates a significant increase in the dihedral angle C^1–C^{8a}–C^8–H^8 [26.2^o and 9.3^o, respectively; c.f. 15.8^o in **10**] which shows there is quite severe bending of the C–H^8 bond away from the plane of the aromatic ring. However, the dihedral angle, N=C^1–C^{8a}–C^8 decreases in **17** [33.2; c.f. 37.4^o in **5**] but the OC^2–Rh–N=C angle remains unchanged [70.3 and 70.4^o in **17** and **5**, respectively]. Also, the angle between the aromatic ring/coordination planes is smaller in **17** [53.6; c.f. 58.7^o in **5**]. The decrease in the aromatic plane angle indicates the flattening of the aromatic ring in **17** due to the greater conformational changes in the alicyclic ring.

Similar to complex **5**, complex **17** also contains close approaches below the coordination plane, between the hydrogens of methyl groups and Rh or Cl atoms. These close approaches have been found between Rh and H^{34} [distance: 2.636 Å] and between Cl and H^{33} [distance: 2.786 Å] (Figure 3.17b).

The QTAIM analysis (Table 3.3) shows a bond path for the Rh····C^8 separation (Figure 3.17c) similar to that in **5** where a Rh····C^8 bcp was also present rather than Rh···H^8. The QTAIM properties show a greater positive value for the Laplacian of electron density in **17** [$\nabla^2\rho$(bcp): 0.0843; c.f. 0.0630 *e*/Bohr^5 in **5**], however, the energy density is significantly more negative than in **5** [*H*(bcp) values: –0.0055 and –0.0002 Hartree/Bohr^3, respectively]. The significant increase in the negative value of energy density in **17** indicates more covalency involved in the interaction which was then identified by the NBO analysis (Table 3.4) where the C–H to Rh–Cσ* donations are significantly larger compared to the other complexes [*E*(2) values for the donation from C–Hσ to Rh–C^{2}σ* and Rh–C^{3}σ*: 2.97 and 3.38 kcal mol^{-1}, respectively] (Figure 3.18a,b). Interestingly, no donation was found from the Rh to the C^8–C^{8a}π* orbital which was significant in **5** [*E*(2) value: 4.33 kcal mol^{-1}] (Table 3.4) but there is now donations from carbon C^8 to the Rh–Cσ* orbital [*E*(2) values for Rh–C^{2}σ* and Rh–C^{3}σ* ligands: 13.38 and 17.59 kcal mol^{-1}, respectively] (Figure 3.18c,d). The QTAIM charges (Table 3.3) reveal a significant increase in the C^8 charge which is now –0.092 compared with –0.020 *e* in the complex **5** and this increase in negative charge builds a stronger attractive interaction with Rh and draws the hydrogen H^8 closer towards Rh. The QTAIM charge on H^8 is also less positive [0.046 *e*] than in **5**

[0.075 *e*] which also indicates less repulsion in **17**. Thus, the electrostatic charges on H^8 and C^8 appear to be a major factor in the metal···H^8 anagostic approaches.

Further analysis by the NCI index approach for **17** (Figure 3.17d) verifies an attractive interaction by revealing a clear dark blue spot in the reduced density gradient iso-surface between the C^8 and Rh. The nature of the Rh···C^8 interaction in complex **17** resembles to the recently reported C-anagostic approach in pincer complexes of rhodium (I).[166]

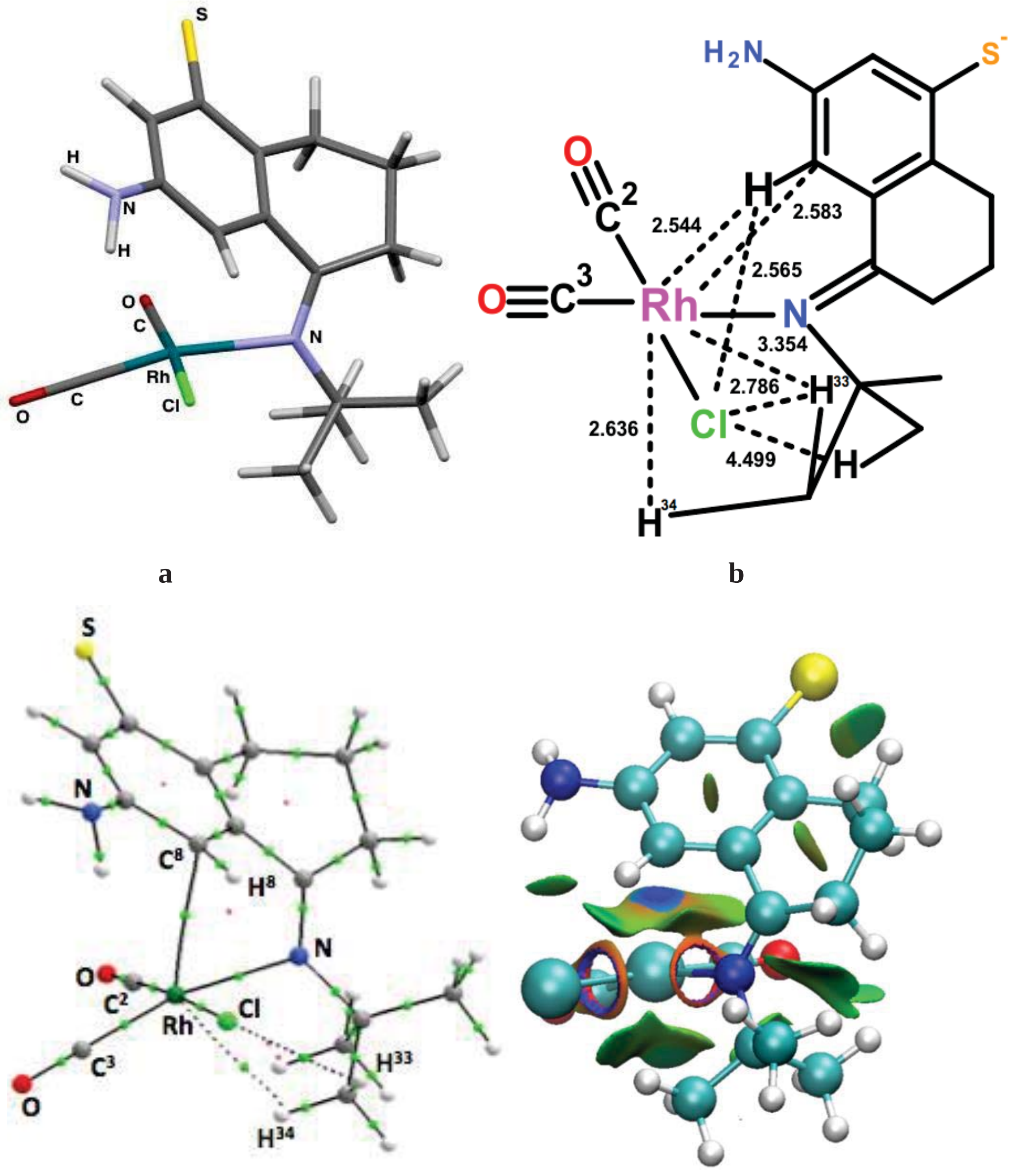

a b

c d

Figure 3.17 a) DFT structure; b) Important separations (Å); c) molecular graph; d) 3D NCI RDG iso-surface diagram for **17**.

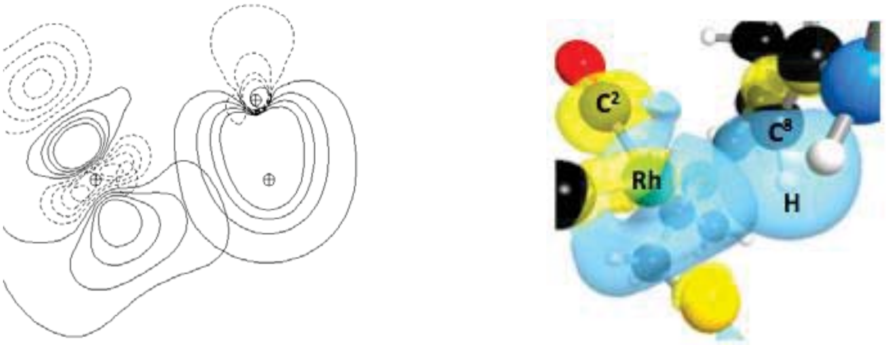

a) C–H to Rh–$C^2\sigma^*$ [$E(2)$ value: 2.97 kcal mol^{-1}]

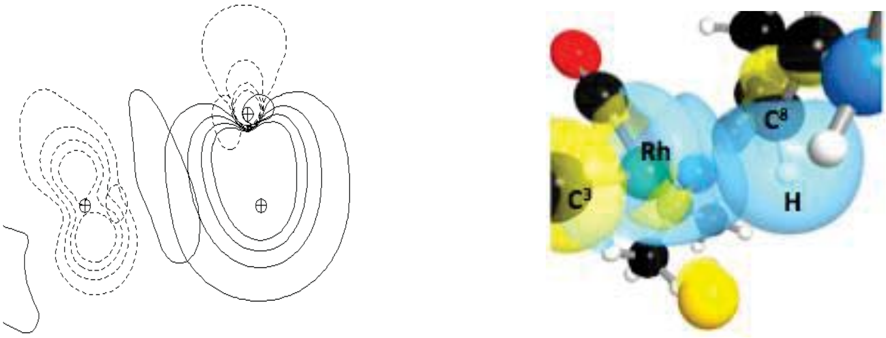

b) C–H to Rh–$C^3\sigma^*$ [$E(2)$ value: 3.38 kcal mol^{-1}]

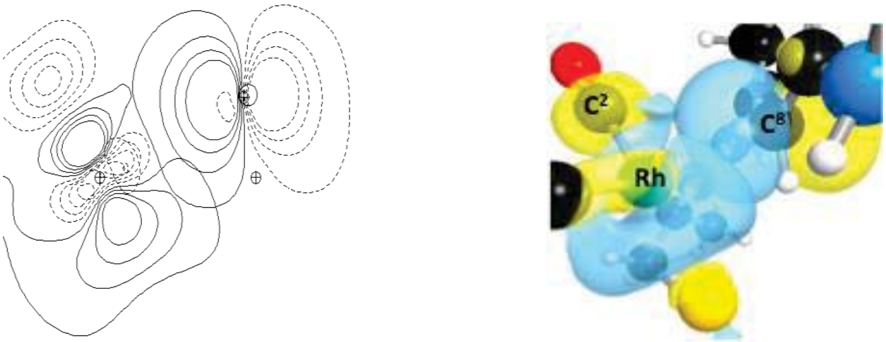

c) LP C^8 to Rh–$C^2\sigma^*$ [$E(2)$ value: 13.38 kcal mol^{-1}]

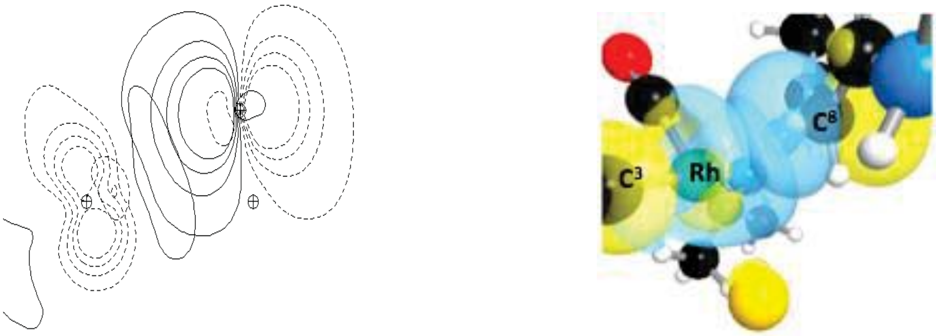

d) LP C^8 to Rh–$C^3\sigma^*$ [$E(2)$ value: 17.59 kcal mol^{-1}]

Figure 3.18 2D Contours (left) and 3D spatial overlap (right) images for important NBO interactions in **17**. The blue and yellow NBO lobes indicate (+) and (–) phases, respectively.[113]

The spectroscopic data for **17** (Table 3.1) reveal no significant changes compared to the other complexes except for the ^{1}H NMR downfield shift which is almost similar in both ligand and complex with a Δδ value of 0.06 ppm. Interestingly and contrary to the NBO analysis which indicates the emergence of the agostic covalency, there is very little change in the ^1JC–H coupling constant [138.7 Hz for the complex; c.f. 135.1 Hz for the free ligand] which in the case of agostic interaction is seen be significantly decreased.

Regarding below the coordination plane approaches in **17**, two bond paths exist for Rh····H^{34} [$\nabla^2\rho$(bcp): 0.0398 *e*/Bohr^5 and *H*(bcp): –0.0002 Hartree/Bohr^3] and Cl···H^{33} [$\nabla^2\rho$(bcp): 0.0321 *e*/Bohr^5 and *H*(bcp): 0.0014 Hartree/Bohr^3] (refer to Table 3.6 in Appendix A.2). The QTAIM charges indicate the former as a repulsive interaction [*q*(Rh): 0.642 *e*; *q*(H^{34}): 0.010 *e*] while the later as an attractive interaction [*q*(Cl): –0.623 *e*; *q*(H^{33}): 0.020 *e*]. The negative energy density value for the Rh···H^{34} bcp indicates a little covalency involved, which was then revealed by the NBO analysis as showing a donation from LP(Rh) to the C^{31}–H^{34}σ* orbitalwith the small *E*(2) value of 1.38 kcal mol^{-1}.

3.6 Conclusion

In summary, work in this chapter shows that both the steric and electronic effects can influence the anagostic interactions. The nature and size of the group attached to the coordinating N-atom play an important role in the positioning of the hydrogen over the metal coordination sphere. For instance, H^8 lies more over the metal when there is an OH group attached to N and by the introducing bulky groups (OCMe$_3$ or CMe$_3$), H^8 positions towards the chloro ligand and weak hydrogen bonding between H^8 and Cl occurs. The CMe$_3$ group at coordinating atom N, complex **5**, significantly influences the Rh–N bond length and flattens the aromatic ring so that C^8 comes close to the metal. Below the coordination plane, the bulky groups (OCMe$_3$ and CMe$_3$) hydrogens make anagostic approaches with Rh and weak hydrogen bonding occurs with the Cl ligand. The H^8 chemical shift value changes with the change in the separation but it was also found that the overall environment around H^8 affects its chemical shift value, in that this effect is greater when H^8 has closer distances with Rh and Cl as in complexes with (N)–OCMe$_3$ (complex **4**) and (N)–CMe$_3$ (complex **5**). As the anagostic interaction is an electrostatic repulsive interaction, therefore the decrease in the H^8 positive charge reduces the repulsion and Rh···H^8 separation gets shorter. However, the increase in the C^8 negative charge builds an attractive Rh···C^8 interaction (complex **17**) which leads to the closeness of the Rh····C^8 separation.

It is seen in the complexes studied that in anagostic interactions the large disparity in energy between the metal and C–H orbitals is the major obstacle to driving the overlap between them. Thus to develop the covalency between the orbitals, the interacting orbitals must have similar orbital energies. The orbital energies were slightly affected by the substituents but not enough to develop a meaningful covalency component.

Chapter 4

A change of metal centre: Steric and Electronic Manipulation of Anagostic interactions in Oxime and Imine Complexes of Palladium (II)

4.1 Introduction

Cyclometallation reactions are important in organometallic chemistry because of their role in C–H bond functionalisations that are involved in the development of pharmaceuticals, natural products, and luminescent materials. The mechanistic studies reveal that the cyclometallated product is formed as a consequence of different types of carbon-hydrogen···metal (C–H····M) interactions which are known as anagostic[31] or pseudoagostic[32], preagostic[33,34] and agostic[28-30] interactions. For these various interactions, the anagostic interaction is known as an electrostatic interaction where there is very little sharing of C–H bond electron density with metal-based orbitals,[28,65] as was indicated by the studies in Chapter 3. The term 'preagostic' has been used for interactions when the metal donates some electron density to the C–H antibonding orbital and there is also some electrostatics involved.[34] On the other hand, the agostic interaction has mainly covalent components involved, where a C–Hσ orbital on the ligand donates electron density to metal orbitals.[28,35] The mechanistic insights into C–H···M interactions reveal that the agostic interaction is preceded by the anagostic or preagostic interaction where the initial coordination of the ligand to the metal places the C–H hydrogen above the coordination plane and close to the metal centre.[28,31–33] Thus, if the anagostic interaction does not occur between the hydrogen and metal, then the agostic interaction is unlikely to arise and subsequently, cyclometallation which forms the metal-carbon bond will not take place. In this respect, precautions are always necessary when selecting the substrates and the metal for the design of catalysts for cyclometallation reactions.[8–10]

In the previous Chapter 3, the steric and electronic effects on the anagostic approach were studied using 1-tetralone oxime and imine ligands and $[Rh(CO)_2Cl]$ as the metal precursor. In that study, some interesting results were seen as the electron donating substituents at the position on the aromatic ring *para* to the C–H bond, drew the C–H group closer towards the metal and the electron withdrawing substituents had opposite effect. It was seen that placing a *tert*-butyl group on the 1-

tetralone oxime ligand caused a significant tilt of C–H group towards the chloro ligand which resulted in the Cl····H^8 separation becoming shorter, from 4.077 Å (N)–OH ligand) to 2.534 Å (N)–$OCMe_3$. The π-electron donating groups S^- and NH_2 at the *para* and *ortho* positions, increased the negative charge at the C–H bond carbon, which resulted in an increase in attraction between the carbon and metal atoms (Chapter 3). As the cyclometallation reactions are common where the palladium precursors are used [9b,10] it was therefore of interest to study the influence of steric and electronic effects using a palladium precursor in addition to the $[Rh(CO)_2Cl]$ precursor that was used in chapter 3.

A commonly used cyclopalladation reagent is the $PdCl_4^{2-}$ dianion which has been shown to be involved in the formation of the anagostic anion $[PdCl_3(L)]^-$, which then moves on to the neutral agostic complex $[PdCl_2(L)]$ before the cyclometallation proceeds.[124] In $[PdCl_3(L)]^-$ anions, the metal has an oxidation state of +2 and by including three anionic Cl ligands, the overall charge of the complex is –1 compared to $[Rh(CO)_2Cl(L)]$ which is a neutral complex with an oxidation state of +1 for the metal. As it was seen in the earlier study for rhodium in chapter 3 that steric and electronic effects were involved in shifting the C–H bond hydrogen towards the chloro ligand, therefore it was of interest to see whether the C–H hydrogen would shift more towards Cl as the overall system is now negatively charged in a $[PdCl_3(L)]^-$ anion. More importantly however, it was of interest to find whether the M····H separation would close up in an anion. Finally, it was interesting to investigate whether a C-anagostic type interaction is formed between Pd and anagostic carbon when bulky or strong electron-donating substituents are used (Chapter 3). To investigate this, a number of complexes were computed, as shown in Scheme 4.1, where the R^3 substituent on the aromatic ring position was used for the steric influence and the R^1 (C^7) and R^2 (C^5) positions were considered for electronic influences.

Scheme:

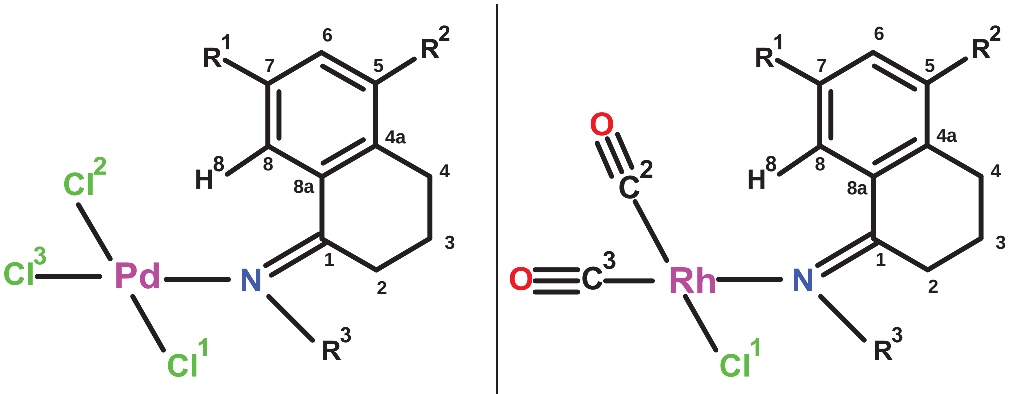

(18)	$R^1 = R^2 = H, R^3 = OH$	**(1)**	$R^1 = R^2 = H, R^3 = OH$
(19)	$R^1 = R^2 = H, R^3 = OMe$	**(2)**	$R^1 = R^2 = H, R^3 = OMe$
(20)	$R^1 = H, R^2 = H, R^3 = Me$	**(4)**	$R^1 = H, R^2 = H, R^3 = Me$
(21)	$R^1 = H, R^2 = H, R^3 = CMe_3$	**(5)**	$R^1 = H, R^2 = H, R^3 = CMe_3$
(22)	$R^1 = H, R^2 = SO_2Cl, R^3 = OMe$	**(8)**	$R^1 = H, R^2 = SO_2Cl, R^3 = OMe$
(23)	$R^1 = H, R^2 = B(OH)_3^-, R^3 = OMe$	**(9)**	$R^1 = H, R^2 = B(OH)_3^-, R^3 = OMe$
(24)	$R^1 = H, R^2 = S^-, R^3 = OMe$	**(10)**	$R^1 = H, R^2 = S^-, R^3 = OMe$
(25)	$R^1 = H, R^2 = NNPO(OEt)_2, R^3 = OMe$	(7)	$R^1 = H, R^2 = NNPO(OEt)_2, R^3 = OMe$
(26)	$R^1 = S^-, R^2 = NH_2, R^3 = CMe_3$	**(17)**	$R^1 = S^-, R^2 = NH_2, R^3 = CMe_3$

Scheme 4.1 Structure of the computed complexes.

4.2 Aim

- To manipulate by steric and electronic effects the anagostic interactions in the oxime and imine complexes of palladium (II).

4.3 Computation Approach

The geometries of the coordination complexes **18–26** were optimised employing the dispersion corrected Grimme's PBE-D3 functional[76,77] by the quantum chemical software Gaussian version G09.[108] A triple-zeta high-quality basis set (aug-cc-pVTZ-PP)[111] was used for Pd; aug-cc-pVTZ[95] for the attached ancillary ligands (Cl) and the anagostic hydrogen atom, and a double-zeta quality basis set (aug-cc-pVDZ)[95] for the remainder of the atoms. All the optimised structures were energy-minimised as verified by vibrational frequency analysis which showed no imaginary frequencies. For the NBO analysis, the calculations were performed by the NBO 6.0 software[113] and NBOVIEW 2.0[113] was used to plot the contours for the donor-acceptor interactions. For the QTAIM analysis, the extended wave function files .wfx files were generated using Gaussian and later calculations were performed by the AIMALL software.[112] The NCI calculations were performed by the NCIPLOT 2.0 software[99] and NCI surfaces were visualised by the VMD program version 1.9.2.[114] For the ligand calculations, the same procedure was employed. The same basis sets were used for the calculation of the NMR spectra. For the calculation of ^{1}JC–H, the basis set was decontracted for the anagostic carbon and hydrogen atoms which allows a more accurate determination of the electron density at the nucleus.

4.4 Results and Discussion

4.4.1 DFT Computed Structure and Properties of Pd(Cl)$_3$(1-tetralone oxime)]$^-$, Complex 18

The PBE-D3 optimised structure of [Pd(Cl)$_3$(1-tetralone oxime)]$^-$, complex **18**, shows noticeable changes in the structural parameters compared to the [Rh(CO)$_2$Cl(1-tetralone oxime)], complex **1** (Table 4.1). Inspection of the structural parameters indicates that the Cl^1 ···HO separation is slightly shorter than was found for analogous rhodium complex **1** [distances: 2.049 and 2.071 Å, respectively] which shows slightly stronger hydrogen bonding. The decrease in the Cl^1 ···HO distance in **1** results in a lengthening of one of the two *trans* related Pd–Cl bonds [Pd–Cl^1: 2.372 Å; Pd–Cl^2: 2.327 Å]. In comparison with the Rh–Cl bond in **1**, there is a slight increase in the Pd–Cl^1 bond length [2.372 Å; c.f. Rh–Cl bond length: 2.356 Å for **1**]. The lengthening of the Pd–Cl bond is an important feature of the cyclometallation reactions[10] as the ancillaty ligand Cl accepts the hydrogen from the C–H group and facilitates the metal-carbon bond formation. In complex **18**, the metal and H atom separations are now shorter as the Pd····H^8 and Pd····C^8 distances are now 2.632 and 3.306 Å, respectively compared to the rhodium complex **1** where the distances were a little longer at 2.820 and 3.354 Å, respectively. The Cl^1 ···H^8 distance is also slightly shorter in palladium complex **18** [value: 3.864 Å; c.f. 4.077 Å in **1**]. The bond lengths around the palladium atom also differ a little as the Pd–N bond length is a little shorter [values: 2.034 and 2.134 Å in **18** and **1**, respectively] and the Pd–Cl^1 bond is slightly longer [values: 2.372 and 2.356 Å in **18** and **1**, respectively].

Turning towards the angles, there are some noticeable variations seen in correlation with the change in distances with the Pd–N=C, Pd····H–C^8 and Cl····H^8–C^8 angles becoming larger in comparison to Rh-complex **1** [Pd–N=C: 134.1 and 132.9°, respectively; Pd···H^8–C^8: 119.3 and 110.1^o, respectively; Cl····H–C^8: 144.3 and 137.5^o, respectively]. Changing the metal centre also influences the torsion angles. For example, the Cl^2–Pd–

N=C dihedral angle is almost 11^{o} larger than in Rh complex **1** [values: 41.9 and 30.6^{o}, respectively] and the N=C^{1}–C^{8a}–C^{8} dihedral angle is slightly smaller in **18** compared to **1** [values: 27.8 and 32.8^{o}, respectively]. The angle between the aromatic ring and coordination plane is 56.2^{o} which is larger by 5.0^{o} than in **1** [51.2^{o}]. The overall structural features indicate that the positioning of H^{8} is now slightly more out towards Cl^{1} (refer to structures **18** and **1** in Figure 4.1).

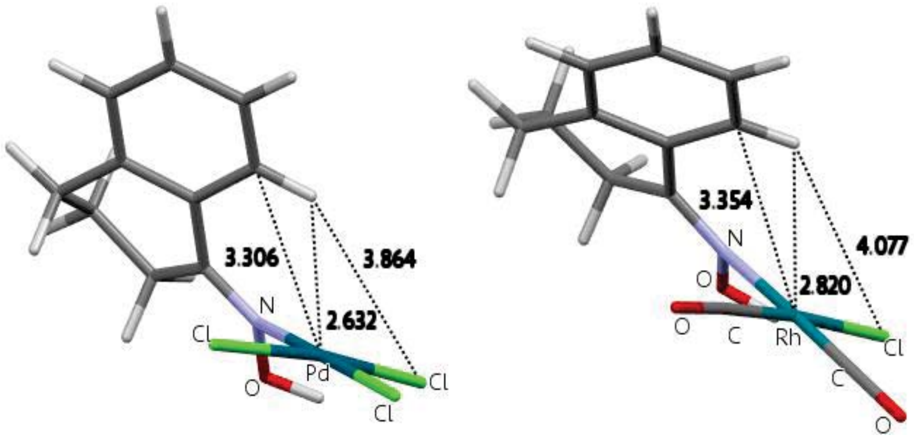

18 **1**

Figure 4.1 Optimised structures with important separations (Å) for $Pd(Cl)_3$(1-tetralone oxime) (complex **18**) and [$Rh(CO)_2Cl$(1-tetralone oxime)] (complex **1**).

Comparing the structural features of the coordinated ligand in complex **18** with the free ligand, there are significant distortions in the dihedral angles in the complex where the N=C–C–C^{8} and C^{1}–C^{8a}–C^{8}–H^{8} dihedral angles are significantly different [values: 27.8 and -2.6^{o}, respectively; –14.5 and -1.5^{o}, respectively for ligand]. The N–O–H angle becomes only slightly smaller in the complex [values: 99.8; c.f. 101.4^{o} for ligand] but the O–H bond distance becomes longer [1.009 and 0.972 Å in the complex and ligand, respectively]. Also, the C^{8}–H bond length is almost unchanged [1.090 and 1.092 Å in ligand and complex respectively] which shows almost no donation of electron density from the C–H bond to the metal, based on the lengthening seen in agostic interactions.

To understand the bonding components involving the close contacts in complex **18**, especially for the Pd····H^{8} and Pd····C^{8} separations, QTAIM and NBO approaches were utilised.[35,41] The QTAIM approach has become very popular in recent times for understanding the nature of M···H interactions as it gives insight from a topological description of the electron density.[51,52] The QTAIM molecular graph obtained from the QTAIM calculations shows whether a bond path for the interacting atoms is present and the QTAIM descriptors such as electron density, Laplacian of electron density and energy density can be used to unveil the nature of the bonding.[51] The NBO approach which gives a valence-bond description to bonding, is very useful to quantify the donor-acceptor interactions by using the second-order perturbation energy, $E(2)$, where larger $E(2)$ value indicates a stronger interaction.[98]

Table 4.1 Selected structural parameters and spectral data for complexes **18–26**.[a,b]

Complex	**18**	**19**	**20**	**21**	**22**	**23**	**24**	**25**	**26**
Bond Length									
Pd–N	2.034	2.027	2.023	2.061	2.028	2.039	2.040	2.035	2.076
	(2.134)	(2.150)	(2.124)	(2.182)	(2.150)	(2.146)	(2.157)	(2.136)	(2.236)
Pd–Cl^1	2.372	2.360	2.359	2.385	2.361	2.368	2.368	2.334	2.410
	(2.356)	(2.351)	(2.348)	(2.382)	(2.349)	(2.371)	(2.378)	(2.335)	(2.422)
C–H^8	1.092	1.092	1.093	1.091	1.093	1.091	1.090	1.091	1.089
	(1.091)	(1.092)	(1.092)	(1.091)	(1.092)	(1.092)	(1.091)	(1.090)	(1.090)
	1.090	**1.090**	**1.090**	**1.090**	**1.090**	**1.091**	**1.096**	**1.090**	**1.090**
Separation									
Pd····H^8	2.632	2.596	2.585	2.564	2.532	2.511	2.532	2.476	2.390
	(2.820)	(2.624)	(2.586)	(2.548)	(2.632)	(2.584)	(2.542)	(2.651)	(2.544)
Pd····C^8	3.306	3.136	3.103	2.934	3.007	3.227	2.229	2.902	3.015
	(3.354)	(3.104)	(3.105)	(2.861)	(3.061)	(3.035)	(2.929)	(3.116)	(2.583)
Cl····H^8	3.864	2.645	2.729	2.430	2.592	2.775	2.775	4.081	2.444
	(4.077)	(2.753)	(2.919)	(2.542)	(2.698)	(2.863)	(2.813)	(4.020)	(2.565)
Angles (^{o})									
Pd–N=C^1	134.1	128.8	126.7	119.2	127.2	133.4	133.4	126.5	124.3
	(132.9)	(127.2)	(127.6)	(118.7)	(126.7)	(126.6)	(125.6)	(128.6)	(115.0)
Pd····H–C^8	119.3	109.7	108.1	98.7	105.1	122.2	120.8	101.7	114.9
	(110.1)	(105.8)	(108.2)	(95.2)	(102.6)	(103.8)	(99.6)	(105.0)	(79.7)
Pd··· C–H^8	44.0	51.2	52.4	59.7	54.4	41.2	42.3	56.7	46.0
	(52.2)	(54.5)	(52.3)	(62.5)	(57.1)	(55.8)	(58.8)	(55.3)	(75.8)
Cl^1····H–C^8	144.3	160.0	158.7	155.3	158.8	156.2	157.0	70.8	171.8
	(137.5)	(156.3)	(154.9)	(150.7)	(154.6)	(154.2)	(151.7)	(71.4)	(133.1)
Dihedrals (^{o})									
Cl^2–Pd–N=C	41.9	75.6	67.4	72.5	73.0	86.2	85.5	106.9	80.5
	(30.6)	(69.2)	(64.6)	(70.4)	(69.1)	(66.9)	(65.8)	(115.0)	(70.3)
Ar-Plane/CP[c]	56.2	72.0	69.0	65.1	65.3	81.7	80.9	59.9	82.1
	(51.2)	(65.4)	(62.7)	(58.7)	(62.5)	(60.9)	(58.8)	(59.7)	(53.6)
N=C^1–C^{8a}–C^8	27.8	33.3	32.7	35.9	34.0	27.1	27.7	-33.8	23.7
	(32.8)	(34.4)	(33.7)	(37.4)	(36.3)	(32.4)	(30.8)	(-36.8)	(33.2)
	-14.5	**-14.4**	**-11.5**	**2.2**	**-14.4**	**-15.7**	**-13.4**	**-13.4**	**6.2**
C^1–C^{8a}–C^8–H^8	-2.6	2.3	1.8	3.8	6.5	1.6	1.8	-12.0	3.4
	(2.3)	(6.3)	(5.7)	(9.3)	(7.5)	(10.4)	(15.8)	(-6.7)	(26.2)
	-1.5	**-1.4**	**-1.1**	**-0.7**	**-2.0**	**-2.9**	**-2.6**	**-1.9**	**-2.5**
C^7–H^7–C^8–H^8	1.0	-1.5	-1.1	-2.5	-3.3	-1.7	-1.8	5.3	-7.0[d]
	(-1.0)	(-2.9)	(-2.2)	(-4.5)	(-3.0)	(-3.7)	(-7.4)	(1.4)	(-12.6)[d]
	-0.0	**-0.1**	**-0.6**	**-0.1**	**-0.2**	**-0.6**	**-1.0**	**-0.6**	**-3.4**[d]
Spectral data									
$\nu_{C\text{-}H}$ (cm^{-1})	3091.5	3091.8	3089.9	3089.3	3087.6	3099.6	3111.4	3089.4	3105.0
	(3105.2)	(3103.1)	(3093.4)	(3103.5)	(3104.5)	(3080.0)	(3105.2)	(3116.4)	(3106.5)
(ligands)	**3133.3**	**3132.9**	**3131.3**	**3130.8**	**3138.6**	**3112.2**	**3126.3**	**3130.8**	**3112.3**
δH^8 (complex)	10.70	11.40	11.32	11.96	11.93	10.89	9.91	11.86	10.78
	(8.65)	(9.46)	(9.66)	(10.10)	(9.80)	(8.37)	(7.72)	(9.09)	(6.85)
(ligand)	**8.13**	**8.22**	**8.55**	**8.76**	**8.44**	**7.61**	**6.92**	**8.47**	**6.79**
Δδ = δC–δL	2.57	3.18	2.77	3.20	3.49	3.28	3.09	3.39	3.99
	(0.52)	(1.24)	(1.11)	(1.34)	(1.36)	(0.76)	(0.80)	(0.62)	(0.06)
^1JC–H^8 (Hz)	142.9	146.9	161.7	147.1	149.7	139.7	142.4	149.0	138.7
	(154.1)	(143.3)	(143.6)	(144.4)	(146.0)	(136.6)	(141.0)	(140.1)	(138.7)
(ligand)	**139.4**	**139.5**	**140.9**	**140.8**	**141.7**	**133.7**	**136.8**	**140.9**	**135.1**

[a] Values in brackets ( ) correspond to rhodium complexes
[b] Bold values in correspond to ligands
[c] Angle between aromatic ring and metal coordination planes
[d] H^7 is replaced by NH$_2$

The NCI index approach[99] was also used to analyse the interaction in a qualitative way. As pointed out in Chapter 3, the NCI index approach is based on reduced density gradient (RDG) which is very useful for the weak interactions if a bcp disappears in the QTAIM calculations.[125] The 3D NCI RDG surfaces obtained from the NCI calculation tell about the nature of interaction based on colour gradients where the blue colour indicates the attractive or stabilising, red for destabilising or repulsive and green for the very weak delocalised interactions.[99] The depth of the colour correlates with the strength of the interaction.[120]

The QTAIM calculations indicate two bond paths for **18** as expected from the close approaches shown by the bond distances. Out of these, the bcp properties for the Cl···C^{8a} separation are very small [ρ(bcp): 0.0090 *e*/Bohr^3; $\nabla^2\rho$(bcp): 0.0296 *e*/Bohr^5; *H*(bcp): 0.0016 Hartree/Bohr^3], indicating a very weak interaction (refer to Appendix B.1 for QTAIM data for Cl^2···C^{8a} bond critical point) The QTAIM properties for the Pd···H^8 close approach show small values for the electron density, Laplacian of electron density and the energy density but compared to the Cl···C^{8a} interaction, the values are larger [ρ(bcp), $\nabla^2\rho$(bcp) and *H*(bcp) values for the Pd···H^8 bcp: 0.0148 *e*/Bohr^3, 0.0373 *e*/Bohr^5 and 0.0001 Hartree/Bohr^3, respectively] (Table 4.2). The positive Laplacian of electron density and the energy density for the Rh···H^8 bcp indicate an electrostatic interaction without covalency (Figure 4.2).

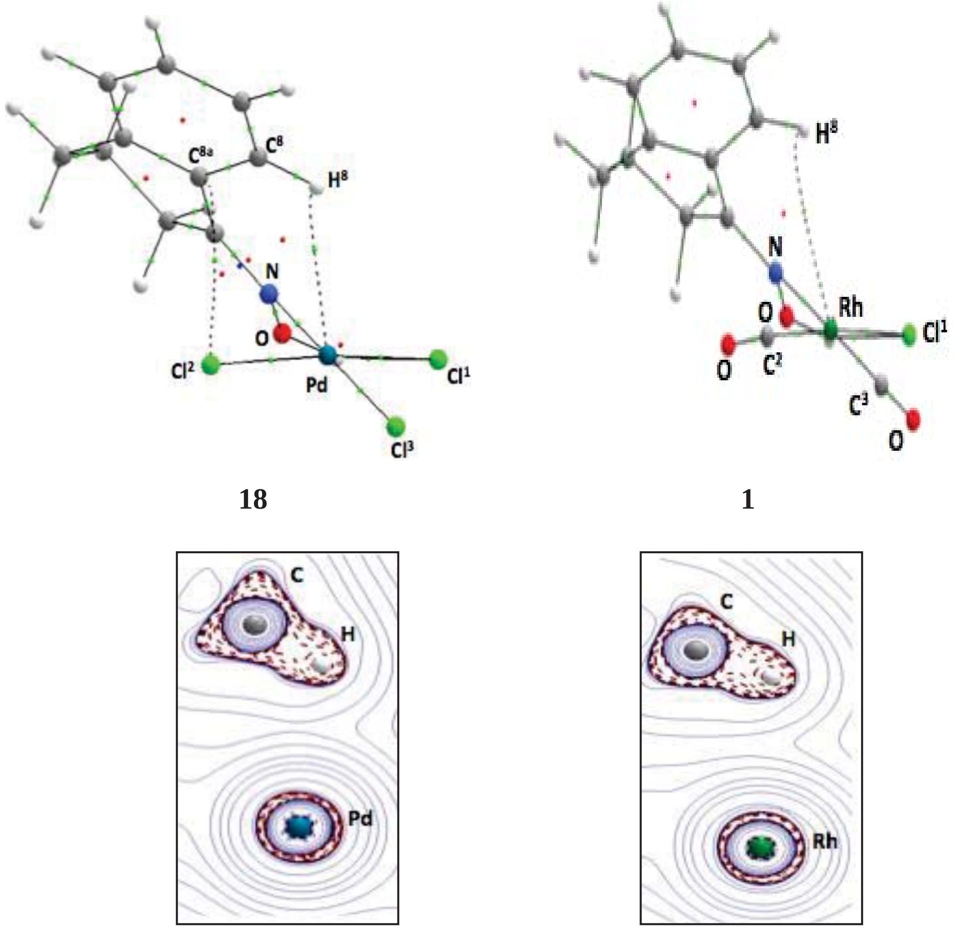

18 **1**

18 **1**

Figure 4.2 QTAIM molecular graphs (top) and Laplacian of electron density ($\nabla^2\rho$) contour plots (for C–H^8 and metal) (bottom) for **18** and **1**.

The sign of the QTAIM charges indicates a repulsive Pd···H anagostic interaction [*q*(Pd): 0.635 *e*; *q*(H^8): 0.051 *e*]. For the Cl^1···HO interaction [separation distance: 2.05 Å], the bcp properties [ρ(bcp), ∇^2ρ(bcp) and *H*(bcp) for Cl^1···HO bcp: 0.0392 *e*/$Bohr^3$, 0.0636 *e*/$Bohr^5$ and –0.0072 Hartree/$Bohr^3$, respectively] show a hydrogen bonding type interaction as the energy density value is negative in this case (refer to Appendix B.1). Comparing the Pd···H^8 bcp properties with the rhodium–tetralone oxime complex **1**, the bcp values are slightly larger in palladium complex **18** [values for bcp Rh···H^8: ρ(bcp): 0.0122 *e*/$Bohr^3$; ∇^2ρ(bcp): 0.0309 *e*/$Bohr^5$; *H*(bcp): 0.0004 Hartree/$Bohr^3$].

The NBO analysis for **18** indicates *E*(2) value of 18.41 kcal mol^{-1} for the donation from a lone pair of Cl to the O–Hσ* orbital as was expected from the shorter OH···Cl distance [2.049 Å] [in case of Rh complex **1**: the *E*(2) value was 15.90 kcal mol^{-1}] (Table 4.3). The donations relevant to any Pd····H–C agostic interaction are below 2.0 kcal mol^{-1} which endorses the QTAIM results indicating electrostatic dominance [*E*(2) values for the C–Hσ to Pd–Cl^2σ* and Pd–Cl^3σ* orbital: 1.07 kcal mol^{-1} and 1.27 kcal mol^{-1}, respectively; c.f. 0.32 and 0.67 kcal mol^{-1}, respectively for Rh complex **1**]. The slightly greater donation into the Pd–Cl^2σ* orbital seems a factor responsible for the increase in bond length compared with the Pd–Cl^3 bond [bond length for Pd–Cl^2 and Pd–Cl^3: 2.327 and 2.292 Å, respectively]. Looking at the driving forces for the presence of any agostic component at all (i.e. C–Hσ to Pd donation) it appears that the smaller difference in the donor-acceptor energies [NBO energies difference for Pd complex **18**: C–Hσ and Pd–Cl^2σ* is 0.0435 a.u.; C–Hσ and Pd–Cl^3σ* is 0.0405 a.u.; NBO energies difference for Rh complex **1**: C–Hσ and Rh–C^2σ* is 0.0999 a.u; C–Hσ and Rh–C^3σ* is 0.2439 a.u.] and the slightly higher values for the overlap matrix , allow slightly more agostic donation in the palladium complex **18** [overlap matrix values for agostic donation in palladium complex **18**: 0.0756 and 0.1036, respectively; 0.0537 and 0.0988, respectively for rhodium complex **1** (refer to Table 4.4 in Appendix B.2)]. There is also a little back-donation of electron density from a lone pair on palladium to the C–Hσ*orbital with *E*(2) value of 1.32 kcal mol^{-1} [in the case of rhodium complex **1**: the *E*(2) value for the Rh lone pair to the C–Hσ* orbital is 0.73 kcal mol^{-1}]. Likewise, in rhodium complex **1** ([Rh$(CO)_2$Cl(1-tetralone oxime)]) where there was little donation found for Rh to C^8–C^{8a}π* orbital donation [*E*(2) value: 0.56 kcal mol^{-1}], in palladium complex **18** this donation is also present but the *E*(2) value is significantly smaller [*E*(2) value: 0.22 kcal mol^{-1}].

Looking at the 3D NCI RDG iso-surface plot for **18** (Figure 4.3), there is a slight blue colouration between H^8 and Pd compared with **1**, which indicates a slightly attractive situation. This attractive situation corresponds to the small agostic donations between C–Hσ and Pd–Clσ* NBOs.

The spectroscopic values (Table 4.1) indicate some differences between the ligand and complex **18** as the IR stretching frequency for the C–H bond is 43 cm^{-1} to lower wavenumber in the complex, which is slightly greater than that found for the rhodium-tetralone oxime complex **1**, where the decrease was 28 cm^{-1} (Table 4.1). The calculated NMR data for **18** shows a downfield shift ($\Delta\delta$) of 2.57 ppm and a little increase in the coupling constant compared to the free ligand [^1JC–H for complex and ligand for **18**: 142.9 and 139.4 Hz, respectively; c.f. 154.1 and 139.4 Hz, respectively for rhodium complex **1**].

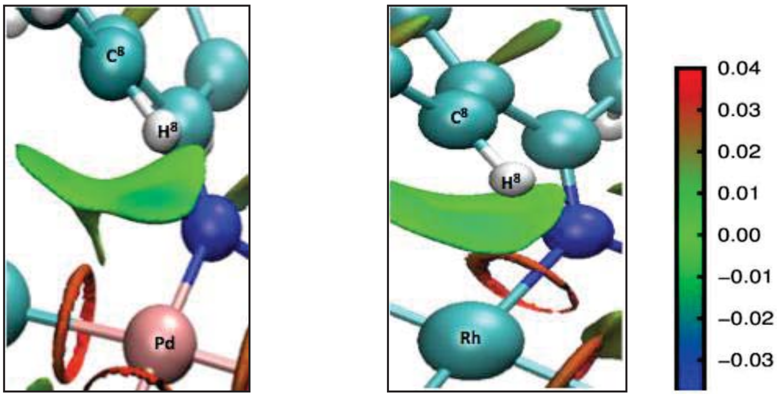

18 **1**

Figure 4.3 3D NCI RDG iso-surfaces for **18** and **1**. The sign of the second Hessian eigenvalue ($\lambda 2$) times the electron density values are shown by the colour map.

4.4.2 Steric Effects at the (N)–R Nitrogen, Complexes 19–21

In the case of the 1-tetralone oxime ligand, it was observed that by changing the metal and ancillary ligands from Rh(CO)$_2$Cl in **1** to PdCl$_3$ in **18**, the separations, as well as the relevant bonding properties for the C^8–H···M interactions were affected. It was seen in **18** that there was a stronger hydrogen bonding component between (N)–OH and M–Cl groups [*E*(2) value of 18.4 kcal mol^{-1}] and this appears to be an influential factor in the increase of the M–Cl bond length. Therefore, it was of interest to remove the hydrogen bonding effect and to increase the steric influence to see whether the anagostic interactions can be influenced in this scenario and also when the metal is in a higher oxidation state (+2 for Pd; +1 for Rh) and where the complex is anionic with the overall charge of -1 rather than neutral. So to proceed with this, the size of the group at the coordinating N atom was increased by changing (N)–OH in **18** to (N)–OMe in **19** in the oxime series and to (N)–Me and (N)–CMe$_3$ in imine complexes **20** and **21**, respectively.

Turning towards the structural features for complex **19**, the C–H^8 bond hydrogen is inclined more towards Cl^1 compared to **18** as a result of a conformational change in the alicyclic ring, whereby the chair-like form changes to a boat-like form (Figure 4.4). Also, as expected, by replacing (N)–OH in **18** to (N)–OCH$_3$ in **19**, the Cl····HO hydrogen-bonding component is absent which leads to a decrease in the Pd–Cl^1 bond length in **19** [2.360 Å; c.f. 2.372 Å in **18**] (Table 4.1). The H^8 hydrogen is slightly closer to Pd with a distance of 2.596 Å [c.f. 2.632 Å in **18**] but it becomes significantly more close to Cl^1 [2.645 Å; c.f. 3.864 Å in **18**]. The distance between Pd and C^8 is also slightly short [3.136 Å; c.f. 3.306 Å in **18)**. Other notable structural changes are seen in the torsions and angles involving the coordinated N atom. The torsion angle, N=C^1–C^{8a}–C^8, increases to 33.3^o from 27.8^o in **18**, the Cl^2–Pd–N=C dihedral angle is significantly increased to 75.6^o [c.f. 41.9^o for **18**], the push-back angle, Pd–N=C, decreases to 128.8^o from 134.1^o (**18**) and the angle between coordination and aromatic ring planes is greatly increased to 72^o compared to 56.2^o in **18**. Below the coordination plane, there are two close approaches present between alkylic hydrogens and Cl^1 atoms [H^{28}····Cl: 2.801 Å; H^{29}····Pd: 2.787 Å].

Table 4.2 Selected QTAIM parameters for complexes **18–26**.[a,b]

Complex	**18**	**19**	**20**	**21**[c]	**22**	**23**	**24**	**25**	**26**
Pd····H–C bond path	Exists	Exists	Exists	Exists	Exists	Exists	Exists	Exists	Exists
ρ(bcp)	0.0148	0.0168	0.0174	0.0204	0.0200	0.0181	0.0175	0.0233	0.0235
∇^{2}ρ(bcp)	0.0373	0.0459	0.0478	0.0601	0.0556	0.0469	0.0456	0.0645	0.0662
H(bcp)	0.0001	0.0003	0.0004	0.0004	0.0003	-0.0001	-0.0001	0.0001	-0.0004
H atomic basin									
Charge *q*(H)	0.051	0.085	0.084	0.095	0.100	0.048	0.045	0.095	0.055
	0.040	**0.040**	**0.051**	**0.054**	**0.057**	**0.003**	**0.000**	**0.052**	**0.006**
Atomic volume	43.2	38.8	39.5	36.5	37.3	40.3	40.7	37.2	34.9
V(H)[d]	**46.5**	**46.5**	**45.6**	**45.1**	**45.0**	**49.1**	**49.7**	**45.2**	**48.4**
C atomic basin									
q(C)	0.018	0.000	0.002	-0.009	0.007	-0.015	-0.026	-0.007	-0.042
	0.001	**0.001**	**0.001**	**0.001**	**0.015**	**-0.025**	**-0.045**	**0.008**	**-0.049**
Pd atomic basin									
q(Pd)	0.635	0.645	0.636	0.646	0.653	0.645	0.648	0.666	0.642
Complex	**1**	**2**	**4**	**5**[c]	**8**	**9**	**10**[c]	**7**	**17**[c]
Rh···H–C bond path	Exists	Exists	Exists	Absent	Exists	Exists	absent	Exists	absent
ρ(bcp)	0.0122	0.0169	0.0177	0.0234	0.0175	0.0188	0.0222	0.0171	0.0401
∇^{2}ρ(bcp)	0.0309	0.0446	0.0459	0.0630	0.0466	0.0493	0.0563	0.0437	0.0843
H(bcp)	0.0004	0.0003	0.0001	-0.0002	0.0003	0.0001	-0.0003	0.0002	-0.0055
H atomic basin									
Charge *q*(H)	0.038	0.061	0.061	0.075	0.078	0.023	0.026	0.039	0.046
	0.040	**0.040**	**0.051**	**0.054**	**0.057**	**0.003**	**0.000**	**0.052**	**0.006**
Atomic volume	44.9	40.4	41.1	38.0	39.4	42.8	42.4	42.6	40.1
V(H)[d]	**46.5**	**46.5**	**45.6**	**45.1**	**45.0**	**49.1**	**49.7**	**45.2**	**48.4**
C atomic basin									
q(C)	-0.001	-0.011	-0.006	-0.020	-0.002	-0.037	-0.056	0.002	-0.092
	0.001	**0.001**	**0.001**	**0.001**	**0.015**	**-0.025**	**-0.045**	**0.008**	**-0.049**
Rh atomic basin									
q(Rh)	0.626	0.635	0.633	0.654	0.632	0.644	0.637	0.634	0.642

[a] ρ(bcp) = *e*/Bohr^3; ∇^{2}ρ(bcp) = *e*/Bohr^5; *H* = Hartree/Bohr^3; *q* = *e*; *E* = Hartree; V =1/Bohr^3. [b] Free ligand values in bold numbers. [c] Bcp M····C^8. [d] 0.001 a.u. iso-surface.

Comparing the relevant separations with the analogous Rh(CO)$_2$Cl complex **2** (Figure 4.4), here again, the close approaches are shorter in palladium complex **19** compared to rhodium complex **2**. For instance, the M···H^8 separation decreases from 2.624 Å in **2** to 2.596 Å in **19**, the H^8 ···Cl separation is decreases from 2.753 Å (**2**) to 2.645 Å (**19)**. The Pd···Cl^1 bond length increases to 2.360 Å while it was 2.351 Å in the case of Rh complex

2. There are also some small variations associated with the angles involved with the separations in **19** and **2**.

The spectroscopic data for **19** (Table 4.1) indicate a slightly larger downfield H^8 chemical shift [Δδ value: 3.18 ppm] compared with 2.57 ppm in **18** [c.f. 1.24 ppm in case of rhodium complex **2**] and the ^1JC–H coupling constant difference between the complex and the free ligand is also increased to 7.4 Hz (**19)** from 3.5 Hz (**18)** [c.f. 3.8 Hz in case of rhodium complex **2**]. However, the decrease in the infra-red (IR) stretching frequency of the $C–H^8$ group compared with the free ligand is essentially identical in both **18** and **19** [a decrease of νC–H cm^{-1} from respective ligands in **19** and **18**: 41.1 cm^{-1} and 41.8 cm^{-1}, respectively] but substantially larger than rhodium complex **2**, where the C–H stretching frequency decrease was 29.8 cm^{-1}.

The QTAIM analysis for **19** indicates a bond path for the $Pd\cdots H^8$ separation with bcp properties (Figure 4.5; Table 4.2) [ρ(bcp): 0.0168 *e*/$Bohr^3$ (0.0148 for **18**); $\nabla^2\rho$(bcp): 0.0459 *e*/$Bohr^5$ (0.0373 for **18**); *H*(bcp): 0.0003 Hartree/$Bohr^3$ (0.0001 for **18**)] which are almost similar to that found in rhodium complex **2** [ρ(bcp): 0.0169 *e*/$Bohr^3$; $\nabla^2\rho$(bcp): 0.0446 *e*/$Bohr^5$ and *H*(bcp): 0.0003 Hartree/$Bohr^3$]. The QTAIM charges for H^8 and palladium both are slightly different compared to **18** and therefore, the nature of the interaction remains unchanged from the repulsive category [$q(H^8)$ and *q*(Pd) for **19**: 0.085 and 0.645 *e*, respectively; c.f. 0.051 and 0.635 *e*, respectively for **18**].

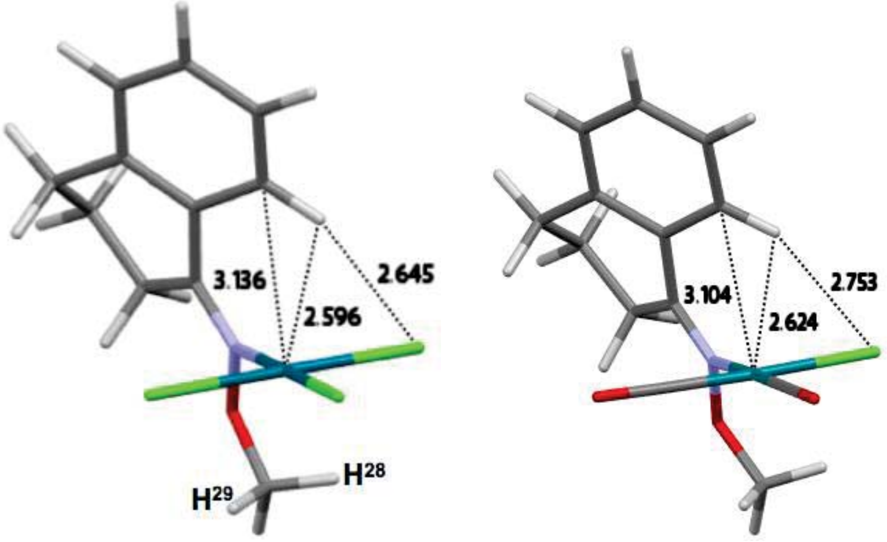

19 **2**

Figure 4.4 Optimised structures with important separations (Å) for **19** and **2**.

The NBO analysis for **19** (Table 4.3) indicates slightly more NBO donation relevant to agostic donation from C–H^{8}σ to the Pd–Cl^{2}σ* and Pd–Cl^{3}σ* orbitals [*E*(2) values: 1.57 and 1.45 kcal mol^{-1}, respectively] than in **18** [1.07 and 1.27 kcal mol^{-1}, respectively]. The agostic donations in **19** are also larger than the similar rhodium complex **2** [*E*(2) values for C–H^8 σ to Rh–C^{2}σ* and Rh–C^{3}σ* orbitals in **2**: 0.90 and 1.01 kcal mol^{-1}, respectively]. For the back donations from LP (1) Pd to the C–H^8 σ* orbital, the *E*(2) values are smaller [0.24 kcal mol^{-1}; 0.30 kcal mol^{-1} in the case of the rhodium complex **2**] compared to **18** [0.73 kcal mol^{-1}]. As it is seen that the H^8 is closer to Cl^1 than in **19** [2.645 Å; c.f. 3.864 Å in **18**] therefore, in **19**, there is comparatively significant donation seen from Cl^1 to the C–Hσ*orbital with *E*(2) values of 2.03 kcal mol^{-1} [0.0 kcal mol^{-1} in **18**]. However, Cl to C–Hσ* donation was also present in the rhodium complex where the *E*(2) value was 1.11 kcal mol^{-1}. Comparing the other donor-acceptor interactions with the analogous rhodium complex **2**, there is no donation present for the metal to C^8–C^{7}π* orbital in the case of palladium complex **19** [*E*(2) value in case of rhodium complex **2**: 2.14 kcal mol^{-1}].

The overall comparisons of the C–H···Pd interactions in complexes **18** and **19** indicate slight differences in the structural and bonding properties. However, interesting features were observed where the Pd···H^8 distance became shorter on going from (N)–OH to the (N)–OCH$_3$ ligand [2.632 and 2.596 Å for **18** and **19**, respectively] and the Pd–Cl^1 bond length became shorter [2.372 and 2.360 for **18** and **19**, respectively]. Thus, a system where the hydrogen bonding component is present, weakens the M–Cl bond somewhat and therefore can be beneficial in cyclometallation reactions where the removal of Cl leads to formation of a Pd–C bond.[10]

As it was seen in the case of the [Rh(CO)$_2$Cl(1-tetralone imine)] complexes, the N-substituents can substantially influence the C–H···M anagostic interactions. Therefore, the N-substituents (N)–CH$_3$ and (N)–CMe$_3$ were used in complexes **20** and **21** to evaluate the steric influence in the palladium tetralone complexes. The structural parameters for complex **20** (Table 4.1) reveal that the Pd···H^8 distance becomes shorter compared to **18** and **19** [values in **20**: 2.585; c.f. 2.596 and 2.632 Å in **19** and **18**, respectively] but unchanged compared with analogous rhodium complex **4** [Rh···H^8: 2.586 Å]. Similarly, the M···C^8 separation is also very similar in both rhodium and palladium complexes (Figure 4.6) [values in palladium complex **20** and rhodium complex **4**: 3.103 and 3.105 Å, respectively]. However, the Cl^1 ····H^8 distance is slightly shorter in the case of palladium [2.729 Å and 2.919 Å in **20** and **4**, respectively]. There are also small differences seen in approaches below the coordination plane as seen in the M····H^{23} separation [3.164 and 2.842 in **20** and **4**, respectively] and Cl···H^{25} separation [2.881 and 2.896 Å in **20** and **4**, respectively]. Regarding the M–Cl^1 bond length, there is an insignificant difference for both **20** and **19** [Pd–Cl^1: 2.359 and 2.360 Å for **20** and **19**, respectively] but it is a bit longer than Rh–Cl in analogous rhodium complex **4** [Rh–Cl distance: 2.348 Å].

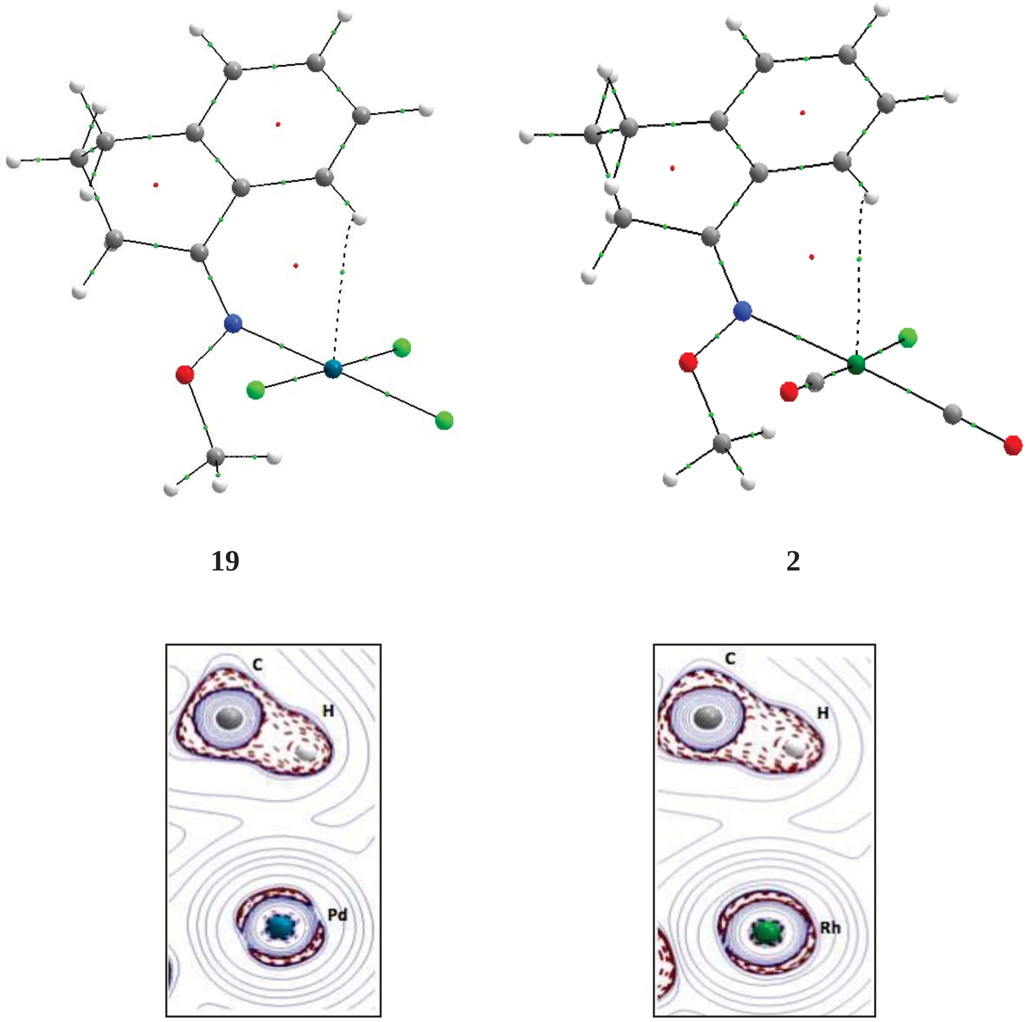

19 **2**

19 **2**

Figure 4.5 QTAIM molecular graphs (top) and Laplacian of electron density ($\nabla^2\rho$) contour plots (for C–H^8 and metal) (bottom) for **19** and **2**.

Turning towards the angles in **20** (Table 4.1), as the C–H group moves away from the Cl^1 ligand, some small changes in the associated angles and torsions occur. In comparing the angles in **19** and **20**, the trend appears that all the angles become smaller in **20**. The most significant change is seen in the Cl^2–Pd–N=C torsion angle which is reduced by 9^o in **20**. Compared with the rhodium complex with an (N)–Me substituent (**4**), most of the angles and torsions are slightly different with the most notable example involving the angle of aromatic-plane/coordination plane which is 69.0° in **20** compared with 62.7° in the case of rhodium **4**.

Table 4.3 Selected NBO parameters for complexes **18**–**26**.

Complex	**18**	**19**	**20**	**21**	**22**	**23**	**24**	**25**	**26**
C–H^{8}σ*bond									
Occupancy	1.9752	1.9744	1.9745	1.9734	1.9738	1.9751	1.9736	1.9749	1.9703
(ligand)	**1.9768**	**1.9770**	**1.9761**	**1.9754**	**1.9761**	**1.9770**	**1.9784**	**1.9781**	**1.9746**
Energy (a.u.)	-0.3218	-0.3146	-0.3148	-0.3090	-0.3419	-0.2069	-0.3372	-0.2006	-0.1965
(ligand)	**-0.4166**	**-0.4163**	**-0.4101**	**-0.4066**	**-0.4425**	**-0.4303**	**-0.2854**	**-0.2947**	**-0.2802**
C–H^{8}σ* bond									
Occupancy	0.0167	0.0244	0.0230	0.0302	0.0255	0.0239	0.0251	0.0225	0.0351
(ligand)	**0.0154**	**0.0162**	**0.0168**	**0.0177**	**0.0153**	**0.0154**	**0.0162**	**0.0165**	**0.0184**
Energy (a.u.)	0.6225	0.5286	0.5261	0.5375	0.5024	0.6303	0.5041	0.6377	0.6459
(ligand)	**0.4055**	**0.4205**	**0.4124**	**0.4127**	**0.3832**	**0.3960**	**0.5061**	**0.5202**	**0.5279**
Pd–Cl^{2}σ* bond									
Occupancy	0.4052	0.4378	0.4379	0.4326	0.4417	0.4288	0.4436	0.4284	0.4145
Energy (a.u.)	0.3653	0.4202	0.4415	0.5810	0.4105	0.5036	0.4202	0.5090	0.6890
Pd–Cl^{3}σ* bond									
Occupancy	0.3591	0.3603	0.3628	0.3555	0.3589	0.3724	0.3626	0.3720	0.3664
Energy (a.u.)	0.3623	0.4649	0.4735	0.6789	0.4481	0.5537	0.4551	0.5597	0.7900
C^{8}–C^{7}**π* bond**									
Occupancy	0.2954	–	0.2978	0.3035	0.2971	0.3190	–	0.4190	0.4132
Energy (a.u.)	0.10642	–	0.1090	0.1138	0.0826	0.2237	–	0.2302	0.2328
Palladium Lone pairs:									
LP (1)									
Occupancy (n)	1.9938	1.9939	1.9939	1.9921	1.9938	1.9934	1.9938	1.9934	1.9919
Energy (a.u.)	-0.0972	-0.0924	-0.0841	-0.0840	-0.1133	-0.0065	-0.1149	-0.0040	0.0055
LP (2)									
Occupancy (n)	1.9846	1.9763	1.9850	1.98405	1.9676	1.9814	1.9684	1.9820	1.9851
Energy (a.u.)	-0.0810	-0.0769	-0.0874	-0.08874	-0.1158	0.0081	-0.1198	0.0106	0.0038
LP (3)									
Occupancy (n)	1.9753	1.9623	1.9716	1.9631	1.9458	1.9627	1.9396	1.9626	1.9759
Energy (a.u.)	-0.1096	-0.0982	-0.0674	-0.0687	-0.1027	-0.0100	-0.1293	-0.0079	0.0198
Cl^{1} **Lone pairs**									
LP (2)									
Occupancy (n)	1.9941	1.9901	1.9904	1.9859	1.9897	1.9906	1.9895	1.9906	1.9885
Energy (a.u.)	-0.4631	-0.4395	-0.4178	-0.2446	-0.4302	-0.3939	-0.4422	-0.3920	-0.2181
LP (3)									
Occupancy (n)	1.9136	1.9817	1.9856	1.9727	1.9797	1.9862	1.9799	1.9862	1.9757
Energy (a.u.)	-0.1465	-0.1063	-0.1142	-0.1002	-0.1213	-0.0216	-0.1171	-0.0196	-0.0186
Donor-Acceptor Interactions: [*E*(2) kcal mol^{-1}]									
C–H^{8}σ to Pd–Cl^{2}σ*	1.07	1.57	1.52	2.93	2.02	2.34	2.54	2.71	6.01
C–H^{8}σ to Pd–Cl^{3}σ*	1.27	1.45	1.46	2.58	1.85	2.25	2.46	2.43	5.41
C^{8}–C^{7}π to Pd–Cl^{2}σ*	<0.05	<0.05	<0.05	1.03	0.65	0.29	0.40	0.29	1.39
C^{8}–C^{7}π to Pd–Cl^{3}σ*	<0.05	<0.05	<0.05	0.91	0.64	0.31	0.51	0.31	1.32
LP (1) Pd to C–H^{8}σ*	<0.05	0.24	<0.05	0.13	<0.05	<0.05	0.33	<0.05	0.47
LP (2) Pd to C–H^{8}σ*	1.32	<0.05	<0.05	<0.05	<0.05	1.21	<0.05	0.96	-
LP (3) Pd to C–H^{8}σ*	1.22	<0.05	1.86	2.99	2.15	0.73	<0.05	<0.05	1.43
LP (2) Cl^{1} to C–H^{8}σ*	<0.05	<0.05	<0.05	0.73	<0.05	<0.05	0.20	<0.05	<0.05
LP (3) Cl^{1} to C–H^{8}σ*	<0.05	2.03	1.57	3.71	2.36	1.05	2.24	1.05	3.41
LP C^{8} to Pd–Cl^{2}σ*	<0.05	<0.05	<0.05	<0.05	<0.05	<0.05	<0.05	1.75	<0.05
LP C^{8} to Pd–Cl^{3}σ*	<0.05	<0.05	<0.05	<0.05	<0.05	<0.05	<0.05	1.77	<0.05

The spectroscopic data for **20** indicate almost similar differences in IR stretching frequency for C–H^{8} in the ligands and the complex as was found for **19**. In both complexes **20** and **19**, there is a decrease of approximately 41 cm^{-1} in νC–H stretching frequency compared to the respective ligands (Table 3.1). However, there is a significant increase in the ^{1}JC–H coupling constant in complex **20** which is 161.7 Hz [c.f. 140.9 Hz for the free ligand] compared to 146.9 Hz [c.f. 139.5 Hz for ligand] in **19** but the chemical shift value in **20** is less downfield than in **19** [Δδ values for **20** and **19**: 2.77 and 3.18 ppm, respectively].

Table 4.3 continued Selected NBO parameters for rhodium complexes.

Complex	**1**	**2**	**4**	**5**	**8**	**9**	**10**	**7**	**17**
C–H^{8}σ bond									
Occupancy	1.9753	1.9734	1.9733	1.9715	1.9709	1.9727	1.9709	1.9734	1.9646
(Ligands)	**1.9768**	**1.9770**	**1.9761**	**1.9754**	**1.9761**	**1.9781**	**1.9784**	**1.9770**	**1.9746**
Energy (a.u.)	-0.4433	-0.4338	-0.4354	-0.4302	-0.3154	-0.3215	-0.3154	-0.4497	-0.3109
(Ligands)	**-0.4166**	**-0.4163**	**-0.4101**	**-0.4066**	**-0.4425**	**-0.2947**	**-0.2854**	**-0.4303**	**-0.2802**
C–H^{8}σ* bond									
Occupancy	0.0159	0.0202	0.0191	0.0239	0.0181	0.0189	0.0181	0.0173	0.0220
(Ligands)	**0.0154**	**0.0162**	**0.0168**	**0.0177**	**0.0153**	**0.0165**	**0.0162**	**0.0154**	**0.0184**
Energy (a.u.)	0.3880	0.4063	0.4020	0.4150	0.5184	0.5090	0.5184	0.3792	0.6632
(Ligands)	**0.4055**	**0.4205**	**0.4124**	**0.4127**	**0.3832**	**0.5202**	**0.5061**	**0.3960**	**0.5279**
Rh–C^{2}σ* bond									
Occupancy	0.3720	0.3866	0.3899	0.3819	0.3741	0.3761	0.3741	0.3964	0.3679
Energy (a.u.)	0.3434	0.3784	0.3910	0.4346	0.5129	0.4784	0.5129	0.3949	0.5905
Rh–C^{3}σ* bond									
Occupancy	0.3203	0.3186	0.3206	0.3110	0.3199	0.3256	0.3199	0.3276	0.3030
Energy (a.u.)	0.1994	0.2298	0.2483	0.3088	0.3686	0.3376	0.3686	0.2264	0.4591
C^{8}–C^{7}**π* bond**									
Occupancy	0.3939	0.3082	0.3016	0.3135	0.3769	0.3357	–	0.3869	–
Energy (a.u.)	-0.0098	-0.0029	-0.0051	-0.0013	-0.0283	0.1174	–	-0.0115	–
Rhodium Lone pairs:									
LP (1)									
Occupancy (n)	1.9762	1.9633	1.9611	1.9458	1.9574	1.9632	1.9574	1.9573	1.9478
Energy (a.u.)	-0.1782	-0.1817	-0.1686	-0.1764	-0.0616	-0.0922	-0.0862	-0.1822	-0.0847
LP (2)									
Occupancy (n)	1.8095	1.8082	1.8065	1.8037	1.8022	1.8029	1.8022	1.8109	1.8009
Energy (a.u.)	-0.2318	-0.2282	-0.2203	-0.2190	-0.1294	-0.1373	-0.1294	-0.2328	-0.1197
LP (3)									
Occupancy (n)	1.7543	1.7590	1.7549	1.7509	1.7465	1.7497	1.7465	1.7548	1.7261
Energy (a.u.)	-0.2357	-0.2294	-0.2221	-0.2205	-0.1277	-0.1372	-0.1277	-0.2334	-0.1380
Cl Lone pairs									
LP (2)									
Occupancy (n)	1.9653	1.9731	1.9738	1.9705	1.9764	1.9762	1.9764	1.9733	1.9739
Energy (a.u.)	-0.2616	-0.2684	-0.2530	-0.2640	-0.1842	-0.1895	-0.1842	-0.2277	-0.1769
LP (3)									
Occupancy (n)	1.9080	1.9453	1.9486	1.9490	1.9589	1.9547	1.9589	1.9453	1.9697
Energy (a.u.)	-0.2730	-0.2335	-0.2277	-0.2263	-0.1392	-0.1464	-0.1392	-0.2339	-0.1303
Donor-Acceptor Interactions: [*E*(2) kcal mol^{-1}]									
LP (1) Rh to C–H^{8}σ*	0.73	0.30	0.59	<0.05	0.19	0.30	0.16	0.32	<0.05
LP (2) Rh to C–H^{8}σ*	<0.05	-	-	<0.05	-	0.08	0.11	0.05	<0.05
LP (3) Rh to C–H^{8}σ*	<0.05	0.12	0.18	0.06	0.10	0.09	0.08	<0.05	<0.05
LP (1) Rh to C^{8}–C^{7}π*	0.56	2.14	2.09	4.33	2.28	2.11	<0.05	2.24	<0.05
C-H σ to Rh–C^{2}σ*	0.32	0.90	0.88	1.91	0.97	1.25	1.34	0.56	2.97
C-H σ to Rh–C^{3}σ*	0.67	1.01	1.10	1.72	1.04	1.47	1.79	1.09	3.38
LP(2) Cl^{1} to C–H^{8}σ*	<0.05	0.25	0.11	0.68	0.32	0.18	0.25	<0.05	1.17
LP(3) Cl^{1} to C–H^{8}σ*	<0.05	1.11	0.63	1.88	1.31	0.63	0.66	<0.05	0.70
LP(1) C^{8} to Rh–C^{2}σ*	<0.05	<0.05	<0.05	<0.05	<0.05	<0.05	<0.05	<0.05	13.38
LP(1) C^{8} to Rh–C^{3}σ*	<0.05	<0.05	<0.05	<0.05	<0.05	<0.05	<0.05	<0.05	17.59

Comparing the spectroscopic properties for **20** with rhodium complex **4** (Table 4.1), there is significantly smaller downfield chemical shift for H^{8} in **4** [Δδ values: 2.77 and 1.11 ppm, respectively] but the increase in ^{1}JC–H is larger in **20** than **4** [^{1}JC–H values for complexes **20** and **4**: 161.7 and 143.6 Hz, respectively; c.f. 140.9 Hz for the free ligand]. Also, there is a slightly smaller decrease in the IR stretching frequency for C–H [a difference of 41 cm^{-1} and 38 cm^{-1} for **20** and **3**, respectively].

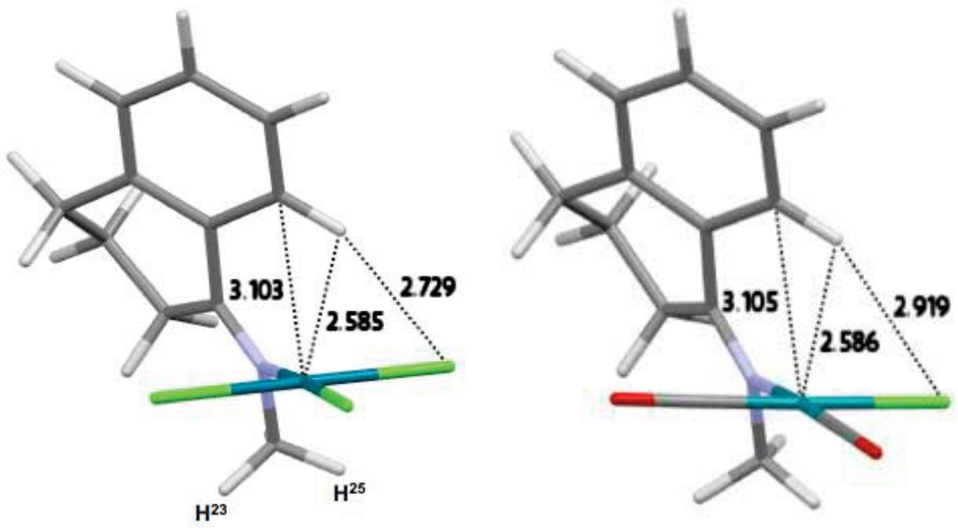

20 **4**

Figure 4.6 Optimised structures with important separations (Å) for **20** and **4**.

Similar to complex **19**, the QTAIM analysis of **20** (Table 4.2) indicates a bcp for the Pd····H^8 separation (Figure 4.7) and the bcp properties are also very similar [ρ(bcp): 0.0174 *e*/Bohr^3; $\nabla^2\rho$(bcp): 0.0478 *e*/Bohr^5; *H*(bcp): 0.0004 Hartree/Bohr^3 in **20**; c.f. ρ(bcp): 0.0168 *e*/Bohr^3; $\nabla^2\rho$(bcp): 0.0459 *e*/Bohr^5; *H*(bcp): 0.0003 Hartree/Bohr^3 in **19**]. The QTAIM charges for Pd and H^8 are also very similar in both complexes [*q*(H^8) for **20** and **19**: 0.084 and 0.085 *e*, respectively; *q*(Pd) for **20** and **19**: 0.636 and 0.645 *e*, respectively]. Thus, the nature of the Pd···H^8 interaction lies in the repulsive category, similar to the other complexes studied in this work so far. In comparison with the QTAIM properties of the Rh···H bcp in Rh-complex **4**, insignificant differences were seen [ρ(bcp): 0.0177 *e*/Bohr^3; $\nabla^2\rho$(bcp): 0.0459 *e*/Bohr^5; *H*(bcp): 0.0001 Hartree/Bohr^3]. However, the QTAIM charge for H^8 is less positive in rhodium complex **4** [*q*(H^8) for **4** and **20**: 0.061 *e* and 0.084 *e*, respectively].

The NBO analysis for **20** indicates (Table 4.3) the C–H^{8}σ to Pd–Cl^{2}σ* and Pd–Cl^3 σ* donations have almost similar *E*(2) values as in **19** [*E*(2) value for the C–H^8 to Pd–Cl^{2}σ* orbital donation: 1.52; c.f. 1.57 for **19** and to the Pd–Cl^{3}σ* orbital: 1.46; c.f. 1.45 for **19**]. However, now in **20**, there is a small but noticeable donation from LP(3) Pd to the C^7–C^8 π*orbital [*E*(2) value: 1.86 kcal mol^{-1}] which was absent in **19**. Compared with the Rh complex **4**, the agostic donations are a bit stronger in Pd complex **20** [*E*(2) values for the C–H^8 to Rh–C^{2}σ* and Rh–C^{3}σ* orbital donations: 0.88 and 1.46 kcalmol^{-1}, respectively in rhodium complex **4**] while the donations from LP(3) Rh to the C^8–C^{8a} π* is almost similar to **20** [*E*(2) values: 2.09 and 1.86 kcal mol^{-1}, respectively].

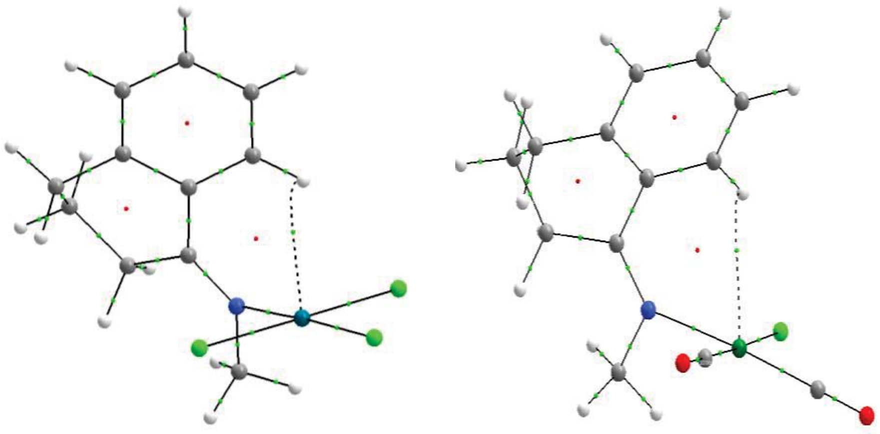

20 **4**

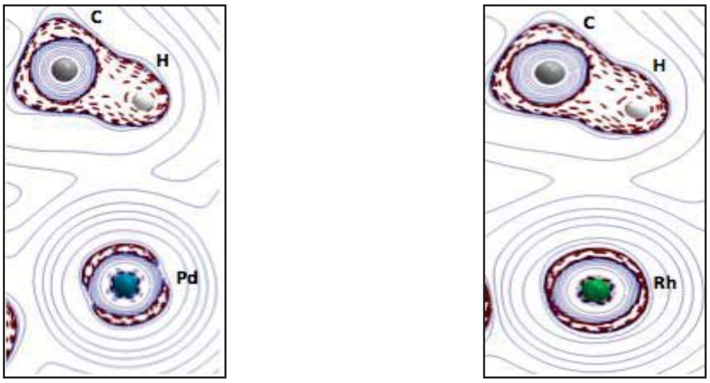

20 **4**

Figure 4.7 QTAIM molecular graphs (top) and Laplacian of electron density ($\nabla^2\rho$) contour plots (for C–H^8 and metal) (bottom) for **20** and **4**.

Moving further to **21** containing the large (N)–CMe$_3$ group there are significant variations in the distances and angles seen (Table 4.1). The C–H group is now much closer to the chloro ligand Cl^1 and the distance between H^8···Cl^1 is 2.430 Å which is shortest so far [Cl^1 ···H^8 in **20**: 2.729 Å; 2.569 Å in rhodium complex **5**] (Figure 4.8). The Pd···H^8 and Pd···C$_8$ separations [distances: 2.564 and 2.934 Å, respectively] are also the shortest ones compared to the other complexes in the comparison [Pd····H^8 and Pd···C^8 values in **20**: 2.585 and 3.103 Å, respectively; Rh····H^8 and Rh···C^8 values in Rh complex **5**: 2.548 Å and 2.861 Å, respectively]. The variations in the angles also correlate with the distances as the Pd–N=C angle is now smaller [119.2^o] compared with 126.7 ^{o} in **20**, the Cl^2–Pd–N=C is almost 5^o smaller in **21** [values: 72.5 and 67.4° for **21** and **20**, respectively] and the angle between aromatic ring and metal coordination planes is also smaller in **21** by 4^o [values: 65.1 and 69.0° for **21** and **20**, respectively]. In **21**, below the coordination plane (refer to Appendix B.1), there are three close approaches found for Cl^1···H^{33} [3.053 Å], Cl^1····H^{30} [2.578 Å] and Pd···H^{32} [2.773 Å]. Regarding the Pd–Cl^1 bond lengths, the Pd–Cl^1 bond length is significantly elongated in comparison to complex **20** [Pd–Cl^1 in **21** and **20**: 2.385 Å and 2.359Å, respectively]. The reason for the elongation would seem to be related to the close approaches of Cl with H^8 and the other alkyl group hydrogen atoms such as Cl^1···H^{30} and Cl^1···H^{33} distances [values: 2.578 and 3.053 Å, respectively]. In the case of rhodium complex **5**, the lengthening of Rh–Cl bond [bond length: 2.382 Å] was also observed when Cl was closer to H^8 and two of the *tert*-butyl hydrogen [distances for Cl^1····H^8, Cl^1····H^{34} and Cl^1····H^{39}: 2.542, 2.912 and 2.627 Å, respectively].

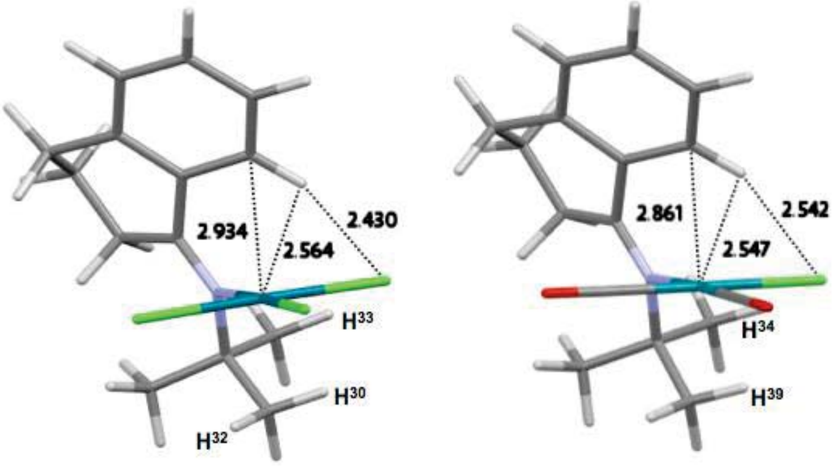

21 **5**

Figure 4.8 Optimised structures with important separations (Å) for **21** and **5**.

The spectroscopic data (Table 4.1) for **21** show that the IR stretching frequency, νC–H^8 for the complex is 41 cm^{-1} less than the corresponding ligand, which shows the involvement of normal modes from other C–H groups. The Δδ value is slightly more downfield than for **20** [values: 3.20 and 2.77 ppm, respectively]. However, the ^1JC–H coupling constant increases much less in **21** compared to **20** with respective to the free ligands [^1JC–H coupling constant difference between ligand and complex **21** and **20**: 6.3 and 20.8 Hz, respectively]. In comparing the spectroscopic properties of **21** with the (N)–CMe$_3$ ligand rhodium-tetralone complex **5**, there is an increase of 3.6 Hz in the ^1JC–H coupling constant [Δ^1JC–H value: 6.3 Hz in **21**] compared with the respective ligand. The C–H stretching frequency is decreased by 27.7 cm^{-1} [c.f. 41 cm^{-1} in **21**) and the chemical shift of H^8 is downfield by 1.34 ppm [c.f. 3.29 ppm in **21**] compared with the respective ligand. The overall changes suggest the interaction is a little stronger in the case of PdCl$_3$ complex complex **21**.

The QTAIM analysis for **21** (Table 4.2) indicates bond paths and bcps for the $H^8\cdots Cl$ and $Pd\cdots\cdot C^8$ separations (Figure 4.9) which were not seen in other palladium complexes studied so far. The analogous Rh (I) complex **5** also indicated bond paths for the $H^8\cdots Cl$ and $Rh\cdots\cdot C^8$ separations (Chapter 3) which shows the stronger influence by the bulky *tert*-butyl group the ligand structure which brings H^8 closer towards Cl^1 and C^8 towards the metal centre. The positioning of the C–H^8 group and the distance between H^8 and Cl^1 suggests the possibility of weak hydrogen bonding.

The bcp properties of the $Pd\cdots C^8$ interaction in **21** show small positive values for the energy density and Laplacian of electron density which is an indication of an electrostatic interaction [ρ(bcp): 0.0204 *e*/Bohr^3; $\nabla^2\rho$(bcp): 0.0601 *e*/Bohr^5 and *H*(bcp): 0.0004 Hartree/Bohr^3]. Also, the negative and positive values of the QTAIM charges for C^8 and Pd [$q(C^8)$: –0.009 *e*; *q*(Pd): 0.646 *e*] suggest an attractive electrostatic interaction. The H^8 $\cdots\cdot$Cl bcp is also a weakly electrostatic attractive interaction as indicated by positive values for the Laplacian of electron density and energy density [ρ(bcp): 0.0183 *e*/Bohr^3; $\nabla^2\rho$(bcp): 0.0526 *e*/Bohr^5 and *H*(bcp): 0.0009 Hartree/Bohr^3] and opposite QTAIM charges [*q*(Cl): –0.592 *e*; $q(H^8)$: 0.095 *e*]. In comparison, the QTAIM data for the Rh-complex **5** shows a negative value for the energy density and a positive value for the Laplacian of electron density for rhe $Rh\cdots C^8$ interaction bcp which indicates some covalency is involved which is also indicated by the energy density value which is negative [ρ(bcp): 0.0234 *e*/Bohr^3; $\nabla^2\rho$(bcp): 0.0630 *e*/Bohr^5 and *H*(bcp): –0.0002 Hartree/Bohr^3]. The QTAIM charges reveal that C^8 is slightly more negatively charged in the Rh complex than in the palladium analogue [$q(C^8)$ in Rh-complex **5** and Pd-complex **21**, –0.020 *e* and –0.009 *e*, respectively] so that the resulting attractive interaction is slightly stronger in case of Rh-complex **5** [the Rh and palladium charges are 0.654 *e* and 0.646 *e*, respectively].

As found for rhodium complex **5**, below the coordination plane there are three bcps found in complex **21** (refer to Appendix B.1 for the QTAIM molecular graphs and bcp properties for below the coordination plane approaches:) which lie in the category of weak electrostatic interactions based on QTAIM properties such as the Laplacian of electron density and energy density. The bcp properties for both the $Cl\cdots H^{33}$ and $Cl\cdots H^{30}$ interaction bcps (Figure 4.9) indicate positive values for the Laplacian of electron density and the energy density [ρ(bcp), $\nabla^2\rho$(bcp) and *H*(bcp) values for $Cl\cdots\cdot H^{33}$ are 0.0057 *e*/Bohr^3, 0.0177 *e*/Bohr^5 and 0.0009 Hartree/Bohr^3, respectively; ρ(bcp), $\nabla^2\rho$(bcp) and *H*(bcp) values for $Cl\cdots\cdot H^{30}$ are 0.0143 *e*/Bohr^3, 0.0418 *e*/Bohr^5 and 0.0009 Hartree/Bohr^3, respectively]. QTAIM charges reveal negative and positive values for Cl^1 and H^8, respectively which indicates that both of these interactions lie in the electrostatic attractive category [*q*(Cl): –0.592 *e*; $q(H^{30})$: 0.0505 *e* and $q(H^{33})$: 0.033 *e*]. Interestingly, despite the close separation between Pd and H^{32} [distance: 2.773 Å], there was no bcp found but instead there was a bond path present for the Pd···C^{22} separation (refer to Figure 4.9 and Applendix B.1 for the QTAIM data for below the plane Bcps) [distance 2.947 Å] with properties [ρ(bcp): 0.0176 *e*/$Bohr^3$; $\nabla^2\rho$(bcp): 0.0650 *e*/$Bohr^5$; *H*(bcp): 0.0016 Hartree/$Bohr^3$] indicative of an interaction. The QTAIM charges for Pd and C^{27} are positive so that the interaction would be weakly repulsive [*q*(Pd): 0.646 *e*; *q*(C^{27}): 0.0241 *e*].

Moving further in the bonding analysis for **21** the NBO results (Table 4.3) indicate a noticeable increase in agostic donations from the C–Hσ orbital to the Pd–Cl^2σ* and Pd–Cl^3σ* orbitals [*E*(2) values for **21**: 2.93 and 2.58 kcal mol^-1, respectively; c.f. 1.52 and 1.46 kcal mol^{-1} for **20**, respectively; *E*(2) values in Rh complex **5**: 1.91 and 1.72 kcal mol^{-1}, respectively]. The slightly increase in the agostic donations are associated with the increase in the overlap matrix values which are now 0.1469 and 0.1321 compared to complex **18** [values: 0.0756 and 0.1026, respectively; c.f. 0.1423 and 0.1411 for **5**, respectively) (refer to Table 4.4 in Appendix B.2 for overlap matrix values). It is seen that the energy difference is still large but by increasing the steric influence, the overlap matrix values become slightly larger which cause the *E*(2) values to become little greater. Thus, structural changes by the bulky group at N favours the spatial overlap between donor-acceptor groups for agostic donation. As expected from the movement of H^8 towards Cl^1 [distance: 2.430 Å], there is now a significant increase in donation from LP(3) on Cl^1 to the C–H antibonding NBO which has *E*(2) value of 3.71 kcal mol^{-1} compared to (N)–Me complex **20** where the *E*(2) value is 1.52 kcal mol^{-1}]. Comparing these NBO interactions with rhodium complex **5**, there are no donations found from the Cl^1 to the C–Hσ antibonding orbital. Instead, Rh complex **5** has a stronger donation from the metal to the C^8–C^{8a}π* NBO [*E*(2) value: 4.33 kcal mol^{-1}] which is substantially larger than in complex **21** and **20** [*E*(2) values: 2.99 and 1.86 kcal mol^{-1} for **21** and **20**, respectively] (in Pd complexes **20** and **21**, the acceptor belongs to C^7–C^8π*).

Summarising the QTAIM and NBO properties of complex **21** in comparison with (N)–CMe_3 rhodium complex **5**, there are some noticeable differences seen. Even though the QTAIM molecular graph is not much different in both complexes, the QTAIM properties are little different with the energy density value in case of rhodium being negative which indicates some covalency involved between metal and the C–H^8 group [bcp Rh···C^8: ρ(bcp), 0.0234 *e*/$Bohr^3$; $\nabla^2\rho$(bcp): 0.0630 *e*/$Bohr^5$; *H*(bcp): –0.0002 Hartree/$Bohr^3$]. This covalency component was seen in the NBO analysis where there was a stronger donation present from a rhodium lone pair to the C^8–C^{8a}π* orbital with corresponding *E*(2) value of 4.33 kcal mol^{-1} compared with 2.99 kcal mol^{-1} in the case of palladium complex **21**. In the complex **21**, there is a bond path between H^8 and Cl^1 which is absent in the case of rhodium complex **5**. The NBO analysis indicates some covalency between Cl^1 and the C–H^8σ antibonding orbital [*E*(2) value: 3.71 kcalmol^{-1}] in complex **21** whereas this donation is slightly smaller in the case of rhodium complex **5** [*E*(2) value: 2.50 kcal mol^{-1}]. Also in **21**, the agostic donations from the C–H^8σ orbital to the Pd–Clσ antibonding orbitals are also stronger [combined *E*(2) value: 5.5 kcalmol^{-1}] than similar donations from C–H^8 to Rh–C antibonding orbitals [combined *E*(2) value: 3.6 kcalmol^{-1}]. The overall analysis indicates that use of the $PdCl_3$ system instead of a $Rh(CO)_2Cl$ system favours the agostic donations.

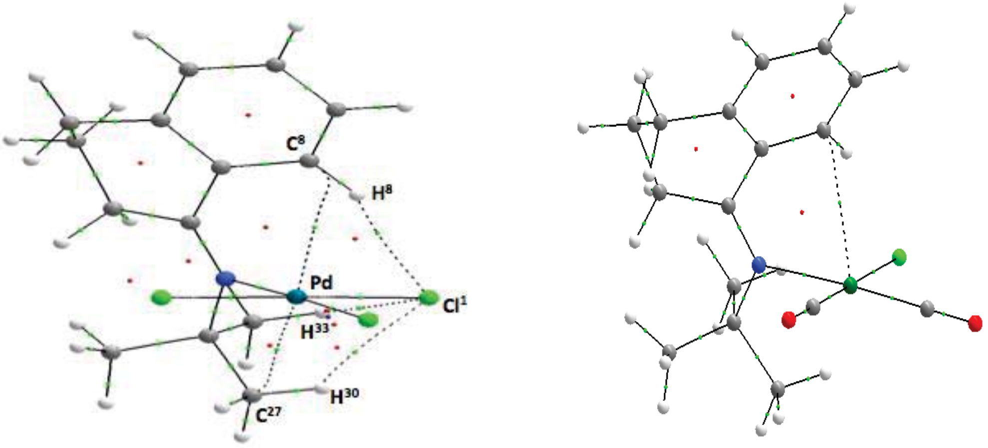

21 **5**

21 **5**

Figure 4.9 QTAIM molecular graphs (top) and Laplacian of electron density ($\nabla^2\rho$) contour plots (for C–H^8 and metal) (bottom) for **21** and **5**.

As there was one bcp seen in **5** for the Rh···C^8 interaction and two bcps for the Pd···C^8 and H^8···Cl^1 interactions in **21**, NCI calculations for both **21** and **5** were performed to compare the 3D iso-surfaces to ascertain whether there was an interaction between H^8 and Cl^1 in **5**. Figure 4.10 shows similar blue iso-surfaces between the C–H and M–Cl^1 atoms so that the Cl···H^8 interaction in **5** is now present in the NCI surface for which bcp was missing in QTAIM calculations. However, the blue spot between Cl and H^8 in **5** is slightly brighter than in **21**. As the depth of color shows the strength of the interaction,[120] therefore the interaction in **5** is slightly stronger. On the other hand, in correlation with the NBO donations from metal to the C^8–$C^{8a}\pi^*$ orbital [$E(2)$ value of 4.33 kcal mol^{-1}], the NCI 3D RDG iso-surface for Rh···C^8 in **5** shows a darker bluish spot which reveals a stronger interaction between Rh and C^8.

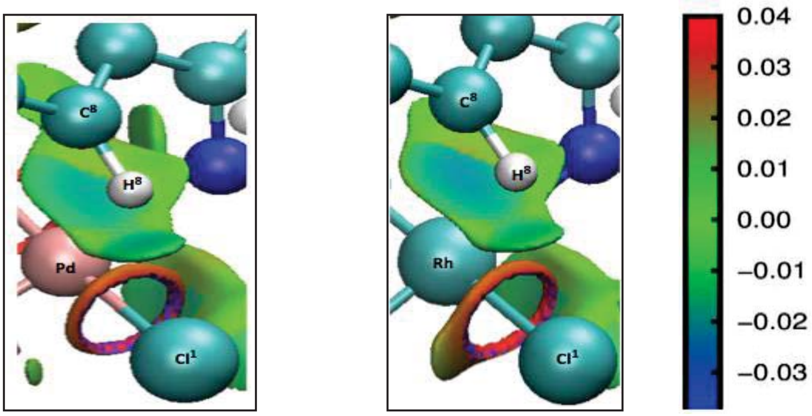

21 **5**

Figure 4.10 3D NCI iso-surfaces for **21** and **5**. The sign of the second Hessian eigenvalue (λ2) times the electron density values are shown by the color map.

4.4.3 Electronic Effects at the C^5 Position of the Aromatic ring (*para* to Anagostic C–H group), Complexes 22–25

It is known from earlier studies that the electron donating and withdrawing substituents on aromatic rings can influence the metal-hydrogen anagostic approach in cyclometallation reactions (Chapter 3).[126] Therefore, to ascertain the electronic influences on the metal····hydrogen separations in the $[PdCl_3(1\text{-tetralone oxime})]^-$ complexes, different electronic substituents with electron withdrawing or electron donating ability, have been introduced at the position on the aromatic ring which lies *para* to the anagostic C–H bond. The *para* position is used as the electronic influence is greater than at the *meta* position.[107] The $[Rh(CO)_2Cl(1\text{-tetralone oxime})]$, complex **2** with an (N)–OMe group, was chosen for the substituent effect study so as to avoid the Cl····HO hydrogen bonding in (N)–OH complex **1** which was found earlier (Chapter 3) to constrain the movement of the oxime ligand. So, complex **19** was substituted with SO_2Cl, (σ-electron withdrawing, F value: 1.16 ; R value: –0.05)[106] giving **22**, $B(OH)_3^-$ (σ-electron donating, F value: –0.42; R value: –0.02)[106] giving **23**, S^- (π-electron donating, F value: 0.03; R value: –1.24)[106] giving **24**, and $N_2PO(OEt)_2$ (π-electron withdrawing, F value: –0.05 ; R value: 0.79)[106] giving **25** (Scheme 4.1).

Turning towards analysis of complexes **22–25**, in **22** which contains an SO_2Cl substituent (electron withdrawal through the σ system), there are changes seen in the structural parameters compared with the unsubstituted complex **19**. The separations between Pd and the C^8 and H^8 atoms become shorter (Table 4.1) [Pd····H^8 and Pd···C^8 distance values: 2.532 and 3.007 Å, respectively; 2.596 and 3.136 Å, respectively in **2**] and the Cl···H^8 separation closes up a little [values in **22** and **19**: 2.592 and 2.645 Å, respectively]. However, the Pd–N and Pd–Cl bond lengths are almost unchanged from **2** [Pd–N bond lengths in **22** and **19**: 2.028 Å and 2.027 Å, respectively; Pd–Cl bond lengths 2.361 and 2.360 Å in **22** and **19**, respectively]. Regarding the bond angles, the differences between **22** and **19** are mostly insignificant except for the angle between the aromatic ring and coordination planes which is 7° smaller in **22** [values: 65.3°; c.f. 72.0° for **19**]. In comparisons to the [Rh(CO)Cl] analogue complex **8** with the *para* SO_2Cl substituent the separations are shorter in palladium complex **22** [separations in **8**: Rh···H^8: 2.632; Rh···C^8: 3.061; Cl····H^8: 2.698 Å] (Figure 4.11).

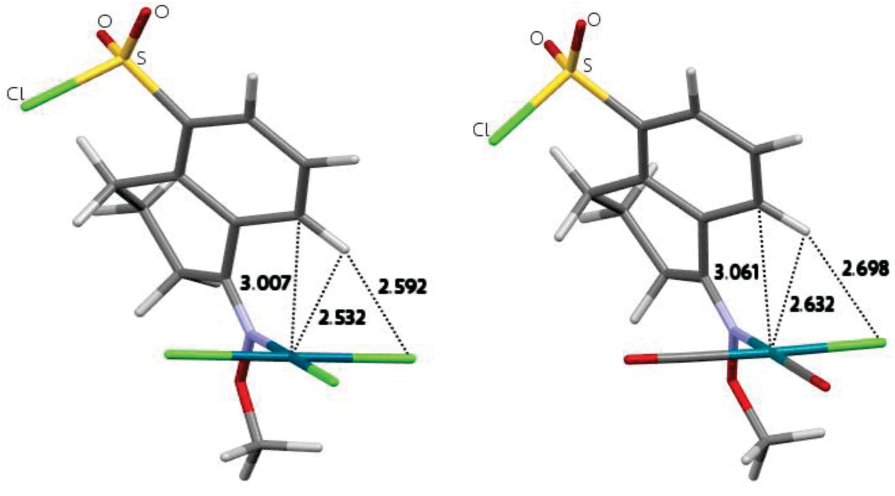

22 **8**

Figure 4.11 Optimised structures with important separations (Å) for **22** and **8**.

Turning towards the bonding analysis of the close approaches in **22**, QTAIM data (Table 4.2) shows a bond path (Figure 4.12) for the Pd···H^8 separation where the bond critical point properties are ρ(bcp): 0.0200 *e*/Bohr^3; $\nabla^2\rho$(bcp): 0.0556 *e*/Bohr^5 and *H*(bcp): 0.0003 Hartree/Bohr^3. As both the Laplacian of electron density and energy density values for the Pd···H^8 interaction are positive, it is thus mainly an electrostatic interaction without any covalency involved. The QTAIM charges indicate a small increase in the hydrogen and carbon atomic charges compared with **19** [$q(\mathrm{H}^8)$ in **22** and **19**: 0.100 and 0.085 *e*, respectively; $q(\mathrm{C}^8)$ in **22** and **19**: 0.007 and 0.000 *e*, respectively]. The more positive charge on H^8 suggests a more repulsive interaction with the metal but surprisingly the Pd····H^8 separation is still longer than **19** [Pd····H^8 separation in compelxes **22** and **19**: 2.532 Å and 2.596 Å, respectively]. However, as the Cl^1 charge is negative in **22** [$q(\mathrm{Cl}^1)$: –0.581 *e*], a greater attraction between Cl^1 and H^8 draws the two atoms closer [the Cl···H separations in **22** and **19** were 2.592 and 2.645 Å, respectively] and this attraction dominates over the Pd····H^8 separation which shows no change as expected by the change in charges.

Comparing the QTAIM bcp properties of **22** with those of the Rh····H^8 complex **8**, there is a small increase found for the electron density and Laplacian of electron density in **22**, however, the energy density is same in both complexes [Rh···H^8 bcp properties in **8**: ρ(bcp): 0.0175 *e*/Bohr^3; $\nabla^2\rho$(bcp): 0.0466 *e*/Bohr^5 and *H*(bcp): 0.0003 Hartree/Bohr^3]. Also in **8**, the QTAIM charges show the hydrogen is less positive whereas the carbon is slightly more negative compared to **22** [$q(\mathrm{H}^8)$ and $q(\mathrm{C}^8)$ for **8**: 0.078 and –0.002 *e*, respectively; c.f. 0.100 and 0.007 *e*, respectively for **22**].

Moving to the NBO analysis for **22** (Table 4.3), there is slightly more donation from the C–Hσ to the Pd–Clσ* NBOs with *E*(2) values of 2.02 and 1.85 kcal mol^{-1}, respectively [c.f. 1.57 and 1.45 kcal mol^{-1}, respectively for **19**; 0.97 and 1.04 kcal mol^{-1}, respectively for Rh-complex **8**]. However, there is a small but noticeable donation from a Pd lone pair to the C^7–$\mathrm{C}^8\pi^*$ orbital [*E*(2) value: 2.15 kcal mol^{-1}] found in **22** which was absent in **19**. Regarding the Cl and H^8 separation, there is a similar kind of donation from the Cl lone pair to C–H^8 as was found in **19** present in **22** with almost identical *E*(2) values [*E*(2) values for **22** and **19**: 2.36 and 2.03 kcal mol^{-1}, respectively] This donation is larger compared to Rh-complex **8**, where the *E*(2) value was 1.88 kcal mol^{-1}.

Looking at the spectroscopic features for **22** (Table 4.1), there is a decrease of 51 cm^{-1} in νC–H^8 compared to the free ligand which is noticeably greater than in **19** [a difference of 41 cm^{-1}] and rhodium complex **8** [a difference of 34 cm^{-1}]. The NMR properties indicate a slightly larger downfield shift for H^8 than in **19** but it is substantially larger than in **8** [Δδ value: 3.49 ppm for **22**; 3.18 and 1.36 ppm for **19** and **8**, respectively]. Also, the difference in the coupling constant ^1JC–H^8 for **22** is greater than in **19** and in **8** [increase in ^1JC–H for complexes **22**, **19** and **8** from respective ligands: 8.0 and 7.4 and 5.3 Hz, respectively].

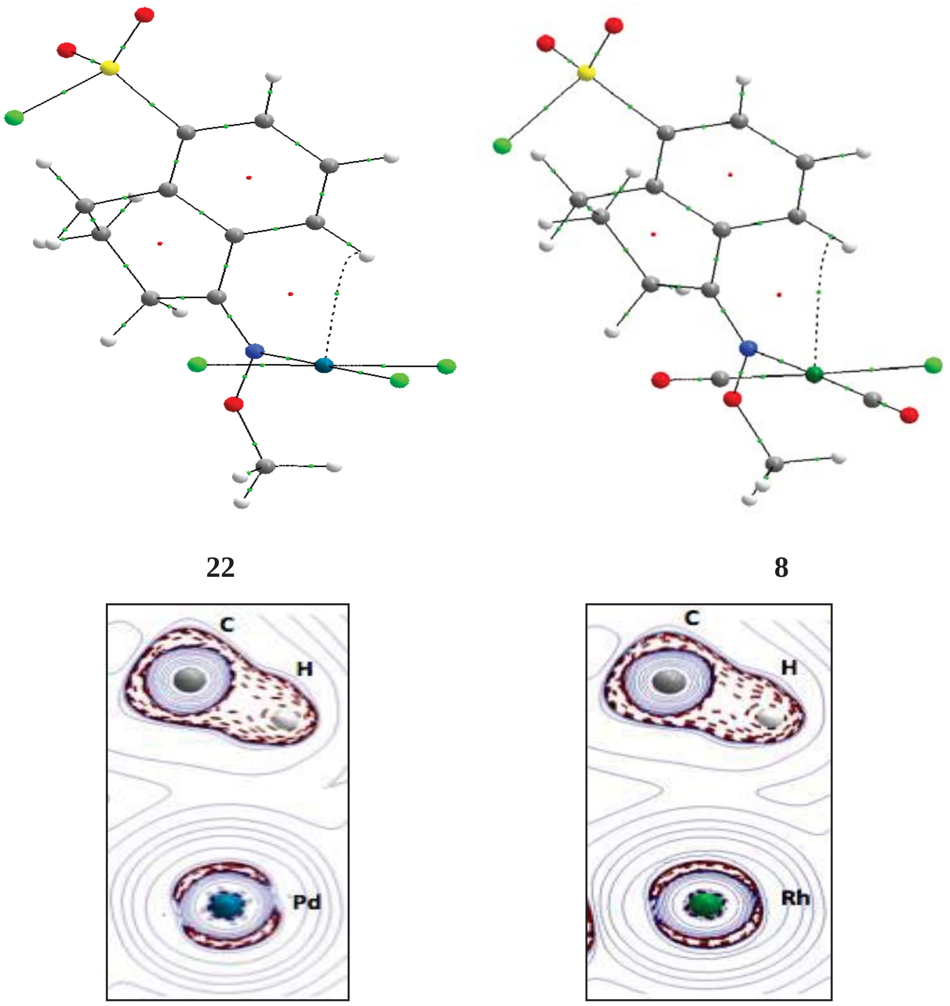

22 **8**

22 **8**

Figure 4.12 QTAIM molecular graphs (top) and Laplacian of electron density ($\nabla^2\rho$) contour plot (for C–H^8 and metal) (bottom) for **22** and **8**.

Turning to complex **23** with the σ-electron donating substituent $B(OH)_3^-$, the positioning of H^8 is now quite close to the metal (Figure 4.13) and the Pd····H^8 separation is the shortest for all the complexes studied so far [Pd····H^8 separations: 2.511 Å; c.f. 2.532 Å and 2.596 Å in **22** and **19**, respectively] (Table 4.1). The Pd···C^8 distance however is now longer [3.227 Å; c.f. 3.007 and 3.136 Å in **22** and **19**, respectively] which appears to result from a conformational change in the alicyclic ring which places the aromatic ring over the metal coordination plane in such a way that the C–H···M angle becomes larger [122.2; c.f. 105.1° and 109.7° in **22** and **19**, respectively]. In this case, there is a now an increase in the Cl···H^8 distance compared to complex **22** (SO_2Cl substituent at C^5) and complex **19** (H at C^5) [Cl···H^8 distances: 2.775 Å in **23**; c.f. 2.592 and 2.645 Å in **22** and **19** respectively]. However, the Cl···H–C^8 angle does not change much [values for **23**, **22** and **19**: 156.2°, 158.8° and 160.0°, respectively]. The angle between the planes (aromatic ring plane and metal coordination plane) is now significantly larger which again indicates greater structural changes which cause flattening of the aromatic ring in **23** [values: 81.7°, 65.3° and 72.0° in **23**, **22** and **19**, respectively].

Comparing the structural features for **23** with those for $B(OH)_3^-$ substituted rhodium complex **9**, there are some changes to the bond lengths and angles associated with the atoms that make up the coordination sphere (Table 4.1). The M–N bond length is shorter in **23** with a value of 2.039 Å compared to 2.146 Å in **9**, but, the M–Cl^1 bond lengths are very similar [values: 2.368 and 2.371 Å in **23** and **9**, respectively]. For the relevant separations, the M···H^8 distance is shorter in **23** [2.511; c.f. 2.584 Å in **9**], the M···C^8 distance is slightly longer in **23** [3.227 and 3.035 Å, respectively] and H^8 moves closer to Cl^1 [2.775 and 2.863 Å in **23** and **9**, respectively].

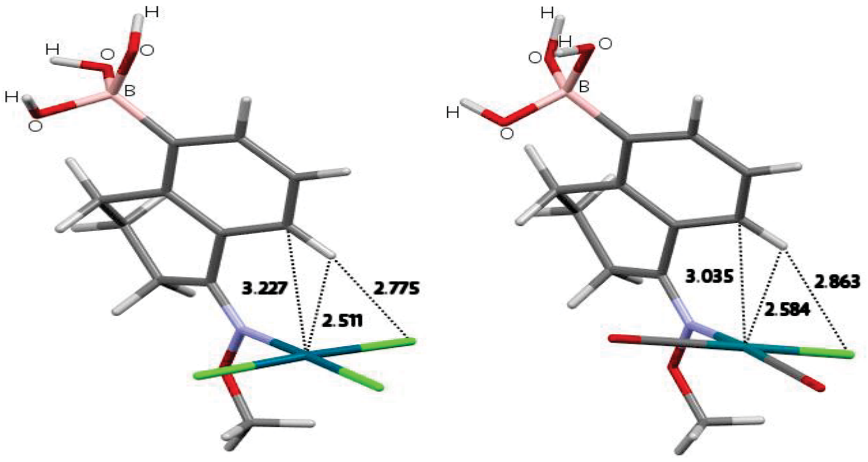

23 **9**

Figure 4.13 Optimised structures with important separations (Å) for **23** and **9**.

The QTAIM analysis indicates a bond path for the Pd····H^8 separation with bcp properties [ρ(bcp): 0.0181 *e*/Bohr^3; $\nabla^2\rho$(bcp): 0.0469*e*/Bohr^5 and *H*(bcp): –0.0001 Hartree/Bohr^3] (Figure 4.14; Table 4.2) which are slightly greater than found for (N)–OMe complex **19** [ρ(bcp): 0.0168 *e*/Bohr^3; $\nabla^2\rho$(bcp): 0.0459 *e*/Bohr^5 and *H*(bcp): 0.0003 Hartree/Bohr^3]. The negative energy density value for **23** [*H*(bcp): –0.0001 Hartree/Bohr^3) suggests there is now some covalency involved in the interaction. The QTAIM charges reveal the influence of the electron donating group as the H^8 charge, *q*(H^8), becomes less positive and *q*(C^8) becomes negative [*q*(H^8): 0.048 *e*, 0.100 and 0.085 *e* in **22** and **19**, respectively; *q*(C^8): –0.015 *e*; 0.0.007 and 0.000 *e* in **22** and **19**, respectively], the difference suggesting less repulsion between the metal and H^8 in **23** on the basis of electrostatics. Comparing with Rh-complex **9**, there is no significant change in the QTAIM properties except for the energy density which has a slight positive value in **9** [for Rh···H^8 bcp properties: ρ(bcp), $\nabla^2\rho$(bcp) and *H*(bcp) are 0.0188 *e*/$Bohr^3$, 0.0493*e*/$Bohr^5$ and 0.0001 Hartree/$Bohr^3$, respectively]. However, the QTAIM charges are substantially different in **9**, where the H^8 is less positive [0.023 *e*; c.f. 0.048 *e* for **23**] while C^8 becomes more negative [–0.037 *e*; c.f. –0.015 *e* for **23**].

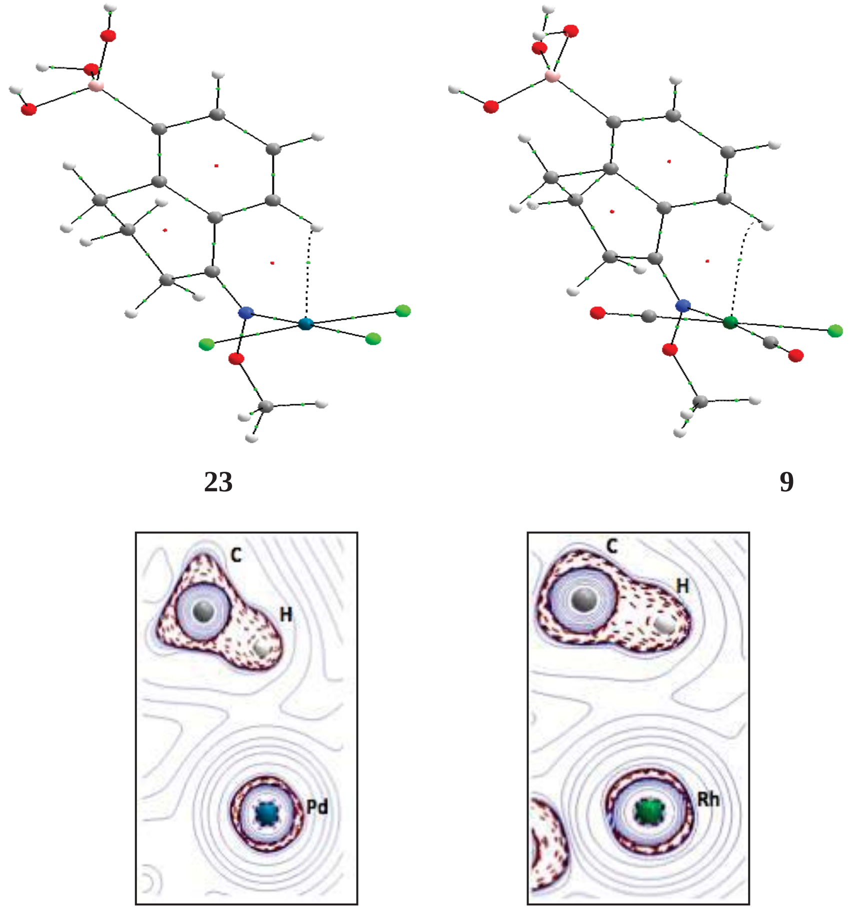

23 **9**

23 **9**

Figure 4.14 QTAIM molecular graphs (top) and Laplacian of electron density ($\nabla^2\rho$) contour plots (for C–H^8 and metal) (bottom) for **23** and **9**.

The NBO analysis for **23** (Table 4.3) indicates some covalency involved in the Pd···H^8 interaction with the C–H bond donating a small amount of electron density to the Pd–Cl^2 and Pd–Cl^3 antibonding NBOs, the *E*(2) values being 2.34 and 2.25 kcal mol^{-1} respectively [c.f. 2.02 and 1.85 kcal mol^{-1} in **22**; 1.57 and 1.45 kcal mol^{-1} in **19**]. Also, there is now back-donation from Pd to the C–H antibonding NBO which has an *E*(2) value of 1.21 kcal mol^{-1} whereas this donation was absent in complexes **19** and **22**. However, the donation from Pd to the C^7–C^8π antibonding NBO is noticeably less than in **22** [*E*(2) values: 0.73 and 2.15 kcal mol^{-1}, respectively]. Compared to rhodium complex **9**, the agostic donation is greater [E(2) values for C–Hσ to the Rh–C$^2\sigma^*$ and to the Rh–C$^3\sigma^*$ NBOs: 1.25 and 1.47 kcal mol^{-1}, respectively] but Pd to C^7–C$^8\pi^*$ NBO donation is significantly less [E(2) values for **9** and **23**: 2.11 and 0.73 kcal mol^{-1}, respectively].

The spectroscopic analysis indicates a substantially smaller decrease in the C–H^8 bond IR stretching frequency in comparison to the free ligand, for **23** (Table 4.1) when compared to **22** and **19** [the decreases of νC–H in **23**, **22** and **19** are 13 cm^{-1}, 51 cm^{-1} and 41 cm^{-1}, respectively]. The decrease in the C–H^8 stretching frequency for **23** is also significantly less than rhodium complex **9** where the decrease was 32 cm^{-1}. The NMR characteristics indicate a 6.0 Hz increase in the ^1JC–H coupling constant in comparison to the free ligand value [8.0 and 7.4 Hz for **22** and **19**, respectively] and the H^8 chemical shift moves downfield by 3.28 ppm in comparison to the free ligand value [3.49 and 3.18 ppm for **22** and **19**, respectively]. In rhodium complex **9**, both the NMR parameters change less than in **23** as the chemical shift value moves downfield by only 0.76 ppm and the coupling constant increases by only 2.9 Hz.

Turning to complex **24**, where the C^5 substituent is the electron donating group S$^-$ which can influence the π-system of the aromatic ring,[106] the optimised structure shows a similar positioning of the C–H^8 group over the metal coordination plane as was seen in the case of σ-electron donating substituent B(OH)$_3^-$ (complex **23**) (Figure 4.15). The Pd–Cl and Pd–N bond lengths in both **24** and **23** are very similar [Pd–N in **24** and **23**: 2.040 and 2.039 Å, respectively; Pd–Cl in **24** and **23**: 2.368 and 2.368 Å, respectively] (Table 4.1). It is worth mentioning here that the Rh-complex with the same ligand structure with S$^-$, showed quite different structural parameters than the Rh-complex with B(OH)$_3^-$. For instance, the Rh–N bond length was 2.157 Å with S$^-$ (**10**) and 2.146 Å in the case of B(OH)$_3^-$ (**9**) and the Rh–Cl bond length was 2.378 and 2.371 Å with S$^-$ (**10**) and B(OH)$_3^-$ (**9**).

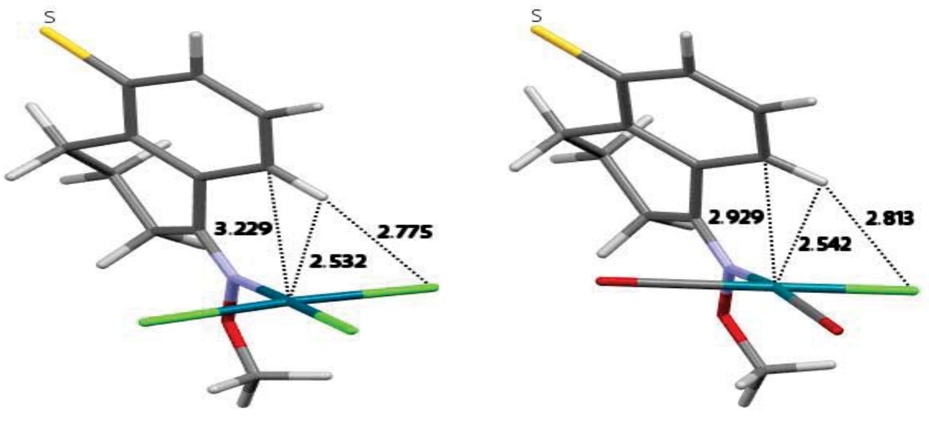

24 **10**

Figure 4.15 Optimised structures with important separations (Å) for **24** and **10**.

For **24**, the Pd····H^{8} and Pd···C^{8} separations are quite similar to those seen for the B(OH)$_3^-$ substituent in complex **23** [distances for the Pd····H^{8} separations in **24** and **23** are 2.532 and 2.512 Å, respectively; for the Pd····C^{8} separations: 3.229 and 3.227 Å, respectively]. For the rhodium (I) complexes, both Rh···H^{8} and Rh···C^{8} separations for S$^-$ (**10**) and B(OH)$_3^-$ (**9**) substituted complexes were slightly short [Rh···H^{8} separation for **10** and **9**: 2.542 and 2.584 Å, respectively; Rh···C^{8} separation for **10** and **9**: 2.929 and 3.035 Å, respectively].

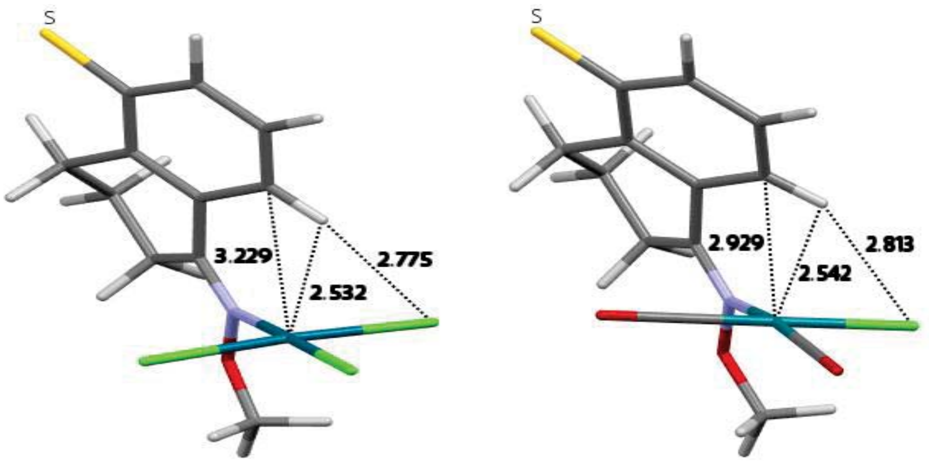

24 **10**

Figure 4.15 Optimised structures with important separations (Å) for **24** and **10**.

The QTAIM properties for the Pd···H^{8} bcp are very similar to those found for complex **23** (Figure 4.16; Table 4.2) [ρ(bcp): 0.0175 and 0.0181 *e*/Bohr^3 for **24** and **23**, respectively; $\nabla^2\rho$(bcp): 0.0456 and 0.0469 *e*/Bohr^5 for **24** and **23**, respectively; *H*(bcp), –0.0001 Hartree/Bohr^3 for both **24** and **23**, respectively]. The QTAIM charges for H^{8} and C^{8} in **24** are also not very different to that found for **23** [*q*(C^{8}): –0.026 *e* and –0.015 *e* in **24** and **23**, respectively; *q(*H^{8}): 0.045 and 0.048 *e* in **24** and **23**, respectively]. In the case of rhodium complex **10** with S$^-$, the C^{8} charge was more negative [*q*(C^{8}) values for S$^-$ complex **10** and B(OH)$_3^-$ complex (**9**) are –0.056 and –0.037 *e*, repectively]. However, the charges for H^{8} are essentially the same [*q*(H^{8}) values for S$^-$ complex **10** and B(OH)$_3^-$ complex **9** complexes are 0.026 and 0.03 *e*, respectively].

Looking at the NBO analysis, the agostic donations are slightly larger in **24** than **23**, with the *E*(2) values for the C–Hσ to Pd–Cl^{2}σ* and Pd–Cl^{3}σ* donations being 2.54 and 2.46 kcal mol^{-1}, respectively in the former and 2.34 and 2.25 kcal mol^{-1}, respectively in the later]. Similarly, for the donation from Cl^1 to the C–Hσ* orbital, the *E*(2) value is slightly greater in **24** [*E*(2) values: 2.24; c.f. 1.05 kcal mol^{-1} in **23**]. The spectroscopic properties for **24** show a decrease of 15 cm^{-1} in C–H bond stretching compared to the free ligand [c.f.

13 cm^{-1} in case of **23**]. The change in the downfield chemical shift of hydrogen H^8 is also not very different from **23** [Δδ values: 3.09 and 3.28 ppm in **24** and **23**, respectively]. At this point, it is interesting to note that with a change in both the metal centre and the overall charge on the complex, the electronic effects are not very different as both σ and π electron donating substituents show somewhat similar structural, spectroscopic and bonding features.

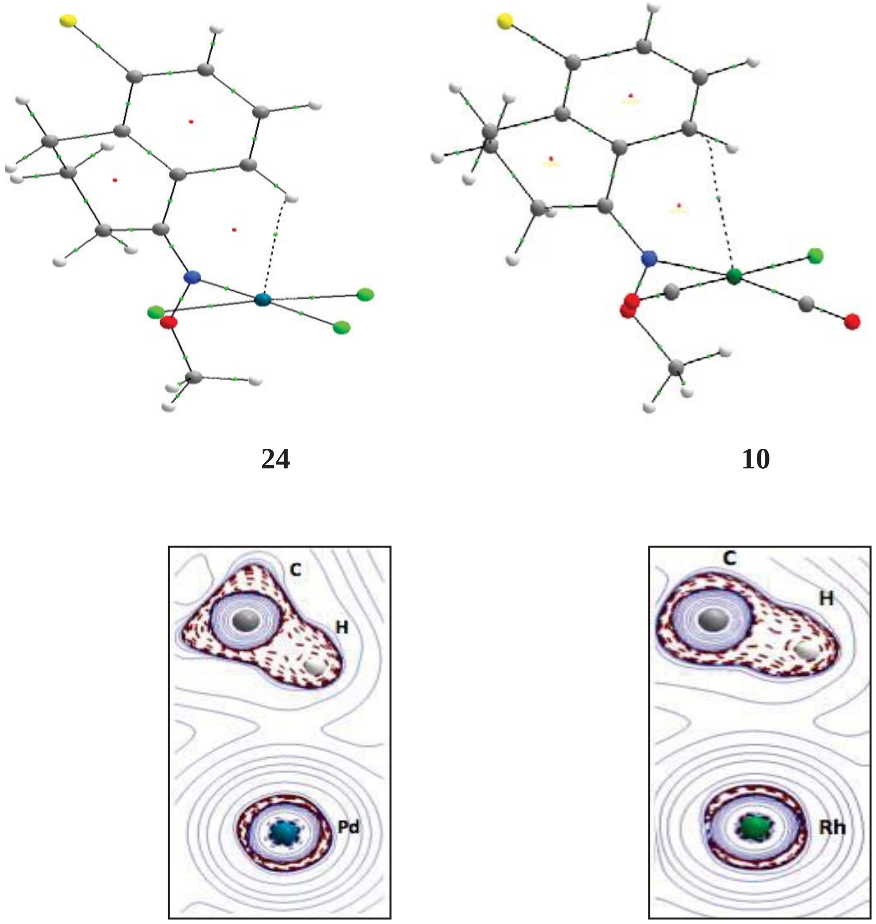

24 **10**

24 **10**

Figure 4.16 QTAIM molecular graphs (top) and Laplacian of electron density ($\nabla^2\rho$) contour plot (for C–H^8 and metal) (bottom) for **24** and **10**.

Although it was seen in the Rh study (Chapter 3), that the N=NPO(OEt)$_2$ substituent changed the alicylic ring conformation due to steric effects and the C–H^8 shifted out over the *cis*-CO ligand in the complex **7**, as there is, no other alternative strong π-electron withdrawing group available,[106] the C^5 N=NPO(OEt)$_2$ substituted palladium complex **25**, was nether-the-less computed. The structural analysis of **25** indicates almost similar positioning of the aromatic ring as was seen in rhodium complex **7** (Figure 4.17) and here also, the C–H^8 group sits over the Cl^2 ligand with a separation distance of 2.582 Å [the distance is 4.185 Å for **19**], opposite to complex **19** where the C–H^8 sits over the Cl^1 with a distance of 2.645 Å [4.081 Å in **25**]. Interestingly, the Pd····H^8 separation in **25** is shorter compared with **19** and **7** [distances: 2.476, 2.596 and 2.651 Å in **25**, **19** and **7**, respectively].

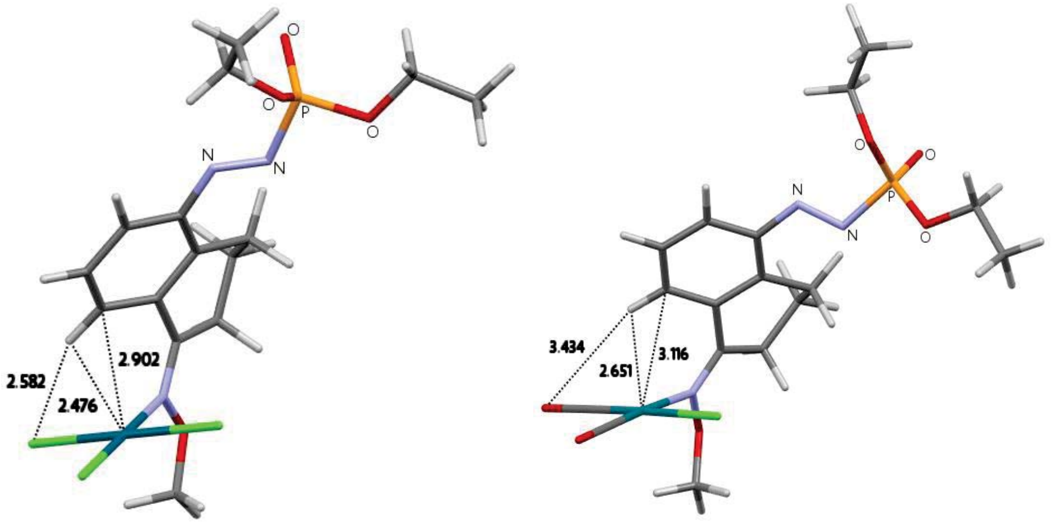

25 **7**

Figure 4.17 Optimised structures with important separations (Å) for **25** and **7**.

The NBO analysis for **25** (Table 4.3) shows donation from Cl^2 to the C–Hσ*orbital with an *E*(2) value of 2.24 kcal mol^{-1} which is not very different from rhodium complex **7** [*E*(2) complex: 2.03 kcal mol^{-1}]. The agostic donation is slightly greater compared with **19** [*E*(2) values for donations from the C–Hσ to Pd–Cl^{2}σ* and Pd–Cl^{3}σ* orbitals are 2.71 and 2.43 kcal mol^{-1}, respectively in **25**; c.f. 1.57 and 1.45 kcal mol^{-1}, respectively in **19**]. The QTAIM analysis (Table 4.2) indicates a bond path for the Pd···H^8 separation in **25** with bcp properties slightly greater than in **19** (Figure 4.18) [ρ(bcp), ∇^2ρ(bcp) and *H*(bcp) for **25**: 0.0233 *e*/Bohr^3; 0.0645 *e*/Bohr^5 and 0.0001 Hartree/Bohr^3, respectively*;* c.f. ρ(bcp), ∇^2ρ(bcp) and *H*(bcp) for **19** are 0.0168 *e*/Bohr^3, 0.0459 *e*/Bohr^5 and 0.0003 Hartree/Bohr^3, respectively]. The QTAIM atomic charges reveal the hydrogen H^8 charge more positive [0.095; c.f. 0.085 *e* for **19**] and C^8 charge slightly negative [–0.003 *e*; c.f. 0.000 *e* for **19**]. In comparisons of complex **25** with Rh-complex **7,** the agostic donations are greater in complex **25** **[***E*(2) values for donations from the C–Hσ to Rh–C^{2}σ* and Rh–C^{3}σ* orbitals are 0.56 and 1.09 kcal mol^{-1}, respectively in **7**, respectively; c.f. 2.71 and 2.43 kcal mol^{-1}, respectively in **25**] (Table 4.3).Similar to complex **25**, the Rh····H^8 bcp properties also indicate a weakly repulsive interaction [ρ(bcp), ∇^2ρ(bcp) and *H*(bcp) for **7**: 0.0177 *e*/Bohr^3, 0.0437 *e*/Bohr^5 and 0.0002 Hartree/Bohr^3, respectively*;* *q*(Rh) and *q*(H^8) values: 0.634 *e* and 0.039 *e*, respectively].

The spectroscopic properties for **25** (Table 4.1) are almost similar to complex **19**, and no significant changes are seen in the νC–H stretching frequency [a decrease of 41.4 cm^{-1} and 41.1 cm^{-1} in **25** and **19**, respectively], NMR coupling coupling ^{1}JC–H [an increase from ligand: 8.1 and 8.0 Hz in **25** and **19**, respectively] as well as the downfield chemical shift values [Δδ: 3.39 and 3.18 ppm for **25** and **19**, respectively].

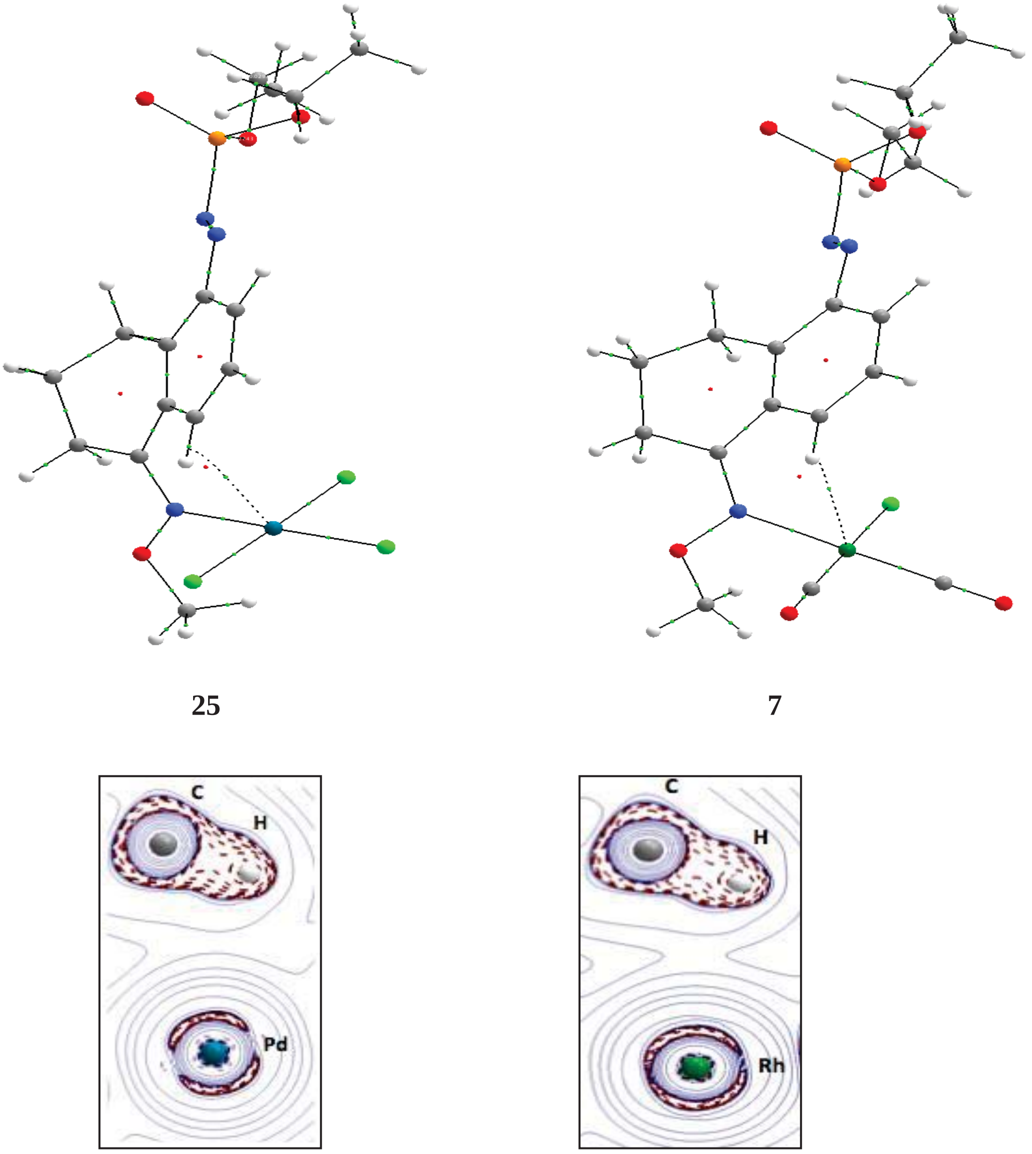

25 **7**

25 **7**

Figure 4.18 QTAIM molecular graphs (top) and Laplacian of electron density ($\nabla^2\rho$) contour plot (for C–H^8 and metal) (bottom) for **25** and **7**.

4.4.4 Combined Electronic and Steric effects: S^- at C^5, NH_2 at C^7, CMe_3 at Nitrogen, Complex 26

In case of the $[Rh(CO)_2Cl(L)]$ complexes (Chapter 3), the closest approach of C^8 and H^8 with the rhodium centre was achieved in a complex which was substituted by NH_2 and S^- at the *ortho* (C^7) and *para* (C^5) positions of the aromatic ring respectively along with a CMe_3 group attached to the ligating N atom which resulted in a structure showing a C-anagostic type interaction rather than H-anagostic interaction (Chapter 3).[126] In the study on the present $[PdCl_3(L)]^-$ complexes, it was therefore of interest to place NH_2 and S^- substituents along with an (N)–CMe_3 group, to see the combined influence on the metal···H–C interaction. In the chapter 3 study it was seen that the (N)–CMe_3 group strongly influenced the close approaches between the metal and the H^8 and C^8 separations in complex **4** where the Pd····H^8 distance was 2.564 Å and the Pd····C^8 distance was 2.934 Å.

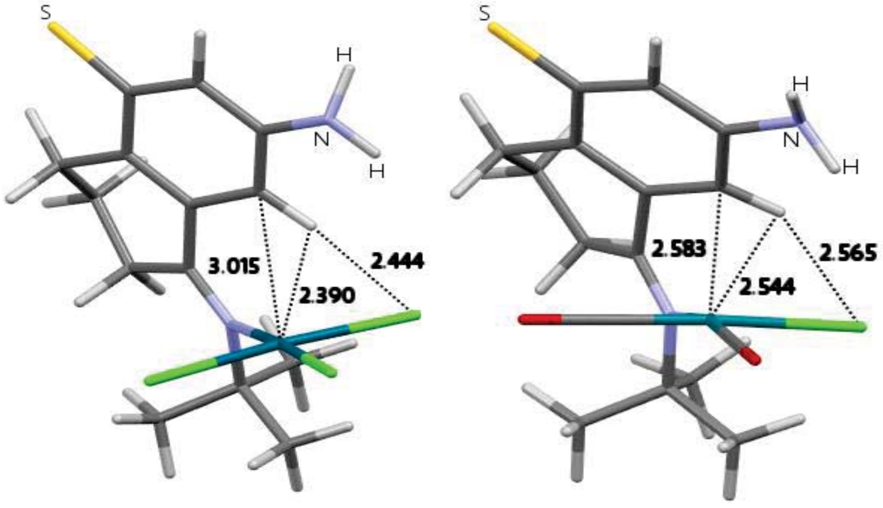

26 **17**

Figure 4.19 Optimised structures with important separations (Å) for **26** and **17**.

Looking at the structural parameters obtained for **26** (Figure 4.19; Table 4.1), in comparison to unsubstituted complex **21**, (N)–CMe_3 ligand without electronic substituents), the ligand is flattened out significantly with the larger Pd···H–C angle of 114.9° [c.f. 98.7 for **21**], which brings H^8 hydrogen closer to the metal [M···H distance: 2.390 Å; c.f. 2.564 Å in **21**]. It is noted that the metal···hydrogen separation of 2.390 Å in **26**, is the shortest approach found so far. The Cl···H^8 distance for **26** is also the shortest among other complexes studied so far [value: 2.444 Å; c.f. 2.564 for **21**] with a more linear angle for Cl···H^8 –C^8 [171.8°; c.f. 155.3° in **21**]. However, the Pd···C^8 approach is a slightly longer than in **21** [distance: 3.015; c.f. 2.934 Å in **21**]. In addition, as in **21**, where the distance between Cl^1 and H^8 was 2.430 Å, and Pd–Cl^1 bond was elongated to 2.385 Å, this situation is also seen in **26**, as the Pd–Cl^1 bond is significantly elongated to 2.410 Å and the distance between Cl^1 and H^8 becomes 2.444 Å. Turning towards the angles shown by **26**, compared to **21**, the push-back angle, Pd–N=C, is now 5° larger [124.3°; c.f. 119.2° in **21**], the Cl^2–Pd–N=C dihedral angle is 8° larger [80.5°; c.f. 72.5° in **21**] and the angle between the aromatic ring and coordination planes is 17° larger [82.1°; c.f. 65.1° in **21**].

In comparing the structural features of **26** with neutral Rh-complex **17**, the metal–N and metal–Cl^1 bond lengths become shorter in **26** [Pd–N and Pd–Cl bond lengths in **26**: 2.076 and 2.410 Å, respectively; c.f. 2.236 and 2.422 Å, respectively in **17**]. The Pd–N=C push-back angle becomes almost 9° larger in **26** [124.3; c.f. 115 in **17**] and the Cl···H–C^8 angle is significantly more linear than in **17** [171.8; c.f. 133.1° in **17**]. In **26**, these angle variations cause the C–H group to point more towards the Cl^1 ligand in which case the C–H separations to the metal and Cl^1 become closer [M···H^8 separation for **26** and **17**: 2.390 and 2.544 Å, respectively; Cl^1 ···H^8 separations: 2.444 and 2.565 Å for **26** and **17**, respectively]. However, with this positioning of the C–H^8 bond, the M···C^8 separation becomes significantly longer in **26** [3.015; c.f. 2.585 Å in **17**]. The longer M···C^8 separation in **26** indicates the absence of a C-anagostic type interaction in comparison to **17** where a C-anagostic interaction was developed (Chapter 3).[126]

The QTAIM analysis for **26** (Table 4.2) shows a Pd···H^8 bond path, contrary to that seen in **21**, where a bcp was present between the Pd and C^8 atoms (Figure 4.20). The QTAIM properties of bcp Pd····H^8 indicate small magnitudes of electron density, Laplacian of electron density and a smaller negative value for energy density [ρ(bcp): 0.0235 *e*/$Bohr^3$; $\nabla^2\rho$(bcp): 0.0662 *e*/$Bohr^5$ and *H*(bcp): –0.0003 Hartree/$Bohr^3$]. The positive value of the Laplacian of electron density, $\nabla^2\rho$(bcp), and the negative value of the energy density, *H*(bcp), indicate some covalency is involved. Comparing the QTAIM charges for H^8 and C^8 in complexes **26** and **21**, it is seen that due to stronger electron-donating effect of both the S^- and NH_2 substituents in **26**, the C^8 negative charge is significantly increased from –0.009 *e* in **21** to –0.042 *e* in **26** and the H^8 positive charge is decreased [0.095 and 0.055 *e* for **21** and **26**, respectively]. The smaller positive charge on H^8 suggests less repulsion and the large negative charge on C^8 indicate a stronger attraction with the metal centre.

Comparing **26** with rhodium complex **17** [$Rh(CO)_2Cl$(1-tetralone imine)] with (N)–CMe_3 and S^- and NH_2 at the *para* and *ortho* position on the aromatic ring], there is now a transit-closed shell interaction (an electrostatic interaction with some covalency involved)[97] between M and H^8 in **26** rather than the M···C^8 interaction [bcp properties for the Rh$\cdots$C^8 separation: ρ(bcp): 0.0401 *e*/Bohr^3; $\nabla^2\rho$(bcp): 0.0843 *e*/Bohr^5 and *H*(bcp): –0.0055 Hartree/Bohr^3]. However, the bcp properties indicate that the M$\cdots$C^8 interaction in the rhodium complex is stronger than the M$\cdots$H^8 interaction in complex **26**. Looking at the QTAIM charges for H^8 and C^8, it is seen that the positive value of *q*(H^8) slightly increases in **26** [0.055 and 0.046 *e* in **26** and **17**, respectively] but the negative value for *q*(C^8) significantly decreases [–0.042 and –0.092 *e* in **26** and **17**, respectively].

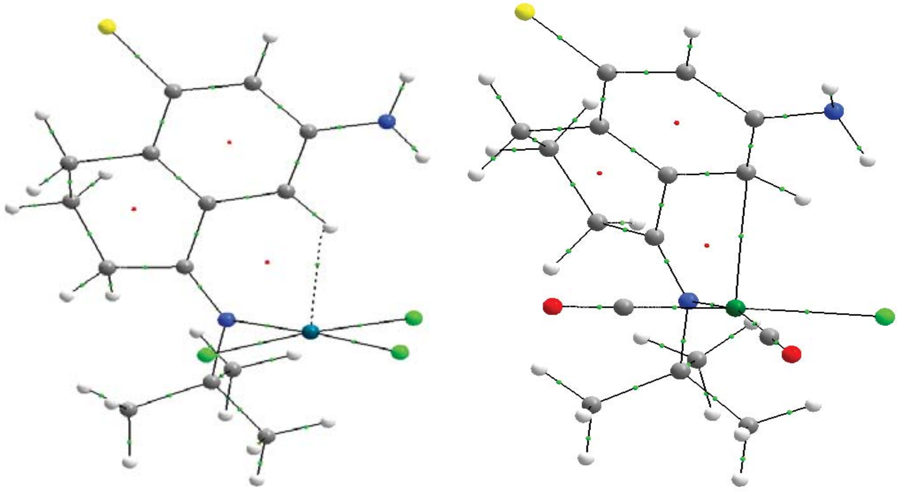

26 **17**

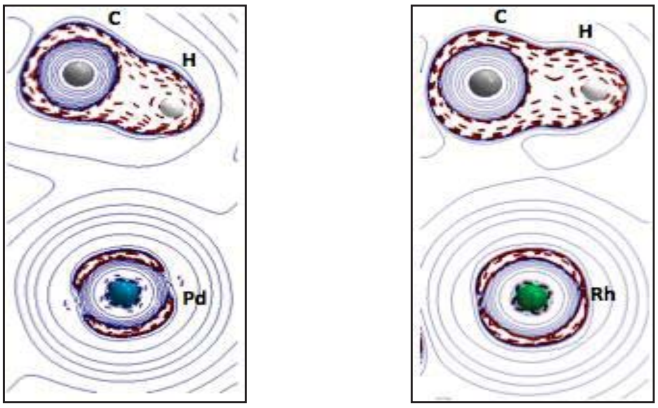

26 **17**

Figure 4.20 QTAIM molecular graphs (top) and Laplacian of electron density ($\nabla^2\rho$) contour plots (for C–H^8 and metal) (bottom) for **26** and **17**.

The NBO analysis for **26** (Table 4.3) indicates stronger agostic donations from the C–Hσ to Pd–Cl^{2}σ* and Pd–Cl^{3}σ* orbitals [*E*(2) values: 6.01 and 5.41 kcal mol^{-1}, respectively; c.f. 2.93 and 2.58 kcal mol^{-1}, respectively for **21**] [*E*(2) values for Rh-complex **17** were 1.91 and 1.72 kcal mol^{-1}, respectively] (Figure 4.21). These *E*(2) values are significantly larger compared to the other palladium complexes studied in this work so far.

Similar to Rh-complex **17**, where the major obstacle to building up a constructive overlap between the C–Hσ and metal centred orbitals was the large difference in the NBO donor-acceptor energies, this difference is also not very supportive in **26** (Table 4.3) [the C–Hσ bond energy is –0.1965 a.u. compared to **17** [–0.3109 a.u.] and the Pd–Cl^{2}σ* and Pd–Cl^{3}σ* energies are 0.6890 and 0.7900 a.u., respectively; NBO energies for the Rh–C^{2}σ* and Rh–C^{3}σ* orbitals in **17** are 0.5905 and 0.4591 a.u., respectively]. However, the overlap matrix values are again supportive for the interaction in complex **26** as for the two agostic donations, the *E*(2) values have increased [overlap matrix values for the C–Hσ to the Pd–Cl^{2}σ* and to the Pd–Cl^{3}σ* orbital donations are 0.1673 and 0.1472, respectively; c.f. 0.1423 and 0.1411, respectively for rhodium complex **17**] (refer to Table 4.4 in Appendix B.2). In addition, the Pd to C^7–C^{8}π* bond donation in **26** is significantly small at 1.43 compared to 4.33 kcal mol^{-1} in the case of Rh complex **17**. The greater metal to C^7–C^{8}π* donation in **17** was one of the driving forces in the formation of the C-anagostic interaction (Chapter 3).[126] There are also some small back-donations from Pd to C–H orbitals seen in **26** which are absent in the case of rhodium complex **17** [LP (1) and LP (3) Pd to C–Hσ*: *E*(2) value 0.47 and 1.43 kcal mol^{-1}, respectively].

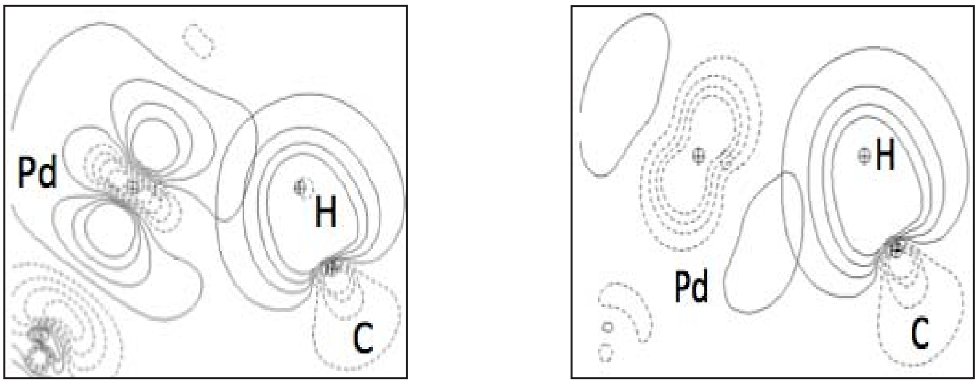

a) C–H to Pd–Cl^{2}σ* [*E*(2): 6.01 kcal mol^{-1}] **b**) C–H to Pd–Cl^{3}σ* [*E*(2): 5.41 kcal mol^{-1}]

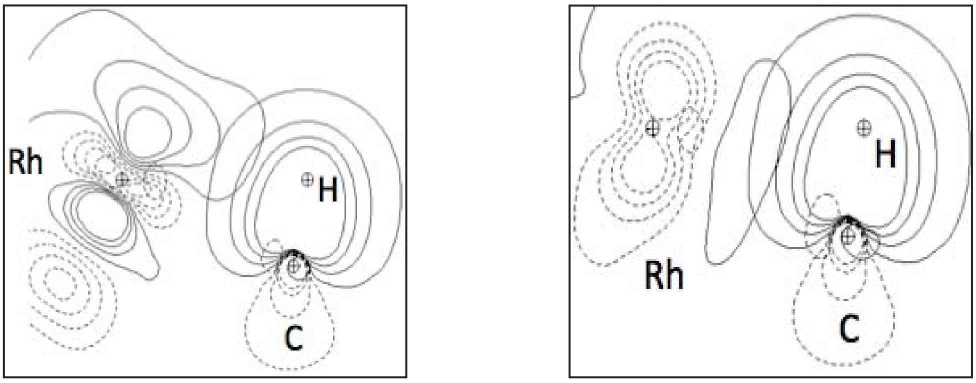

c) C–H to Rh–C^{2}σ* [*E*(2): 2.97 kcalmol^{-1}] **d**) C–H to Rh–C^{3}σ* [*E*(2): 3.38 kcalmol^{-1}]

Figure 4.21 Contour plots showing the NBOs overlap for agostic donations from C–H to metal NBOs for both **26** (a,b) and **17** (c,d).

Regarding the Cl^1 to $C–H^8$ donations, similar to **21**, these donations are also present in **26** [*E*(2) values: 3.71 and 3.41 kcal mol^{-1}, respectively] which correlates with the closer distance of H^8 and Cl^1 [$Cl^1 \cdots H^8$ distance: 2.444 and 2.430 Å, respectively]. As there was a slightly longer $Cl \cdots H^8$ distance in **17** [2.565 Å], the donations from Cl to the C–Hσ* orbital are smaller than in **26** [*E*(2) values for **17**: 1.20 kcal mol^{-1}]. In **26**, no donations were found from LP C^8 to the Pd–Cl^2σ* or Pd–Cl^3σ* orbitals which was the major driving force in building up the C-anagostic interactions in **17** (Chapter 3) [*E*(2) values: 13.38 and 17.59 kcal mol^{-1}, respectively].

Turning to the spectroscopic data for **26** (Table 4.1), the IR stretching frequency for the $C–H^8$ bond is only 7 cm^{-1} less than the ligand compared to **21** where the IR stretching frequency decrease was 41 cm^{-1}. The reason for the smaller decrease is that there is almost no involvement of normal modes of other C–H groups. Compared with Rh complex **17**, there was also less change seen in the C–H stretching frequency $\nu C–H^8$ [a difference of 6 cm^{-1}] suggesting presence of anagostic type interaction without the covalency components between the C–H and metal centred orbitals.[35] However, the NMR chemical shift for H^8 is further downfielded compared to **21** [Δδ for **26** and **21** are 3.99 and 3.20 ppm, respectively] which was only 0.06 ppm in case of rhodium complex **17** suggesting that very close approaches of H^8 with Cl and Pd influence the H^8 chemical shift value. Regarding the ^1JC–H coupling constant, there is an increase of approximately 4.0 Hz in complex **26** compared to the free ligand which is slightly less than in **21** [Δ^1JC–H: 7 Hz]. Surprisingly, the decrease in the H^8 coupling constant in **26** is similar to that seen in the case of rhodium complex **17** [Δ^1JC–H: 4.0 Hz].

As QTAIM analysis showed no bcp between C^8 and Pd in **26** (Figure 4.20) despite the carbon charge being significantly more negative than in **21**, to elucidate whether an attractive interaction between C^8 and Pd is present, an NCI calculation was carried out for **26**. The 3D NCI RDG iso-surface (Figure 4.22) shows a light blue spot between C^8 and Pd which indicates that an attractive interaction is still present. However as the $Pd \cdots C^8$ distance is above 3.0 Å, the interaction is comparatively weaker than was seen in **17** where there was a clear dark blue spot present. Also, there is a blue spot between H^8 and Cl in both **26** and **17**, which reveals an attractive situation. However, the blue spot for the $Cl \cdots H^8$ interaction is darker in the case of **26** which indicates a slightly stronger interaction than **17**. Thus, the $[Pd(Cl)_3(L)]^-$ system does not favour a C-anagostic type interaction which was developed by the $[Rh(CO)_2Cl(L)]^-$ system (Chapter 3) but rather supports a strong interaction between the C–H hydrogen and ancillary ligand Cl. This attraction between hydrogen and Cl is an important aspect of the cyclometallation process.[10]

The significant differences in the nature of interactions between anionic $[Pd(Cl)_3(L)]^-$ (i.e. complex **26**) and neutral $[Rh(CO)_2Cl(L)]$ (i.e. complex **17**) complexes where the former supports an agostic-like interaction between C–H and palladium centred orbitals while the other supports a C-angostic type interaction, suggest a role for the metal oxidation state and the ancillary ligands around the metal. The palladium has oxidation state +2 and thus has more tendency to accept the electron density from the C–Hσ orbitals whereas the rhodium is in oxidation state of +1 and relatively less tendency to accept the electron density from the C–Hσ orbitals. The other factor which causes the difference in the interactions is the nature of the ancillary ligands as the palladium (II) system is anionic due to three Cl ligands attached while the rhodium (I) has only one ancillary Cl ligand attached. Due to the more anionic nature of the palladium (II) system, there is a stronger attraction between C–H and Cl^1 which brings the C–H group more over the vicinity of the metal centre.

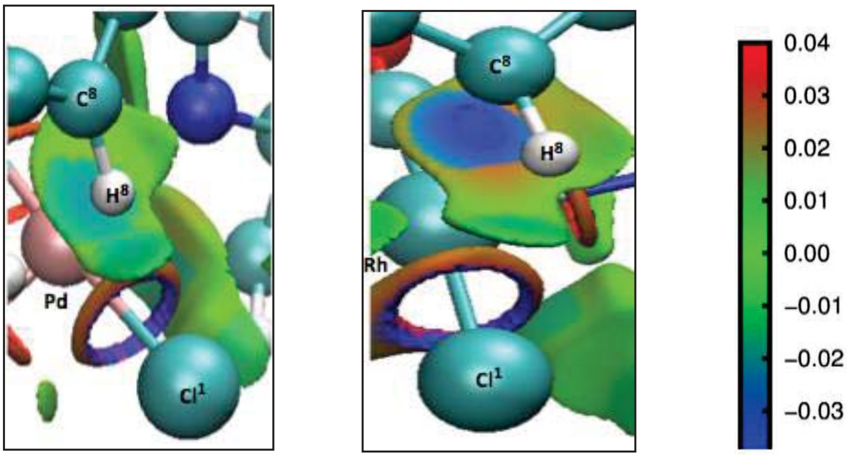

26 **17**

Figure 4.22 3D NCI RDG iso-surfaces for **26** and **17**. The sign of the second Hessian eigenvalue (λ2) times the electron density values are shown by the colour map.

4.5 Conclusion

This study has shown that the steric and electronic effects play differently with the two metal precursors (which are $PdCl)_3$ and $Rh(CO)_2Cl$). Similar to the $[Rh(CO)_2Cl$ (1-tetralone)] oxime and imine neutral complexes, by using the $Pd(Cl)_3$ precursor in $[Pd(Cl)_3$(1-tetralone)] oxime and imine anionic complexes, steric and electronic effects also influence the metal$\cdots$$H^8$ close approaches. The steric influence was almost identical in both palladium (II) and rhodium (I) complexes where the bulky steric group at coordinating N atom was involved in positioning the C–H over the metal coordination plane. However, the steric effect is more pronounced in $[Pd(Cl)_3$(1-tetralone imine)$]^-$

complex **21** whereby the bulky group shifts the C–H group towards the ancillary Cl ligand where a stronger attractive interaction between $Cl^1 \cdots\cdot H^8$ was observed.

Regarding the electronic effects, unlike the rhodium-tetralone complexes (Chapter 3), it is noted that both the σ and π-substituents are not separable with the palladium complexes as similar kinds of effects on the separations were seen for both σ and π-substituents where the electron-withdrawing groups were involved in increasing the positive charge on the hydrogen which led to a more repulsive interaction with the metal while the electron donating substituents were involved in decreasing the positive charge on H^8 and but reducing the charge on the carbon which led to a less repulsive interaction between metal and H^8 and more attractive interaction between metal and C^8.

The shortest metal···hydrogen, H^8**,** close approach of 2.390 Å was obtained in the case of the combined steric (N-CMe_3) and electronic (S^- at *para* and NH_2 at *ortho* position of aromatic ring) influences (complex **26**) whereby the steric influence at coordinating atom N by the bulky *tert*-butyl group caused the anagostic hydrogen to become closer to the metal and the ancillary chloro ligand, where a weak Cl···H interaction was developed. It was seen that the weak Cl···H interaction at anagostic like geometries can play a significant role in bringing the C–H group closer to the metal where agostic donations can develop ([*E*(2) values for donations from C–Hσ to Pd–Cl^2 σ* and Pd–Cl^3σ* orbitals: 6.01 and 5.41 kcal mol^{-1}, respectively] (complex **26**). Analysis of the driving force for these agostic donations shows that the bulky steric group (CMe_3) at the coordinating N-atom favors the spatial overlap between the C–Hσ and metal centred orbitals.

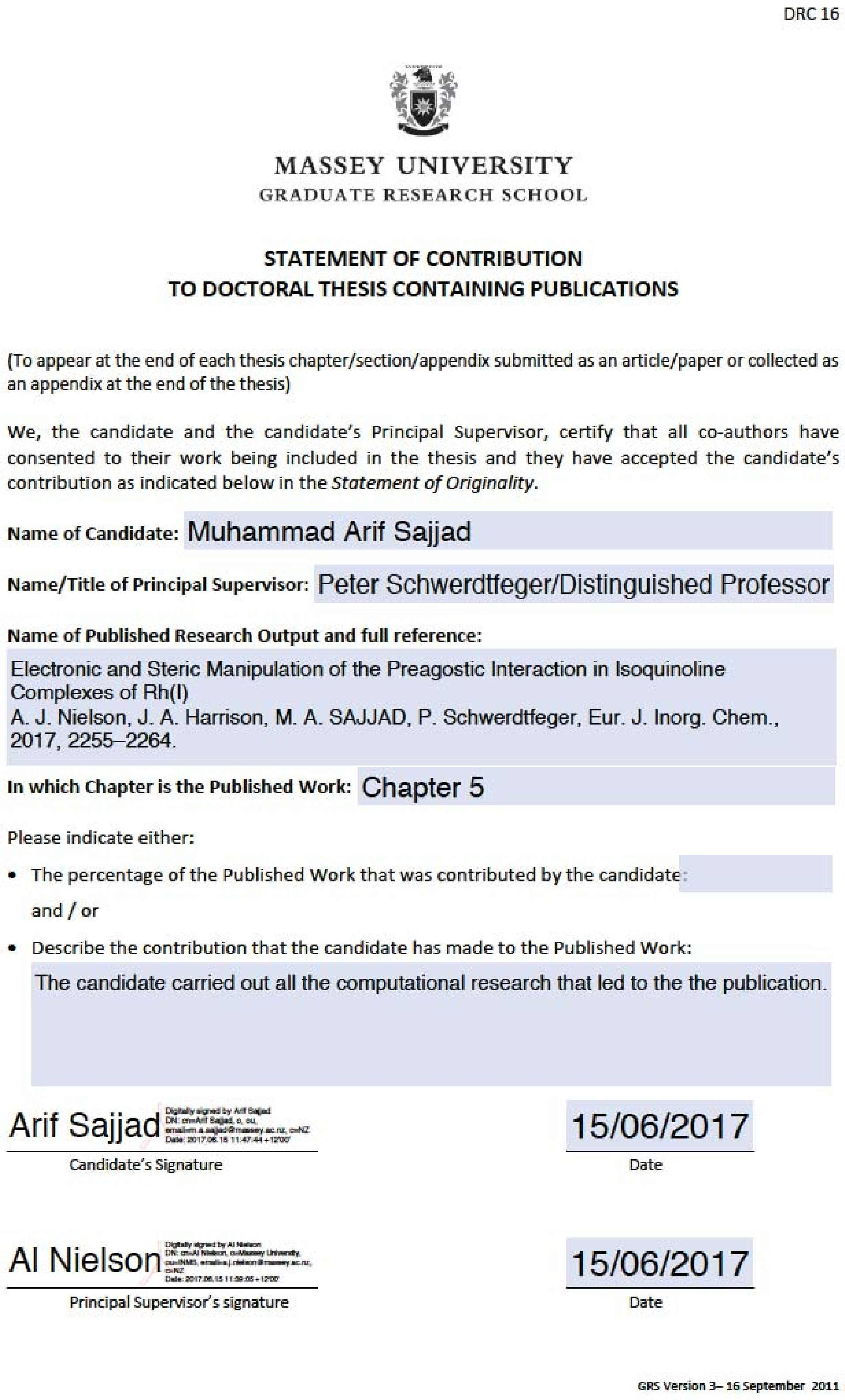

DRC 16

MASSEY UNIVERSITY
GRADUATE RESEARCH SCHOOL

STATEMENT OF CONTRIBUTION TO DOCTORAL THESIS CONTAINING PUBLICATIONS

(To appear at the end of each thesis chapter/section/appendix submitted as an article/paper or collected as an appendix at the end of the thesis)

We, the candidate and the candidate's Principal Supervisor, certify that all co-authors have consented to their work being included in the thesis and they have accepted the candidate's contribution as indicated below in the *Statement of Originality*.

Name of Candidate: Muhammad Arif Sajjad

Name/Title of Principal Supervisor: Peter Schwerdtfeger/Distinguished Professor

Name of Published Research Output and full reference:

Electronic and Steric Manipulation of the Preagostic Interaction in Isoquinoline Complexes of Rh(I)
A. J. Nielson, J. A. Harrison, M. A. SAJJAD, P. Schwerdtfeger, Eur. J. Inorg. Chem., 2017, 2255–2264.

In which Chapter is the Published Work: Chapter 5

Please indicate either:

- The percentage of the Published Work that was contributed by the candidate:

  and / or

- Describe the contribution that the candidate has made to the Published Work:

  The candidate carried out all the computational research that led to the the publication.

Arif Sajjad Digitally signed by Arif Sajjad DN: cn=Arif Sajjad, o, ou, email=m.a.sajjad@massey.ac.nz, c=NZ Date: 2017.06.15 11:47:44 +12'00'
Candidate's Signature

15/06/2017
Date

Al Nielson Digitally signed by Al Nielson DN: cn=Al Nielson, o=Massey University, ou=INMS, email=a.j.nielson@massey.ac.nz, c=NZ Date: 2017.06.15 11:39:05 +12'00'
Principal Supervisor's signature

15/06/2017
Date

GRS Version 3– 16 September 2011

Chapter 5

Changing the Nature of the Ligand: Steric and Electronic Manipulation of Anagostic interactions in *iso*-Quinoline Complexes of Rhodium (I)

5.1 Introduction

Based on the distances between aromatic hydrogens and metal in d^8 square planar complexes, two types of anagostic approaches have been recognised.[34] The first type is the short M····H–C approach where the M···H distance is usually less than 2.5 Å and the nature of the interaction is electrostatic with some covalency involved whereas the second anagostic type has longer M····H distances usually in the range of 2.51–2.80 Å[34] and the nature of the interaction is purely electrostatic without covalency components.[28] In the previous computational work on anagostic interactions (Chapter 3), it was seen that the longer M····H–C interactions could be influenced by both steric and electronic substituents.[126] In particular, it was shown that electron donating substituents decrease the positive charge on the hydrogen which results in a smaller repulsive interaction with the rhodium (I) metal. It was seen that the stronger electron-donating group on the aromatic ring *para* to the anagostic hydrogen increases the negative charge on the carbon of the anagostic C–H group, which results in an attractive ‘C-anagostic’ type interaction.[66,126]

The key factor in the study was the flexibility of the tetralone ligand system that allowed the anagostic hydrogen to swing over the metal coordination sphere in a back and forth manner which avoided a very close approach with the rhodium metal. The closest approach found between metal and hydrogen with this flexible ligand was 2.544 Å and the nature of interaction was mainly electrostatic (Chapter 3).[126] Therefore, it is of interest to replace the flexible ligand with an inflexible ligand which could keep the hydrogen over the top of the metal. In this regard, the inflexible *iso*-quinoline ligand has the capability to keep anagostic hydrogen over the top of the metal rather than swinging over the metal coordination sphere. The question to answer in this part of the work is 'can we manipulate the metal····H interaction when an inflexible ligand is used?' To answer this question, some [$Rh(CO)_2Cl$(*iso*-quinoline)] complexes were computed in the present work to assess the steric and electronic influences on the M···H separation by various substituents (Scheme 5.1).

5.2 Aim

- To manipulate by steric and electronic manipulation the anagostic interactions in *iso*-quinoline complexes of rhodium (I).

5.3 Choice of *iso*-Quinoline Ligands

To characterise close approaches of anagostic hydrogens with the d^8 metal centre, the *benzo*-quinoline (*iso*-quinoline) ligand was chosen. The general structure of the *iso*-quinoline ligand has two benzenoid ring junctions which make it inflexible enough to allow the opportunity for a close contact of the H^{10} hydrogen with the metal centre once the nitrogen N atom coordinates (Scheme 5.1). Contrary to the previous study on $[RhCl(CO)_2(L)]$ (L = 1-tetralone oximes and imines) complexes (Chapter 3) for which no crystal structures were obtainable due to decomposition of the crystals during crystallisation process,[104a] [RhCl(CO)$_2$(*iso*-quinoline) is a known complex but here also the instability of the crystals is the major obstacle in recrystallisation.[127] Therefore, a crystal structure is not available for comparison purpose with the computational structure. The alternative to this is to choose a similar structure to [RhCl(CO)$_2$(*iso*-quinoline)] which can be used for the comparison. Fortunately, the crystal structure of [PtCl$_2$(*iso*-quinoline)(PEt$_3$)][128] is available and initial computations including functional testing and structural parameter comparisons were carried out on this complex.

Various ligands were chosen to monitor the influence of electronic and steric substituents on the metal···H^{10} approach as shown in Scheme 5.1. The electronic effects were studied using the strongest electron donating or withdrawing groups which can influence either the σ or π-systems of the aromatic ring but not both at the same time.[106] Choice of the *para* substituents was based on the stronger electronic influence at the *para* position than at the *meta* position, and the *ortho* position to the C–H^{10} group was used to evaluate the combined steric and electronic effects.[107] The substituents used for σ- and π-electron withdrawing effects were SO_2Cl (F value: 1.16; R value: –0.05)[106] (complex **28**) and $N{=}NPO(OCH_2CH_3)_2$ (F value: –0.05; R value: 0.79)[106] (complex **29**), respectively. While, the substituents used for σ- and π-electron withdrawing effects were $B(OH)_3^-$ (F value: –0.42; R value: –0.02)[106] (complex **30**), and S^- (F value: –0.03; R value: –1.24)[106] (complex **31**). The effects were then compared to the complex with the unsubstituted ligand structure, (complex **27**). To further influence the metal····H^{10} close approach, a combined electronic effect was used in **32** and **33** where NH_2 (F value: –0.08; R value: –0.74)[106] at R^1 and S^- at R^2 and S^- at both R^1 and R^2 were used respectively.

As was seen in the earlier study on anagostic interactions with the flexible ligand (Chapter 3), steric influences play a pivotal role in the positioning of the anagostic hydrogen over the metal coordination sphere. So now it was of interest to assess the steric effects with the inflexible *iso*-quinoline ligand, therefore, in the current study, steric pressure was introduced by placing the substituents at the R^3 position of the ligand i.e. methyl in complex **34**, isopropyl in **36**, *tert*-butyl in **37** and phenyl in **38** as shown in Scheme 5.1.

Scheme 5.1:

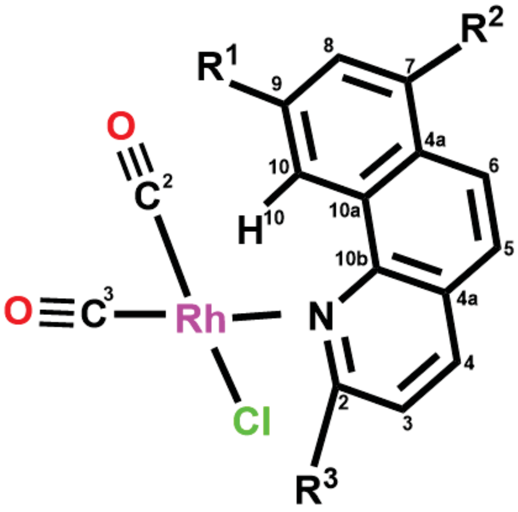

(**27**) R^1, R^2, R^3 = H
(**28**) R^1, R^3 = H, R^2 = SO_2Cl
(**29**) R^1, R^3 = H, R^2 = $N{=}NPO(OEt)_2$
(**30**) R^1, R^3 = H, R^2 = $B(OH)_3^-$
(**31**) R^1, R^3 = H, R^2 = S^-
(**32**) R^1 = NH_2, R^2 = S^-, R^3 = H
(**33**) R^1, R^2 = S^-, R^3 = H
(**34**) R^1, R^2 = H, R^3 = Me
(**35**) R^1 = H, R^2 = S^-, R^3 = Me
(**36**) R^1, R^2 = H, R^3 = $CHMe_2$
(**37**) R^1, R^2 = H, R^3 = CMe_3
(**38**) R^1, R^2 = H, R^3 = Ph
(**39**) R^1 = H, R^2 = S^-, R^3 = Ph
(**40**) R^1 = NH_2, R^2 = S^-, R^3 = Ph
(**41**) R^1, R^2 = S^-, R^3 = Ph

Scheme 5.1 Structures of the $[RhCl(CO)_2$(*iso*-quinoline)] complexes.

To see the maximum compression on the Rh···H^{10} separation, the final choice of ligands was based on a combination of steric and electronic substituents. For this purpose, a methyl group was used at the C^2 position and an S^- substituent at the *para* position to the anagostic hydrogen (complex **35)** and then for complexes **39**–**41**, along with the phenyl group at the C^2 position, S^- at the *para*-position (complex **39**), S^- at the *para* position and NH_2 at the *meta* position (complex **40)** and then S^- *ortho* and *para* to the anagostic hydrogen (complex **41**). were placed.

5.4 Computation Approach

Geometry optimisations and frequency calculations by dispersion corrected Grimme PBE-D3 functional[76,77] using Gaussian09 (G09) software.[108] For complex **27**, structural parameter comparisons between experimental and computational were made using B3LYP[73] and BP86[72] functionals. A triple-zeta high-quality basis set (aug-cc-pVTZ-PP)[111] was used for Rh; cc-pVTZ[95] was used for the attached ancillary ligands (CO and Cl) and the anagostic hydrogen atom, and a double-zeta quality basis set (cc-pVDZ)[95] for the remainder of the atoms. All the optimised structures were energy-minimised, and a vibrational analysis was carried out in order to verify that a minimum of the potential energy surface was obtained. The NBO calculations were performed by the NBO 6.0 package[113], and NBOView 2.0[113] was used to visualise the NBO overlaps. QTAIM calculations were performed with the AIMALL software[112]. The same procedure was employed for the ligand calculations. The same basis sets were used for the calculation of the NMR spectra. For the calculation of ^1JC–H, the basis set was decontracted for the C and H to allow for a more accurate determination of the electron density at the nucleus. For the NCI index calculations, 3D RDG iso-surfaces were obtained by the NCIPLOT software[99] and visualised by the VMD program[114].

5.5 Results and Discussion

5.5.1 Computed Structure and Properties of [RhCl(CO)$_2$(*iso*-quinoline)], Complex 27

One of the usual approaches in the computational studies of transition metal complexes is to test the relevancy of the DFT functionals. Therefore, for this testing purpose, the most popular functionals for the study of rhodium complexes such as BP86, B3LYP, and PBE-D3 were used.[80] As the crystal structure of [RhCl(CO)$_2$(*iso*-quinoline)] is not available but the crystal structure of [PtCl$_2$(*iso*-quinoline)(PEt$_3$)] which resembles complex **27** is available, so the later complex was used for the comparison purposes. The testing results show that PBE-D3 gives closer agreement with the experimental structure (Figure 5.1; Table 5.1). For instance, the calculated Pt–N and Pt–P bonds compare well with the crystal structure, but the Pt–Cl bonds are not in the close range. In this regard, it should be noted that the crystal structure can be influenced by crystal packing forces and intermolecular interactions contrary to the computational results which do not include these factors.

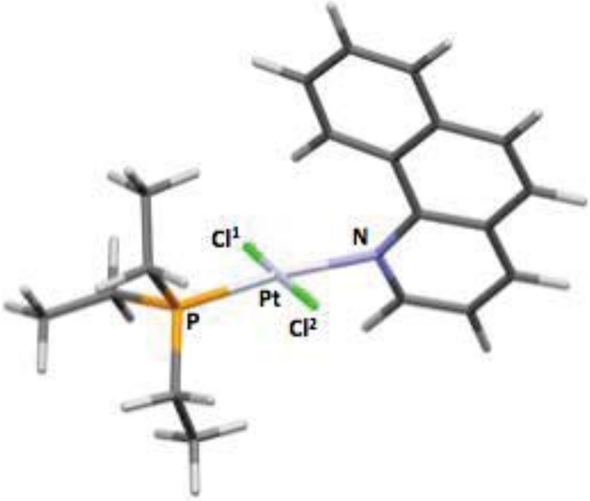

Figure 5.1 The energy minimised structure of [PtCl$_2$(CO)$_2$(*iso*-quinoline)(PEt$_3$)].

Although PBE-D3 shows good comparison with the experimental structure, functional testing was done again with complex **27** [RhCl(CO)$_2$(*iso*-quinoline)] to verify that there is no large discrepancy among the functionals used. Table 5.2 shows the structural parameter comparisons for **27** optimised by B3LYP, BP86, and PBE-D3 functionals; it is seen that the most of the parameters for the PBE-D3 functional lie between the B3LYP and BP86 functionals. However, both PBE-D3 and BP86 structures show close approaches below 2.40 Å [2.386 and 2.357 Å, respectively] compared to B3LYP where the Rh$\cdots$H^{10} separation is 2.424 Å. In addition, there are only small differences seen in the angles and torsions and the trend is that the PBE-D3 values lie in between B3LYP and BP86 (Table 5.2). As the work on anagostic interactions (Chapter 3)[126] showed that PBE-D3 is the most reliable functional for the series of rhodium (I) complexes[66] and considering the comparisons results for [$PtCl_2$(*iso*-quinoline)(PEt_3)], this functional has been employed for the remainder of this work.

The DFT PBE-D3 energy minimised structure of [$RhCl(CO)_2$(*iso*-quinoline)], complex **27** (Figure 5.2a) shows that the *iso*-quinoline ligand coordinates to the metal via the nitrogen atom so that ring A is tilted away from the metal centre in order to avoid a clash between the metal and H^{10}. The distance between H^{10} and the metal is 2.386 Å which lies in the category of short metal···hydrogen approaches (Table 5.3).[34] Looking at the structural parameters for complex **27** (Table 5.3), it appears that the H^{10} hydrogen is accommodated above the coordination plane as a result of two key features. Firstly, there is a rotation about the Rh–N bond as defined by the C–N/coordination plane dihedral angle which at 52.6° rotates the ligand sideways. Secondly, there is a significant twisting in the dihedral angle, $N–C^{10b}–C^{10a}–C^{10}$, in the complex compared to the free ligand [12.5° for the complex; 0.0° for the free ligand]. Both these features appear to assist the ligand in avoiding the $Rh{\cdots}H^{10}$ clash.

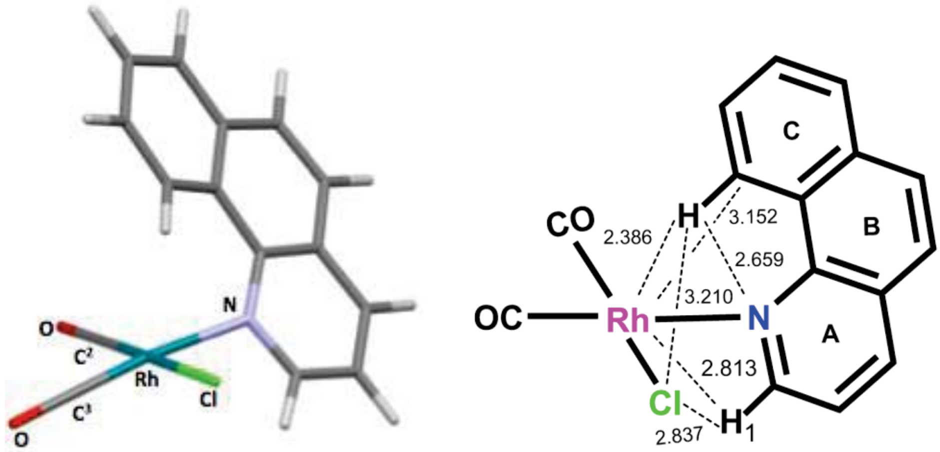

a

b

Figure 5.2 a) The PBE-D3 energy minimised structure of [$RhCl(CO)_2$(*iso*-quinoline)] (**27**); b) Important separations for **27**.

Other important separations in complex **27** (Figure 5.2b) indicate that despite the severe twisting of the ring system, the $Rh{\cdots}C^{10}$ and $H^{10}{\cdots}Cl$ separations [3.152 and 3.210 Å, respectively] are still not as close as was found for the flexible 1-tetralone imine ligands (Chapter 3).[126] Below the coordination plane, there is a close contact between H^1 and both the Cl and Rh atoms [distance: 2.837 and 2.813 Å, respectively] and also a close contact exists between H^{10} and the ligand nitrogen atom [distance: 2.659 Å]. It should be noted that the distance between H^{10} and the nitrogen atom in the free ligand is 2.477 Å. The increase in the $N\cdots C^{10}$ distance in the complex can be attributed to the twisting of the ring system.

To determine the nature of the interactions of the close contacts in **27** especially the $Rh\cdots H^{10}$ separation, computational approaches known for evaluating the $C–H\cdots\cdot M$ interactions were employed.[66,126] The QTAIM analysis which gives a topological description of bonding features based on the electron density, shows a bond path and associated bond critical points between the interacting atoms in a molecule. However, it is also seen that in some cases, a bcp can disappear when a ring critical point is too close to the bond critical point, and a degenerate bond critical point can be formed.[125] Therefore, precautions are always needed for the weak interactions where the distance between a bcp and rcp becomes shorter, and the chances for degenerate bcps are increased. However, to tackle the situation of a degenerate bond critical point, recently, a qualitative approach named as the non-covalent interaction (NCI) index has been introduced as a solution to the problem of 'missing' bcps. The non-covalent interaction (NCI) index is based on the electron density and involves analysis of the reduced density gradient at lower densities. This qualitative approach then allows the nature of weakly interacting molecular regions to be resolved from 3D NCI iso-surface plots which are based on color gradients where red indicates destabilising interactions (repulsive), blue for stabilising interactions (attractive) and green for very weak delocalised (weakly attractive) interactions.[99]

To determine the nature of the covalency of the $M\cdots\cdot H–C$ interaction, NBO analysis, which is based on the Lewis concept of chemical bonding and gives second order stabilisation energy $E(2)$ values, is used. These $E(2)$ values are associated with the two electron stabilisation interactions from a donor to the acceptor in the sense that the greater values relate to the stronger interaction and vice versa. The final part of the analysis is the interpretation of the spectroscopic data corresponding to the $C–H^{10}$ group especially the NMR chemical shift σ (ppm) of the H^{10} hydrogen, nuclear coupling constant (Hz) $^{1}JC–H^{10}$ and the infra-red stretching frequency $\nu C–H^{10}$ (cm^{-1}).[35,126]

Table 5.1 Selected geometrical parameters comparison for [PtCl$_2$(*iso*-quinoline)(PEt$_3$)] using different functionals.

Parameter	B3LYP	PBE-D3	BP86	Experimental + 3σ
Bond length (Å)				
Pt–N	2.184	2.145	2.158	2.154
Pt–Cl^1 (*cis* to C–H)	2.344	2.328	2.335	2.306
Pt–Cl^2 (*trans* to C–H)	2.351	2.338	2.343	2.300
Pt–P	2.251	2.231	2.243	2.229
C–H^{10}	1.081	1.093	1.094	1.050
Separation (Å)				
Pt····H^{10}	2.489	2.440	2.418	2.77
Pt····C^{10}	3.248	3.171	3.215	3.40
Cl^1····H^{10}–C^{10}	3.048	3.064	3.105	-
Cl^2····H^{10}–C^{10}	3.760	3.670	3.619	-
Angles (^{o})				
Pt····N–C	128.1	125.9	128.1	130.1
Pt····H–C^{10}	126.3	123.1	128.6	-
Cl^1····H–C^{10}	159.7	160.2	157.4	-
Cl^2····H–C^{10}	90.6	85.9	91.7	-
Dihedral angles (^{o})				
Cl^1–Pt–N–C	123.2	127.7	124.5	113.7
Cl^2–Pt–N–C	-58.2	-53.8	-57.1	-72.4
Ar-Plane/CP[a]	77.6	72.3	75.9	83.1

[a] CP = coordination plane

Table 5.2 Selected geometrical parameters comparison for complex **27** using different functionals.

Parameter	B3LYP	PBE-D3	BP86
Bond length (Å)			
Rh–N	2.186	2.161	2.164
Rh–Cl	2.355	2.336	2.341
C–H^{10}	1.081	1.091	1.095
Separation (Å)			
Rh····H^{10}	2.424	2.386	2.357
Rh····C^{10}	3.210	3.152	3.176
Cl····H^{10}–C^{10}	3.233	3.210	3.221
Angles (^{o})			
Rh····N–C	129.3	127.8	129.2
Rh····H–C	128.5	125.8	130.3
Cl····H–C	155.8	156.6	153.9
Dihedral angles (^{o})			
OC^2–Rh–N–C	56.3	52.6	57.9
Ar-Plane/CP[a]	71.5	67.0	70.8

[a] CP = coordination plane

For complex **27**, the QTAIM analysis shows only one bond path which corresponds to the Rh···H^{10} separation [2.386 Å] (Figure 5.3). However, the 3D NCI RDG iso-surface plot (Figure 5.4) reveals that only two approaches including Rh····C^{10} and H^{10}····Cl [distances: 3.152 and 3.210 Å, respectively] (Figure 5.2b) are without interactions. Interestingly, the NCI iso-surface plot exhibits a second anagostic approach below the coordination plane involving the Rh····H^1 separation. As the emphasis is the identification of the nature of the Rh···H^{10} separation, therefore, the major part of the analysis is based on quantitative topological approach such as QTAIM.

The QTAIM properties for the Rh···H^{10} bcp in complex **27** indicate a positive value for the Laplacian of the electron density [$\nabla^2\rho$(bcp): 0.0573 *e*/Bohr^5] (Table 5.4) and a negative value for the energy density [*H*(bcp): –0.011 Hartree/Bohr^3] which shows a weak electrostatic type interaction. Both the positive and negative values for the Laplacian of electron density and energy density indicate a 'transit-closed shell' type interaction[97], which means electron density is not confined to the atomic basins. The contour plot of the Laplacian of electron density shows very little accumulation of charge density between C–H^{10} and the metal which can be associated with the transit-closed shell nature of the interaction where the electrostatics predominate, however, a little covalency is also involved (Figure 5.3b). The QTAIM atomic basin properties indicate there are positive charges for both Rh and H^{10} [*q*(H) and *q*(Rh) values: 0.053 and 0.604 *e*, respectively], thus the Rh···H^{10} interaction seems to be repulsive. The QTAIM charge for C^{10} is slightly negative [*q*(C^{10}): –0.008 *e*] which suggests a weak Rh···C^{10} attractive interaction. An increase in C^{10} negative charge was found to draw the Rh···C^{10} separation closer in the case of flexible rhodium 1-tetralone imine complexes (Chapter 3).[126]

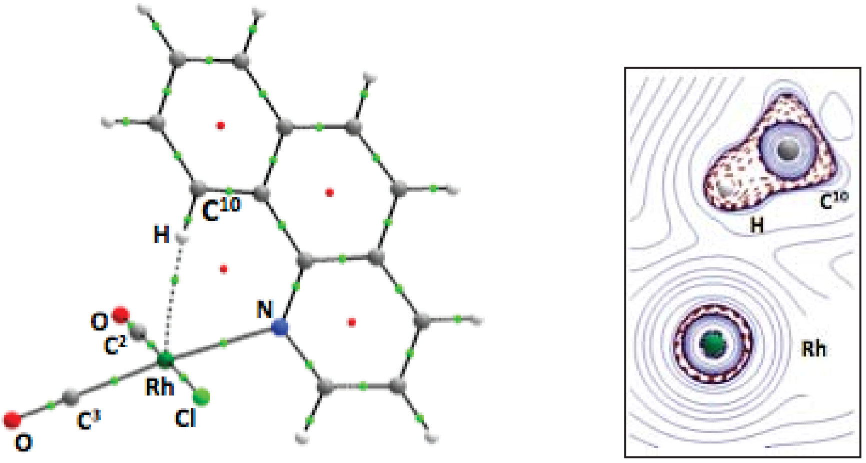

a b

Figure 5.3 a) QTAIM molecular graph; b) Contour plot of Laplacian of electron density (for C–H^{10} and metal) for [RhCl(CO)$_2$(*iso*-quinoline)], complex **27**.

Table 5.3 Selected structural parameters and spectral data for complexes **27–41**.

Complex	**27**	**28**	**29**	**30**	**31**	**32**	**33**	**34**
Bond Length (Å)								
Rh–N	2.161	2.161	2.159	2.156	2.162	2.165	2.175	2.184
Rh–Cl	2.336	2.334	2.334	2.356	2.360	2.364	2.396	2.359
C–H^{10}	1.093	1.092	1.094	1.094	1.093	1.094	1.094	1.092
(Ligands)	**1.091**	**1.090**	**1.089**	**1.091**	**1.090**	**1.092**	**1.089**	**1.091**
Separation (Å)								
Rh····H^{10}	2.386	2.397	2.390	2.417	2.434	2.390	2.424	2.372
Rh····C^{10}	3.152	3.113	3.128	3.130	3.081	2.999	3.023	3.027
Cl····H^{10}	3.210	3.095	3.147	3.293	3.262	3.112	3.578	2.638
Angles (^{o})								
Rh–N–C^{10b}	127.8	127.0	127.1	126.6	125.8	125.0	125.2	123.0
Rh····H^{10}–C^{10}	125.8	121.6	123.4	121.4	116.5	113.5	112.9	116.9
Cl····H^{10}–C^{10}	156.6	160.5	158.4	156.9	156.4	157.6	149.7	167.0
Dihedrals (^{o})								
OC^{2}–Rh–N–C	52.6	52.4	52.9	49.1	47.8	51.3	39.9	67.7
Ar-Plane/CP[b]	67.0	65.7	66.6	63.5	60.3	59.7	48.2	73.9
C^{10b}–C^{10a}–C^{10}–H^{10}	2.94	4.67	3.66	5.15	8.33	12.74	13.78	7.12
(Ligands)	**0.00**	**0.29**	**-1.05**	**0.21**	**0.00**	**-0.55**	**-0.00**	**0.00**
N–C–C–C^{10}	12.5	14.8	14.0	13.9	15.9	15.5	16.8	16.9
(Ligands)	**-0.00**	**-0.35**	**1.16**	**0.14**	**-0.00**	**-0.02**	**-0.00**	**-0.00**
H^{9}–C^{9}–C^{10}–H^{10} (C–H deformation)	-1.2	-1.6	-2.3	-2.3	-4.0	-11.0	-7.2	-3.7
(Ligands)	**0.00**	**0.17**	**0.10**	**0.12**	**-0.00**	**-2.59**[a]	**0.00**[a]	**0.00**
Spectral data								
νC–H^{10} (cm^{-1})	3053.4	3065.5	3059.0	3047.8	3066.1	3052.2	3052.2	3079.2
(Ligands)	**3127.2**	**3139.6**	**3132.4**	**3124.9**	**3132.2**	**3103.6**	**3114.9**	**3126.5**
δH^{10} (complex)	11.74	11.93	11.95	10.33	9.11	8.56	8.73	11.71
(Ligands)	**9.85**	**10.13**	**10.04**	**9.14**	**8.00**	**7.45**	**8.08**	**9.85**
Δδ	1.89	1.80	1.91	1.19	1.11	1.11	0.65	1.86
^{1}JC–H^{10} (Hz)	138.9	141.8	140.4	133.7	137.6	134.7	137.5	140.4
(Ligands)	**142.0**	**143.8**	**143.2**	**136.5**	**139.0**	**135.7**	**138.9**	**141.6**

Complex	**35**	**36**	**37**	**38**	**39**	**40**	**41**
Bond Length (Å)							
Rh–N	2.186	2.225	2.249	2.190	2.183	2.192	2.173
Rh–Cl	2.388	2.349	2.351	2.352	2.361	2.364	2.384
C–H^{10}	1.091	1.087	1.087	1.097	1.093	1.093	1.093
(Ligands)	**1.090**	**1.090**	**1.090**	**1.091**	**1.090**	**1.091**	**1.090**
Separation (Å)							
Rh····H^{10}	2.376	2.868	2.986	2.187	2.238	2.280	2.311
Rh····C^{10}	2.859	3.248	3.295	3.094	3.045	2.925	2.912
Cl····H^{10}	2.678	4.632	4.795	3.303	3.612	3.755	3.909
Angles (^{o})							
Rh–N–C^{10b}	120.3	111.4	108.0	127.1	125.6	123.1	121.3
Rh····H^{10}–C^{10}	105.0	100.6	96.7	138.3	128.9	115.7	112.7
Cl····H^{10}–C^{10}	160.6	78.8	78.7	100.3	92.6	79.8	78.9
Dihedrals (^{o})							
OC^{2}–Rh–N–C	65.6	114.6	112.7	111.8	112.3	116.4	116.0
Ar-Plane/CP[b]	65.4	80.9	80.7	74.4	73.7	64.8	66.5
C^{10b}–C^{10a}–C^{10}–H^{10}	16.39	-3.82	-3.55	-0.48	-4.63	-13.74	-11.42
(Ligands)	-0.00	-0.00	-0.00	-0.35	-0.55	1.27	0.00
N–C^{10b}–C^{10a}–C^{10}	19.2	-16.8	-17.2	-8.0	-12.5	-16.4	-20.4
(Ligands)	0.00	-0.00	0.00	-0.48	-0.69	0.64	0.00
H^{9}–C^{9}–C^{10}–H^{10} (C–H deformation)	-9.41	2.3	2.4	-0.2	2.0	5.1	5.7
(Ligands)	0.00	0.00	-0.00	0.20	0.27	2.10[a]	0.00[a]
Spectral data							
νC–H^{10} (cm^{-1})	3077.8	3157.7	3152.9	2980.2	3036.6	3053.2	3067.8
(Ligands)	**3124.0**	**3126.2**	**3126.0**	**3126.7**	**3123.7**	**3102.9**	**3115.3**
δH^{10} (complex) (ppm)	8.85	10.08	9.81	12.84	10.10	9.39	9.69
(Ligand)	**8.02**	**9.88**	**9.86**	**9.96**	**8.22**	**7.66**	**7.98**
Δδ (ppm)	0.83	0.20	-0.05	2.88	1.88	1.73	1.71
^{1}JC–H^{10} (Hz)	138.7	139.2	139.6	132.4	130.4	130.1	133.3
(Ligands)	**138.8**	**141.4**	**141.1**	**141.3**	**138.4**	**135.2**	**139.2**

[a] H^{7}-hydrogen is replaced by nitrogen or sulfur. [b] CP = metal coordination plane

The 3D NCI RDG iso-surface plot (Figure 5.4) for complex **27** reveals a central light blue region indicating weakly attractive interaction and a surrounding greenish-yellow region that can be interpreted as a weakly repulsive interaction. The light blue region between Rh and H^{10} indicates little covalency involved between the C–H^{10} and the rhodium metal which will be revealed in the NBO analysis.

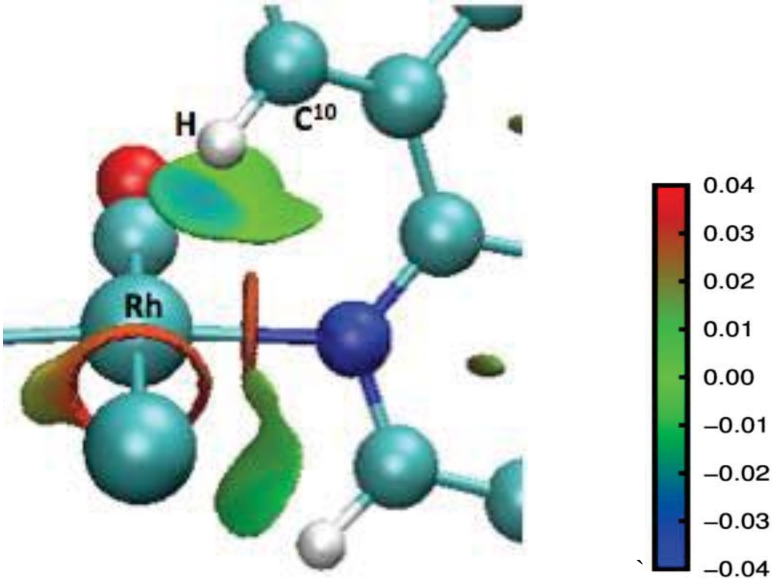

Figure 5.4 3D NCI reduced density gradient (RDG) iso-surface plot showing blue spot between C–H and rhodium (Rh) metal for complex **27**. The sign of the second Hessian eigenvalue (λ_2) times the electron density (ρ) is shown by the colour map.

The NBO analysis for the Rh····H^{10} separation in **27** (Table 5.5) shows that there are small donations from metal lone pairs (LP's) to the C–Hσ* orbital [*E*(2) values for Rh LP(1) and LP(3) to C–Hσ*: 1.49 and 0.32 kcal mol^{-1}, respectively] and also from the C–Hσ orbital to the Rh–Cσ* orbital [*E*(2) values for C–Hσ to Rh–C^2σ* and Rh–C^3σ*: 0.45 and 0.94 kcal mol^{-1}, respectively]. Figure 5.5 shows the spatial overlap for the largest donation found in complex **27**. By relating the NBO donations with the NCI iso-surface plot, it is clear that these small donations correspond to the light blue spot in the NCI iso-surface plot. Thus, the Rh····H^{10} interaction is weakly repulsive based on electrostatics and weakly attractive based on covalency, and this also relates to the QTAIM results where the energy density for Rh···H^{10} bcp was slightly negative [–0.0011 Hartree/Bohr^3]. This is also reflected in the calculated spectroscopic data (Table 5.3) where there is a significant shift to lower CH stretching frequency on coordination [ΔνC–H^{10}: 73.8 cm^{-1}] and there is a slight lowering of ^1JC–H^{10} [1.9 Hz]. Both of these features are found to a significantly larger extent in agostic interactions.[54]

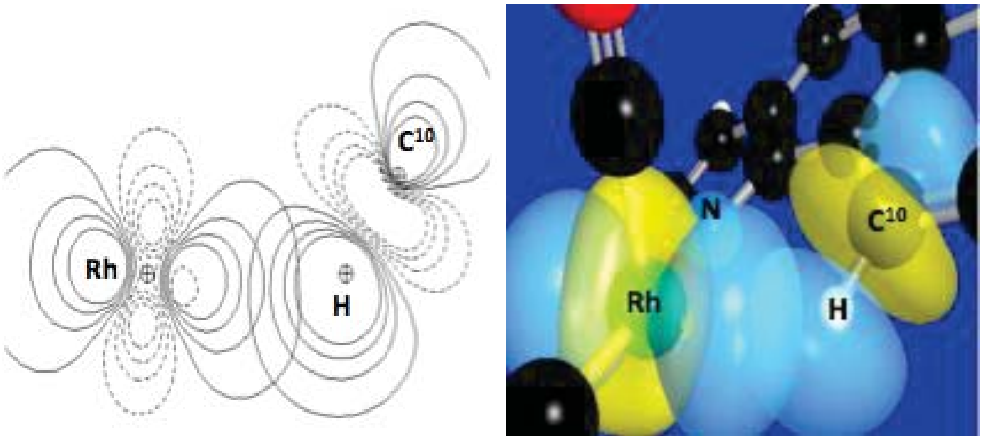

a b

Figure 5.5 NBO diagrams for the donation from Rh to C–Hσ* [*E*(2) value of 1.49 kcal mol^{-1}] for **27**: a) Contour plot; b) 3D Spatial overlap image. Blue and yellow NBO lobes indicate (+) and (-) phases, respectively. (Outermost contour value: 0.0316 a.u.).[113]

As mentioned earlier, there is no crystal structure available for complex **27**. Therefore, in the absence of a crystal structure, there is always the possibility that actual crystallisation can involve the formation of different energy structures. Thus to confirm the energy minimised conformation of complex **27**, one calculation of a second possible conformation of $[RhCl(CO)_2$(*iso*-quinoline)] was performed whereby the C–H hydrogen points out towards the *cis*-CO ligand rather than Cl. It was found that the structure **27a** (Figure 5.6a) is only 1 kcal mol^{-1} less stable than complex **27**. Here, it is noteworthy that this orientation can also be a viable alternative. However, structure **27** is more relevant to cyclometallation reactions[10] and also more stable, so the orientation of low energy structure **27** is adopted in further calculations. The structure parameters of **27a** (Figure 5.6b) indicate a closer $Rh\cdots H^{10}$ separation [2.246 Å] compared to **27** [2.386 Å]. The shorter $Rh\cdots H^{10}$ distance in **27a** indicates less distortion of the ring system as depicted by the angle OC^2–Rh–N–C^{10b} [68.0 and 52.6° in **27a** and **27**, respectively]. As the Cl ligand in **27a** is on the opposite side compared to **27**, the distance between H and Cl is now longer in **27a** [3.364 and 3.210 Å in **27a** and **27**, respectively]. (A comparison table of the geometrical parameters for both of the orientations for **27** and **27a** is included in Appendix C.1).

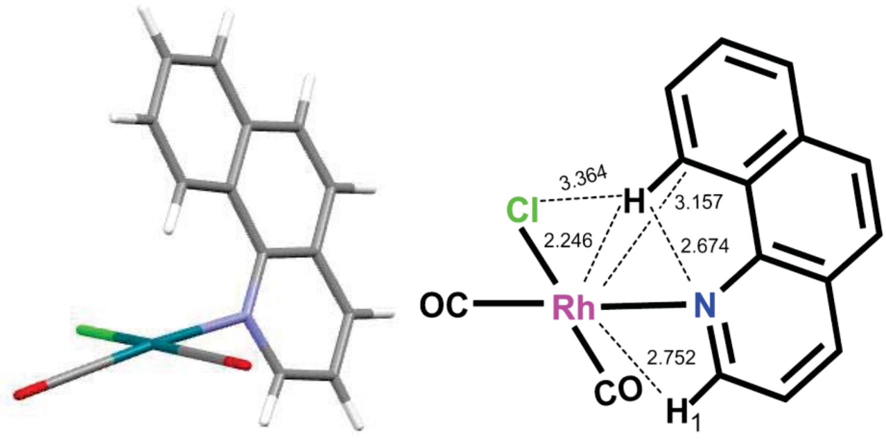

a **b**

Figure 5.6 a) The energy-minimised structure of [RhCl(CO)$_2$(*iso*-quinoline)] complex **27a**; b) Important separations for **27a**.

5.5.2 Electronic Effects at the R^1 and R^2 Positions on Aromatic Ring C, Complexes 28–31

Electronic effects on the separation between above-plane C–H hydrogen and the metal were studied using the strongest electron donating or withdrawing groups. It can be seen from the structural data for complexes **28** and **29** (Table 5.3) that there is a small increase in the Rh····H^{10} separation for both the σ- (SO_2Cl) and π-electron withdrawing [$N{=}NPO(OCH_2CH_3)_2$] substituents compared with unsubstituted complex **1** [2.397 and 2.390 Å, respectively; c.f. 2.386 Å for **27**]. This increase in the Rh····H^{10} separation can be attributed to the increase in the H^{10} atomic charges [$q(H^{10})$ values: 0.068 and 0.061 *e* for **28** and **29**, respectively; c.f. 0.053 *e* for **27**] due to electron withdrawing effect of the substituents. However, the other separations in the **28** and **29** in Figure 5.7 show that the ligand has made small changes in the way in which it sits over the metal by rotation and also the C–H bond deformation of the C ring. These changes can be seen in the increase in the C^{10b}–C^{10a}–C^{10}–H^{10} dihedral angle in both complexes **28** and **29** compared to **27** [values: 4.67° and 3.66° for **28** and **29**, respectively; c.f. 2.94° for **27**] (Table 5.3).

Moving further to the σ- and π-electron donating substituents in **30** and **31**, it is seen that the Rh····H^{10} separations slightly increase [2.417 and 2.434 Å, respectively; c.f. 2.386 Å for **27**] even though the H^{10} atomic charges are less positive [0.015 *e* in **30** and **31**]. The other separations are also slightly changed in **30** and **31** (Figure 5.7). There is a significant increase in the C^{10b}–C^{10a}–C^{10}–H^{10} dihedral angle in **30** and **31** compared to **27** [values: 8.33°, 5.15° and 2.94°, respectively] (Table 5.3). It should be noted that in the *iso*-quinoline complexes, the separation changes are smaller compared to 1-tetralone imine complexes, where the separations were significantly changed by the electron donating effects (Chapter

3).[126] The small changes in the separations in the *iso*-quinoline complexes is due to the inflexibility of the *iso*-quinoline ligand compared to the 1-tetralone-imine complexes where the flexible alicyclic ring changed the conformation from chair-like to boat-like (Chapter 3).[126]

Table 5.4 Selected QTAIM parameters for complexes **27–41**.[a,b]

Complex	**27**	**28**	**29**	**30**	**31**	**32**	**33**	**34**
Rh····H^{10}–C^{10} bond path	Exists	Exists	Exists	Exists	Exists	Exists	Exists	Exists
Electron density, ρ(bcp)	0.0236	0.0234	0.0231	0.0225	0.0219	0.0243	0.0231	0.0244
Laplacian of electron density, $\nabla^2\rho$(bcp)	0.0573	0.0579	0.0567	0.0559	0.0551	0.0649	0.0620	0.0647
Energy density, *H*(bcp)	-0.0011	-0.0009	-0.0009	-0.0008	-0.0006	-0.0003	-0.0001	-0.0008
H^{10} atomic basin								
Charge, *q*(H)	0.053	0.068	0.061	0.015	0.015	0.010	0.014	0.065
	0.052	**0.070**	**0.065**	**-0.003**	**0.011**	**0.008**	**0.009**	**0.050**
Atomic volume, *V*(H)[c]	39.5	38.7	39.3	41.8	42.4	41.7	42.4	36.7
	45.7	**44.1**	**44.4**	**48.3**	**48.5**	**48.4**	**49.2**	**45.8**
C^{10} atomic basin								
Charge, *q*(C)	-0.008	0.002	-0.004	-0.035	-0.046	-0.062	-0.048	-0.015
	0.003	**0.016**	**0.010**	**-0.002**	**-0.037**	**-0.055**	**-0.038**	**0.002**
M atomic basin								
q(M)	0.604	0.599	0.603	0.617	0.611	0.608	0.609	0.613
Complex	**35**	**36**	**37**	**38**	**39**	**40**	**41**	
Rh····H^{10}–C^{10} bond path	Exists	Absent	Absent	Exists	Exists	Exists	Exists	
Electron density, ρ(bcp)	0.0261	–	–	0.0350	0.0318	0.0307	0.0294	
Laplacian of electron desnity, $\nabla^2\rho$(bcp)	0.0704	–	–	0.0770	0.0777	0.0816	0.0798	
Energy density, *H*(bcp)	-0.0006	–	–	-0.0045	-0.0028	-0.0016	-0.0010	
H^{10} atomic basin								
Charge, *q*(H)	0.033	0.036	0.035	0.047	0.005	0.004	0.014	
	0.010	**0.051**	**0.050**	**0.051**	**0.011**	**0.006**	**0.015**	
Atomic volume, v(H)[c]	39.2	41.5	42.3	36.4	38.9	38.8	38.9	
	48.6	**46.0**	**46.3**	**46.2**	**48.8**	**49.0**	**49.1**	
C^{10} atomic basin								
Charge, *q*(C)	-0.061	-0.002	-0.001	-0.008	-0.046	-0.064	-0.048	
	-0.037	**-0.002**	**-0.003**	**-0.002**	**-0.038**	**-0.051**	**-0.027**	
M atomic basin								
q(M)	0.621	0.616	0.614	0.619	0.639	0.633	0.657	

[a] [ρ(bcp) = e/Bohr^3; $\nabla^2\rho$(bcp) = e/Bohr^5; H = Hartree/Bohr^3, $q = e$; E = Hartree; M= e*Bohr; V =1/Bohr^3].
[b] Free ligand values in bold numbers.
[c] 0.001 a.u. iso-surface.

Comparisons of the Rh···H^{10} and Rh···C^{10} separations shown in Figure 5.7 indicate that the largest influence is applied by the π-donor para S^{-} substituent, complex **31**. In further attempts to influence the nature of interaction by electron donation, another π-donor substituent NH_2 was placed at the C^9-position, complex **32**. The addition of the NH_2 group in **32** shortens the Rh···H^{10} separation compared to **31** [2.390 and 2.434 Å, respectively] and is almost similar to **27** where an H atoms occupy both positions [separation in **27**: 2.386 Å].

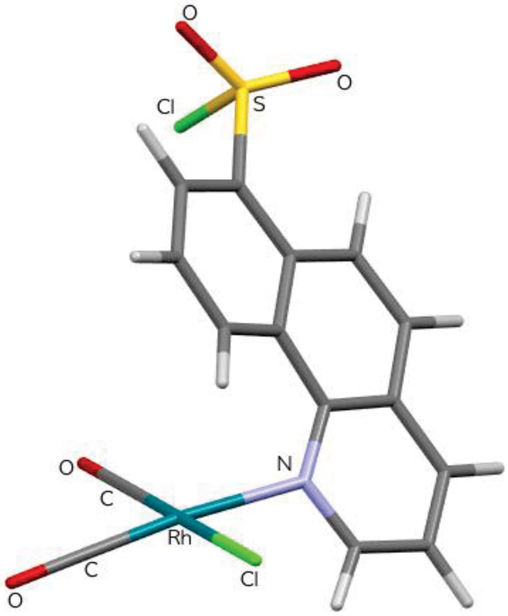
O
O
Cl
S
N
O
C
Rh
C
Cl
O

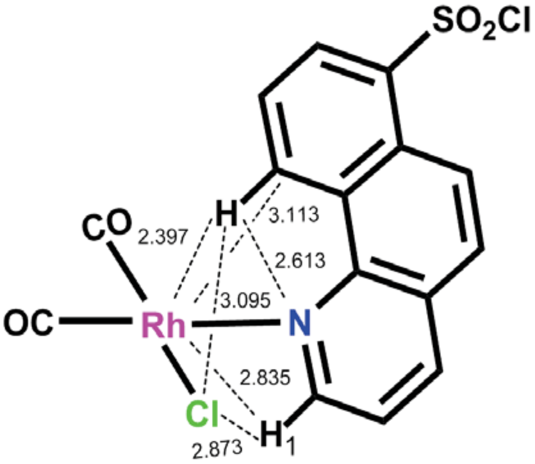
SO2Cl
CO
2.397
H
3.113
2.613
3.095
OC
Rh
N
2.835
Cl
H1
2.873

28

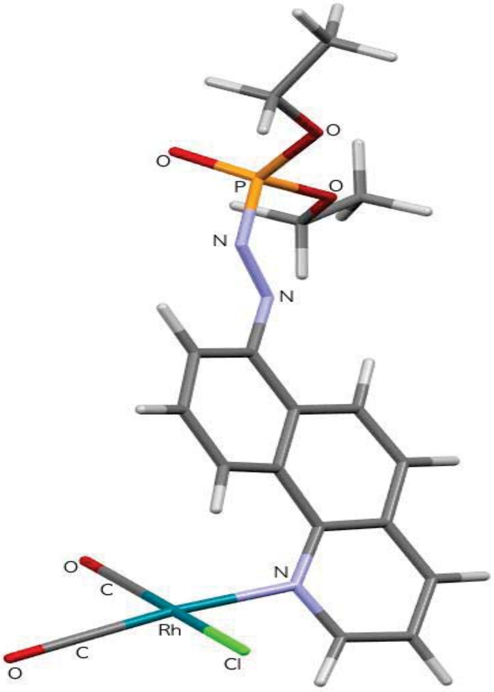
O
O
P
O
N
N
O
C
N
Rh
O
C
Cl

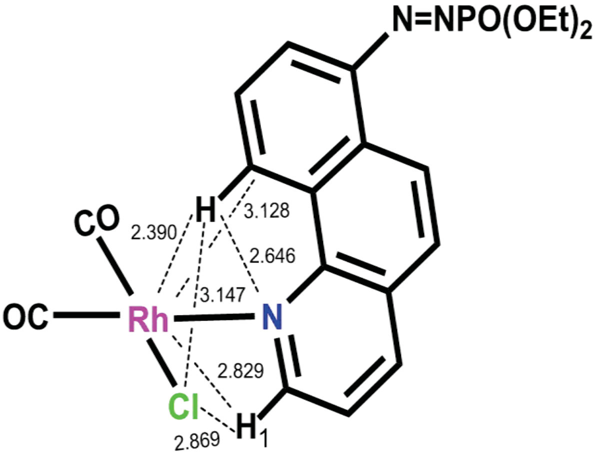
N=NPO(OEt)2
CO
2.390
H
3.128
2.646
3.147
OC
Rh
N
2.829
Cl
H1
2.869

29

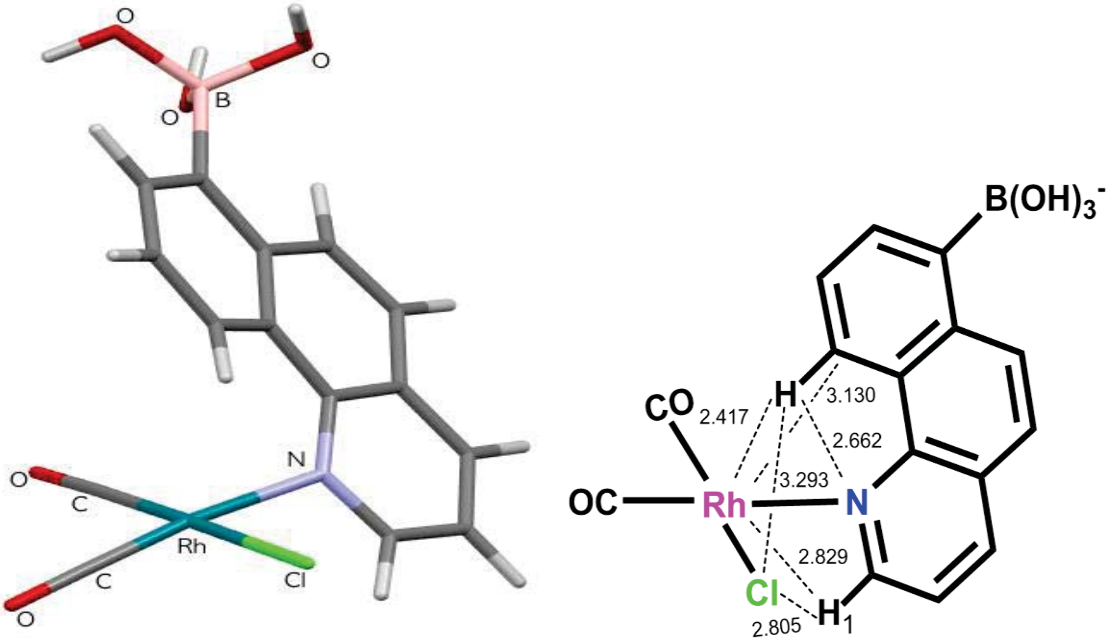

30

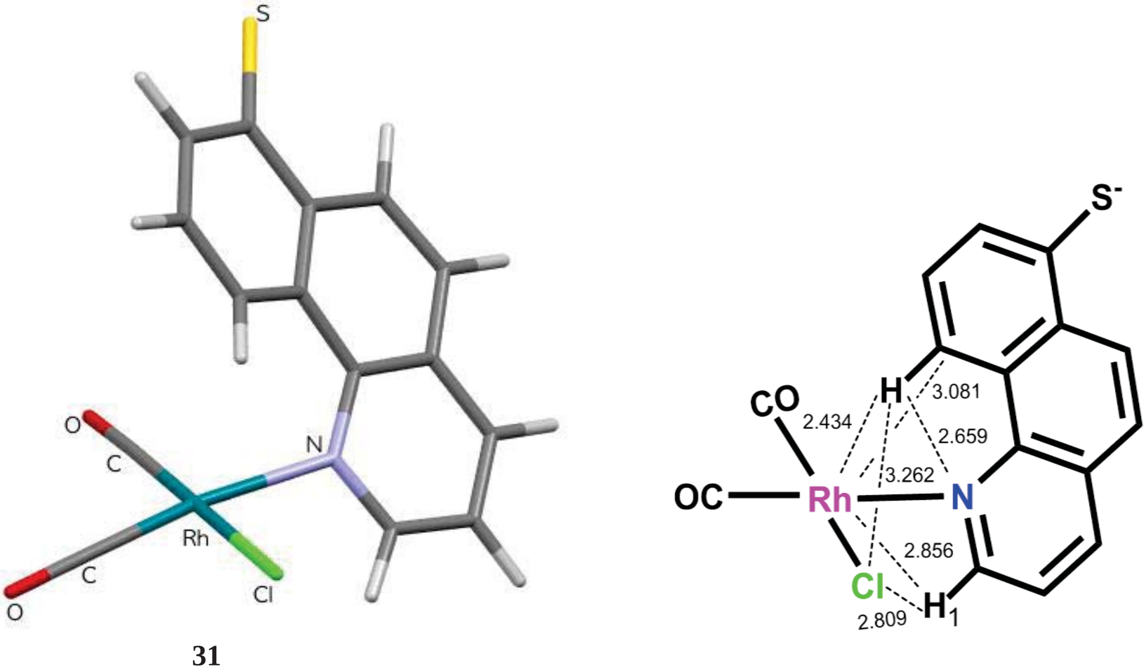

31

Figure 5.7 Optimised structures (left) and important separations (Å) (right) with change in *para* substituent in complexes **28**–**31**.

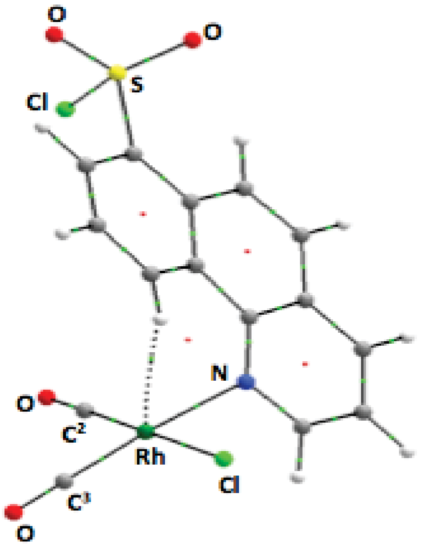

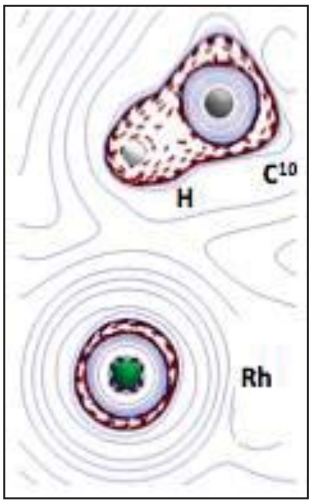

28

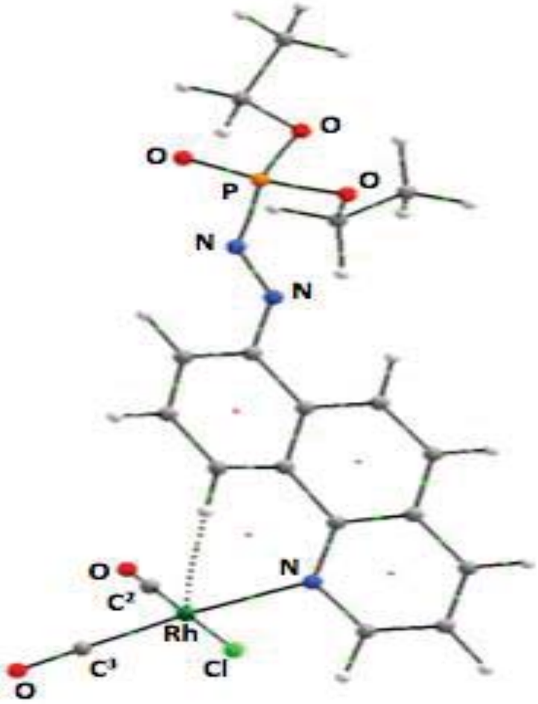

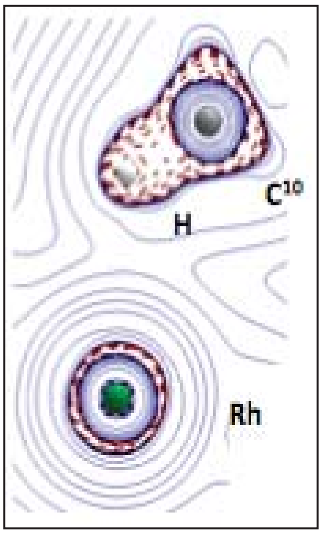

29

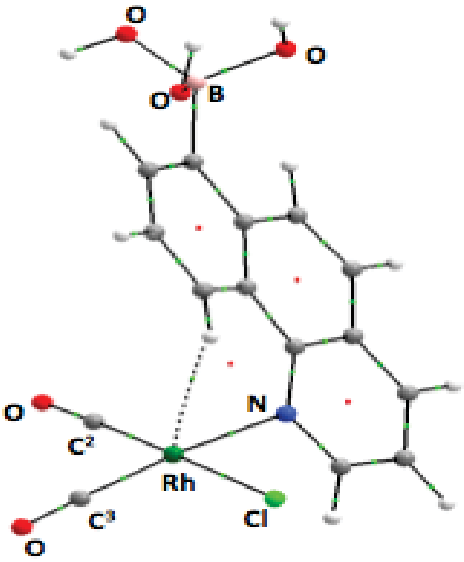

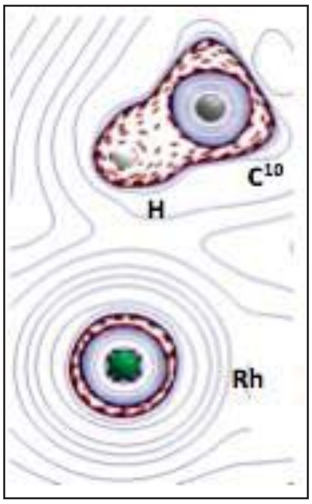

30

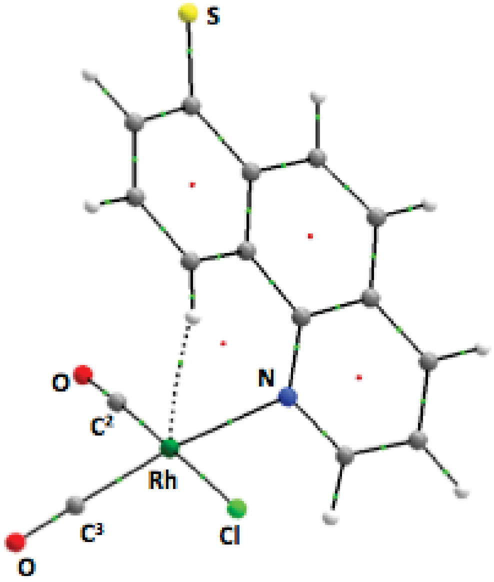

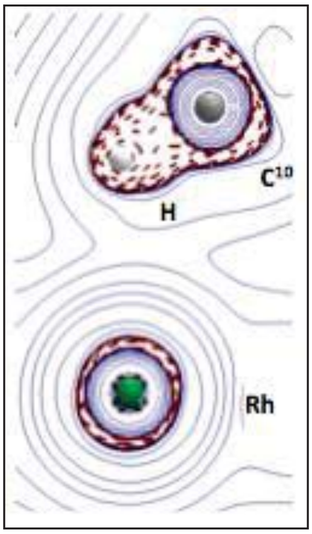

31

Figure 5.8: QTAIM molecular graphs (left) and Laplacian of electron density contour plots (for C–H^{10} and metal) (right) for **28**–**31**.

In complex **32**, the Rh···C^{10} separation becomes slightly shorter than in **31** [2.999 and 3.081 Å, respectively] but is only moderately shorter than in **27** [3.152 Å] and this occurs when a considerable negative charge develops on the carbon C^{10} [q(C^{10}) values: –0.065 and –0.008 *e* in **31** and **32**, respectively; c.f. –0.046 *e* in **27**]. A similar shortening of the Rh···C^{10} separation was also found for the same substituents in the 1-tetralone imine complex (Chapter 3).[126]

Although the effect with the *iso*-quinoline ligand is not as great as was seen with the flexible 1-tetralone imine, it appears that the ligand is still trying to accommodate the Rh and C$_{10}$ atomic charges. As in the structure of complex **32**, significant rotational and torsional changes re-position the ligand over the metal coordination plane (Table 5.3; Figure 5.7). In **6**, the most significant structural changes were seen in the dihedrals C^{10b}–C^{10a}–C^{10}–H^{10} [values: 12.74, 8.33 and 2.94° in **32**, **31** and **27**, respectively] and H^{9}–C^{9}–C^{10}–H^{10} (C–H deformation) [values: –11.0, –4.0 and –1.2° in **32**, **31** and **27**, respectively].

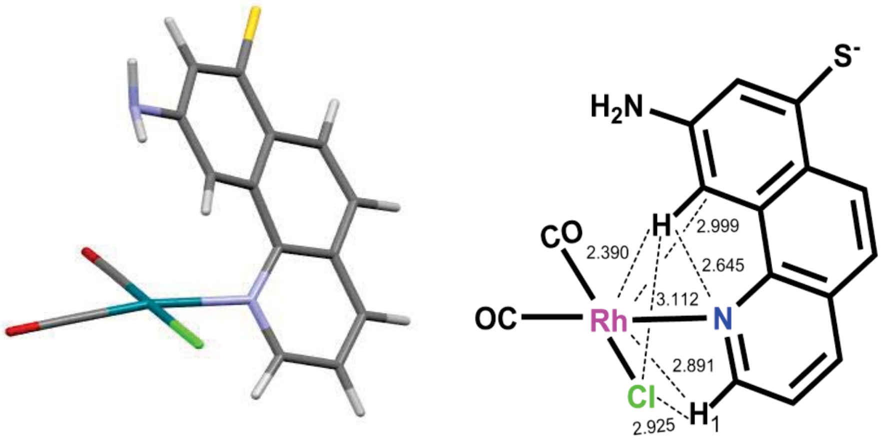

32

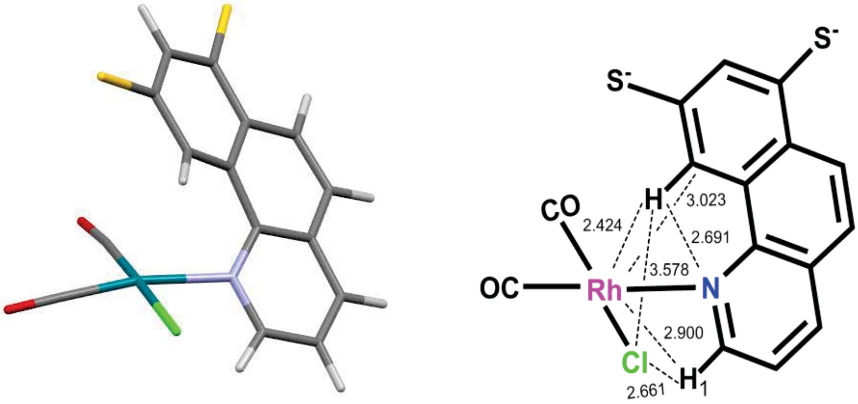

33

Figure 5.9 Optimised structures (left) and important separations (right) with *para* and *ortho* electron donating substituents in complexes **32** and **33**.

As seen earlier, the separations in complex **32**, were influenced by the increase in the negative charge on C^{10}. Therefore, to further influence the electronics of the system, the NH_2 substituent was replaced with S^- which is a stronger electron-donating group than NH_2, complex **33**.[106] Placing two S^- substituents at the *para* and *ortho* positions in **33** repositions the ligand and here contrary to **32**, the Rh···H^{10} and Rh···C^{10} separations become larger [Rh···H^{10} and Rh···C^{10} distances in **33**: 2.424 and 3.023 Å, respectively; c.f. 2.390 and 2.999 Å in **32**, respectively] (Table 5.3; Figure 5.8). However, it is apparent that there is now a small steric effect operating as the *cis*-CO ligand bends slightly away from the coordination plane by 4.3° which was not seen in the case of *ortho* NH_2 complex **32**. It is interesting to note for **33** that the C–H deformation dihedral and the Rh–N/coordination plane dihedral becomes smaller compared to **32** [C–H deformation torsion: –7.2 and –11.0°, respectively] [Rh–N/coordination plane dihedral: 39.9 and 51.3°, respectively] (Table 5.3).

The QTAIM analyses (Table 5.4) for **28**–**33** indicates the bcp for Rh···H^{10} and associated bcp properties, the Laplacian of electron density $\nabla^2\rho$(bcp) and energy density *H*(bcp), are positive and negative respectively and there is no remarkable change in the strength of the interaction. However, it is noticed that the energy density value becomes less negative in going from **28** to **33** [*H*(bcp) value in **28** and **33**: –0.0009 Hartree/Bohr^3 and –0.0001 Hartree/Bohr^3, respectively]. Therefore, the interaction is still electrostatic but with some covalency components involved. The covalency components can be seen in Table 5.5 where small donations between Rh and the C–H bond NBOs are present (Table 5.5). The Laplacian of the electron density contour plots for the C–H^{10}····Rh interactions in Figure 5.8 show slight changes in the charge density in correlation with the small changes in the Laplacian of the electron density values as shown in Table 5.4. However, there is little charge density accumulation between the C–H bond and the metal as shown in the case of the $B(OH)_3^-$ and S^- substituents (complexes **30** and **31**, respectively). For complex **33** (with S^- at the *ortho* and *para* positions), there is another bond path existing Cl and H^{28} (H^1). The QTAIM properties indicate a weakly attractive interaction [$\nabla^2\rho$(bcp) and *H*(bcp): 0.0426 *e*/Bohr^5 and 0.0016 Hartree/Bohr^3, respectively; *q*(Cl) and *q*(H^{28}): –0.638 *e* and 0.055 *e*, respectively] (refer to Table 5.7 in Appendix C.2 for QTAIM properties for Cl····H^{28} bcp).

The NBO results (Table 5.5) show a noticeable increase in donations from C–Hσ to the Rh–C^2(*cis*)σ* and to the Rh–C^3(*trans*)σ* orbitals in **32** and **33** compared to **27** [*E*(2) values: 0.72 and 1.51 kcal mol^{-1} in **32**, respectively; 0.65 and 1.70 kcal mol^{-1} in **33**, respectively; c.f. 0.45 and 0.94 kcal mol^{-1} in **27**, respectively]. These donations are small but as they are relevant to agostic interactions, they therefore cannot be ignored in this case.

The spectroscopic analysis (Table 5.3) indicates that the IR stretching frequency is significantly lower in **32** and **33** compared with the respective ligands [ΔνC–H^{10}: 48.6 and 62.7 cm^{-1}, respectively; c.f. 73.8 cm^{-1} in **27**]. The NMR properties show that the chemical shift δ is relatively less downfield in **33** [Δδ: 0.65 ppm) compared to the other complexes and ^{1}JC–H^{10} shows only a slight decrease in complexes **31**, **32** and **33** [Δ^{1}JC–H^{10} values: 1.4, 1.0 and 1.4 Hz, respectively] compared to complex **27** [Δ^{1}JC–H^{10}: 3.1 Hz].

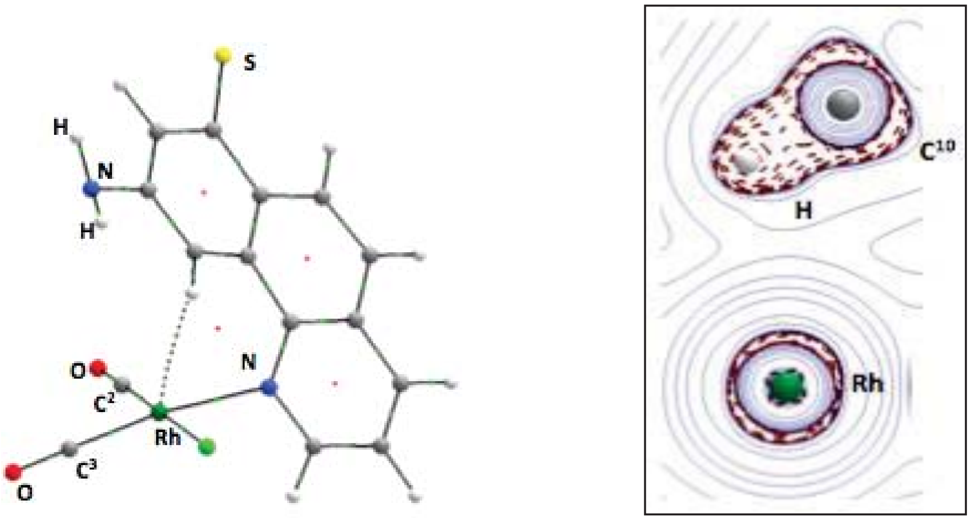

32

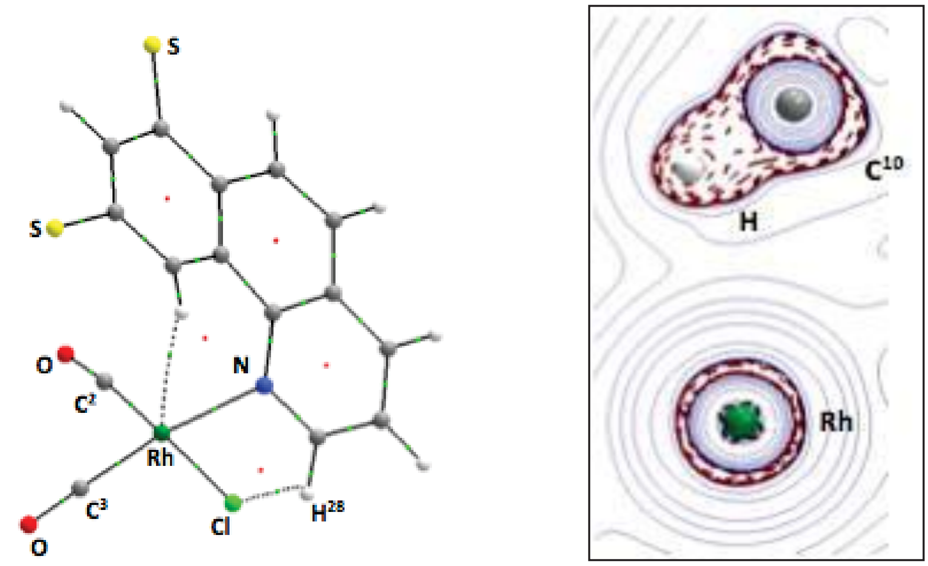

33

Figure 5.10 QTAIM molecular graphs (left) and Laplacian of electron density contour plots (for C–H^{10} and metal) (right) for **32** and **33**.

Table 5.5 Selected NBO Parameters for *iso*-Quinoline complexes **27**–**41**.

Complex	**27**	**28**	**29**	**30**	**31**	**32**	**33**	**34**
C–H^{10}σ bond								
Occupancy	1.9707	1.9707	1.9714	1.9709	1.9698	1.9660	1.9651	1.9692
(Ligands)	**1.9770**	**1.9761**	**1.9769**	**1.9790**	**1.9787**	**1.9756**	**1.9779**	**1.9770**
Energy (a.u.)	-0.4352	-0.4570	-0.4464	-0.3202	-0.3123	-0.3131	-0.1877	-0.4302
(Ligands)	**-0.4123**	**-0.4370**	**-0.4261**	**-0.2893**	**-0.2780**	**-0.2780**	**-0.1409**	**-0.4100**
C–H^{10}σ* bond								
Occupancy	0.0231	0.0226	0.0226	0.0215	0.0197	0.0205	0.0203	0.0264
(Ligands)	**0.0164**	**0.0166**	**0.0168**	**0.0178**	**0.0170**	**0.0175**	**0.0185**	**0.0167**
Energy (a.u)	0.3955	0.3762	0.3849	0.5031	0.5126	0.5053	0.6276	0.4100
(Ligands)	**0.4156**	**0.3937**	**0.4044**	**0.5299**	**0.5417**	**0.5343**	**0.6727**	**0.4171**
Rh–C^{2}σ* bond								
Occupancy	0.3968	0.3986	0.3980	0.3857	0.3829	0.3851	0.3678	0.3969
Energy (a.u.)	0.3966	0.3859	0.3947	0.4815	0.4874	0.5022	0.5820	0.4277
Rh–C^{3}σ* bond								
Occupancy	0.2867	0.2943	0.2968	0.3088	0.3066	0.3821	0.3048	0.3017
Energy (a.u)	0.2334	0.2231	0.2312	0.3288	0.3403	0.5022	0.4504	0.2569
C^{10}–C^{9}π* bond								
Occupancy	0.2706	0.2610	0.2848	0.3113	0.4597	0.4735	0.4154	0.2743
Energy (a.u.)	-0.0059	-0.0278	-0.0176	0.1153	0.1183	0.1217	0.2359	-0.0015
Rh LP (1)								
Occupancy (n)	1.9701	1.9629	1.9633	1.9746	1.9743	1.9729	1.9720	1.9639
Energy (a.u)	-0.1768	-0.1881	-0.1827	-0.0889	-0.0809	-0.0768	0.0265	-0.1782
Rh LP (2)								
Occupancy (n)	1.8123	1.8138	1.8127	1.8053	1.8048	1.8056	1.8105	1.8120
Energy (a.u.)	-0.2247	-0.2366	-0.2302	-0.1341	-0.1255	-0.1224	-0.0155	-0.2239
Rh LP (3)								
Occupancy (n)	1.7600	1.7636	1.7624	1.7473	1.7460	1.7452	1.7356	1.7576
Energy (a.u.)	-0.2259	-0.2383	-0.2321	-0.1342	-0.1246	-0.1214	-0.0134	-0.2252
Cl LP (2)								
Occupancy (n)	1.9697	1.9694	1.9697	1.9732	1.9736	1.9752	1.9764	1.9716
Energy (a.u.)	-0.2628	-0.2743	-0.2679	-0.1808	-0.1750	-0.1731	-0.0762	-0.2666
Cl LP (3)								
Occupancy (n)	1.9434	1.9422	1.9427	1.9517	1.9544	1.9568	1.9632	1.9447
Energy (a.u.)	-0.2301	-0.2415	-0.2353	-0.1447	-0.1377	-0.1350	-0.0427	-0.2282
***E*(2) Rh LP to C–H^{10}σ* (kcal mol^{-1})**								
Rh LP(1) to C–Hσ*	1.49	1.07	1.27	1.06	0.72	0.59	0.62	0.45
Rh LP (2) to C–Hσ*	–	–	–	–	–	0.10	–	–
Rh LP(3) to C–Hσ*	0.32	0.37	0.33	0.26	0.25	0.30	0.22	0.43
***E*(2) Rh LP to C^{10}–C^{9}π* (kcal mol^{-1})**								
Rh LP(1) to C–Cπ*	0.36	0.57	0.48	0.39	0.66[a]	1.06[a]	0.65[a]	1.04
***E*(2) C–Hσ to Rh–Cσ* (kcal mol^{-1})**								
C–Hσ to Rh–C^{2}σ*	0.45	0.45	0.48	0.62	0.59	0.72	0.65	0.68
C–Hσ to Rh–C^{3}σ*	0.94	0.90	0.93	1.20	1.28	1.51	1.70	0.86
***E*(2) Cl LP to C–H^{10}σ* (kcal mol^{-1})**								
Cl LP(2) to C–Hσ*	–	0.06	–	–	–	0.07	–	0.35
Cl LP(3) to C–Hσ*	0.18	0.26	0.22	0.12	0.13	0.25	–	1.41

[a] C–Cπ* belongs to C^{10}–C^{10a} π*

Table 5.5 continued Selected NBO parameters for *iso*-Quinoline complexes **27**–**41**.

Complex	**35**	**36**	**37**	**38**	**39**	**40**	**41**
C–H^{10}σ bond							
Occupancy	1.9653	1.9733	1.9738	1.9673	1.9657	1.9620	1.9628
(Ligands)	**1.9788**	**1.9772**	**1.9772**	**1.9771**	**1.9785**	**1.9755**	**1.9775**
Energy (a.u.)	-0.3105	-0.4358	-0.4355	-0.4263	-0.3108	-0.3138	-0.1943
(Ligands)	**-0.2774**	**-0.4118**	**-0.4121**	**-0.4131**	**-0.2866**	**-0.2874**	**-0.1615**
C–H^{10}σ* bond							
Occupancy	0.0227	0.0171	0.0164	0.0349	0.0287	0.0258	0.0257
(Ligands)	**0.0172**	**0.0165**	**0.0165**	**0.0167**	**0.0172**	**0.0177**	**0.0185**
Energy (a.u.)	0.5207	0.4057	0.4014	0.3965	0.5119	0.5043	0.6262
(Ligands)	**0.5417**	**0.4147**	**0.4144**	**0.4138**	**0.5336**	**0.5260**	**0.6557**
Rh–C^{2}σ* bond							
Occupancy	0.3744	0.3923	0.3923	0.3966	0.3934	0.3934	0.3783
Energy (a.u.)	0.5506	0.4072	0.4075	0.4996	0.5886	0.5900	0.7065
Rh–C^{3}σ* bond							
Occupancy	0.3079	0.2875	0.2801	0.2985	0.3121	0.3115	0.3150
Energy (a.u.)	0.3860	0.2429	0.2503	0.2954	0.3903	0.3917	0.4982
C^{10}–C^{9}π* bond							
Occupancy	0.4722	0.2757	0.2757	0.2658	0.4416	0.4566	0.3775
Energy (a.u)	0.1192	-0.0010	-0.0010	0.0037	0.1246	0.1259	0.2372
Rh LP (1)							
Occupancy (n)	1.9601	1.9632	1.9623	1.9541	1.9582	1.9580	1.9521
Energy (a.u.)	-0.0809	-0.1740	-0.1770	-0.1756	-0.0823	-0.0829	0.0192
Rh LP (2)							
Occupancy (n)	1.8032	1.8104	1.8110	1.8118	1.7999	1.7985	1.7973
Energy (a.u.)	-0.1238	-0.2226	-0.2228	-0.2215	-0.1299	-0.1285	-0.0245
Rh LP (3)							
Occupancy (n)	1.7411	1.7495	1.7502	1.7599	1.7426	1.7353	1.7348
Energy (a.u.)	-0.1221	-0.2245	-0.2247	-0.2221	-0.1295	-0.1269	-0.0229
Cl LP (2)							
Occupancy (n)	1.9744	1.9685	1.9675	1.9719	1.9727	1.9724	1.9753
Energy (a.u.)	-0.1763	-0.2693	-0.2708	-0.2607	-0.1694	-0.1682	-0.0699
Cl LP (3)							
Occupancy (n)	1.9570	1.9468	1.9478	1.9497	1.9510	1.9538	1.9774
Energy (a.u.)	-0.1322	-0.2244	-0.2247	-0.2220	-0.1308	-0.1280	-0.0311
***E*(2) Rh LP to C–H10σ* (kcal mol^{-1})**							
Rh LP(1) to C–Hσ*	0.07	–	–	4.38	2.62	1.42	0.91
Rh LP (2) to C–Hσ*	0.18	–	–	0.22	0.31	0.31	0.18
Rh LP(3) to C–Hσ*	0.17	–	–	–	–	–	–
***E*(2) Rh LP to C^{10}–C^{9}π* (kcal mol^{-1})**							
Rh LP(1) to C–Cπ*	1.72[a]	0.27	0.51	0.11	0.55[a]	1.17[a]	1.31[a]
***E*(2) C-Hσ to Rh–Cσ* (kcal mol^{-1})**							
C–Hσ to Rh–C^{2}σ*	1.13	0.07	–	0.52	0.67	0.69	0.81
C–Hσ to Rh–C^{3}σ*	1.58	0.37	0.26	1.09	1.54	1.76	1.69
***E*(2) Cl LP to C–H^{10}σ* (kcal mol^{-1})**							
Cl LP(2) to C–Hσ*	0.46	–	–	–	–	–	–
Cl LP(3) to C–Hσ*	0.97	–	–	–	–	–	–

[a] C–Cπ* belongs to C^{10}–C^{10a} π*

5.5.3 Steric Effects at R^{3} and Electronic Effects at R^{1} and R^{2} Positions

Substitution of a methyl group at the ring A (R^{3}-position) of the *iso*-quinoline ligand in complex **34**, straightens the ligand up over the metal compared to unsubstituted complex **27** [OC^{2}–Rh–N–C rotation angles: 67.7 and 52.6°, respectively] which causes the Rh···H^{10} and Rh···C^{10} separations to become slightly closer [values: 2.372 and 3.027 Å, respectively; c.f. 2.386 and 3.152 Å in **27**, respectively]. In addition, the H^{10} ···Cl distance is now significantly shorter than in **27** [2.638 Å and 3.210 Å, respectively]. The close $H^{10}\cdots$Cl distance is associated with torsional changes in the N–C–C–C^{10} dihedral angle [16.9 and 12.5° for **34** and **27**, respectively], the OC^2–Rh–N–C dihedral angle [67.7 and 52.6° for **34** and **27**, respectively], and the C^{10b}–C^{10a}–C^{10}–H^{10} dihedral angle [7.12 and 2.94° in **34** and **27**, respectively]. Below the coordination plane, the hydrogens of the substituted methyl group (H^{30}) and (H^{31}) make close approaches with Cl and Rh [$H^{30}\cdots\cdot$Cl distance: 2.702 Å; $H^{31}\cdots\cdot$Rh distance: 2.723 Å] (Figure 5.11).

The QTAIM analysis indicates bcps (Figure 5.12) for the Rh$\cdots\cdot H^{10}$ separation [$\nabla^2\rho$(bcp): 0.0244 *e/*Bohr^5; [*H*(bcp): –0.0008 Hartree/Bohr^3] (Table 5.4), the Cl$\cdots H^{30}$ separation [$\nabla^2\rho$(bcp): 0.0350 *e*/Bohr^5; [*H*(bcp): 0.0013 Hartree/Bohr^5] and the Rh$\cdots H^{31}$ separation [$\nabla^2\rho$(bcp): 0.0442 *e*/Bohr^5; [*H*(bcp): 0.0008 Hartree/Bohr^3] (refer to Table 5.7 in Appendix C.2 for QTAIM data for below the plane bcps). Based on QTAIM atomic basin charges, the Rh$\cdots H^{10}$ interaction [*q*(Rh): 0.613 *e*; *q*(H^{10}): 0.065 *e*] and the Rh$\cdots H^{31}$ interaction [*q*(Rh): 0.613 *e*; *q*(H^{31}): 0.035 *e*] are repulsive in nature and the Cl$\cdots\cdot H^{30}$ close approach [*q*(Cl): –0.563 *e*; *q*(H^{30}): 0.076 *e*] involves an attractive interaction. Also, it appears that the increase in the C^{10} negative charge has a significant effect on both the Rh$\cdots C^{10}$ and Rh$\cdots H^{10}$ separations. For instance, the increase in negative charge at C^{10} in **34** compared to **27** [*q*(C^{10}): –0.015 and –0.008 *e* respectively] in effect draws C^{10} closer to the metal and with this change, the hydrogen H^{10} also becomes closer to the metal [Rh$\cdots H^{10}$ and Rh$\cdots C^{10}$ separations in **34**: 2.372 Å and 3.027 Å, respectively; c.f. 2.386 and 3.152 Å in **27**, respectively].

The NBO results for **34** indicate a small increase in the Rh LP(1) to C^{10}–$C^9\pi^*$ orbital donation compared with **27** [*E*(2) values: 1.04 and 0.36 kcalmol^{-1}, respectively] but as observed for all the complexes so far in this section, the *E*(2) values are very small anyway and do not represent any meaningful donation (Table 5.5). The spectroscopic data (Table 5.3) for **34** show that there is a smaller decrease in νC–H^{10} and ^1JC–H^{10} relative to the free ligand in comparison to **27** [ΔνC–H^{10}: 47.3 and 73.8 cm^{-1}, respectively; Δ^1JC–H^{10}: 1.2 and 3.1 Hz, respectively].

As it was found earlier in complexes **27**–**33** that electronic changes on the aromatic A-ring could influence separation distances it was of interest to ascertain how electronic effects would operate when the C^2 methyl group was present in complex **34**. Hence, along with CH_3 at the R^1 position, an S^- substituent was placed at the *para*-position (R^2 in complex **35)** but structural parameters show very little change to the Rh–H^{10} separation [2.376; c.f. 2.372 Å in **34**] (Figure 5.11). A significant increase in negative atomic charge on C^{10} is seen in **35** [–0.061 and –0.015 *e* for **35** and **34**, respectively] (Table 5.4) and the structural geometry again shows the positioning of the ligand effects the Rh$\cdots C^{10}$

separation with it closing up significantly [2.859 and 3.027 Å in **35** and **34**, respectively] (Figure 5.11). In particular, the C^{10b}–C^{10a}–C^{10}–H^{10} torsion angle is approximately 9° larger in complex **35** compared to **34** and C–H deformation (H^{9}–C^{9}–C^{10}–H^{10} dihedral) becomes larger by 5.7° in **35** (Table 5.3).

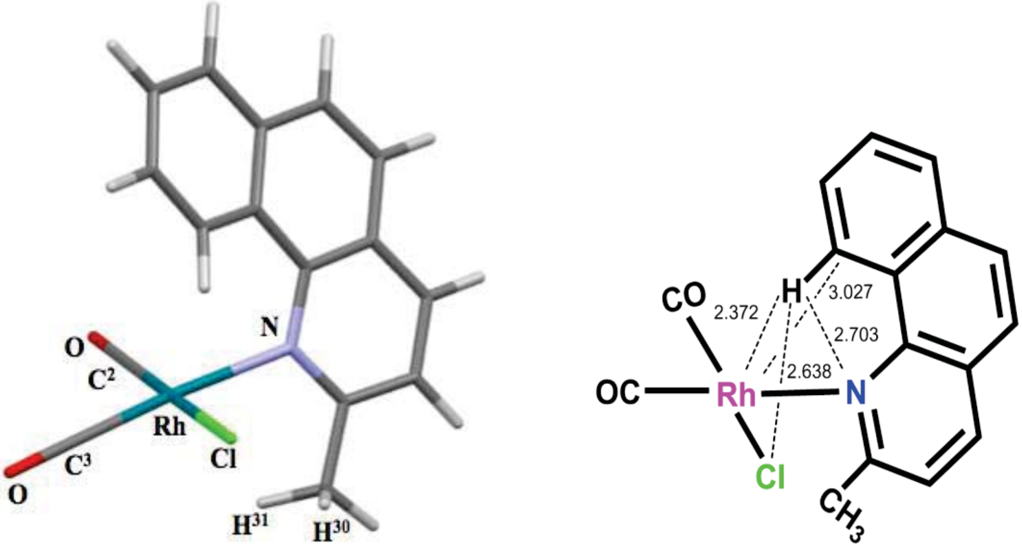

34

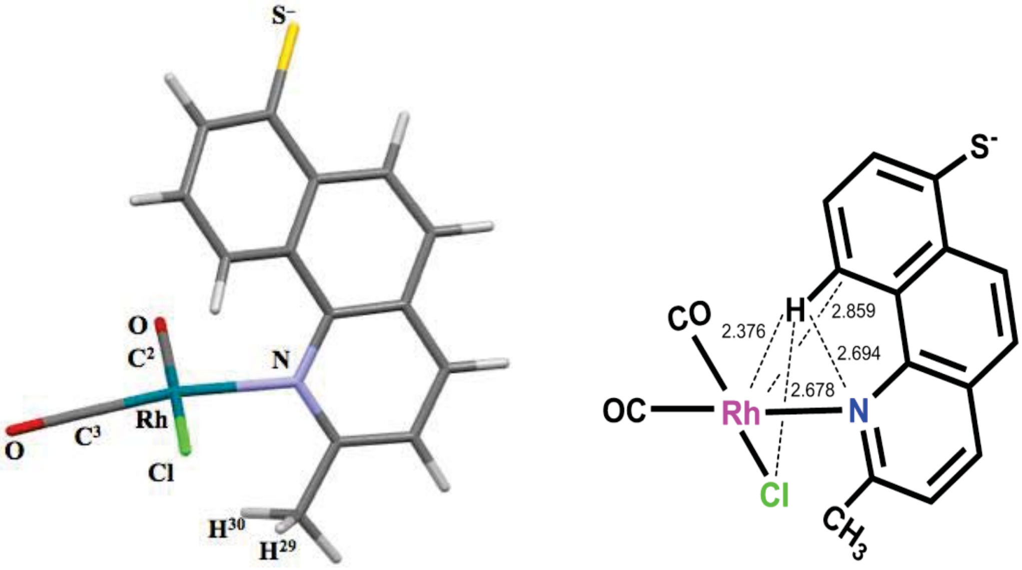

35

Figure 5.11 The energy minimised structures (left) and important separations (Å) (right) for complexes **34** and **35**.

The QTAIM analysis for complex **35** indicates three bcps (Figure 5.12) as similarly found for **34**. In **35** the C^{10} charge becomes more negative [–0.061 *e*; c.f. –0.015 *e* in **34**] and the H^{10} charge is less positive [0.033 *e*; c.f. 0.065 *e* in **34**) which would point to a comparatively stronger attraction between the metal and C^{10} and less repulsion between the metal and H^{10} than seen for **34**. Surprisingly, the energy density and Laplacian of electron density values for the Rh···H^{10} bcp are not very different in both **35** and **34** [$\nabla^2\rho$(bcp): 0.0704 and 0.0647 *e*/Bohr^5, respectively; *H*(bcp): –0.0006 and –0.0008 Hartree/Bohr^3, respectively] (Table 5.4).

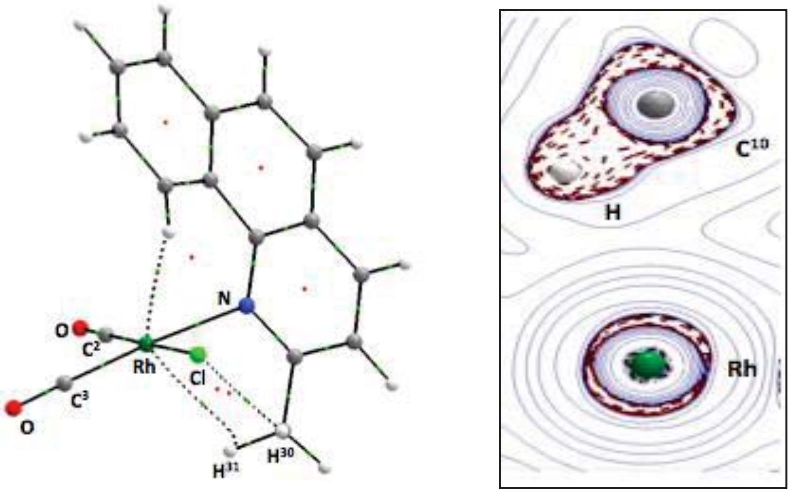

34

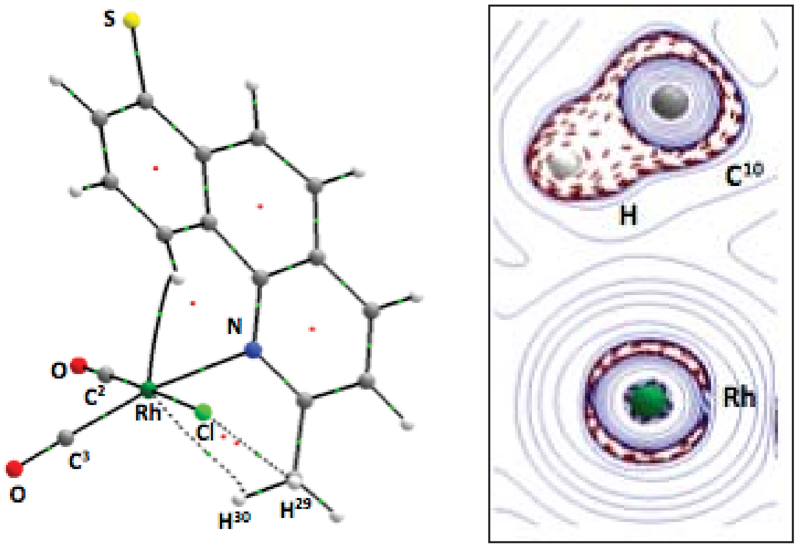

35

Figure 5.12 QTAIM molecular graphs (left) and Laplacian of electron density contour plots (for C–H^{10} and metal) (right) for **34** and **35**.

However, the covalency components for the Rh···H^{10} interaction are revealed by the NBO analysis which shows there is a small but noticeable increase in the agostic and back-bonding donations in **35**. The second-order stabilisation energy *E*(2) values for the agostic C–Hσ to the Rh–C^{2}σ* and to the Rh–C^{3}σ* orbitals in **35** increase a little to 1.13 and 1.58 kcal mol^{-1} [c.f. 0.68 and 0.86 kcal mol^{-1} in case of **34**] and for the back-bonding LP Rh to C^{10}–C^{10a}π* donation, the *E*(2) value increases to 1.72 kcal mol^{-1} [c.f. 1.04 kcal mol^{-1} in case of **34**]. Looking at the NBO energies for the donor-acceptors, it is revealed that the substituent S$^-$ (complex **35**) affects the energies quite significantly as the Rh–C^{2}σ* and Rh–C^{3}σ* energies become 0.5506 and 0.3860 a.u. [c.f. 0.3966 a.u and 0.2334 in **34**], the C^{10}–C^{10a}π* energy is now 0.1192 a.u. [c.f. –0.0015 a.u. in complex **34**], and the C–Hσ energy becomes –0.2774 a.u. [c.f. –0.4100 a.u. in **34**] (Table 5.5).

The QTAIM properties for the Rh····H^{30} interaction [$\nabla^2\rho$(bcp): 0.0393 *e*/Bohr^5; *H*(bcp): 0.0006 Hartree/Bohr^3; *q*(Rh): 0.621 *e*; *q*(H^{30}): 0.035 *e*] and for the Cl···H^{29} interaction [$\nabla^2\rho$(bcp): 0.0353 *e*/Bohr^5; [*H*(bcp): 0.0012 Hartree/Bohr^3; *q*(Cl): 0.600 *e*; *q*(H^{29}): 0.058 *e*] in complex **35** both lie in the category of pure-closed shell interactions (i.e. only involve electrostatics) where the former is a repulsive and the later is attractive based on the relative QTAIM charges (refer to Table 5.7 in Appendix C.2).

To further elucidate steric effects, the size of the C^2-group was increased to CHMe$_2$, complex **36**, and a dramatic impact on the structure was observed, as now the *iso*-quinoline ligand has the C-ring out to the side of the *cis*-CO ligand (Figure 5.13). The Rh···H^{10} separation [2.868 Å] is now slightly longer than the longer variety of anagostic interactions (2.51–2.80 Å)[34] and the Rh···C^{10} is very long [3.248 Å] (Table 5.3).

In complex **36**, the ligand is clearly in a strained environment, as the *cis*-CO ligand bends slightly (3°) towards *trans*-CO ligand that has not seen before. Underneath the coordination plane, the isopropyl group orientates with the two-methyl groups facing the coordination plane, and one of the hydrogens makes a close approach to the metal centre [Rh···H^{32} separation: 2.492 Å]. In **36**, significant changes in the angles and torsions were seen compared with **34**. For instance, compared to **34**, the Rh–N–C angle is smaller [111.4° and 123.0° in **36** and **34**, respectively] and the OC^2(*cis*)–Rh–N–C torsion becomes significantly larger [114.6° and 67.7° in **36** and **34**, respectively] (Table 5.3). Due to significant changes in the angles in **36**, H^{10} now lies close to the *cis*-CO ligand [OC(*cis*)····H^{10} distance: 2.443; c.f. 3.492 Å in **34**]. Other than this, two close approaches are also found below the coordination plane between the Rh···H^{32} [2.492 Å] and OC(*cis*)···H^{35} [2.467 Å] (Figure 5.13). The QTAIM analysis (Table 5.4) shows a bond critical point between H^{10}····CO(*cis*) along with two more bond critical points for the Rh····H^{32} and OC(*cis*)·····H^{35} separations (Figure 5.14) in complex **36**. The QTAIM properties, for the H^{10} ⋯CO(*cis*) interaction [$\nabla^2\rho$(bcp): 0.0383 a.u.; *H*(bcp): 0.0013 a.u.; *q*(H^{10}) and *q*(C): 0.036 *e* and 0.932 *e*, respectively] indicate a repulsive interaction whereas for the Rh⋯⋯H^{32} interaction [$\nabla^2\rho$(bcp): 0.0431 *e*/Bohr^5; *H*(bcp): –0.0015 Hartree/Bohr^3; *q*(Rh) and *q*(H): 0.616 and 0.016 *e*, respectively], a transit-closed shell interaction which has an electrostatic component along with some covalency, is indicated (srefer to Table 5.6 in Appendix C.2).

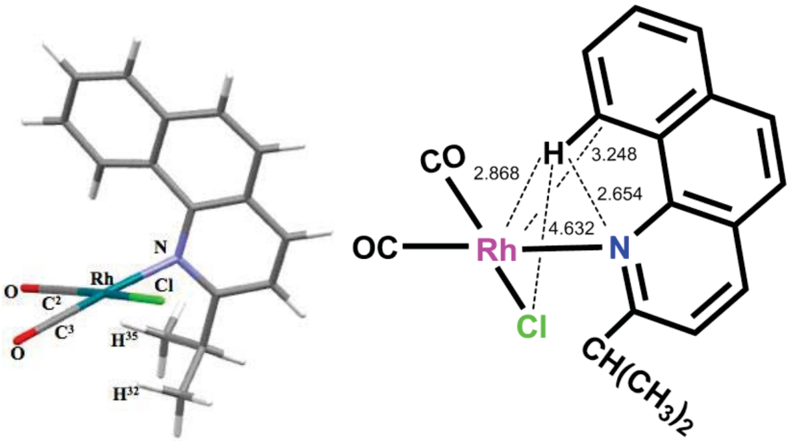

36

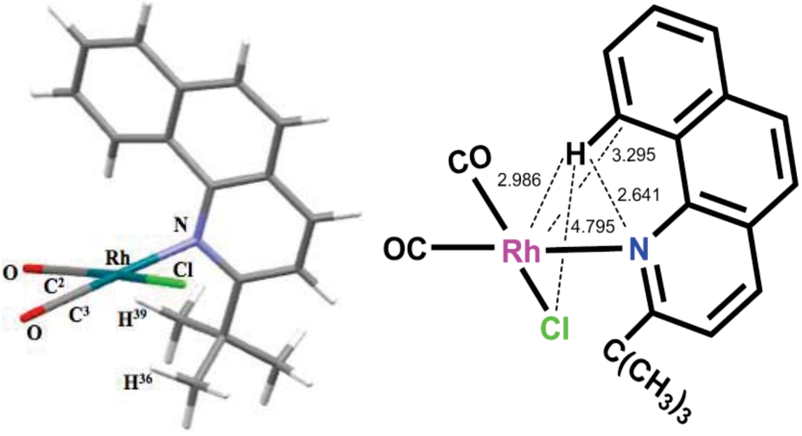

37

Figure 5.13 Optimised structures (left) and important separations (right) for complexes **36** and **37**.

The covalency component for the Rh⋯⋯H^{32} separation is then revealed by NBO analysis which shows very small agostic donations from the C–H^{32}σ to the Rh–C(*cis*)σ* and to the Rh–C(*trans*)σ* orbitals [*E*(2) values: 0.42 and 0.52 kcalmol^{-1}, respectively] and from LP(1) Rh to the C–H^{32}σ*orbital *[E*(2) value*:* 2.53 kcal mol^{-1}] which is the back-bonding component from the metal to the C–H antibonding orbital. The third bcp, which is for the OC(*cis*)⋯H^{35} interaction, has QTAIM parameters, indicating a purely electrostatic repulsive interaction [$\nabla^2\rho$(bcp): 0.0321 *e*/Bohr^5; *H*(bcp): 0.0009 Hartree/Bohr^3; *q*(C) and *q*(H): 0.932 and 0.005 *e*, respectively].

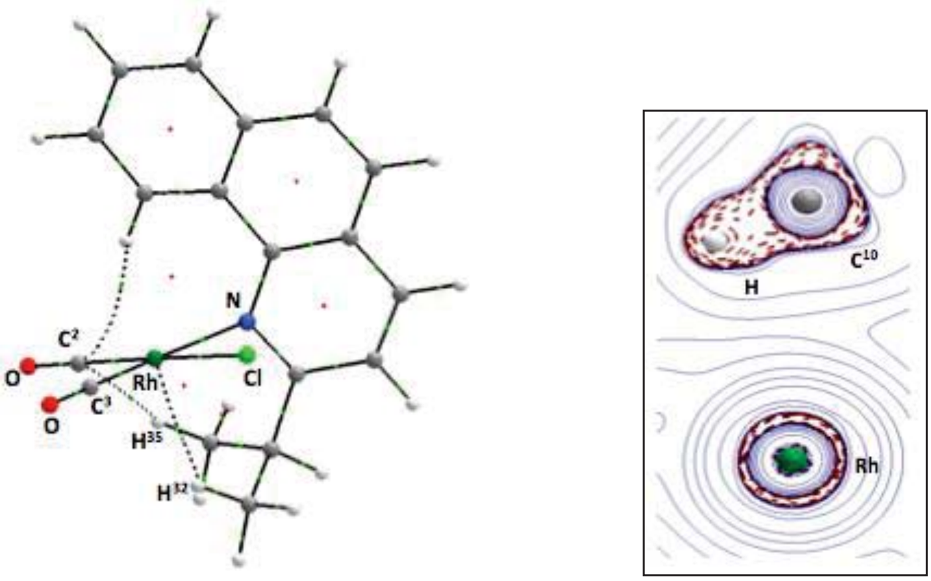

36

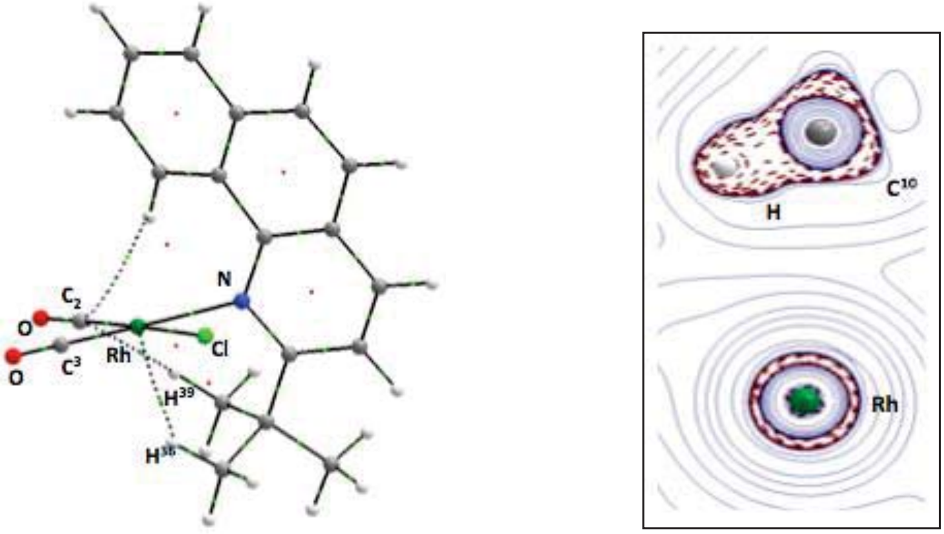

37

Figure 5.14 QTAIM molecular graphs (left) and Laplacian of electron density contour plots (for C–H^{10} and metal) (right) for **36** and **37**.

As there was no Rh···H^{10} bcp present in the QTAIM analysis of **36**, the NCI approach was used to understand whether an interaction between Rh and H^{10} did not exist or the bcp is missing because of coalescence of a bcp and ring critical point.[125] The 3D NCI reduced density gradient iso-surface plot of complex **36** (Figure 5.15) indicates a slightly blue-green area which shows that the interaction is not completely switched off and a weak electrostatic interaction might be present.

As a notable effect by an isopropyl group was seen at the R^3 position, it was then of further interest to see whether an increase in the size of the alkyl group at the C^2 position could further switch off the interaction. Thus, a *tert*-butyl group was placed at the R^3-position, complex **37**. The energy minimised structure of this complex shows that two of the t*ert*-butyl group methyls position underneath the coordination plane similar to isopropyl complex **36** so that the *iso*-quinoline ligand positions in a similar manner (Figure 5.13).

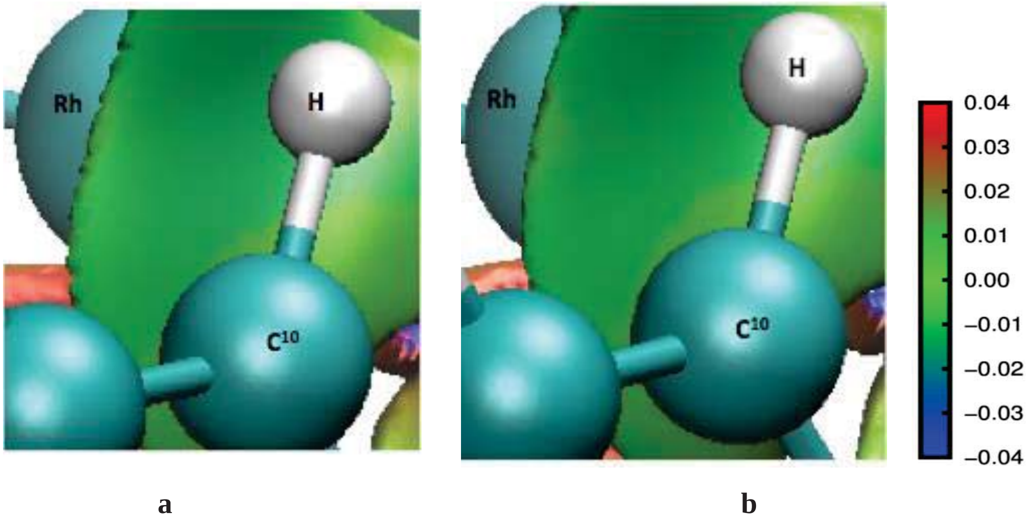

Figure 5.15 NCI iso-surfaces for the C–H interaction with the rhodium centre; a) [RhCl(CO)$_2$(2-isopropyl *benzo*-Quinoline)] (**36**); b) [RhCl(CO)$_2$(2-*tert*butyl *benzo* Quinoline)] (**37**). The sign of the second Hessian eigenvalue (λ_2) times the electron density (ρ) is shown by the color map.

However, the Rh···H^{10} separation is now longer in **37** than in **36** [Rh····H^{10} separations: 2.986 and 2.868 Å, respectively] (Figure 5.13) but the 3D NCI RDG iso-surfaces still indicate interactions are present as reduced density gradient (RDG) based NCI descriptor can show not only stabilising interactions but also weak interactions with a small amount of electron density[99] (Figure 5.15b). Similar to **36**, close separations below the coordination plane are also present in **37** [Rh···H^{36}: 2.395 Å; OC^2···H^{39}: 2.467 Å] (Figure 5.13) and QTAIM analysis also reveals the bcp for these separations. The nature and strength of these interactions are similar that seen in complex **36 (**refer to Table 5.7 in Appendix C.2 for QTAIM properties for below the place bcps).

The NBO data (Table 5.5) indicates a significant decrease in donation from the Rh LP to the C^9–$C^{10}\pi^*$orbital in **36** and **37** compared to **34** [*E*(2) values: 0.27, 0.51 and 1.04 kcal mol^{-1}, respectively]. The other donations are also smaller in **36** and **37** compared to **34**

(Table 5.5b). Spectroscopic properties (Table 5.3) for the C–H^{10} bond in **36** and **37** are also quite different compared to the other complexes as expected from the structural changes occurring. There is change in the chemical shift difference between the complex and the free ligand for the two complexes [the Δδ values for **36** and **37** are 0.20 ppm and –0.05 ppm respectively; c.f. Δδ: 1.86 ppm for **34**] which suggests that an anagostic interaction is absent in both these complexes (Table 5.3). The other spectroscopic properties show less change in **36** and **37** compared to **27** as there is a smaller decrease in the ^{1}JC–H coupling constant in **36** and **37** [values: 2.2 and 1.5 Hz, respectively; c.f. 3.0 Hz in **27**] and the IR stretching frequency instead of decreasing, is observed to increase in both complexes **36** and **37** compared to the ligands by 31 cm^{-1} and 27 cm^{-1}, respectively.

After seeing the dramatic effect of steric size at the R^{3} position of the *iso*-quinoline ligand, it was of interest to further manipulate the system and this was carried out by the addition of a phenyl ring at C^{2} as in complex **38**. In this case, the *iso*-quinoline ligand lies out to the side of the *cis*-CO ligand (Figure 5.16) but not nearly as much as in C^{2}-isopropyl or *tert*-butyl complexes **36** and **37** (Figure 5.13).

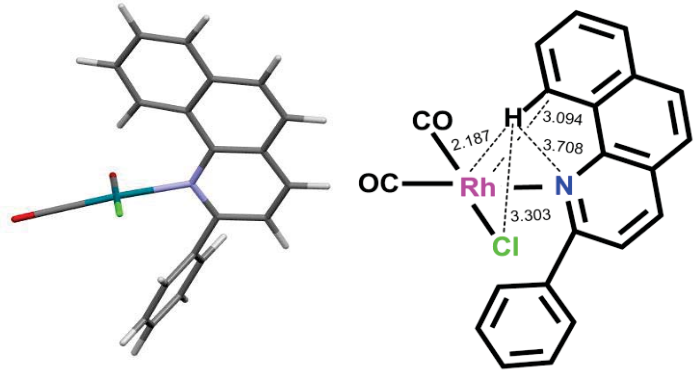

38

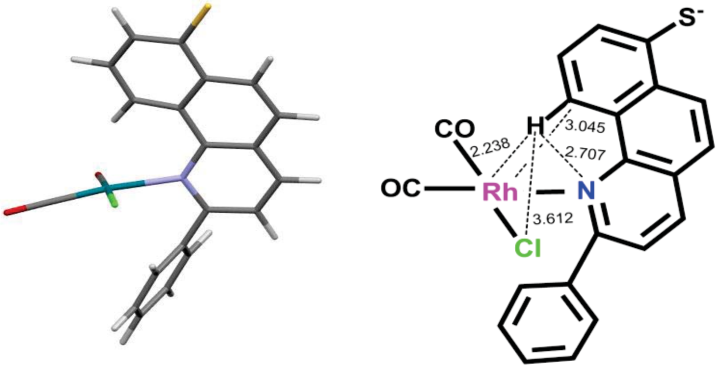

39

Figure 5.16 Molecular structures (left) and important separations (right) for **38** and **39**.

The Rh····H^{10} separation is now significantly shorter [2.187 Å] which is the closest separation achieved so far. This occurs without close contact of the metal with the C^{10} carbon [Rh····C^{10} separation: 3.094 Å], however, the other structural properties for the ligand indicate it in under much less stress (Table 5.3). In **38**, the phenyl group straightens the ligand up so that H^{10} lies right over the top of the metal. The notable changes in the structure are seen in the Rh–N–C angle which is now larger than in **37** [values: 127.1^{o} and 108.0^{o}, respectively; c.f. 127.8^{o} in **27**], the Rh····H^{10} –C^{10} angle becomes larger compared to other complexes so far [138.3^{o}; c.f. 96.7 and 125.8^{o} in **37** and **27**, respectively] (Table 5.3) and the C^{10b}–C^{10a}–C^{10}–H^{10} dihedral angle becomes slightly smaller at –0.48^{o} compared with **37** and **27** [–3.55^{o} and 2.94^{o}, respectively].

QTAIM analysis for **38** indicates a bond path and associated bcp for the Rh···H^{10} separation (Figure 5.19). The bcp properties (Table 5.4) such as the Laplacian of electron density is more positive [$\nabla^2\rho$(bcp): 0.0770 *e*/Bohr^5] and the energy density is more negative [*H*(bcp): –0.0045 Hartree/Bohr^3] than other complexes studied so far, which indicates a 'transit closed-shell' type interaction or otherwise an electrostatic interaction involving some covalency.[97] Interestingly, the NBO analysis reveals significantly greater back-donation from Rh LP's to the C–Hσ* orbital [LP(1) to C–Hσ* donation: 4.38 kcal mol^{-1}; LP(2) to C–Hσ* donation: 0.22 kcal mol^{-1}] compared to other complexes so far. The increase in donation from the metal to the C–Hσ* orbital is a feature of 'preagostic interactions', which have been categorised as electrostatic with partial covalency.[34] Looking at the driving force for the significant increase in the back-donation, it is surprising that the donor-acceptor energies for **38** are not very different to the other bulky steric group substituted complexes **36** and **37** [LP(1) Rh energies: –0.1756, –0.1740 and –0.1770 a.u., respectively; C–Hσ* energies; 0.3965, 0.4014 and 0.4057 a.u. respectively]. However, the spatial overlap matrices indicate a significant increase for **38** as the NBO overlap matrix value for LP(1) Rh to the C–Hσ* orbital is 0.2211 which can be compared to **27** [overlap matrix value: 0.1438] which has third largest *E*(2) value of 1.49 kcal mol^{-1}. Further, the spectroscopic parameters for the complex **38** are also quite different to the other complexes as the NMR chemical shift is significantly downfield by 2.88 ppm, ^{1}JC–H^{10} is 8.9 Hz lower and νC–H is 146 cm^{-1} to lower wavelength compared with the free ligand (Table 5.3). These features especially, the NMR parameters, are also relevant to preagostic type interactions.[34]

As shown in the molecular graph for complex **38** in Figure 5.19, there is also a bond path existing between C^{15} carbon and the rhodium atom. The QTAIM properties for the Rh····C^{15} interaction [$\nabla^2\rho$(bcp): 0.0496 *e*/Bohr^5; *H*(bcp): 0.011 Hartree/Bohr^3] and atomic charges [q(Rh) and q(C^{15}): 0.619 and –0.012 e, respectively] indicate a weakly attractive electrostatic interaction (refer to Table 5.7 in Appendix C.2).

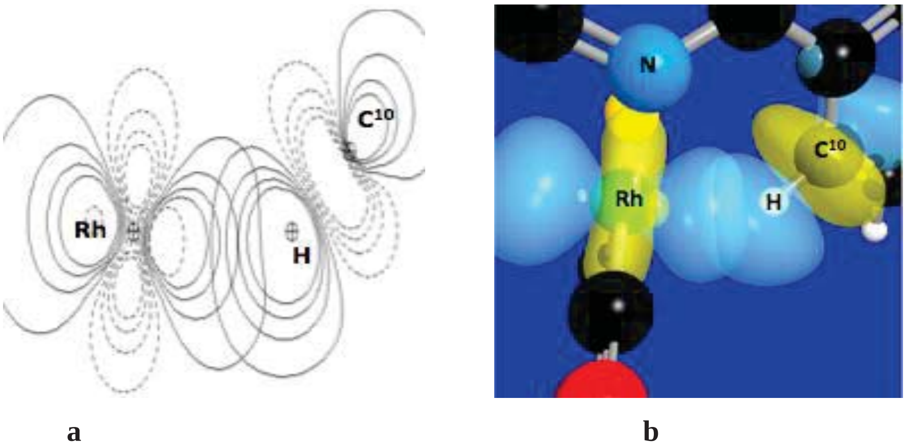

Figure 5.17 NBO diagrams for the Rh to C–H^{10}σ* [E(2) donation of 4.4 kcal mol^{-1}] in **38**; a) contour plot; b) 3D surface plot showing spatial overlap. (Outermost contour value: 0.0316 a.u.).[113]

The 3D NCI diagram (Figure 5.18) indicates a rounded blue spot between Rh and H^{10} which is evidence for a strongly attractive interaction in the region. As NCI is also a useful tool for covalent interactions along with non-covalent interactions,[99] thus now the combined picture of QTAIM, NCI, and NBO in **38** strengthens the evidence for a preagostic interaction.

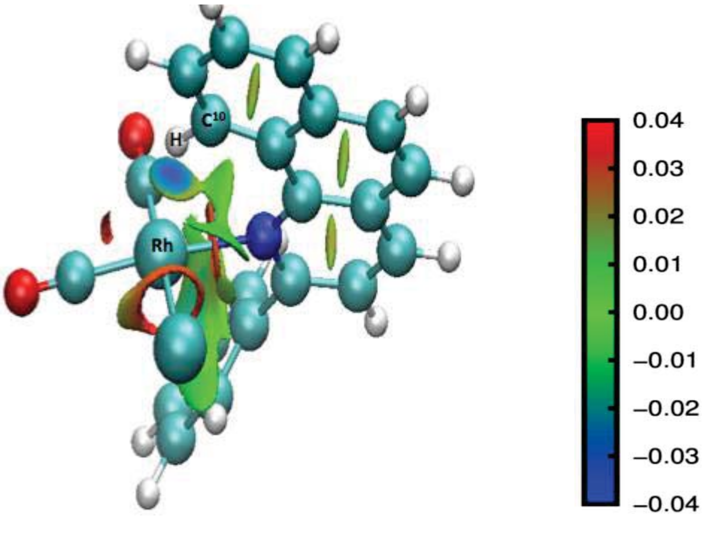

Figure 5.18 3D NCI RDG iso-surface diagram for complex **38**. The sign of the second Hessian eigenvalue (λ_2) times the electron density (ρ) is shown by the colour map.

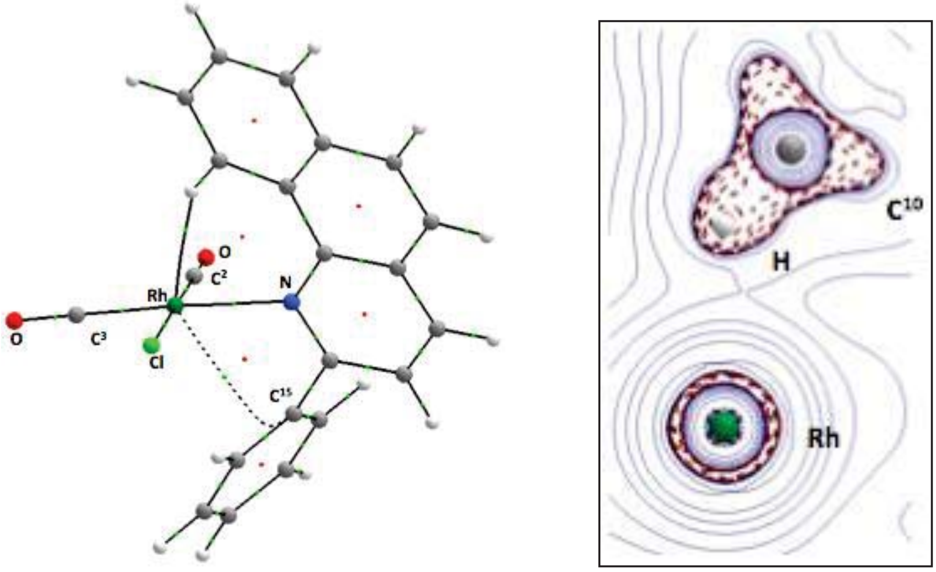

38

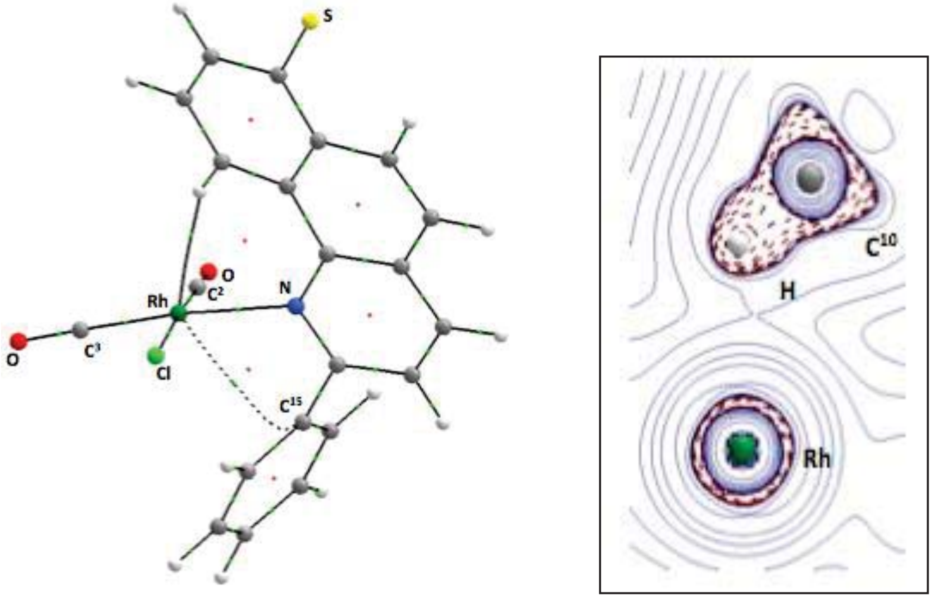

39

Figure 5.19 QTAIM molecular graphs (left) and Laplacian of electron density contour plots (for C–H^8 and metal) (right) for **38** and **39**.

As complex **38** contains the closest approach of the complexes studied so far [Rh···H^{10} separation: 2.187 Å] and back-donation relevant to the literature interpretation of a preagostic interaction,[34] was emerging, it was of interest to elucidate the effect of electronic changes on the interaction especially as to whether the agostic and back donations could be further enhanced. Thus the π-donor substituent S^- [106] was placed at the R^2 position (i.e. the position on the aromatic C ring *para*-to the anagostic C–H bond) as in complex **39**. In this case, the Rh····H^{10} separation increases to 2.238 Å from 2.187 Å in **38** (Table 5.3; Figure 5.16) and again the effect of increasing negative charge on carbon C^{10} [–0.046 and –0.008 *e* in **39** and **38**, respectively] (Table 5.4) comes into play with a decrease in the Rh····C^{10} separation occuring [3.045; c.f. 3.094 Å in **38**]. The Laplacian of electron density for Rh···H^{10} bcp is almost similar to **38** [$\nabla^2\rho$(bcp) values: 0.0777 and 0.0770 *e*/Bohr^5 in **39** and **38**, respectively] but energy density value is slightly smaller [*H*(bcp): –0.0028 and –0.0045 Hartree/Bohr^3 in **39** and **38**, respectively]. The Laplacian contour plots for the C–H····M interaction in **39** (Figure 5.19) are almost similar to **38** which shows some accumulation of charge density between the metal and the H^{10} which is an indication of some covalency involved in the interaction.[51]

The QTAIM molecular graph for **39** (Figure 5.19) also reveals a similar kind of electrostatic attractive interaction between Rh and carbon C^{15} of the substituted phenyl group with properties [$\nabla^2\rho$(bcp): 0.0454 *e*/Bohr^5; H(bcp): 0.0011 Hartree/Bohr^3; *q*(Rh) and *q*(C): 0.639 and -0.002 *e*, respectively] (refer to Table 5.7 in Appendix C.2).

The NBO analysis (Table 5.5) shows a decrease in the back-donation in **39** [*E*(2) values for Rh LP(1) to the C–$H^{10}\sigma^*$ orbital: 2.62; c.f. 4.38 kcal mol^{-1} for **38**]. The NMR chemical shift is less downfield [$\Delta\delta$: 1.88 ppm; c.f. 2.88 ppm for **38**], however the decrease in the ^1JC–H^{10} coupling constant is almost similar to that in **38** compared to the respective ligands [Δ^1JC–H^{10}: 8.9 Hz; c.f. 8.0 Hz in **38**] (Table 5.3). The vibrational frequency for the C–H^{10} bond in **39** decreases by 87.1 cm^{-1} compared to the free ligand which is much less in comparison to complex **38** where the decrease was 146.0 cm^{-1} (Table 5.3).

Continuing with electronic manipulation, S^- and NH_2 substituents were added at C^7 or the R^2 and C^9 or R^1 positions as in complex **40** and in this case Rh····H^{10} separation increases further to 2.280 Å [c.f. 2.238 Å for **39**) Figure 5.20) (Table 5.3) even though the H-atomic charge is essentially the same as in S^- complex **39** [*q*(H): 0.004 and 0.005 *e*, respectively] (Table 5.4). However, as expected with the increase in negative charge on C^{10} [*q*(C) values: –0.064, –0.046 and –0.008 *e* for **40**, **39** and **38**, respectively], there are various changes to the angles that come into play. In particular, the N–C^{10b}–C^{10a}–C^{10} torsion angle flattens a little [–16.4° and –12.5° in **40** and **39**, respectively] and the C–H bond is deformed slightly more [5.1 and 2.0° in **40** and **39**, respectively]. The most significant change is seen in the C^{10b}–C^{10a}–C^{10}–H^{10} torsion angle in **40** compared to **39** and **38** [values: –13.74, –4.63 and –0.48°, respectively]. The QTAIM properties (Table 5.4) for the Rh···H^{10} bcp lie in the category of an electrostatic interaction with partial covalency [$\nabla^2\rho$(bcp) and *H*(bcp): 0.0816 *e*/Bohr^5 and –0.0016 Hartree/Bohr^3, respectively].

In **40**, the Rh····C^{10} separation is shorter compared with **39** and the NBO analysis shows a slightly larger donation from the metal to the C^{10}–$C^{10a}\pi^*$ orbital [*E*(2) values: 1.17

and 0.55 kcal mol^{-1}, respectively] and with the flattening out of the C-ring of the ligand, the agostic donation also increases a little [*E*(2) values: 0.69 and 1.76, respectively in **40**; c.f. 0.67 and 1.54 kcal mol^{-1} in **39**, respectively] (Table 3.5b) but back-donation from the metal to the C–Hσ* orbital is less prominent [*E*(2) values: 1.42 and 0.31, respectively in **40**; c.f. 2.62, 0.31 kcal mol^{-1}, respectively]. It should again be remembered here that the *E*(2) values are not particularly large and do not represent any major bonding contributions but rather point to some emergence of bonding components. The NMR and IR spectroscopic data for the C–H^{10} bond are very similar to **39** (Table 5.3), but in **40**, there are decreases in the ^{1}JC–H coupling constant **[**5 Hz; c.f. 8 Hz in **39**], in υC–H [50 cm^{-1}; c.f. 88 cm^{-1} in **39**] and the H^{10} chemical shift [Δδ: 1.73 ppm; 1.88 ppm in **39**] compared with the respective free ligands.

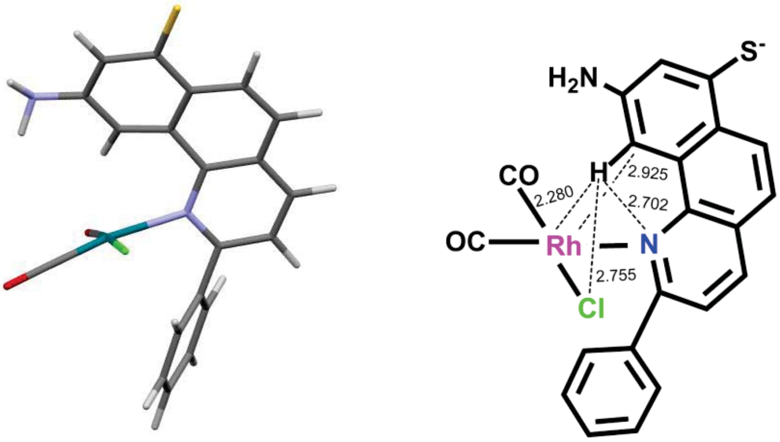

40

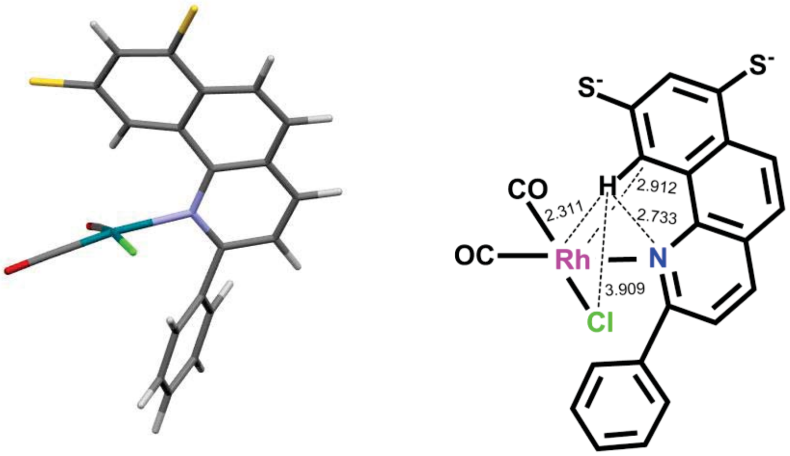

41

Figure 5.20 Molecular structures (left) and important separations (right) for **40** and **41**.

As similarly found for **38** and **39**, the QTAIM molecular graph for **40** shows a bcp between the substituted phenyl carbon, C^{22}, and Rh (Figure 5.21) but now the carbon involved in the interaction is not the same as was seen in **38** and **39**. However, the QTAIM properties for the new Rh···C^{22} bcp are not much different than in **38** and **39** [$\nabla^2\rho$(bcp) and H(bcp) values: 0.0401 e/Bohr^5 and 0.0011 Hartree/Bohr^3, respectively; q(Rh) and q(C) values: 0.633 and –0.019 e, respectively] indicate an electrostatic attractive interaction, especially the atomic charges (refer to Table 5.7 in Appendix C.2).

A small increase in the donation from a Rh LP to the C^{10}–$C^{10a}$$\pi$*orbital was seen in **40**, so therefore to see whether this donation or any of the others could be further enhanced, S^- substituents were placed at both the R^1 and R^2 positions of the ligand, as in complex **41**. The energy minimised structure shows a larger C-ring flattening with the N–C–C–C^{10} torsion angle increasing to –20.4^o [c.f. –16.4^o and –12.5 in **39** and **40**, respectively] and there is also an increase in the C–H^{10} deformation angle to 5.7^o compared to **40** and **39** [5.1 and 2.0^o, respectively]. Comparing complexes **41** and **40**, the Rh····H^{10} separation lengthens [2.311 and 2.280 Å, respectively] but the Rh····C^{10} separation decreases a little [2.912 and 2.925 Å, respectively] (Table 5.3). These changes occur when the H^{10}-atomic charge becomes more positive in **41** [q(H^{10}) values: 0.014 and 0.004 e, respectively] whereas the C^{10} atomic charge becomes less negative [q(C^{10}) values: –0.048 and –0.064 e, respectively] (Table 5.4). NBO analysis (Table 5.5) shows a very small and possibly negligible increase in donation from Rh LP to the C^{10}–$C^{10a}$$\pi$*orbital in **41** [$E$(2) values: 1.31; c.f. 1.17 kcal mol^{-1} in **40**].

The QTAIM properties for the Rh···H^{10} bcp (Figure 5.21) are slightly different compared to **40** [$\nabla^2\rho$(bcp) and H(bcp) values: 0.0798 e/Bohr^5 and –0.0010 Hartree/Bohr^3, respectively; c.f. 0.0816 e/Bohr^5 and –0.0016 Hartree/Bohr^3 in **40**] (Table 5.4) but the changes are very small and are hardly significant. In **41**, there is also an attractive interaction existing between phenyl C^{22} carbon and Rh with almost similar QTAIM properties as were observed in complex **40** [$\nabla^2\rho$(bcp) and H(bcp) values: 0.0431 e/Bohr^5 and 0.0013 Hartree/Bohr^3, respectively; q(Rh) and q(C^{22}) values: 0.657 and –0.025 e, respectively]. Overall, the structural and bonding properties in complex **41** are not much different to those seen in **40**.

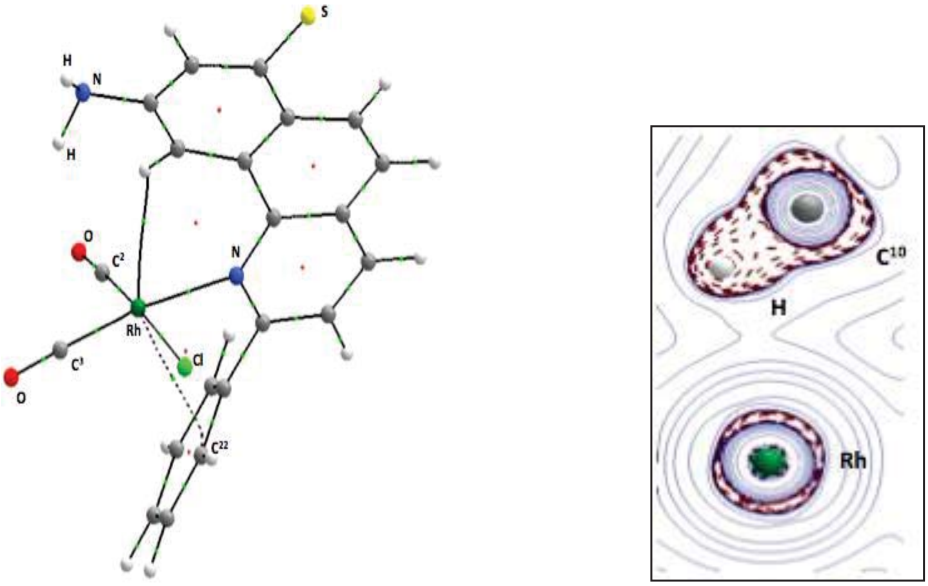

40

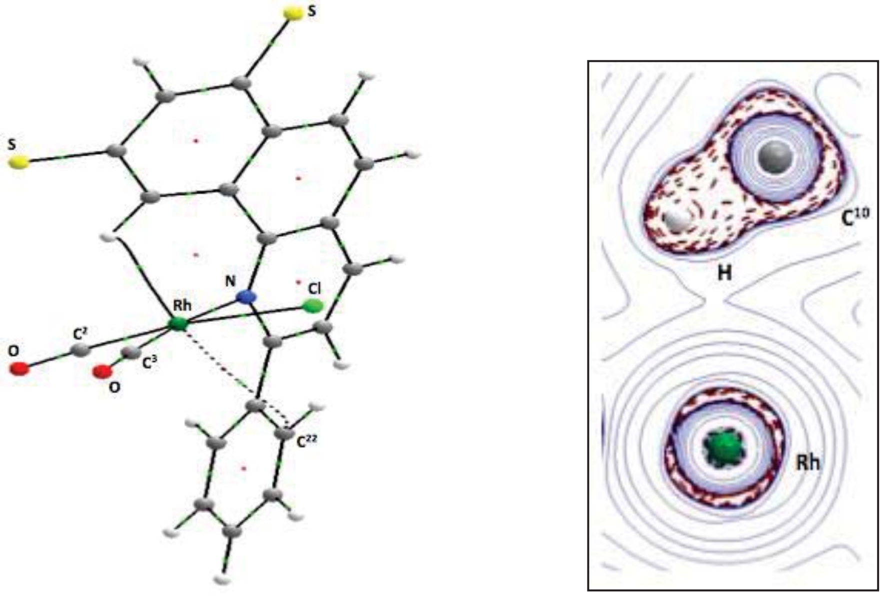

41

Figure 5.21 QTAIM molecular graphs (left) and Laplacian of electron density contour plots (for C–H^{10} and metal) (right) for **40** and **41**.

5.6 Conclusion

It has been shown that for the *iso*-quinoline ligand which might be expected to show limited flexibility due to the aromatic ring junctions, distortion of the planar ring system does take place to accommodate the H^{10} hydrogen over the metal sphere. All the reported interactions have mainly electrostatic components and the inflexible nature of the *iso*-quinoline ligand only favours an H-anagostic type interaction and not a C-anagostic interaction which was evident with the flexible 1-tetralone ligands in complexes studied in chapter 3. Also, it is seen that with the inflexible *iso*-quinoline system, the electronic effects *para* to the anagostic H^{10} hydrogen are not as influential as were observed with the more flexible 1-tetralone system (Chapter 3).[126] However, the strongest π-electron donating substituent S^{-} at the *para*-position significantly influences the donor-acceptor energies which favours some covalency in the interaction (i.e. complexes **31**–**33** and complex **35**). It is also seen that steric effects at the C^2 carbon can significantly influence the $Rh\cdots\cdot H^{10}$ interaction. In this regard, the isopropyl (complex **36**) and *tert*-butyl (complex **37**) groups at C_2 change the interaction by placing the $C–H^{10}$ group on the other side of the metal coordination plane. However, with a phenyl ring at the C^2 position of aromatic ring A (complex **38**) there is a somewhat more favourable spatial overlap between the Rh metal and C–Hσ* antibonding NBOs which results in some small amount of covalency developing indicated so that the nature of the interaction now lies more into the preagostic category.

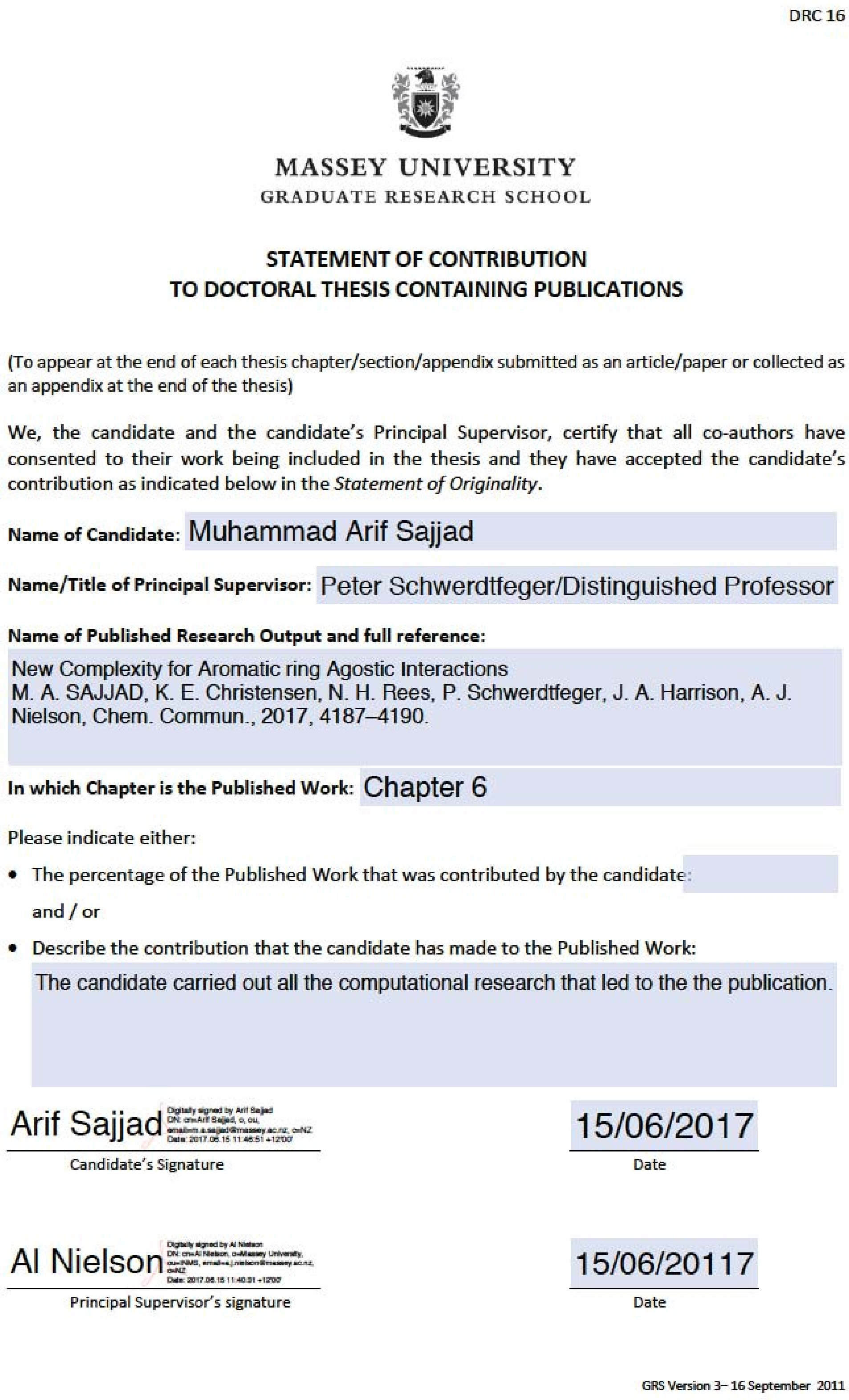

DRC 16

MASSEY UNIVERSITY
GRADUATE RESEARCH SCHOOL

STATEMENT OF CONTRIBUTION TO DOCTORAL THESIS CONTAINING PUBLICATIONS

(To appear at the end of each thesis chapter/section/appendix submitted as an article/paper or collected as an appendix at the end of the thesis)

We, the candidate and the candidate's Principal Supervisor, certify that all co-authors have consented to their work being included in the thesis and they have accepted the candidate's contribution as indicated below in the *Statement of Originality*.

Name of Candidate: Muhammad Arif Sajjad

Name/Title of Principal Supervisor: Peter Schwerdtfeger/Distinguished Professor

Name of Published Research Output and full reference:

New Complexity for Aromatic ring Agostic Interactions
M. A. SAJJAD, K. E. Christensen, N. H. Rees, P. Schwerdtfeger, J. A. Harrison, A. J. Nielson, Chem. Commun., 2017, 4187–4190.

In which Chapter is the Published Work: Chapter 6

Please indicate either:

- The percentage of the Published Work that was contributed by the candidate:

  and / or

- Describe the contribution that the candidate has made to the Published Work:

  The candidate carried out all the computational research that led to the the publication.

Arif Sajjad Digitally signed by Arif Sajjad
DN: cn=Arif Sajjad, o, ou,
email=m.a.sajjad@massey.ac.nz, c=NZ
Date: 2017.06.15 11:46:51 +12'00'

Candidate's Signature

15/06/2017

Date

Al Nielson Digitally signed by Al Nielson
DN: cn=Al Nielson, o=Massey University,
ou=INMS, email=a.j.nielson@massey.ac.nz,
c=NZ
Date: 2017.06.15 11:40:31 +12'00'

Principal Supervisor's signature

15/06/20117

Date

GRS Version 3– 16 September 2011

Chapter 6

Steric and Electronic Manipulation of Agostic interaction in Oxime and Imine Complexes of Palladium (II)

6.1 Introduction

Transition-metal catalysed C–H functionalisations, driven by cyclometallation reactions, where a new metal-carbon (M–C) σ bond forms after cleavage of a C–H bond attached to an aryl or alkyl ligand, have received special attention in organometallic chemistry. By using the cyclometallation approach, a wide range of products, such as pharmaceuticals, natural products and luminescent materials can be obtained.[9-10,101] The product after a cyclometallation reaction is a metallacycle in the form of a heterocyclic ring where other functional groups can be inserted and new C–X functionalities can be achieved.[10] One of the main features of cyclometallation reactions is the selective C–H bond functionalisation where metal is coordinated with the pre-existing directing groups containing heteroatoms like nitrogen, oxygen, phosphorous and sulfur, etc, which assist the C–H bond interaction with the metal.[10,103,129] However, it has been known that the nature of the directing groups is important as sometimes the thermal stability of the developed M–C bond in the metallacycle, in the case of N-donor ligands can prevent post-functionalisation reactions. It has also been seen that weakly coordinating O-donor ligands form less-stable metallacycles in which the metal-carbon bond is more reactive. Therefore, the design of the ligand in cyclometallation driven C–H functionalisation reactions is one of the crucial components along with selection of the metal and precursors.[130]

Most C–H functionalisation reactions are performed by a bench-synthesis approach where the mechanistic investigation of the intermediates is not a common routine. Therefore, a proper investigation of the reaction intermediates in terms of the factors influencing their formation, stability and reactivity could be highly advantageous in understanding C–H functionalisation reactions and for developing new synthetic routes and methodologies.[131]

A key step in any cyclometallation reaction is the weakening of the C–H bond in a partially covalent interaction, known as the agostic interaction, in which C–H σ bond donates electron density to the metal.[28,35,41,132] Later, an anionic base ligand such as Cl^- or AcO^- assists in the removal of the hydrogen. Despite the fact that characterisation of the agostic interaction has been described in the literature,[28,35,41,132] studies on how steric and electronic effects influence the bonding components of this important interaction are still missing. A deeper understanding of these effects can be very useful in understanding cyclometallation reactions.[10]

In the present work, DFT studies have been carried out to uncover the bonding complexity for the agostic interaction when electronic and steric groups have been placed on the aromatic ring of the substrates used for the cyclometallation reactions. The choice of electronic group is based on σ- or π-electron donating or withdrawing properties as described in Hammett-protocol (Table 6.1).[106]

Table 6.1 Electron withdrawing and donating groups used in the present work.[106]

	σ_m	σ_p	F	R
Electron withdrawing groups				
SO_2Cl	1.20	1.11	1.16	–0.05
$N{=}NPO(OCH_2CH_3)_2$	0.16	0.74	–0.05	0.79
Electron donating groups				
$B(OH)_3^-$	–0.48	–0.44	–0.42	–0.02
S^-	–0.36	–1.21	–0.03	–1.24

σ_m = Electronic influence at *meta* position
σ_p = Electronic influence at *para* position
F = Electronic effect at sigma-bond
R = Electronic effect at pi-bond
(Negative and positive signs for the values are associated with the electron donating and electron withdrawing effect, respectively)

As a strategy for uncovering the nature of the interactions in the present study, first the geometries of the various agostic complexes were optimised (Scheme 6.1) and then to important metrics compared for the structural features. Then, spectroscopic data was computed to give an initial indication of the change in properties, to relate to experimental studies, followed by in-depth analysis of the interactions using QTAIM and NBO analysis. This type of approach to understanding underlying fundamentals greatly reduces the need for bench synthesis.[35,54]

Scheme:

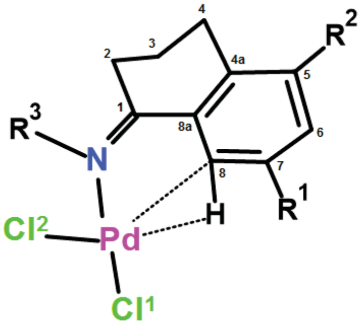

42) $R^1 = R^2 = H, R^3 = OH$
43) $R^1 = R^2 = H, R^3 = OMe$
44) $R^1 = R^2 = H, R^3 = CMe_3$
47) $R^1 = H, R^2 = SO_2Cl, R^3 = OH$
48) $R^1 = H, R^2 = N_2PO(OEt)_2, R^3 = OH$
49) $R^1 = H, R^2 = B(OH)_3^-, R^3 = OH$
50) $R^1 = H, R^2 = S^-, R^3 = OH$
51) $R^1 = R^2 = S^-, R^3 = OH$
52) $R^1 = Me, R^2 = H, R^3 = OH$
53) $R^1 = CHMe_2, R^2 = H, R^3 = OH$
54) $R^1 = CMe_3, R^2 = H, R^3 = OH$
55) $R^1 = H, R^2 = SO_2Cl, R^3 = OMe$
56) $R^1 = H, R^2 = N_2PO(OEt)_2, R^3 = OMe$
57) $R^1 = H, R^2 = B(OH)_3^-, R^3 = OMe$
58) $R^1 = H, R^2 = S^-, R^3 = OMe$
59) $R^1 = CMe_3, R^2 = H, R^3 = CMe_3$
60) $R^1 = CMe_3, R^2 = SO_2Cl, R^3 = CMe_3$
61) $R^1 = CMe_3, R^2 = B(OH)_3^-, R^3 = CMe_3$
62) $R^1 = CMe_3, R^2 = S^-, R^3 = CMe_3$
63) $R^1 = R^2 = S^-, R^3 = CMe_3$

45)

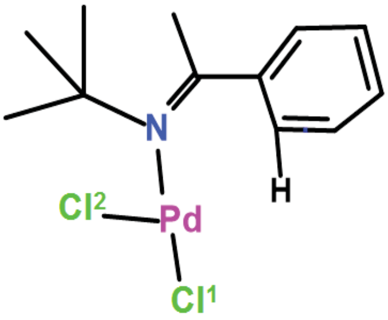

46)

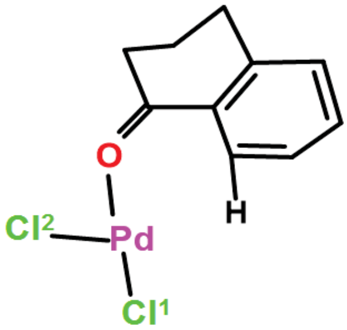

64)

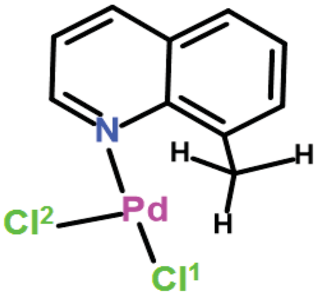

Scheme 6.1 Structure of the computed complexes.

6.2 Aim

- To manipulate by steric and electronic effects the agostic interaction in 1-tetralone oxime and imine complexes of palladium (II).

6.3 Computation Approach

The 'synthesis by computation' approach[54,126,133] was used to optimise the geometries of the coordination complexes employing the dispersion corrected Grimme PBE-D3 functional[76,77] using the G09 software.[108] A triple-zeta high quality basis set (aug-cc-pVTZ-PP)[111] was used for Pd; aug-cc-pVTZ[95] for the attached ancillary ligands (CO and

Cl) and the agostic hydrogen atom and a double-zeta quality basis set (aug-cc-pVDZ)[95] was used for the remainder of the atoms. All the optimised structures were energy-minimised as no imaginary frequency was found in the vibrational analysis. The NBO calculations were performed by NBO 6.0 software,[113] and NBOVIEW version 2.0[113] was used to visualise the contours and surfaces of donor-acceptor interactions. For the QTAIM analysis, the extended wavefunction (.wfx) input files were generated by Gaussian09[108] and QTAIM calculations were performed with the AIMALL software.[112] For the non-covalent interaction index analysis (NCI), the NCIPLOT 2.0 software[99] was used to obtain the three-dimensional NCI surfaces,[99] and the VMD program[114] was used to visualise the NCI surfaces. The same procedure was used for the ligand calculations. The same basis sets were used for the NMR spectral calculations, however, for coupling constant ^1JC–H calculations, the basis set was decontracted for the agostic carbon C^8 and hydrogen H^8 to allow more flexibility of electron density around the nucleus.

6.4 Results and Discussion

6.4.1 Computational Characterisation of the Agostic Interaction in [PdCl$_2$(1-tetralone oxime)], Complex 42

The optimised geometries for the palladium (II) complexes of the [PdCl$_2$(L)] (L = 1-tetralone oxime and imine) series (Scheme 5.1) where the C^8–H bond (*ortho*-hydrogen) positions towards the metal centre in such a way that an agostic interaction can develop, were obtained by using the DFT PBE-D3 functional. An earlier synthetic study indicates an upfield chemical shift for the hydrogen of the C–H^8 group in a Pd-tetralone oxime complex which was evidence of an agostic interaction. However, due to instability problems in the crystallisation process, there was no X-ray structure obtained for the intermediate.[124]

In the present work, the dispersion-corrected PBE-D3 functional was again employed as it includes dispersion factors, which are necessary for a correct description of weak interactions.[76,77] In the earlier study of anagostic interactions on the 1-tetralone framework ligands (Chapter 3),[126] testing of popular DFT functionals was done and it was found that PBE-D3 and BP86 give similar results, but due to the necessity of including dispersion factors for the weak interaction,[76] the PBE-D3 functional was used. Other studies on anagostic and agostic interactions also endorse the use of the PBE-D3 functional.[66,134] Therefore, in the current computational study the PBE-D3 functional is employed.

Turning towards characterisation of the agostic interaction in the [PdCl$_2$(1-tetralone oxime)] complex **42**, which is an intermediate formed by the cyclometallation reaction of the 1-tetralone oxime ligand and $PdCl_4^{2-}$,[124] the optimised structure (Figure 6.1a) shows that the oxime ligand coordinates to the metal in such a way that the C^8–H bond positions in the coordination plane *trans* to the Cl^2 ligand. With this orientation, H^8 lies more in the coordination plane while C^8 positions over the metal with a Cl^1 –Pd···C^8 angle of 166.3°. The separations achieved for Pd····C^8, and Pd···H^8 [2.240 Å and 1.819 Å, respectively] with the Pd···H–C angle of 95.2° are in the range of agostic interactions (Table 6.2).[28,35,41] In comparison with the ligand structure, there were some noticeable changes observed in the complex. For instance, the alicyclic ring changes conformation from chair-like in the free ligand to boat-like in the complex, similar to what was seen in the anagostic rhodium complexes (Chapter 3). The other factor is the weak hydrogen bonding between the ancillary ligand Cl^1 and the (N)–OH group [(N)–OH···Cl distance: 2.092 Å]. In complex **42**, with the Pd–N=C bond rotation angle at 120.0°, the benzene ring lies at a plane angle of 34.5° to the palladium coordination plane. The dihedral angles of N=C^1–C^{8a}–C^8, C^1–C^{8a}–C^8–H^8 and H^7–C^7–C^8–H^8 (C–H deformation) are 15.1°, 38.2° and –27.2°, respectively and these changes occur when H^8 bends away from the plane and tries to accommodate the clash with the metal. One of the major features of the agostic interaction is the lengthening of the C–H bond[28,35] and in the complex **42**, there is a lengthening of the C–H bond to 1.152 Å compared with 1.090 Å for the free ligand. The C–H bond length in the complex is within the range (1.13–1.19 Å) for agostic C–H groups.[28,35] X-ray crystallographic studies indicate both C–H bond lengthening and deformation for the complexes showing aromatic ring agostic interactions.[135]

Calculated spectroscopic properties indicate an upfield chemical shift of 1.54 ppm for the H^8 hydrogen in the complex, compared with ligand **42** (Table 6.2). The upfield chemical shift for the hydrogen upon formation of the agostic interaction has been used as a crucial indicator and is known to arise from the anisotropic environment around the metal centre.[136] However, a recent study shows that the extent of the shift can not be related to the interaction strength as the equatorial electron density about the metal can vary.[121]

Spectroscopic properties that relate to the interaction strength are associated with the donation of electron density from the C–H bond to the metal. When this occurs there should be a significant decrease in the coupling constant, ^1JC–H and stretching frequency, νC–H in the complex compared with the ligand.[28,35] For complex **42**, a significant decrease occurs in the ^1JC–H in comparison to the free ligand [103.0 and 139.4 Hz, respectively] and the C–H stretching frequency shifts to lower energy by 670 cm^{-1} [νC–H values for the complex and free ligand: 2462.8 cm^{-1} and 3133.3 cm^{-1}, respectively].

Examining the bonding characteristics, QTAIM analysis indicates a bond path between the metal and H^8 (Figure 6.1b) and bond critical point properties for Pd····H^8 indicate an agostic interaction. The common features for the agostic interaction, in the context of QTAIM, are the ρ(bcp) [value range: 0.04–0.05 e/Bohr^3] and $\nabla^2\rho$(bcp) [value range: 0.15–0.25 e/Bohr^5].[52] The QTAIM properties for the Pd····H^8 bcp (Table 6.3) lie in the agostic interaction range as values for the electron density [ρ(bcp): 0.0820 e/Bohr^3] and Laplacian of the electron density [$\nabla^2\rho$(bcp): 0.2631 e/Bohr^5] both indicate an electrostatic type interaction, but the slightly negative energy density [H(bcp) value: –0.0210 Hartree/Bohr^3] and a value above 1 for |V|/G (|V| = absolute potential energy density, G = kinetic energy density) indicate some covalency is also involved. It is established that a positive Laplacian of the electron density, negative energy density, and |V|/G (value > 1 < 2) show a transit-closed shell type interaction which is on the way to covalency.[52,137] The two-dimensional contour plot of the Laplacian of the electron density (Figure 6.1c) shows some accumulation of the charge density as indicated as the contour lines of the C–H bond and the metal are very close together. In comparison with the free ligand, the C–H bond electron density in the complex is reduced [ρ(bcp) values: 0.2333 and 0.2810 e/Bohr^3 complex and free ligand, respectively], the Laplacian of the electron density is less negative [–0.6268 e/Bohr^5; c.f. –0.9458 e/Bohr^5 for free ligand] and the ellipticity is increased [0.1059; c.f. 0.1026 for free ligand]. All these features indicate a weakening of the C–H bond strength due to delocalisation of the electron density onto the metal.[41] It is noted that the ellipticity at the bcp of the Pd···H bond path is very large [ε(bcp): 5.3365] which shows strain in the bond, making it less stable, however, it is known that the larger bond ellipticities for agostic interactions at the M···H bcp can provide a qualitative measure of the delocalisation within the QTAIM framework.[41]

The QTAIM atomic basin properties for H^8, C^8, and Rh also comply well with that expected for an agostic interaction. Compared with the free ligand, the charge on H^8 becomes slightly positive [q(H) values: 0.056 and 0.040 e in the complex and free ligand, respectively]; the total atomic energy becomes more negative [E(H) values: –0.631 and –0.609 a.u., respectively]; the dipolar polarisation becomes slightly less positive [M(H) values: 0.099 and 0.126 a.u., respectively] and the atomic volume decreases significantly [V(H) values: 36.0 and 46.5 a.u., respectively]. The atomic charge on carbon C^8 becomes more negative compared with the free ligand [q(C) values: –0.084 e and 0.001 e, respectively].

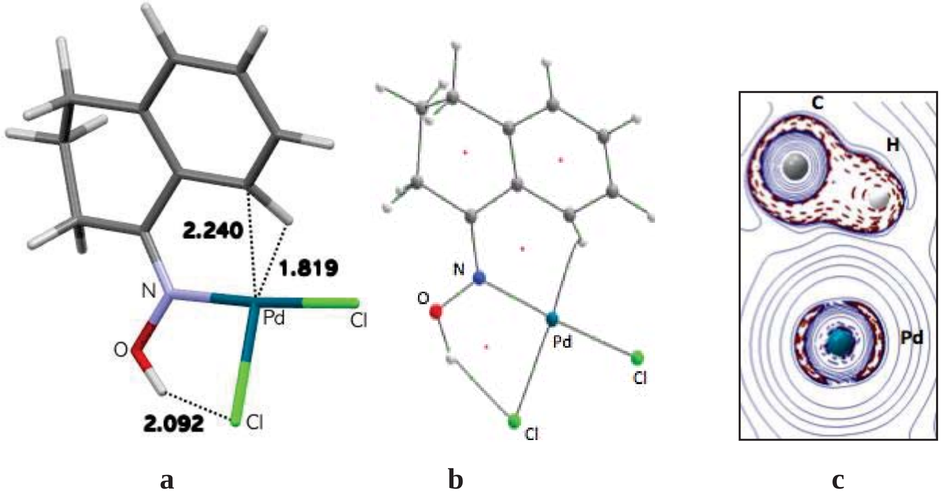

Figure 6.1 a) Optimised geometry and important separations (Å); b) QTAIM molecular graph showing bond paths for $H^8\cdots$Pd and OH$\cdots$Cl separations; c) 2D contour plot of the Laplacian of the electron density for C–H^8 and Pd interaction for complex **42**.

Based upon the atomic basin charges, the agostic hydrogen H^8 atom would form a repulsive interaction with metal [q(H) and q(M) values: 0.056 and 0.641 *e*, respectively] and the carbon C^8, which is negatively charged, will have a weak attractive interaction with the metal [q(C) and q(M) –0.084 and 0.641 *e*, respectively] (Table 6.3). With this electrostatic situation, the bending of the hydrogen atom away from the metal centre appears to be driven by the repulsive electrostatic situation.

NBO analysis which is based on a valence bond approach to bonding is used to quantify the donor-acceptor interactions in chemical systems.[98] NBO analysis measures the C–H bond electron delocalisation in an agostic interaction by evaluating the second order perturbation energy, *E*(2), between overlapping NBOs. The larger the *E*(2) value, the stronger is the interaction.[98]

For **42**, the NBO analysis shows two agostic donations from C–Hσ to Pd–Cl_{trans}σ* and Pd–Cl_{cis}σ* NBOs, with *E*(2) values 58.60 and 10.0 kcal mol^{-1}, respectively (Table 6.4) (Figure 6.2a,b). In addition, there are small back bonding donations from the metal to the C–Hσ* antibonding NBO [*E*(2) value for LP(3) Pd and LP(4) Pd to C–Hσ*: 2.85 and 4.87 kcal mol^{-1}, respectively] (Figure 6.2e,f). The agostic donation from C–H to Pd–Clσ* bond is clearly significantly stronger than the back-donation. Surprisingly, the NBO analysis also indicates strong donations from C^7–C^8π to Pd–Cl_{trans}σ* and Pd–Cl_{cis}σ* [*E*(2) values: 20.33 and 6.48 kcal mol^{-1}, respectively] (Figure 6.2c,d). The larger donations from C^7–C^8π to metal have not been previously reported in the literature, despite only weak electrostatic interaction [q(C) and q(M) values: –0.084 and 0.641 *e,* respectively], these donations still provide a clip for the agostic interaction and is termed 'syndetic' which means 'serving to unite' from the Greek word syndetikos or sundeo (sunde´u).[29,30] Thus, the agostic interaction is not fixed only by the C–H bond donation to the metal but, in this case, other components also contribute to it, making the interaction more complex than previously thought. The interaction of the C^7–$C^8\pi$ NBO in the aromatic ring with the metal potentially has consequences for the formation of the metal-carbon bond during cyclometallation reactions.[100] To further analyse the agostic interaction, the C–H^8 occupancy in the complex decreases to 0.1311 *e* [C–Hσ occupancy in complex and ligand: 1.8457 and 1.9768 *e*, respectively] which indicates donation of electron density to the metal centred orbitals.

The Wiberg bond index for the C–H bond, which is an indication of the strength of the interaction,[98] shows a decrease of 0.1491 in the complex compared with the ligand [values: 0.7615 and 0.9106, respectively) which further verifies a weakening of the C–H bond in the complex as a result of the loss of electron density.[133] It is noted that the Wiberg bond index value for the Pd···C separation is greater than for the Pd···H separation which shows a building up of a Pd–C covalency [Wiberg bond index values for the Pd···C and Pd····H separations: 0.1061 and 0.2281, respectively] (refer to Table 6.6. in Appendix D.1 for Wiberg bond index values). The overlap matrix which indicates the spatial overlap between the orbitals,[98] has the value of 0.4488 for the agostic donation into the Pd–$Cl_{trans}\sigma^*$ orbital [E(2) value: 58.60 kcal mol^{-1}] and 0.0788 for the agostic donation into the Pd–$Cl_{cis}\sigma^*$ orbital [E(2) value: 10.0 kcal mol^{-1}) (refer to Table 6.7. in Appendix D.1 for overlap matrix values). Due to the correlation between the second order perturbation energy, *E*(2), and the trend of changes in the Wiberg bond index and the overlap matrix values, most of the analysis is based on *E*(2) values.

In addition to the NBO analysis, an NCI (non-covalent interaction index) analysis[99] was also performed for **42** to examine the qualitative description of the agostic interaction. The NCI approach is very useful especially for weak electrostatic situations where the QTAIM analysis does not show a bond path due to a degenerate bond critical point.[125] The colour coded 3D NCI reduced density gradient iso-surface plots obtained from the NCI analysis give useful information on the nature of interactions where: red indicates destabilising interactions; blue for stabilising interactions; and green for the very weak delocalised stabilising interactions.[99] The depth of the particular color is related to the strength of the interaction.[99b]

For **42**, the 3D NCI plot (Figure 6.3) indicates agostic interaction by a large rounded disc which has blue colour bits inside showing an attractive interaction. There is also an outer red disc showing the depletion which sometimes has been interpreted as a region for steric crowding.[99b] Similar kind of blue discs have been seen in Pd–Cl bonds but not for

Pd–N. The little brown disc corresponds to a ring critical point and indicates a weak repulsive situation associated with the ring formation.[99] For the hydrogen bonding interaction between (N)–OH···Cl there is a light blue iso-surface which correlates well with the NBO analysis [*E*(2) values for LP(3) Cl to O–Hσ*: 16.63 kcal mol^{-1}]. The 3D NCI reduced density gradient iso-surface plot also reveals a small green surface for the weak intramolecular interactions between the C^7–H atom with the Cl(*cis*) ligand [distance: 3.048 Å] and the (N)–OH oxygen atom with an adjacent alicyclic ring hydrogen [distance: 2.640 Å].

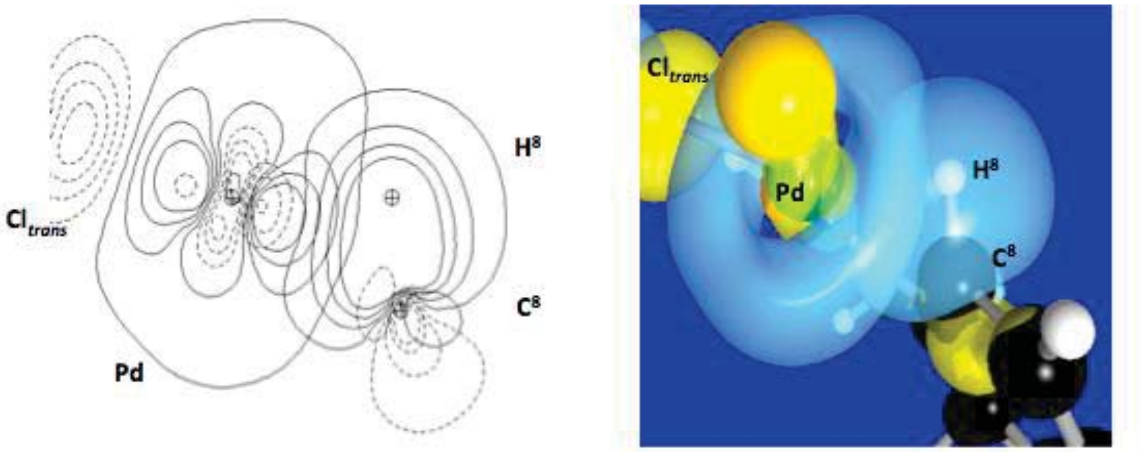

2D contour **3D spatial overlap image with orbital lobes**

a) C^8–H^{8}σ to Pd–Cl$_{trans}$σ* [agostic donation: *E*(2) = 58.60 kcal mol^{-1}]

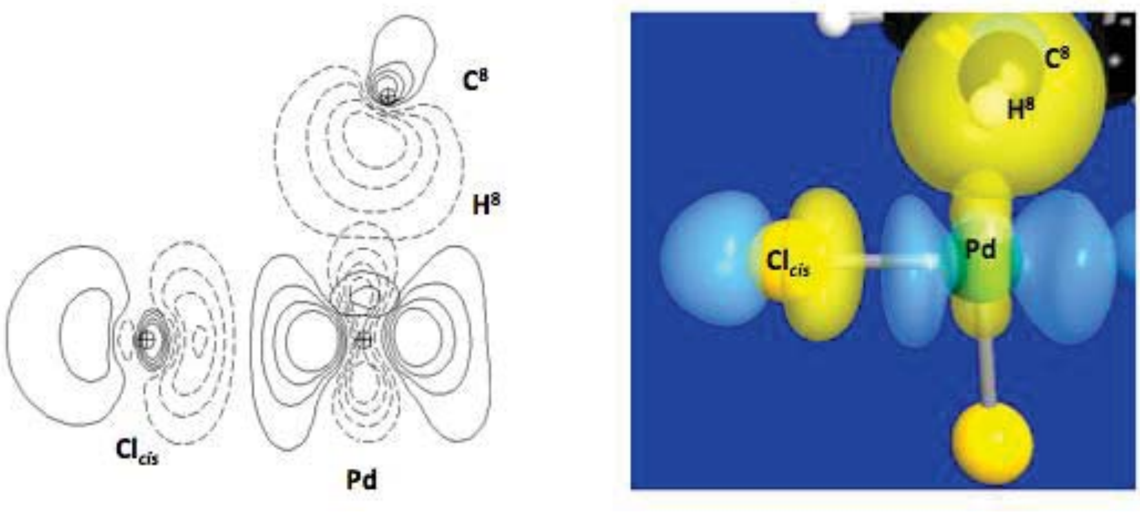

2D contour **3D spatial overlap image with orbital lobes**

b) C^8–H^{8}σ to Pd–Cl$_{cis}$σ* [agostic donation: *E*(2) = 10.0 kcal mol^{-1}]

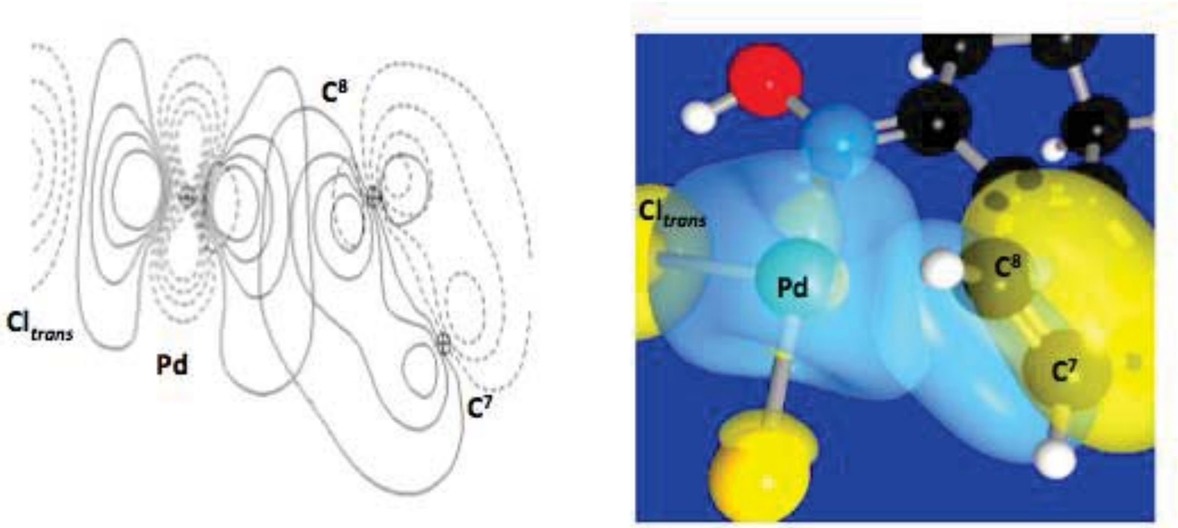

2D contour **3D spatial overlap image with orbital lobes**

c) C^7–$C^8\pi$ to Pd–$Cl_{trans}\sigma^*$ [syndetic donation: $E(2)$ = 20.33 kcal mol^{-1}]

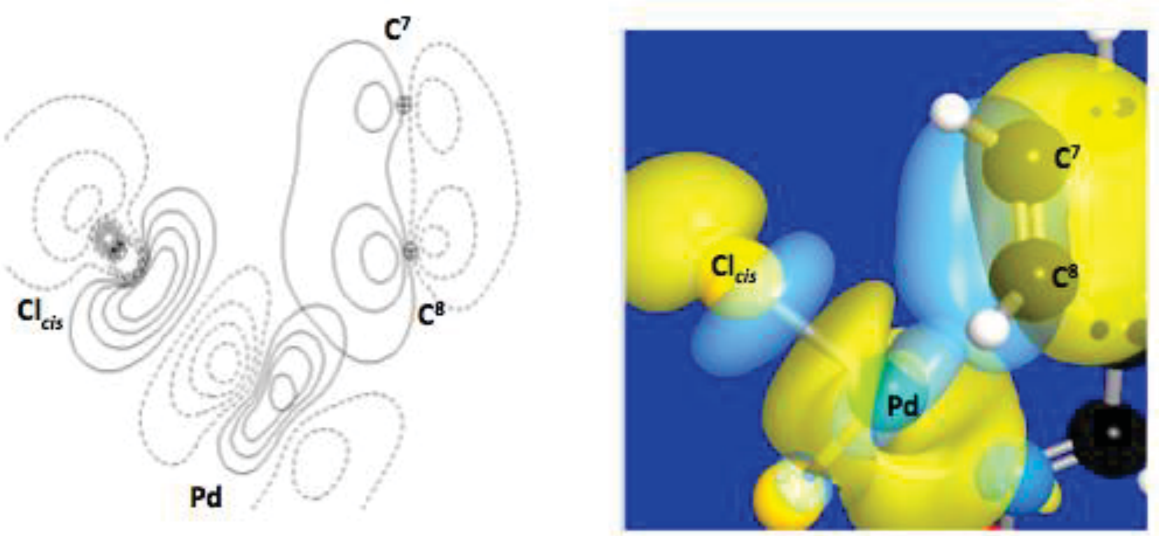

2D contour **3D spatial overlap image with orbital lobes**

d) C^7–$C^8\pi$ to Pd–$Cl_{cis}\sigma^*$ [syndetic donation: $E(2)$ = 6.48 kcal mol^{-1}]

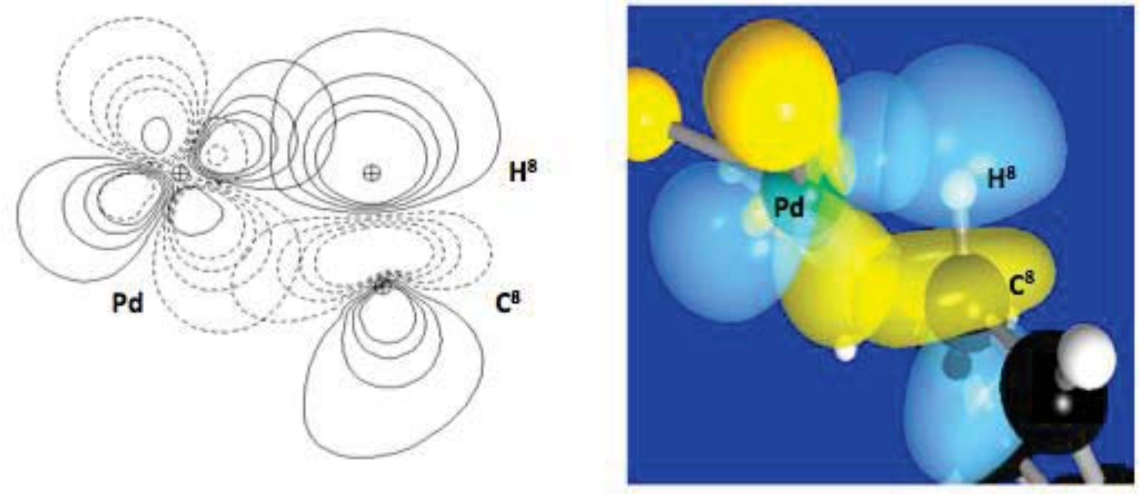

2D contour **3D spatial overlap image with orbital lobes**

e) Lone pair (3) Pd to C^8–$H^8\sigma^*$ [$E(2)$ = 2.85 kcal mol^{-1})

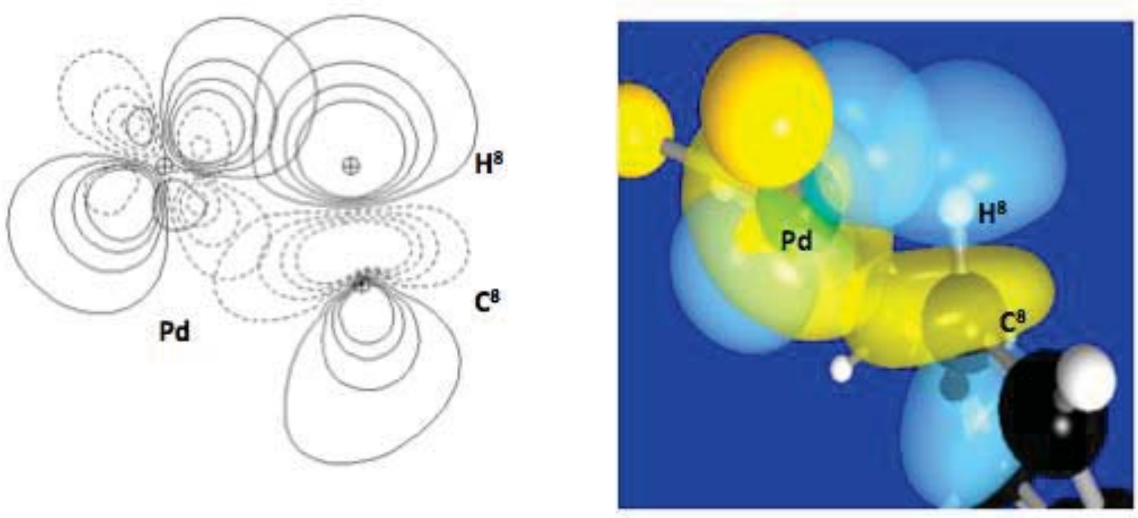

2D contour **3D spatial overlap image with orbital lobes**

f) Lone pair (4) Pd to C^8–$H^8\sigma^*$ [back-bonding donation: $E(2)$ = 4.87 kcal mol^{-1}]

Figure 6.2 NBO overlap diagrams showing the agostic (a,b), 'syndetic' (c,d) and back-bonding interactions (e, f). Blue and yellow NBO lobes indicate (+) and (-) phases, respectively. The outermost value (0.0316 a.u.) of the contour corresponds roughly to the empirical van der Waals radius).[113]

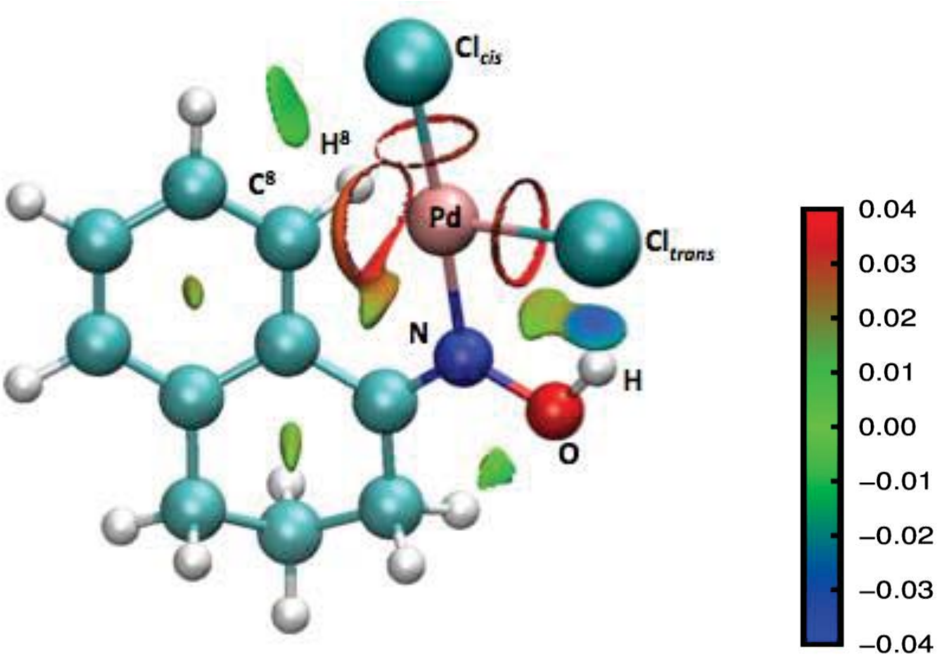

a b

Figure 6.3 a) NCI 3D reduced density gradient iso-surface plot for **42**; b) Colour map showing the values of the electron density times the sign of the second Hessian eigenvalue (λ_2).

Table 6.2 Selected structural parameters and spectral data for complexes **42–63**.[a]

Complex	**42**	**43**	**44**	**45**	**46**	**47**	**48**	**49**	**50**	**51**	**52**
Structural data											
Bond Length (Å)											
Pd–N	2.015	2.053	2.090	2.075	2.088[b]	2.016	2.014	2.009	2.003	2.006	2.011
Pd–Cl (*cis*)	2.272	2.279	2.288	2.287	2.260	2.267	2.271	2.293	2.303	2.304	2.268
Pd–Cl (*trans*)	2.293	2.280	2.292	2.291	2.252	2.285	2.290	2.339	2.406	2.502	2.291
C–H^8	1.152	1.151	1.148	1.151	1.164	1.156	1.155	1.138	1.113	1.103	1.138
(Ligand)	**1.090**	**1.090**	**1.090**	**1.090**	**1.090**	**1.089**	**1.089**	**1.090**	**1.090**	**1.089**	**1.091**
Separation (Å)											
Pd····H^8	1.819	1.841	1.884	1.863	1.786	1.802	1.813	1.901	2.180	2.356	1.894
Pd····C^8	2.240	2.224	2.177	2.174	2.206	2.229	2.221	2.208	2.146	2.172	2.321
Cl····HO(–N)	2.092	2.908[a]	2.814[a]	2.821[a]	2.921[a]	2.098	2.100	2.073	2.010	1.998	2.069
Angles (°)											
Pd–N=C	120.0	116.7	112.1	112.5	114.3[b]	120.2	120.2	120.0	119.8	118.0	120.4
Pd····H–C^8	95.2	93.2	88.3	89.0	94.4	95.3	94.3	89.6	73.4	66.8	96.7
Pd····C–H^8	54.0	55.7	59.9	59.0	53.9	53.7	54.5	59.4	76.8	85.4	54.2
Dihedrals (°)											
Cl (*cis*)–Pd–N=C	–25.2	–40.8	–71.0	–69.3	–36.8[b]	–27.2	28.5	–34.8	–24.9	57.2	–13.3
Ar-Plane/CP^b	34.5	51.4	68.9	66.1	42.6	35.6	36.0	33.0	33.6	43.5	35.5
N=C^1–C^{8a}–C^8	15.1	14.7	20.7	18.4	11.1[b]	15.1	–15.7	14.0	18.5	23.8	18.2
C^1–C^{8a}–C^8–H^8	38.2	32.7	25.7	25.2	38.4	39.1	–39.3	45.0	57.0	52.4	32.3
C–H^8 deformation	–27.2	–26.0	–23.4	–24.3	–28.0	–27.6	28.2	–31.1	–43.7	–28.5[c]	–21.6
Spectral data											
νC–H^8 (cm^{-1})	2462.8	2473.0	2531.0	2495.9	2346.8	2414.0	2438.9	2616.8	2877.0	2960.8	2596.8
(Ligand)	**3133.3**	**3132.9**	**3130.8**	**3131.7**	**3119.9**	**3139.2**	**3137.4**	**3111.7**	**3125.6**	**3117.4**	**3114.0**
Difference	*670.6*	*659.9*	*599.9*	*635.8*	*773.1*	*725.2*	*689.5*	*494.9*	*248.5*	*156.7*	*517.2*
δH^8	6.59	5.27	5.49	5.48	4.75	6.08	6.22	7.81	8.14	7.42	6.64
(Ligand)	**8.13**	**8.22**	**8.76**	**8.87**	**8.33**	**8.31**	**8.37**	**7.50**	**6.72**	**7.33**	**7.95**
Δδ	*–1.54*	*–2.95*	*–3.27*	*–3.39*	*–3.58*	*–2.23*	*–2.15*	*0.31*	*1.42*	*0.09*	*–1.31*
^1JC–H^8 (Hz)	103.2	105.9	107.4	106.3	103.8	103.5	102.5	102.9	118.0	123.5	107.4
(Ligand)	**139.4**	**139.5**	**140.8**	**141.2**	**141.1**	**141.7**	**140.8**	**133.3**	**136.5**	**137.9**	**137.5**
Difference	*36.2*	*33.6*	*33.4*	*34.9*	*37.3*	*38.2*	*38.3*	*30.4*	*18.5*	*14.4*	*30.1*

Table 6.2 continued Selected structural parameters and spectral data for complexes **42–63**.

Complex	**53**	**54**	**55**	**56**	**57**	**58**	**59**	**60**	**61**	**62**	**63**
Structural data											
Bond Length (Å)											
Pd–N	2.011	2.006	2.052	2.025	2.040	2.044	2.095	2.101	2.082	2.094	2.112
Pd–Cl (*cis*)	2.272	2.267	2.276	2.232	2.298	2.308	2.288	2.287	2.293	2.311	2.307
Pd–Cl (*trans*)	2.289	2.284	2.273	2.261	2.312	2.364	2.291	2.283	2.330	2.376	2.460
C–H^8	1.138	1.111	1.155	1.091	1.144	1.114	1.091	1.091	1.093	1.097	1.099
(Ligand)	**1.091**	**1.089**	**1.090**	**1.090**	**1.091**	**1.089**	**1.088**	**1.089**	**1.090**	**1.087**	**1.089**
Separation (Å)											
Pd$\cdots$H^8	1.899	2.128	1.833	2.594	1.874	2.133	2.534	2.575	2.460	2.446	2.452
Pd$\cdots$C^8	2.345	2.457	2.205	3.016	2.219	2.175	2.264	2.262	2.247	2.179	2.142
Cl$\cdots$HO(–N)	2.067	2.076	2.912[a]	3.248[a]	2.937[a]	2.890[a]	2.282[a]	2.243[a]	2.429[a]	2.554[a]	2.613[a]
Angles (°)											
Pd–N=C	120.6	119.6	117.0	125.9	117.7	116.9	96.5	95.8	100.4	104.0	105.2
Pd$\cdots$H–C^8	98.0	93.4	92.3	102.0	91.4	77.1	63.3	61.2	65.9	63.0	60.8
Pd$\cdots$C–H^8	53.3	59.8	56.1	57.3	57.6	73.0	91.2	93.8	87.8	90.4	92.6
Dihedrals (°)											
Cl(*cis*)–Pd–N=C	–8.36	55.6	–44.1	–66.8	–44.8	–38.5	15.9	19.8	–0.45	–2.54	–10.0
Ar-Plane/CP[b]	35.8	46.5	53.7	59.5	45.0	48.1	75.5	76.2	73.7	73.3	72.4
N=C^1–C^{8a}–C^8	18.4	26.8	14.6	–36.8	12.7	17.4	43.8	45.8	38.8	31.9	28.9
C^1–C^{8a}–C^8–H^8	30.4	20.3	34.2	–6.9	38.3	46.7	10.2	10.1	16.6	30.5	37.7
C–H^8 deformation	–18.0	–8.1	–27.1	2.7	–28.4	–37.7	–13.9	–13.0	–16.2	–22.6	–22.7
Spectral data											
νC–H^8(cm^{-1})	2592.5	2882.0	2440.4	3114.8	2558.8	2864.7	3108.3	3103.8	3073.4	3041.3	3007.9
(Ligand)	**3109.3**	**3143.8**	**3138.6**	**3131.0**	**3112.2**	**3126.3**	**3141.5**	**3141.3**	**3133.7**	**3148.0**	**3131.7**
Difference	*516.8*	*216.8*	*698.3*	*16.1*	*553.4*	*261.7*	*33.2*	*37.5*	*60.3*	*106.7*	*123.8*
δH^8	6.87	8.89	4.90	11.05	6.06	7.48	7.36	7.12	7.18	6.73	7.04
(Ligand)	**7.96**	**8.24**	**8.39**	**8.45**	**7.62**	**6.82**	**8.86**	**9.10**	**8.15**	**7.30**	**7.99**
Δδ	*–1.09*	*0.65*	*–3.49*	*2.60*	*–1.56*	*0.66*	*–1.50*	*–1.98*	*–0.97*	*–0.57*	*–0.95*
^1JC–H^8 (Hz)	107.4	120.3	106.6	144.3	102.7	118.1	138.9	139.9	130.6	128.5	128.7
(Ligand)	**137.1**	**137.2**	**141.7**	**140.8**	**133.6**	**136.8**	**138.6**	**140.6**	**133.4**	**136.5**	**139.7**
Difference	*29.7*	*16.9*	*35.1*	*–3.5*	*30.9*	*18.7*	*–0.3*	*0.7*	*2.8*	*8.0*	*11.0*

[a] Separations with alkylic hydrogens. [b] Directing group O instead of N. [c] Torsion S^7–C^7–C^8–H^8.

Table 6.3 Selected QTAIM parameters for complexes **42–63**.[a]

Complex	**42**[b]	**43**[c]	**44**[c]	**45**[c]	**46**[c]	**47**[b]	**48**[c]	**49**[c]	**50**[c]	**51**[c]	**52**[b]
Pd···X bond path	Pd···H	Pd···C	Pd···C	Pd···C	Pd···C	Pd···H	Pd···C	Pd···C	Pd···C	Pd···C	Pd···H
ρ(bcp)	0.0820	0.0820	0.0873	0.0883	0.0864	0.0841	0.0841	0.0844	0.0969	0.0936	0.0694
$\nabla^2\rho$(bcp)	0.2631	0.2107	0.1791	0.1858	0.2636	0.2743	0.2564	0.1720	0.1172	0.0946	0.2256
H(bcp)	-0.0210	-0.0244	-0.0344	-0.0311	-0.0249	-0.0225	-0.0228	-0.0281	-0.0394	-0.0367	-0.0141
–V/G	1.2424	1.3169	1.4075	1.4013	1.2744	1.2471	1.2628	1.3956	1.5737	1.6080	1.1998
ε(bcp)	5.3365	2.2016	0.6224	0.7407	13.7800	5.0049	14.1840	1.0045	0.1174	0.0562	4.0339
C^8–H^8 bond critical point											
ρ(bcp)	0.2333	0.2346	0.2379	0.2360	0.2286	0.2315	0.2322	0.2392	0.2566	0.2670	0.2418
(Ligand)	**0.2810**	**0.2810**	**0.2819**	**0.2820**	**0.2810**	**0.2825**	**0.2823**	**0.2778**	**0.2774**	**0.2779**	**0.2797**
$\nabla^2\rho$(bcp)	-0.6268	-0.6350	-0.6569	-0.6442	-0.5984	-0.6170	-0.6196	-0.6582	-0.7695	-0.8380	-0.6797
(Ligand)	**-0.9458**	**-0.9460**	**-0.9557**	**-0.9564**	**-0.9500**	**-0.9602**	**-0.9573**	**-0.9184**	**-0.9117**	**-0.9178**	**-0.9354**
ε(bcp)	0.1059	0.1005	0.0962	0.0999	0.1024	0.1050	0.1070	0.1080	0.0704	0.0456	0.0892
(Ligand)	**0.0126**	**0.0126**	**0.0118**	**0.0121**	**0.0096**	**0.0087**	**0.0091**	**0.0182**	**0.0291**	**0.0328**	**0.0157**
Atomic basin properties:											
H^8 atomic basin											
Charge, *q*(H)	0.056	0.044	0.040	0.041	0.050	0.060	0.058	0.053	0.051	0.027	0.040
(Ligand)	**0.040**	**0.040**	**0.054**	**0.054**	**0.055**	**0.057**	**0.052**	**0.001**	-0.003	**-0.004**	**0.032**
Total energy, *E*(H)	-0.631	-0.633	-0.631	-0.633	-0.634	-0.616	-0.619	-0.623	-0.619	-0.631	-0.636
(Ligand)	**-0.609**	**-0.609**	**-0.604**	**-0.604**	**-0.602**	**-0.602**	**-0.605**	**-0.622**	-0.622	**-0.620**	**-0.611**
Dipolar polarisation, *M*(H)	0.099	0.108	0.119	0.118	0.105	0.097	0.100	0.120	0.149	0.163	0.105
(Ligand)	**0.129**	**0.130**	**0.132**	**0.131**	**0.128**	**0.125**	**0.126**	**0.143**	**0.148**	**0.162**	**0.132**
Volume, *V*(H)[d]	36.0	37.2	38.9	38.6	36.5	35.6	36.0	38.5	44.2	46.7	37.0
(Ligand)	**46.5**	**46.5**	**45.1**	**45.1**	**45.7**	**45.0**	**45.2**	**49.1**	**49.6**	**50.6**	**46.6**
C^8 atomic basin											
Charge, *q*(C)	-0.084	-0.070	-0.065	-0.067	-0.066	-0.073	-0.080	-0.112	-0.089	-0.068	-0.091
(Ligand)	**0.001**	**0.001**	**0.001**	**0.000**	**0.002**	**0.015**	**0.009**	**-0.025**	-0.040	-0.032	-0.006
Pd atomic basin											
Charge, *q*(Pd)	0.641	0.627	0.630	0.635	0.659	0.649	0.647	0.616	0.570	0.534	0.630

Table 6.3 continued Selected QTAIM parameters for complexes **42–63**.[a]

Complex	**53**[b]	**54**[c]	**55**[c]	**56**[b]	**57**[c]	**58**[c]	**59**[c]	**60**[c]	**61**[c]	**62**[c]	**63**[b]
Pd····X bond path	Pd···H	Pd···C	Pd···C	Pd···H	Pd···C	Pd···C	Pd···C	Pd···C	Pd···C	Pd···C	Pd···H
ρ(bcp)	0.0676	0.0478	0.0851	0.0185	0.0827	0.0898	0.0720	0.0735	0.0732	0.0876	0.0977
$\nabla^2\rho$(bcp)	0.2201	0.1402	0.2029	0.0524	0.1843	0.1249	0.1607	0.1719	0.1379	0.1237	0.1033
H(bcp)	-0.0134	-0.0069	-0.0273	0.0004	-0.0262	-0.0344	-0.0203	-0.0203	-0.0228	-0.0332	-0.0402
–V/G	1.1964	1.1641	1.3498	0.9646	1.3626	1.5241	1.3355	1.3213	1.3986	1.5177	1.6096
ε(bcp)	2.4282	1.7463	1.5133	0.9928	1.3572	0.1388	1.3049	2.4118	0.3022	0.0965	0.0471
C^8–H^8 bond critical point											
ρ(bcp)	0.2415	0.2618	0.2334	0.2825	0.2366	0.2558	0.2800	0.2803	0.2755	0.2723	0.2714
(Ligand)	**0.2795**	**0.2825**	**0.2825**	**0.2823**	**0.2799**	**0.2775**	**0.2833**	**0.2846**	**0.2809**	**0.2806**	**0.2800**
$\nabla^2\rho$(bcp)	-0.6805	-0.8143	-0.6292	-0.9638	-0.6428	-0.7637	-0.9345	-0.9385	-0.8981	-0.8726	-0.8692
(Ligand)	**-0.9339**	**-0.9525**	**-0.9602**	**-0.9575**	**-0.9194**	**-0.9128**	**-0.9622**	**-0.9752**	**-0.9386**	**-0.9333**	**-0.9349**
ε(bcp)	0.0871	0.0566	0.0995	0.095	0.1082	0.0786	0.0249	0.0187	0.0353	0.0432	0.0403
(Ligand)	**0.0158**	**0.0162**	**0.0088**	**0.0093**	**0.0180**	**0.0289**	**0.0152**	**0.0116**	**0.0199**	**0.0295**	**0.0307**
Atomic basin properties:											
H^8-atomic basin											
Charge, *q*(H)	0.035	0.045	0.049	0.068	0.039	0.046	0.047	0.048	0.027	0.021	0.018
(Ligand)	**0.031**	**0.037**	**0.057**	**0.052**	**0.003**	**-0.002**	**0.053**	**0.069**	**0.020**	**0.015**	**0.013**
Total energy, *E*(H)	-0.636	-0.633	-0.618	-0.620	-0.629	-0.620	-0.638	-0.626	-0.641	-0.640	-0.634
(Ligand)	**-0.612**	**-0.615**	**-0.602**	**-0.605**	**-0.621**	**-0.622**	**-0.609**	**-0.602**	**-0.621**	**-0.621**	**-0.616**
Dipolar polarisation, *M*(H)	0.104	0.114	0.108	0.111	0.118	0.149	0.128	0.128	0.137	0.144	0.165
(Ligand)	**0.133**	**0.119**	**0.125**	**0.127**	**0.143**	**0.148**	**0.121**	**0.118**	**0.129**	**0.131**	**0.153**
Volume, *V*(H)[d]	36.6	35.8	37.1	40.6	38.3	43.5	41.8	42.8	42.8	43.6	48.0
(Ligand)	**46.4**	**42.2**	**45.0**	**45.3**	**49.0**	**49.5**	**40.8**	**39.8**	**42.9**	**43.3**	**48.6**
C^8-atomic basin											
Charge, *q*(C)	-0.089	-0.087	-0.059	-0.006	-0.100	-0.092	-0.055	-0.044	-0.081	-0.078	-0.058
(Ligand)	**-0.008**	**-0.010**	**0.014**	**0.008**	**-0.025**	**-0.040**	**-0.014**	**-0.002**	**-0.034**	**-0.047**	-0.029
Pd-atomic basin											
Charge, *q*(Pd)	0.630	0.625	0.637	0.629	0.613	0.573	0.631	0.642	0.608	0.568	0.535

[a] Atomic units: [ρ(bcp) = e/Bohr^3; $\nabla^2\rho$(bcp) = e/Bohr^5; *H* = Hartree/Bohr^3; ε(bcp) = dimensionless; *q* = e; *E*= Hartree; *M*=e*Bohr; *V*=1/Bohr^3]. [b] Pd···H^8 bcp properties. [c] Pd···C^8 bcp properties. [d] 0.001 iso-surface.

6.4.2 Changing the Nature of the Coordinating Ligand Nitrogen Atom

a) (N)–OMe Complex 43

The literature shows that in cyclometallation reactions, an increase in steric influence at the coordinating atom forces the C–H hydrogen atom towards the metal and consequently favours the reaction.[105] Therefore, to assess the effect of steric hindrance on the agostic interaction, the (N)–OH group (**42**) was replaced by (N)–OMe (**43**). In this case, the ligand moves slightly upwards, and (N)–OH····Cl hydrogen bonding is no longer present (Figure 6.4a). However, one of the methoxy hydrogens, H^{28}, becomes closer to the Cl(*trans*) ligand with a distance of 2.507 Å. The other structural changes appear when the Pd–N bond becomes significantly longer [2.053 Å in complex **43** from 2.015 Å in complex **42**] as a result of an increase in the dihedral angle, Cl(*cis*)–Pd–N=C [–40.8°; c.f. –25.2° in **42**] and in the aromatic/coordination plane angle [51.4°; c.f. 34.5° for **42**]. However, the dihedral angle $N{=}C^1–C^{8a}–C^8$ [14.7°; c.f. 15.1° in **42**] and the C–H deformation angle $H^7–C^7–C^8–H^8$ are only slightly changed [–26.0°; c.f. –27.2° in **42**] (Table 6.2). As a result of these structural changes, the $Pd\cdots H^8$ separation becomes longer to 1.841 Å [c.f. 1.819 Å in **42**] but the $Pd\cdots C^8$ separation becomes slightly shorter [2.224 Å; c.f. 2.240 Å in **42**], which show that by increasing the steric size, the hydrogen H^8 goes away from the metal and the carbon draws more towards the metal.

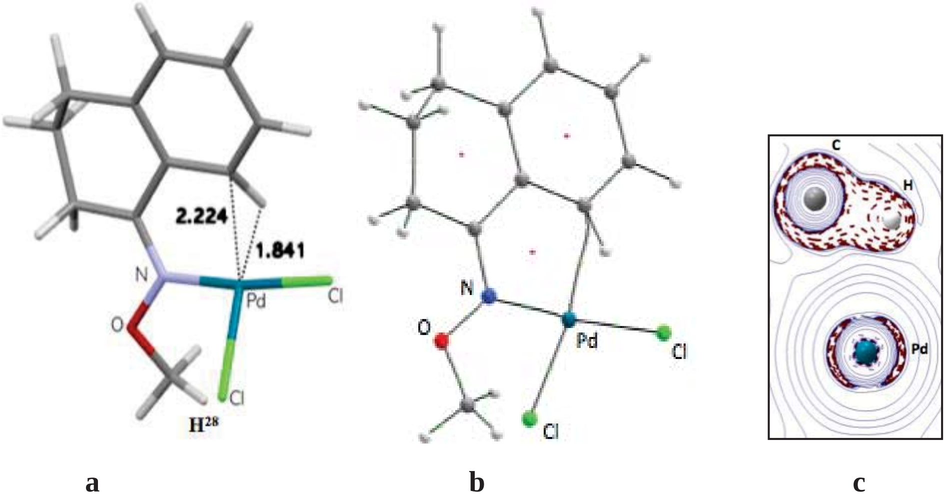

Figure 6.4 a) Optimised geometry and important separations (Å); b) QTAIM molecular graph showing $C^8\cdots Pd$ bond path; c) 2D contour plot of the Laplacian of the electron density for $C–H^8$ and Pd interaction for **43**.

The calculated spectroscopic properties for **43** (Table 6.2) indicate an upfield chemical shift for H^8 compared with the ligand as the hydrogen moves into a new anisotropic region [upfield shift (–*Δδ*) values for **43** and **42**: 2.95 and 1.54 ppm, respectively] and a slightly larger ^1JC–H value [105.9 and 103.2 Hz for complexes **43** and **42**, respectively; ligand values are essentially the same at 139.5 and 139.4 Hz, respectively] revealing a little weakening of the agostic interaction as measured in terms of the strength of the C–H bond. The C–H stretching frequency also reflects the weakness in the agostic interaction as there is now a smaller shift to lower energy compared with **42** [ΔυC–H: 659.9 and 670.6 cm^{-1} for **43** and **42**, respectively].

Looking at QTAIM properties, contrary to **42**, there is a bond critical point between Pd···C^8 (Figure 6.4b) with the same amount of electron density as for **42** [ρ(bcp): 0.0820 *e*/Bohr^3], but the Laplacian of the electron density is lower than **42** [∇^2ρ(bcp): 0.2107; 0.2631 *e*/Bohr^5 for **42**]. In QTAIM analysis, a ∇^2ρ(bcp) greater than zero indicates electron density depletion between two atoms[51] and this can be seen in Figure 6.4c where there is little charge concentration between the two atoms, similar to that which was seen in **42**. The ellipticity value is significantly reduced to 2.2016 compared with 5.3365 in **42** which indicates that now the bond is less unstable.[51] The ratio of absolute potential energy density and kinetic energy density is now slightly positive [1.3169; c.f. 1.2424 for **42**]. There is a slight decrease in the change of C–H electron density in the complex **43** compared with the ligand [ρ(bcp) differences: 0.0464 and 0.0477 *e*/Bohr^3 in **43** and **42**, respectively]. The larger decrease indicates delocalisation of some of the electron density from C–H to another bond. There is also a decrease in the value of the Laplacian of the electron density for the C–H bond, which also shows little depletion of the electron density [∇^2ρ(bcp) values for complex and ligand **43**: –0.6350 and –0.9460 *e*/Bohr^5, respectively]. The ellipticity value is increased to 0.1005 in complex **43** compared with 0.0126 in ligand which also indicates a decrease in the strength of the C–H bond.[41] It is interesting to note that, even though complexes **42** and **43** have bcps for Pd····H^8 and Pd···C^8 separations, the trends in the C–H bond critical point properties compared with the ligand is almost identical.

The differences in atomic basin properties indicate similar trends when compared with the respective ligand, as was seen in **42**. The H^8 atomic charge is slightly positive in complex **43** compared with respective ligand but becomes less positive compared with the complex **42** (Table 6.3) where the decrease was large [the difference in *q*(H^8) in complex and ligand **43** and **42**: 0.004 and 0.016 *e*, respectively]. However, although the C^8 atomic charge is decreased significantly, it is again slightly less in magnitude compared with the complex **42** [the difference in *q*(C^8) in **43** and **42** with respect to the ligands: –0.069 and –0.083 *e*, respectively]. Hence, there is still a repulsive situation for Pd···H^8 [*q*(Pd) and *q*(H^8): 0.627 and 0.044 *e*, respectively] and an attractive situation for Pd···C^8 [*q*(Pd) and *q*(C^8): 0.627 and –0.070 *e*, respectively]. The other atomic properties are also only slightly changed in complex **43** compared with the respective ligand.

Turning towards NBO analysis for complex **43** (Table 6.4), the agostic, syndetic and back-bonding donations all are slightly decreased compared with complex **42**. The corresponding *E*(2) values for the agostic interaction: C–Hσ to Pd–Cl_{trans}σ* and to Pd–Cl_{cis}σ are 57.68 and 9.45 kcal mol^{-1}, respectively; c.f. 58.60 and 10.00 kcal mol^{-1}, respectively in **42**; for syndetic interaction: C^7–C^8π to Pd–Cl_{trans}σ* and to Pd–Cl_{cis}σ* are 18.94 and 5.95 kcal mol^{-1}, respectively; c.f. 20.33 and 6.48 kcal mol^{-1}, respectively in **42** and for back-bonding: LP(3) and LP(4**)** Pd to C–Hσ* are 1.34 and 5.95 kcal mol^{-1}, respectively; c.f. 2.85 and 4.87 kcal mol^{-1} in **42**, respectively. As in **43**, the Pd–N bond length is slightly increased to 2.053 Å [c.f. 2.015 Å for **42**], there is also a small decrease seen in donations from LP(N) to Pd–Cl_{trans}σ* and to Pd–Cl_{cis}σ* compared with **42** [*E*(2) values for **43**: 18.80 and 96.31 kcal mol^{-1}, respectively; c.f. 17.57 and 105.35 kcal mol^{-1} for **42**, respectively]. Thus, by changing the steric size, the strength of the Pd–N bond is affected.

b) (N)–CMe_3 Complex 44

It was seen in the earlier study on the anagostic interaction in rhodium-tetralone complexes that the CMe_3 group attached to N brings the C^8–H moiety closer to the metal, and short distances were achieved in those complexes where the CMe_3 groups were included (Chapter 3).[126] Therefore, to see a more comprehensive change in both the donor properties and steric influence for the agostic interaction, a CMe_3 substituent was used. The structural features for **44** (Figure 6.5a; Table 6.2) now show a significant increase in the Rh–N bond length compared with the complex **43** [2.090 Å; c.f. 2.053 Å for **43**] and the C^1–C^{8a}–C^8–H^8 dihedral angle drops to 25.7° from 32.7° in **43**, which results in increased bending of the C–H^8 moiety in such a way that the C^8 carbon becomes closer to the metal and hydrogen H^8 goes slightly further away [Pd····C^8 distance: 2.177 and 2.224 Å in **44** and **43**, respectively; Pd····H^8 distance: 1.884 and 1.841 Å in **44** and **43**, respectively]. The other structural changes seen are: dihedral angle Cl^2–Pd–N=C becomes large [51.4° and 37.2° in **44** and **43**, respectively]; the dihedral angle N=C^1–C^{8a}–C^8 increases to 20.7° from 14.7° in **43** and the angle between the aromatic ring and coordination planes increases to 68.9° [c.f. 51.4° in **43**]. In addition, the C–H^8 dihedral deformation angle H^7–C^7–C^8–H^8 is slightly reduced [values for **44** and **43**: –23.4 and –26.0°, respectively]. However, the C–H bond length is significantly increased from the respective ligand [values: 1.148 and 1.090 Å, respectively] which gives a clue as to the existence of an agostic interaction.

Looking at the spectroscopic properties for **44** (Table 6.2), there is now a shift to lower frequency for the C–H stretching frequency compared to the change observed for **43** [ΔυC–H: 599.9 cm^{-1}; c.f. 659.9 cm^{-1} for **43**]. The change in the coupling constant ^1JC–H is almost the same as was seen for **43** [changes in ^1JC–H compared with the respective ligands, 33.4 and 33.6 Hz in **44** and **43**, respectively]. There is a slightly greater upfield chemical shift for H^8 compared to complex **43** [Δδ: 3.27 ppm; c.f. 2.95 ppm in the case of **43**].

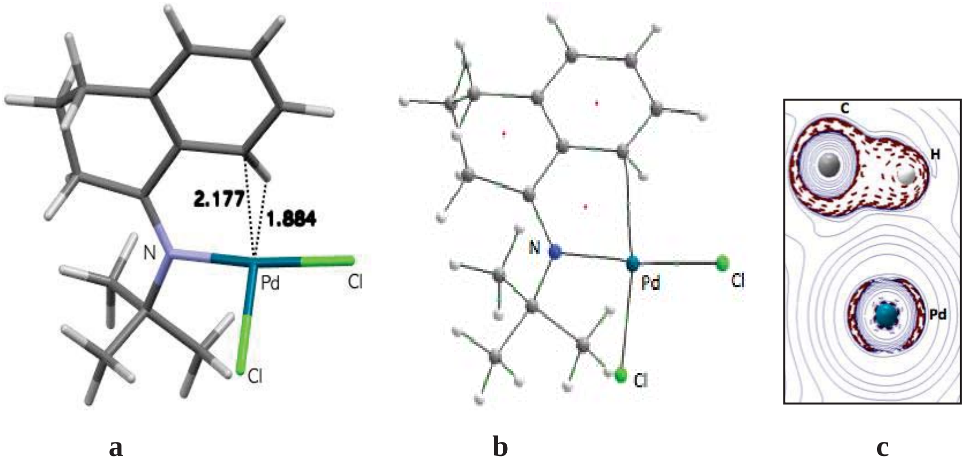

Figure 6.5 a) Optimised geometry and important separations (Å); b) QTAIM molecular graph showing bond paths between H^8···Pd and OH···Cl separations; c) 2D contour plot of the Laplacian of the electron density for the C–H^8 and metal interaction in **44**.

For the QTAIM data for **44** (Table 6.3), similar to complex **43**, there is also a bond path present for the Pd···C^8 interaction (Figure 6.5b) with a slightly higher electron density value at the bcp [ρ(bcp): 0.0873 *e*/Bohr^3; c.f. 0.0820 *e*/Bohr^3 in **43**]. However, the Laplacian of the electron density becomes smaller [∇^2ρ(bcp): 0.1791 and 0.2107 *e*/Bohr^5 in **44** and **43**, respectively] and the ellipticity value, ε, significantly drops to 0.6224 from 2.2016 in **43** which shows a relatively more stable Pd···C^8 interaction. The smaller positive value of ∇^2ρ(bcp) indicates slightly higher charge concentration between the C–H group and metal as shown in figure 6.4c where the contour lines are slightly closer than seen in **42** or **43**. Comparing the QTAIM properties of the C–H^8 group for both the complex and ligand **44** (Table 6.3), it appears that there is again the same trend of changes as was seen in the case of **43**: a decrease in the electron density [ρ(bcp) for complex and ligand: 0.2379 and 0.2819 e/Bohr^3, respectively]; a decrease in the negative value of the Laplacian of the electron density [∇^2ρ(bcp) for complex and ligand: –0.6569 and –0.9557 *e*/Bohr^5, respectively]; and an increase in the ellipticity value [ε(bcp) for complex and free ligand: 0.0962 and 0.0118, respectively]. All these changes in the C–H^8 bcp show weakening of the C–H bond as a result of delocalisation of electron density to antibonding orbitals. This situation complies well with the requirements of the agostic interaction where the C–H donates electron density to the metal.[54]

Turning to the NBO analysis for **44** (Table 6.4a), there is a noticeable increase in the donation from LP(N) to Pd–Cl$_{trans}$σ* and to Pd–Cl$_{cis}$σ* [*E*(2) values: 28.39 and 106.73 kcal mol^{-1}, respectively; 18.80 and 96.31 kcal mol^{-1} for **43**, respectively] indicating strengthening of the Pd–N bond. As complex **44** has a similar kind of positioning of the C–H group in the metal coordination plane to complex **43**, there is an insignificant change in the agostic donation from the C–H to the Pd–Cl$_{trans}$σ* orbital compared with complex **43** [*E*(2) values for **44**: 57.07 and 57.68 kcal mol^{-1}, respectively]. There is a slight increase in agostic donation from the C–Hσ to the Pd–Cl$_{cis}$σ* orbital [*E*(2) values for **44** and **43** respectively: 11.6 and 9.5 kcal mol^{-1} respectively]. The NBO donations for the back-bonding from metal to the antibonding C–H orbital are not very different, as LP(4) Pd to C–Hσ* donation is essentially the same [*E*(2) values: 5.48 and 5.69 kcal mol^{-1} in **44** and **43**, respectively] and the LP(3) Pd to C–Hσ* donation is slightly smaller [*E*(2) values: 0.72 and 1.34 kcalmol^{-1} for **44** and **43**, respectively]. It is noted that this donation gets smaller in going from **42** to **44** [*E*(2) value for **42**: 2.85 kcal mol^{-1}]. However, for the syndetic donations (C^7–C^8π to the Pd–Cl$_{trans}$σ* and to the Pd–Cl$_{cis}$σ*) there is a slight increase observed [*E*(2) values: 20.03 and 6.63 kcal mol^{-1}, respectively; c.f. 18.94 and 5.95 kcal mol^{-1} in the case of **43**, respectively]. The overall NBO analysis indicates increase in both the syndetic and agostic donations by increasing the steric influence at the coordinating N atom.

c) Acetophenone Imine Complex 45

Acetophenone imine complex **45**, an analog of complex **44** where the alicyclic ring has been replaced with CH_3, was chosen with the aim that the aromatic ring-free rotation might allow greater aromatic π-ring access to the metal. These aromatic ligands are commonly used for directed C–H functionalisation reactions.[138] Comparisons of structural features of the complex **45** with **44** (Table 6.2) indicate a slightly shorter separation for the Pd····H^8 separation (Figure 6.6a) [values: 1.863 and 1.884 Å, respectively], but the Pd···C^8 distance becomes slightly shorter [2.174 and 2.177 Å, respectively]. The C–H bond length is slightly increased [1.151; c.f. 1.048 Å in complex **44**, both of the free ligands have a C–H bond length of 1.090 Å] whereas the Rh–N bond length is slightly decreased to 2.075 Å compared with **44** [2.090 Å]. Similarly, there are only small changes in the angles and torsions seen in complex **45** compared with **44**, for instance: the Rh–N=C^1 push-back angle is not increased [values in complex **45** and **44**: 112.5 and 112.1°, respectively]; the N=C^1–

C^{8a}–C^8 dihedral angle is slightly reduced to 18.4° from 20.7° in **44**; the C–H deformation angle is almost unchanged [values in complex **45** and **44**: –24.3 and –24.4°, respectively]; and the angle between the aromatic ring and coordination planes is only 2.8° smaller than **44** [values: 66.1 and 68.9°, respectively].

The IR and NMR spectroscopic data (Table 6.2) also show only slight changes in value when compared with complex **44**, as the NMR chemical shift is upfield by 3.39 ppm [Δδ: 3.27 for **44**] and the ^1JC–H coupling constant is reduced by 34.9 Hz compared to the ligand, slightly greater than that observed for complex **44**, where the C–H coupling constant was reduced by 33.4 Hz. Regarding the C–H stretching frequencies for complex **45**, it is seen that there is a greater C–H stretching frequency shift to lower energy in complex **45** as now the difference between complex and ligand C–H stretching frequency is about 635.8 cm^{-1} compared with complex **44** where the difference was 599.9 cm^{-1}.

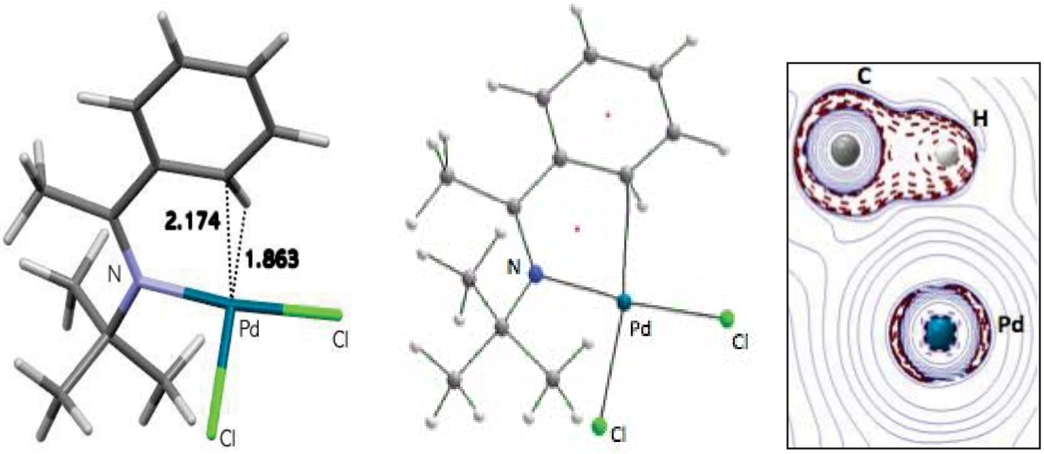

a **b** **c**

Figure 6.6 a) Optimised geometry and important separations (Å); b) QTAIM molecular graph showing bond paths for $C^8\cdots$Pd separation; c) 2D contour plot of the Laplacian of the electron density for the C–$H^8\cdots$metal interaction for **45**.

Turning towards the QTAIM analysis (Table 6.3), which shows a bcp for the Pd$\cdots C^8$ separation (Figure 6.6b), similar to complex **44**. However, values for the bcp properties are slightly different to **4** [ρ(bcp): 0.0883 and 0.0873 *e*/$Bohr^3$; $\nabla^2\rho$(bcp): 0.1858 and 0.1791 *e*/$Bohr^5$; *H*(bcp) values: –0.0311 and –0.0344 Hartree/$Bohr^3$ and –V/G, 1.4013 and 1.4075 for **45** and **44**, respectively]. The Laplacian contour plot for the C–H$\cdots\cdot$M separation in **45** (Figure 6.6c) is similar to that which was seen in **44**. The Pd$\cdots C^8$ bcp properties indicate less electron density between the two atoms and the C–H bcp data reinforce this as there is a slight decrease in the electron density for the C–H bond [a difference in C–H bcp properties with respect to the ligand, ρ(bcp) values: 0.0460 and 0.0440 *e/*$Bohr^3$; $\nabla^2\rho$(bcp) values: 0.3122 and 0.2988 *e*/Bohr^5; and the ellipticity, ε(bcp), values: 0.0460 and 0.0821 for **45** and **44**, respectively]. The QTAIM atomic basin properties for complex **45** are similar to complex **44**, with no significant changes observed (Table 6.3).

Looking at the NBO data (Table 6.4), the C–H donation to Pd–Cl$_{trans}$σ* and Pd–Cl$_{cis}$σ* is slightly reduced which correlates with the QTAIM analysis for the C–H electron density [$E(2)$ values: 54.70 and 9.84 kcal mol^{-1}, respectively; 57.07 and 11.64 kcal mol^{-1} in **44**, respectively]. Regarding the syndetic donations, there is also a slight decrease in $E(2)$ values in **45** [$E(2)$ values for the donation from C^7–C^{8}π to Pd–Cl$_{trans}$σ* are 19.50 and 20.03 kcal mol^{-1}for complex **45** and **44**, respectively; the $E(2)$ value for C^7–C^{8}π to Pd–Cl$_{cis}$σ* for complex **45** and **44** is 6.20 and 6.63 kcal mol^{-1}, respectively]. For the back bonding donation, the $E(2)$ value for LP(3) Pd to C–Hσ* is effectively unchanged [0.68 and 0.72 kcal mol^{-1} for **45** and **44**, respectively], however, for LP(4) Pd to C–Hσ* it is slightly greater in **45** [6.09 kcal mol^{-1}; c.f. 5.48 kcal mol^{-1} for **44**].

d) 1-Tetralone Ketone Complex 46

To explore C–H functionalisation reactions involving different directing groups[8-10], in complex **46** the nitrogen atom N has been replaced by oxygen O (Figure 6.7a). In this case, the Pd–O bond length is greater than the oxime complexes [Pd–O bond length: 2.088 Å; Pd–N bond lengths: 2.015 Å and 2.053 Å for (N)–OH (**42**) and (N)–OMe (**43**) complexes] but similar to the (N)–CMe$_3$ complex **44** [2.090 Å] (Table 6.2). With oxygen as a coordinating atom, the Pd···H^8 separation decreases [1.786 Å], becoming closer than all the nitrogen ligands [Pd···H^8 separations: 1.819, 1.841 and 1.884 Å for (N)–OH, (N)–OMe and (N)–CMe$_3$ derivatives, respectively] where the ligand aromatic ring was moved towards the Cl ancillary ligand (away from the metal) by increasing the steric size at the nitrogen atom. However, the Pd···C^8 separation for O–Pd complex **46** has a value in between the (N)–OMe and (N)–CMe$_3$ complexes where by substituting OCH$_3$ and CMe$_3$, the ligand aromatic ring flattened, and C^8 became closer to the palladium metal [Pd···C^8 distance in oxo complex **(46)**, (N)–OMe (**43)** and (N)–CMe$_3$ (**44)** complexes: 2.206, 2.224 and 2.177 Å, respectively]. The C–H bond length increases a little when compared with other complexes [C–H bond length in oxo complex (**46)**, (N)–OH (**42)**, (N)–OMe (**2)** and (N)–CMe$_3$ (**44)**: 1.164, 1.152, 1.151 and 1.148 Å, respectively].

Table 6.4 Selected NBO analysis parameters for complexes **42–63**. (Bold values for ligands).

Complex	**42**	**43**	**44**	**45**	**46**	**47**	**48**	**49**	**50**	**51**	**52**
C^8–H^{8}σ bond											
Occupancy (n)	1.8457	1.8525	1.8615	1.8558	1.8464	1.8375	1.8401	1.8511	1.9013	1.9391	1.8751
	1.9768	**1.9770**	**1.9754**	**1.9753**	**1.9766**	**1.9761**	**1.9770**	**1.9782**	**1.9781**	**1.9781**	**1.9763**
Energy (a.u.)	-0.4451	-0.4429	-0.4387	-0.4438	-0.4463	-0.4513	-0.4399	-0.3212	-0.3185	-0.1911	-0.4481
	-0.4166	**-0.4163**	**-0.4066**	**-0.4098**	**-0.4235**	**-0.4439**	**-0.4319**	**-0.2946**	**-0.2856**	**-0.1550**	**-0.4122**
C^7–C^{8}π bond											
Occupancy	1.6494	1.6373	1.6222	1.6178	1.6369	1.6309	1.6078	1.6344	1.6887	1.7247	1.6357
	1.6766	**1.6770**	**1.6720**	**1.6649**	**1.6598**	**1.6506**	**1.6459**	**1.7189**	**1.7151**	**1.6372**	**1.6675**
Energy (a.u)	-0.2574	-0.2541	-0.2501	-0.2544	-0.2656	-0.2730	-0.2678	-0.1227	-0.1350	-0.0188	-0.2471
	-0.2241	**-0.2234**	**-0.2201**	**-0.2230**	**-0.2343**	**-0.2535**	**-0.2397**	**-0.0953**	**-0.0859**	**0.0440**	**-0.2186**
C^8–H^{8}σ* bond											
Occupancy (n)	0.0613	0.0611	0.0565	0.0597	0.0746	0.0636	0.0569	0.0508	0.0346	0.0231	0.0503
	0.0154	**0.0162**	**0.0177**	**0.0174**	**0.0166**	**0.0153**	**0.0155**	**0.0166**	**0.0157**	**0.0186**	**0.0170**
Energy (a.u.)	0.2527	0.2572	0.2684	0.2595	0.2316	0.2290	0.2494	0.3893	0.4505	0.5988	0.2760
	0.4055	**0.4205**	**0.4127**	**0.4114**	**0.3979**	**0.3807**	**0.3951**	**0.5202**	**0.5308**	**0.6534**	**0.4025**
C^7–C^{8}π* bond											
Occupancy (n)	0.3666	0.3655	0.3727	0.3683	0.3468	0.3531	0.3516	0.4112	0.2816	0.2718	0.3855
	0.2972	**0.2992**	**0.2865**	**0.2873**	**0.2811**	**0.2816**	**0.2937**	**0.3276**	**0.3916**	**0.4349**	**0.3103**
Energy (a.u.)	-0.0255	-0.0211	-0.0171	-0.0214	-0.0303	-0.0382	-0.0260	0.1073	0.1085	0.2282	-0.0157
	0.0112	**0.0169**	**0.0156**	**0.0119**	**0.0009**	**-0.0170**	**-0.0039**	**0.1394**	**0.1461**	**0.2695**	**0.0213**
Pd–Cl$_{trans}$σ* bond											
Occupancy (n)	0.3208	0.3113	0.3039	0.3073	0.2938	0.3131	0.4016	0.3888	0.3590	0.3527	0.3051
Energy (a.u.)	0.2970	0.2897	0.3774	0.2533	0.2440	0.2607	0.1806	0.3969	0.4442	0.5716	0.2805
Pd–Cl$_{cis}$σ* bond											
Occupancy (n)	0.3980	0.3906	0.3874	0.3870	0.3137	0.3984	0.3234	0.4181	–	–	0.3944
Energy (a.u.)	0.2146	0.2159	0.3049	0.2851	0.1555	0.1761	0.2611	0.3115	–	–	0.2283
Pd Lone pairs:											
LP(1)											
Occupancy (n)	1.9914	1.9898	1.9888	1.9887	1.9908	1.9912	1.9911	1.9920	1.9931	1.9942	1.9920
Energy (a.u.)	-0.2401	-0.2487	-0.2233	-0.2283	-0.2501	-0.2594	-0.2479	-0.1328	-0.1129	0.0084	-0.2365
LP(2)											
Occupancy (n)	1.9786	1.9742	1.9847	1.9847	1.9881	1.9790	1.9788	1.9778	1.9766	1.9785	1.9787
Energy (a.u.)	-0.2730	-0.2620	-0.2442	-0.2468	-0.2526	-0.2935	-0.2813	-0.1601	-0.1133	0.0224	-0.2663
LP(3)											
Occupancy (n)	1.9560	1.9636	1.9678	1.9650	1.9728	1.9546	1.9558	1.9610	1.9637	1.9660	1.9603
Energy (a.u.)	-0.2624	-0.2571	-0.2541	-0.2581	-0.2588	-0.2817	-0.2694	-0.1511	-0.1232	-0.0082	-0.2585
LP(4)											
Occupancy (n)	1.9010	1.8857	1.8745	1.8715	1.9609	1.8850	1.8862	1.9173	1.9079	1.9101	1.9172
Energy (a.u.)	-0.2606	-0.2541	-0.2465	-0.2499	-0.2586	-0.2812	-0.2687	-0.1465	-0.1171	0.0037	-0.2544
Donor-acceptor interactions:											
[*E*(2) value (kcal mol^{-1})]											
C-H σ to Pd–Clσ*											
C^8–H^{8}σ to Pd–Cl$_{trans}$σ*	58.60	57.68	57.07	54.70	64.37	75.57	70.17	64.00	–	–	44.46
C^8–H^{8}σ to Pd–Cl$_{cis}$σ*	10.00	9.45	11.64	9.84	9.33	14.98	13.80	13.81	3.10	2.70	8.66
C–Cπ to Pd–Clσ*											
C^7–C^{8}π to Pd–Cl$_{trans}$σ*	20.33	18.94	20.03	19.50	17.91	27.55	0.05	41.92	–	–	18.34
C^7–C^{8}π to Pd–Cl$_{cis}$σ*	6.48	5.95	6.63	6.20	5.38	10.47	0.15	16.00	–	–	5.88
Pd to C–Hσ*											
Pd LP(3) to C^8–H^{8}σ*	2.85	1.34	0.72	0.68	1.05	2.39	2.05	2.53	–	–	2.97
Pd LP(4) to C^8–H^{8}σ*	4.87	5.69	5.48	6.09	8.08	5.35	5.01	2.70	–	–	2.66
Pd to C–Cπ*											
Pd LP(4) to C^7–C^{8}π*	1.60	2.38	3.04	2.81	2.98	1.63	0.09	0.51	–	–	0.71
Cl to O–Hσ*											
Cl LP(3) to O–Hσ*	16.63	–	–	–	–	16.31	16.22	17.80	23.10	23.67	17.82

Table 6.4 continued Selected NBO Analysis parameters for complexes **42–63**.

Complex	**53**	**54**	**55**	**56**	**57**	**58**	**59**	**60**	**61**	**62**	**63**
C^{8}–H^{8}σ bond											
Occupancy (n)	1.8773	1.9299	1.8465	1.9752	1.8483	1.9107	1.9694	1.9709	1.9637	1.9559	1.9519
	1.9746	**1.9743**	**1.9761**	**1.9770**	**1.9781**	**1.9784**	**1.9724**	**1.9711**	**1.9733**	**1.9738**	**1.9768**
Energy (a.u.)	-0.4487	-0.4554	-0.4508	-0.4493	-0.3195	-0.3294	-0.4473	-0.4668	-0.3376	-0.3236	-0.1917
	-0.4110	**-0.4129**	**-0.4425**	**-0.4303**	**-0.2947**	**-0.2854**	**-0.4011**	**-0.4254**	**-0.2864**	**-0.2802**	**-0.1548**
C^{7}–C^{8}π bond											
Occupancy (n)	1.6357	1.6236	1.6137	1.6267	1.6496	1.6745	1.5634[a]	1.5675[a]	1.5866[a]	1.6663[a]	1.7068
	1.6527	**1.6370**	**1.6511**	**1.6469**	**1.7194**	**1.7157**	**1.6534**[a]	**1.6218**[a]	**1.7106**[a]	**1.6376**[a]	**1.6657**
Energy (a.u.)	-0.2471	-0.2476	-0.2684	-0.2535	-0.1246	-0.1327	-0.2398[a]	-0.2650[a]	-0.1270[a]	-0.1260[a]	-0.0185
	-0.2128	**-0.2114**	**-0.2523**	**-0.2385**	**-0.0956**	**-0.0865**	**-0.2099**[a]	**-0.2363**[a]	**-0.0924**[a]	**-0.0806**[a]	**0.0325**
C^{8}–H^{8}σ* bond											
Occupancy (n)	0.0498	0.0314	0.0623	0.0185	0.0545	0.0312	0.0204	0.0196	0.0215	0.0238	0.0231
	0.0175	**0.0180**	**0.0153**	**0.0154**	**0.0165**	**0.0162**	**0.0207**	**0.0212**	**0.0208**	**0.0197**	**0.0192**
Energy (a.u.)	0.2791	0.3312	0.2366	0.3858	0.3835	0.4443	0.3870	0.3681	0.4844	0.4889	0.6073
	0.4022	**0.4061**	**0.3832**	**0.3960**	**0.5202**	**0.5061**	**0.4211**	**0.4009**	**0.5303**	**0.5397**	**0.6547**
C^{7}–C^{8}π* bond											
Occupancy (n)	0.3548	0.3511	0.3588	0.3109	0.3888	0.3061	0.4937	0.4763	0.3918	0.3239	0.3051
	0.2947	**0.3099**	**0.2811**	**0.2934**	**0.3258**	**0.3898**	**0.2839**	**0.2721**	**0.3157**	**0.4769**	**0.4448**
Energy (a.u.)	-0.0144	-0.0142	-0.0322	-0.0181	-0.1092	0.1072	-0.0355	-0.0552	0.1081	0.1153	0.2277
	0.0266	**0.0227**	**-0.0155**	**-0.0025**	**0.1392**	**0.1457**	**0.0331**	**0.0079**	**0.1541**	**0.1529**	**0.2645**
Pd–Cl$_{trans}$σ* bond											
Occupancy (n)	0.2966	0.2629	0.3066	0.3894	0.3609	0.4512	0.3132	0.3099	0.3484	0.4435	–
Energy (a.u.)	0.2882	0.2727	0.2544	0.1501	0.3963	0.4158	0.4333	0.4201	0.5354	0.5329	–
Pd–Cl$_{cis}$σ* bond											
Occupancy (n)	0.3933	0.3863	0.3920	0.1770	0.4087	0.4148	0.3868	0.3884	0.3919	0.4096	0.3277
Energy (a.u.)	0.2362	0.2437	0.1784	0.1292	0.3233	0.3549	0.3005	0.2708	0.4229	0.4411	0.6978
Pd Lone pairs											
LP (1)											
Occupancy (n)	1.9919	1.9931	1.9898	1.9945	1.9900	1.9909	1.9912	1.9916	1.9912	1.9911	1.9919
Energy (a.u.)	-0.2362	-0.2419	-0.2487	-0.2525	-0.1221	-0.1033	-0.2293	-0.2473	-0.1202	-0.1014	-0.0183
LP (2)											
Occupancy (n)	1.9790	1.9817	1.9745	1.9773	1.9732	1.9749	1.9815	1.9804	1.9820	1.9804	1.9800
Energy (a.u.)	-0.2659	-0.2419	-0.2819	-0.2443	-0.1525	-0.1088	-0.2348	-0.2522	-0.1274	-0.1100	0.0060
LP (3)											
Occupancy (n)	1.9612	1.9729	1.9627	1.9679	1.9657	1.9633	1.9687	1.9663	1.9700	1.9689	1.9679
Energy (a.u.)	-0.2578	-0.2597	-0.2768	-0.2561	-0.1514	-0.1295	-0.2429	-0.2640	-0.1320	-0.1080	0.0162
LP (4)											
Occupancy (n)	1.9220	1.9320	1.8642	1.9437	1.9074	1.9087	1.8531	1.8305	1.9016	1.9045	1.9101
Energy (a.u.)	-0.2535	-0.2479	-0.2752	-0.2666	-0.1435	-0.1127	-0.2400	-0.2587	-0.1254	-0.1004	0.0161
Donor-acceptor interactions:											
[E(2) (kcal mol^{-1})]											
C–H σ to Pd–Clσ*											–
C^{8}–H^{8}σ to Pd–Cl$_{trans}$σ*	41.51	19.76	72.11	1.15	66.48	24.11	7.51	6.33	10.62	12.81	
C^{8}–H^{8}σ to Pd–Cl$_{cis}$σ*	8.14	5.07	13.80	1.03	14.02	3.94	3.66	3.37	4.29	4.31	2.75
C–Cπ to Pd–Clσ*											
C^{7}–C^{8}π to Pd–Cl$_{trans}$σ*	17.78	15.01	26.73	0.57	34.41	–	59.62[a]	57.85[a]	2.80[a]	4.55[a]	–
C^{7}–C^{8}π to Pd–Cl$_{cis}$σ*	5.89	4.25	10.26	0.75	13.47	–	15.67[a]	13.83[a]	0.71[a]	3.19[a]	–
Pd to C–Hσ*											
Pd LP(3) to C^{8}–H^{8}σ*	3.31	0.99	1.08	–	1.56	0.52	0.14	0.22	0.07	0.22	–
Pd LP(4) to C^{8}–H^{8}σ*	2.44	0.47	6.00	–	4.30	0.94	0.21	0.23	0.16	0.13	–
Pd to C–Cπ*											
Pd LP(4) to C^{7}–C^{8}π*	0.62	–	2.74	–	0.87	–	18.85	21.45	2.52	2.24	0.60
Cl to O–Hσ*											
Cl LP(3) to O–Hσ*	17.91	17.22	–	–	–	–	–	–	–	–	–

[a] C–Cπ corresponds to C^{8}–C^{8ahab}π

However, the dihedral angle C^1–C^{8a}–C^8–H^8 in oxo complex **46** is similar to that seen in the (N)–OH complex **42** [values: 38.4 and 38.2°, respectively] but is quite different from those complexes where the steric size was increased [32.7 and 25.2° for (N)–OMe and (N)–CMe$_3$, respectively]. The deformation angle C^7–H^7–C^8–H^8 in the oxo complex is slightly larger than for the N coordinating ligands [values in oxo (**46**), (N)–OH (**42**), (N)–OMe (**43**) and (N)–CMe$_3$ (**44**) complexes: –28.0, –25.2, –26.0 and -24.4°, respectively]. As seen previously where the angle between the aromatic/coordination planes was increased due to an increase in the steric size at N, in the oxo complex, this angle is larger than the (N)–OH complex but smaller than for (N)–OMe and (N)–CMe$_3$ [angle between aromatic and coordination planes in oxo complex **46**: (N)–OH **(42)**, (N)–OMe **(43)** and (N)–CMe$_3$ **(44)**: 42.6, 34.5, 51.4 and 69.0°, respectively].

The spectroscopic data (Table 6.2) indicate that there is a large change in the C–H stretching frequency to lower energy compared to the all the N–R complexes so far [a difference of 773.1 cm^{-1}; 670.6, 659.9 and 600.0 cm^{-1} for (N)–OH (**42**), (N)–OMe (**43**) and (N)–CMe$_3$ (**44**), respectively]. Similarly, a larger high field chemical shift for H^8 is observed [$\Delta\delta$ = 3.58 ppm] compared to the N–R complexes [$\Delta\delta$ value for (N)–OH, (N)–OMe and (N)–CMe$_3$: 1.54, 2.95 and 3.27 ppm, respectively]. The C–H coupling constant, ^1JC–H, is also decreased more significantly than for the other complexes [a difference with the respective ligands: 37.3 Hz compared with (N)–OH (**42**), (N)–OMe (**43**), and (N)–CMe$_3$ (**44**),: 36.2, 33.6 and 33.4 Hz, respectively].

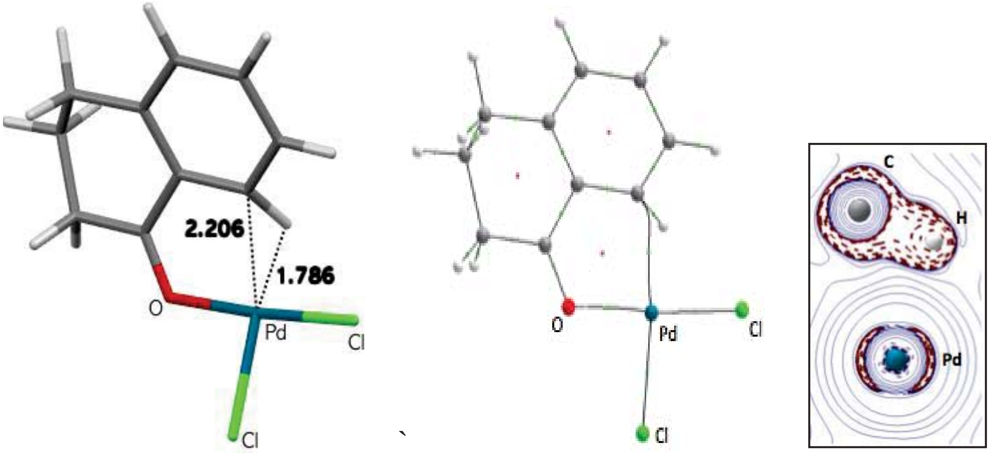

a **b** **c**

Figure 6.7 a) Optimised geometry and important separations (Å); b) QTAIM molecular graph showing bond paths for C$^8\cdots$Pd separation; c) 2D contour plot of the Laplacian of the electron density for C–H^8 and metal interaction for **46**.

NBO data (Table 6.4) shows greater agostic donation than for the N–R complexes [*E*(2) value for the donation from C–H to Pd–Cl$_{trans}$σ* and Pd–Cl$_{cis}$σ* are 64.37 and 9.33, respectively; c.f. 58.60 and 10.0 kcal mol^{-1}, respectively for complex **42** (the second highest)]. On the other hand, the syndetic donation, which refers to the donation from C^7–C^{8}π to the Pd–Cl$_{trans}$σ* and Pd-Cl$_{cis}$σ*orbitals, is relatively small [*E*(2) value for oxo complex **46**: 17.91 and 5.38 kcal mol^{-1}, respectively; c.f. 18.94 and 5.95 kcal mol^{-1}, respectively for **43** (the second lowest), respectively]. Interestingly, the back-donation from LP(4) Pd to the C–Hσ* orbital is greater in oxo complex **46** than the N–R complexes [*E*(2) value: 8.08 kcal mol^{-1}; c.f. 5.48 kcal mol^{-1} in **44** (second highest back donation)] and this might be the reason of increase in the C–H bond length to 1.164 Å (greater than the other complexes). The donation from the oxygen lone pair to the Pd–Cl$_{trans}$σ* and Pd–Cl$_{cis}$σ* orbitals is significantly less compared to the N–R complexes [*E*(2) values: 6.03 and 58.22 kcal mol^{-1}; c.f. 17.57 and 105.35 kcal mol^{-1} in **42**].

The QTAIM analysis indicates a bond path between Pd and C^8 (Figure 6.7b) similar to the (N)–OMe (**43**) and (N)–CMe$_3$ (**44**) cases but different from the (N)–OH complex which had a Pd···H^8 bcp instead. However, the electron density for all of these bcps are similar, whereas the Laplacian of the electron density is closer to complex **42**, which has a Pd···H^8 bcp, but larger than the (N)–OMe (**43**) and (N)–CMe$_3$ (**44**) which have Pd···C^8 bcps [ρ(bcp) and ∇^2ρ(bcp) values in oxo complex **46**: 0.0864 *e*/Bohr^3 and 0.2636 *e*/Bohr^5, respectively; (N)–OMe (**43**): 0.0820 *e/*Bohr^3 and 0.2107 *e*/Bohr^5, resepctively; (N)–CMe$_3$: 0.0873 *e*/Bohr^3 and 0.1791 *e/*Bohr^5 , respectively and (N)–OH (**42**) (bcp Pd···H^8): 0.0820 *e*/Bohr^3 and 0.2631 *e*/Bohr^5, respectively]. The Laplacian contour plot is not very different from earlier complexes as expected from the similar values listed above (Figure 6.6c). The energy density, *H*, for oxo complex **46** is also negative and resembles the other complexes, however, the ellipticity ε is unexpectedly higher than at the other Pd···C^8 bcps in (N)–OMe (**43**) and (N)–CMe$_3$ (**44**) complex [ε(bcp) for oxo complex **46**, (N)–OMe complex **43**, and (N)–CMe$_3$ complex **44**: 13.7800, 2.2016 and 0.6224, respectively]. The larger ε value indicates instability of the Pd···C^8 bond due to delocalisation of the electron density.

6.4.3 Electronic Effects on the Aromatic Ring, Complexes 47–51

Electronic influences on the agostic interaction in [Pd(Cl)$_2$(1-tetralone oxime)] complex **42** were studied by placing strong σ or π-electron donating, or withdrawing, groups at the *para* position of the aromatic ring.[106] The choice of the *para* position is based upon having a greater influence for the electronic substituents than at the *meta* position.[107] However, in some complexes, the *ortho* position is also used to see a combined electronic influence on the interaction.[107] The electron withdrawing groups used were SO_2Cl (σ-electron withdrawing substituent with F value 1.16; R value –0.05)[106], **47** and $N{=}NPO(OEt)_2$ (π-electron withdrawing substituent with F value: –0.05; R value: 0.79) [106], **48** while the electron donating groups included were $B(OH)_3^-$, (σ-electron donating substituent with F value: –0.42; R value: –0.02)[106], **49** and S^-, (π-electron donating substituent with F value: 0.03; R value: –1.24)[106], **50**. The combined electronic influence was studied by placing two of the strongest π-electron donating substituent, S^-, at both C^7 and C^5 positions of the aromatic ring, **51**. These effects were then compared with the unsubstituted complex **42** which has only hydrogen in the *para* position.

The bonding parameters associated with the different substituents show that the Pd–N and Pd–Cl bond lengths are significantly affected in the case of electron donating groups (Table 6.2). The Pd–N bond length is below 2.010 Å where there are electron donating substituents, however, in the case of electron withdrawing substituents, it is almost unaffected [Pd–N bond length and **47**–**51**: 2.016 Å (**47**); 2.014 Å (**48**); 2.009 Å (**49**); 2.003 Å (**50**) and 2.006 Å (**51**); c.f. 2.015 Å in **42**]. Similarly, the $Pd–Cl_{trans}$ bond length is slightly reduced where there are electron withdrawing substituents while it is increased in the case of electron donating substituents [e.g., $Pd–Cl_{trans}$ in the case of **47** and **50**: 2.285 and 2.406 Å, respectively compared with **42**: 2.293 Å].

Analysing the structural parameters for complex **47**, which is substituted with SO_2Cl at the *para* position, in comparison with unsubstituted complex **42**, indicates that the aromatic ring in **47** is rolled slightly upwards [$Cl^2–Pd\cdots C^8$ in **47** and **42** is 169.9° and 171.6°, respectively] and the angle between the aromatic and coordination planes flattens a little [35.6 and 34.5° for **47** and **42**, respectively] (Figure 6.8; Table 6.2). There is an insignificant change in the push-back angle, Pd–N=C, which is almost identical in **47** and **42** [values: 120.2 and 120.0°, respectively]. Regarding the agostic approach, both $Pd\cdots C^8$ and $Pd\cdots H^8$ separations become slightly shorter [$Pd\cdots C^8$ in **47** and **42**: 2.229 and 2.240 Å, respectively; $Pd\cdots H^8$ in **47** and **42**: 1.802 and 1.819 Å, respectively]. Since the changes in separations are small the angles associated with these separations are almost unchanged in **47** [Pd···C–H in **47** and **42**: 53.7 and 54.0°, respectively; Pd···H–C in **47** and **42**: 95.3 and 95.2°, respectively]. The C–H deformation and other torsion angles remain unchanged.

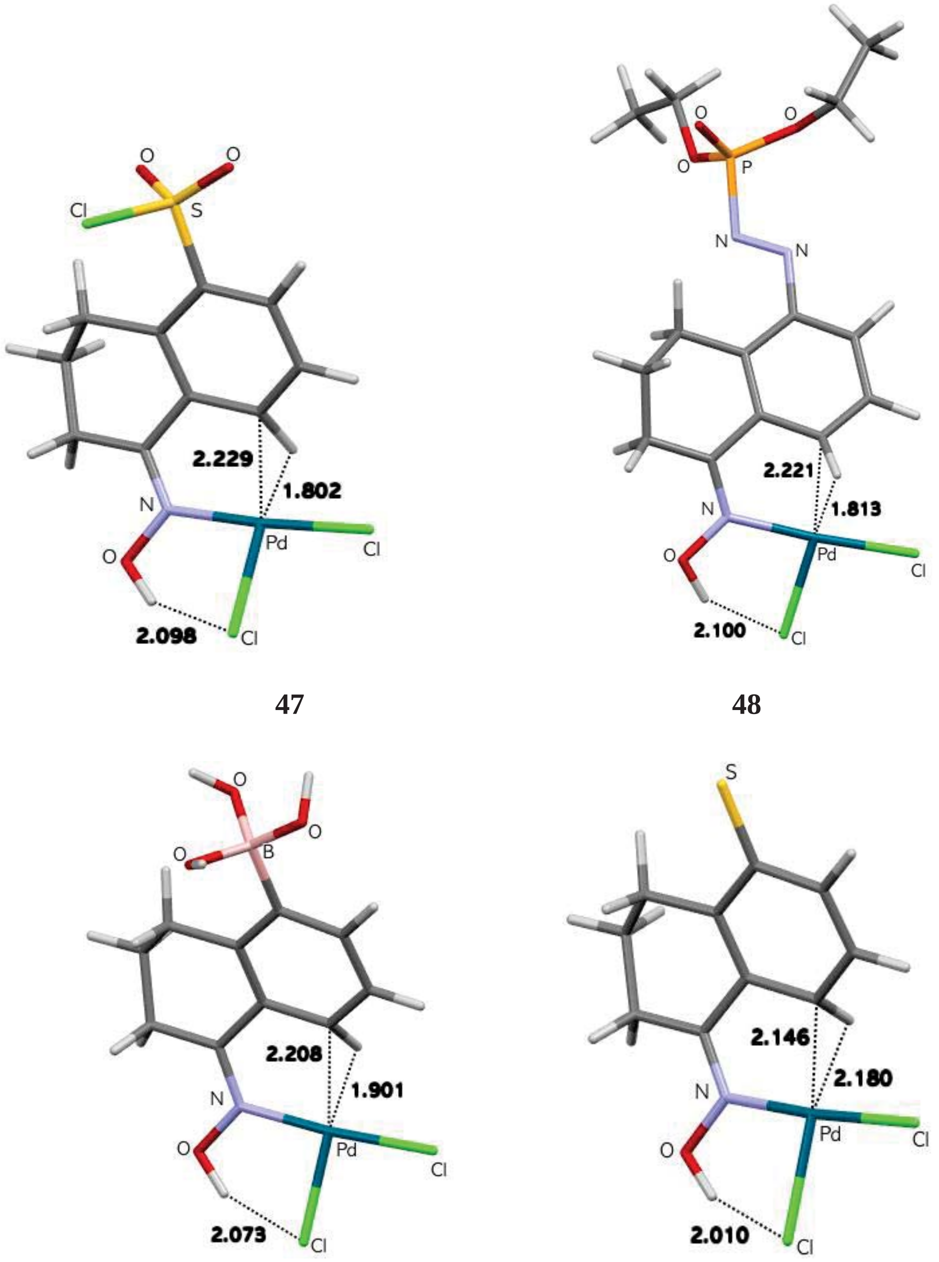

47 **48**

49 **50**

Figure 6.8 Optimised geometries with important separations (Å) for complexes **47–50**.

For the spectroscopic data, the C–H coupling constant, ${}^{1}J$C–H in **47** is reduced by 38.2 Hz compared with the respective ligand which is slightly greater compared with complex **42,** where the decrease was 36.2 Hz. In addition, the C–H stretching frequency shifts to slightly lower energy [ΔνC–H: 725.2 and 670.6 cm^{-1} for **47** and **42**, respectively], which indicates greater donation from the C–H to the metal in **47**.

From the QTAIM analysis for **47**, there is a bond path between H^{8} and the metal indicative of an interaction (Figure 6.9), with greater values than **42** for the bcp properties

(Table 6.3) [ρ(bcp) and $\nabla^2\rho$(bcp) values in **47**: 0.0841 e/Bohr^3 and 0.2743 e/Bohr^5, respectively; c.f. 0.0820 and 0.2631 e/Bohr^5 in **42**; H(bcp) values: –0.0225 and 0.0210 Hartree/Bohr^3 in **47** and **42**, respectively and |V|/G value: 1.2471 and 1.2424 in **47** and **42**, respectively]. However, the ellipticity value in **47** is slightly reduced in comparison with **42** [ε(bcp) values: 5.0049 and 5.3365, respectively]. Comparing the QTAIM properties of the C^8–H bond critical points of the complex with the ligand indicate that there is a greater decrease in the electron density in the C^8–H bond on complex formation [Δρ(bcp) in **47** and **42**: 0.0510 and 0.0477 e/Bohr^3, respectively] and at the same time, the ellipticity change is slightly greater in **42** [difference in the ε(bcp) values between complex and ligands is 0.0963 and 0.0933 for **47** and **42**, respectively].

The bcp properties for the C^8–H bond thus show a greater agostic donation in the case of the σ-electron withdrawing SO$_2$Cl substituent. Looking at the QTAIM charges (Table 6.3) to see the effect on the electrostatics, there is now a more positive charge on H^8 and a less negative charge on C^8 [q(H^8) values for complexes **47** and **42**: 0.060 and 0.056 e, respectively; q(C^8): –0.073 e and –0.084 e, respectively] but comparing the charges between complex and free ligand it appears that the change on complex formation is slightly less for complex **47** [q(C^8) in ligands **47** and **42**: 0.015 and 0.001 e, respectively; q(H^8) in ligands **47** and **42**: 0.057 and 0.040 e, respectively]. In addition, by looking at the ligand charges, it appears that the electron withdrawing effect is also influencing the C^8 and H^8 atomic basin charges.

Turning towards the NBO analysis for **47**, the agostic donation is significantly increased with the SO$_2$Cl substituent [E(2) values for C–Hσ donation to the Pd–Cl$_{trans}$σ* and Pd–Cl$_{cis}$σ*orbitals: 75.57 and 14.98 kcal mol^{-1}, respectively; c.f. 58.60 and 10.0 kcal mol^{-1}, respectively for **42**] and similarly the syndetic donation also substantially increases in **47** [E(2) values for the C^7–C^{8}π to the Pd–Cl$_{trans}$σ* and Pd–Cl$_{cis}$σ*donations: 27.55 and 10.47 kcal mol^{-1}, respectively for **47**; 20.33 and 6.48 kcal mol^{-1}, respectively for complex **42**] (Table 6.4). The strengthening of the syndetic donation involving the Pd–Cl$_{trans}$σ* orbital is correlated with the (smaller) difference in energies between the C^7–C^{8}π and Pd–Cl$_{trans}$σ* NBOs; NBO energy differences: 0.0072 a.u. for **47**; c.f. 0.0729 a.u. in **42**]. However, the overlap matrix values are almost the same [values are 0.1731 and 0.1764 for **47** and **42**, respectively]. There is also a small increase in the back-bonding donation from the metal to the C–Hσ* orbital [E(2) values for donations from Pd LP(3) and Pd LP(4) to C–Hσ* in **47**: 2.39 and 5.35, respectively; c.f. 2.85 and 4.87 kcal mol^{-1} in **42**, respectively]. Regarding the hydrogen bonding between Cl···H–O below the coordination plane which has a slightly larger distance [2.098 and 2.092 Å in **47** and **42**, respectively, there is now an insignificant decrease in the donation from Cl to O–Hσ* [*E*(2) values for **47** and **42**: 16.31 and 16.63 kcal mol^{-1}, respectively].

Moving further to complex **48** which is substituted by the π-electron withdrawing N=NPO(OEt)$_2$ substituent, the bulky ligand effect is also seen here, similar to the anagostic case (Chapter 3).[126] The C–H^8 bond now positions at the other side of the coordination plane, compared to the other complexes studied so far (Figure 6.8). However, with this orientation, there is a decrease in both the Pd····H^8 and Pd····C^8 separations [respective values: 1.813 and 2.221 Å in **48**; c.f. 1.819 and 2.240 Å in **42**] (Table 6.2). In particular, the Pd···C^8 separation of 2.221 Å is slightly shorter than the SO$_2$Cl substituted complex **47**, where the Pd···C^8 separation was found to be 2.229 Å. Even though, the steric influence of the N=NPO(OEt)$_2$ changes the C–H deformation angle almost opposite to that observed in **42**, but it does not prevent the C–H approach to the metal. Surprisingly, despite the flattening of the ring, the plane angle is only slightly changed from **47** and **42** [plane angle in **48**, **47** and **42**: 36.0, 35.6 and 34.5°, respectively]. The other torsions and angles are not significantly different to **42**.

Looking at the spectroscopic data for **48** (Table 6.2), there is now a 689.5 cm^{-1} shift of the C–H stretching frequency to lower energy with respect to the ligand, a greater shift than that seen for **42** [670.6 cm^{-1}] but lower than **47** [725.2 cm^{-1}]. Similarly, there is a slight decrease in the change in coupling constant on complex formation, ^1JC–H compared to **42** [difference between complex and ligand ^1JC–H values: 38.3 and 36.2 Hz for **48** and **42**, respectively], but the decrease is of the same magnitude as was seen for **47** [38.2 Hz].

Inspection of the QTAIM data for **48**, conversely to **42** and **47**, there is now a bcp present for the Pd···C^8 separation (Figure 6.9). The reason for the formation of the bond path between Pd···C^8 is because of the flattening of the ring which positions the C–H on the opposite side than was seen in **42** and **47**. Comparison of QTAIM properties of Pd···C^8 in **48** with Pd···H^8 in **42** or **47** surprisingly shows that the electron density, Laplacian of the electron density, and energy density values are not that different (Table 6.3) [ρ(bcp), ∇^2ρ(bcp) and H(bcp) for Pd···C^8 for **48**: 0.0841 *e*/Bohr^3, 0.2564 *e*/Bohr^5 and –0.0228 Hartree/Bohr^3, respectively]. However, there is now a dramatic increase in the ellipticity value which is now 14.1840, much larger than was found for the Pd···H^8 bcp in **42** and **47** [ε(bcp): 5.3365 and 5.0049 for **42** and **47**, respectively]. A comparison of C^8–H bcp properties between complex and ligand indicates a decrease of electron density by 0.0501 *e*/Bohr^3, a decrease in the negative value of the Laplacian of the electron density by 0.3385 *e*/Bohr^5 and a significant increase in the ellipticity, all these properties show that there is a reduction in the C–H electron density in the complex. The QTAIM charges indicate a slightly greater influence for the π-withdrawing substituent N=NPO(OEt)$_2$ on the H^8 and

C^8 atomic charges than was seen for the case of the σ-electron withdrawing SO_2Cl substituent, **47** as the H^8 is more positive by 0.006 *e* [0.003 *e* in **47**] and the carbon is more negative by 0.071 *e* compared to **47** [0.056 *e*].

NBO analysis of **48**, despite the different positioning of the C–H group over the metal compared to complex **42** and **47**, indicates there is still agostic donation present with larger *E*(2) values than **42** but slightly smaller than **47** [*E*(2) values for the C–Hσ to Pd–Cl_{trans}σ* and Pd–Cl_{cis}σ* orbitals for **48**: 70.17 and 13.80 kcal mol^{-1}, respectively; c.f. 58.60 and 10.0 kcal mol^{-1}, respectively for **42** and 75.57 and 14.98 $kcalmol^{-1}$, respectively for **47**] (Table 6.4). Surprisingly, aromatic ring syndetic donations from the C^7–C^8**π** to Pd–Cl_{trans}σ* and Pd–Cl_{cis}σ* orbitals are now insignificant, instead there is now significant donation from the C^8 to the Pd–Cl_{trans}σ* and Pd–Cl_{cis}σ* orbitals with significant *E*(2) values of 38.08 and 93.55 kcal mol^{-1}, respectively]. In addition, the back-bonding donations are almost in the middle of the magnitudes to those found for **42** and **47** [*E*(2) values from LP(3) and LP(4) Pd to the C–Hσ* orbital: 2.05 and 5.01 kcal mol^{-1}, respectively]. A general comparison of both σ- and π-electron withdrawing substituents, SO_2Cl (complex **47**) and $N{=}NPO(OEt)_2$ (complex **48**) respectively, shows that SO_2Cl increases the agostic donations, but syndetic donations are also present, however, the $N{=}NPO(OEt)_2$ shows agostic donation but the aromatic syndetic donation almost disappears being apparently replaced by strong Pd–C^8 covalency.

Turning to the σ-electron withdrawing substituent $B(OH)_3^-$, complex **49**, there is now a significant increase in the Pd····H^8 separation [1.901; c.f. 1.819 Å for **42**], but there is also a decrease in the Pd···C^8 separation [2.208; c.f. 2.240 Å for **42**] (Figure 6.8; Table 6.2). These changes occur when the ligand is moved downwards as a result of the torsional changes compared to **42** as the Cl_{cis}–Pd–N=C dihedral in **49** is increased to –34.8° compared to **42** where the angle was –25.2°, however, the torsion N=C^1–C^{8a}–C^8 is now 14.0° compared to 15.1° in **42**. Also, there is a slight decrease in the plane angle (angle between ligand aromatic ring and metal coordination planes) [a decrease by 1.5° in **49**]. Interestingly, there is now a dramatic decrease in the C–H bond length compared to the other (N)–OH complexes so far [C–H bond length for **49** and **42**: 1.138 and 1.152 Å, respectively] and similarly the other bond lengths around the metal are also significantly changed; as the Pd–N bond length drops to 2.009 Å [c.f. 2.015 Å in **42**]; the Pd–Cl_{cis} distance increases to 2.293 Å [c.f. 2.272 Å in **42**]; and the Pd–Cl_{trans} distance increases to 2.339 Å [c.f. 2.293 Å in **42**]. Spectroscopic data indicate a slight decrease in the ^1JC–H in the complex compared to the free ligand [difference in ^1JC–H between complex and ligand: 30.4 Hz in **49**; c.f. 36.2 Hz in **42**] and the calculated C–H stretching frequency shift to lower energy is less than **42** [ΔυC–H: 494.9 and 670.6 cm^{-1} for **49** and **42**, respectively].

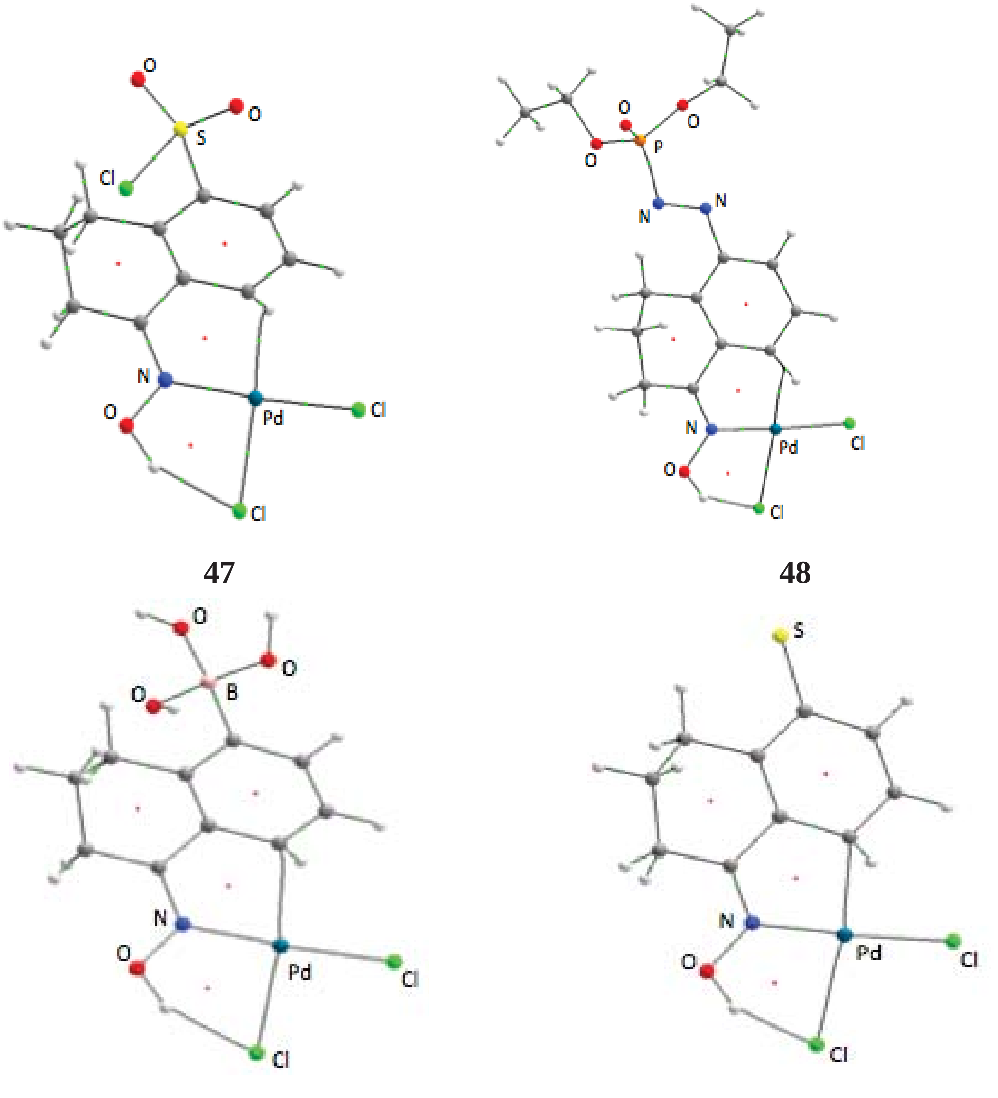

47 **48**

49 **50**

Figure 6.9 QTAIM molecular graphs showing the bond paths for Pd···C^8 and OH····Cl^2 separations in complexes **47–50**.

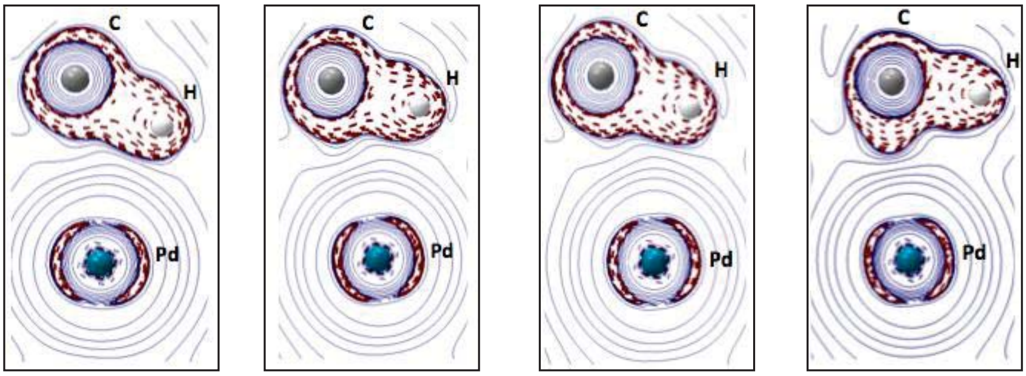

47 **48** **49** **50**

Figure 6.10 2D contour plots of the Laplacian of the electron density for the C–H^8 and Pd interaction in complexes **47–50**.

Turning to the QTAIM data for **49**, as in complex **47** there is a bond path between Pd and C_8 (Figure 6.9). The Pd···C^8 bcp properties show similar magnitude for the electron density as was seen for **47** (Table 6.3) but there is now substantially lower ellipticity [ρ(bcp) for **49** and **47**: 0.0844 and 0.0841 *e/*Bohr^3, respectively; ε(bcp) for **49** and **47**: 1.0045 and 14.1840, respectively]. Comparison between the ligand and complex C–H^8 bcp, indicates that the reduction in the electron density and ellipticity values for **49** compared to **47** is not as large [Δρ(bcp) for **49** and **47**: 0.0386 *e*/Bohr^3 and 0.0501*e*/Bohr^3, respectively; Δε(bcp) for **49** and **47**: 0.0898 and 0.0979, respectively]. The smaller decrease in the C–H electron density and ellipticity for complex **49** indicates a reduced agostic donation. The QTAIM charges for C^8 and H^8 indicate a significant increase in negative charge on C^8 by 0.087 *e*, compared with the ligand [increase in the C^8 negative charges $q(C^8)$ in **47** and **42**: 0.083 *e* and 0.071 *e*, respectively]. However, the positive charge q(H) shows a significant change of 0.053 *e* in **49** [0.060 and 0.016 *e* in **47** and **42**, respectively]. The increase in the C^8 negative charge originates from the electron donating effect associated with the σ-electron donating substituent, $B(OH)_3^-$.

Looking at the NBO characteristics, the agostic donation is slightly greater than for complex **42** (Table 6.4a) [*E*(2) values for C–Hσ to the Pd–Cl_{trans}σ* and to the Pd–Cl_{cis}σ*orbitals: 64.0 and 13.81 kcal mol^{-1}, respectively; c.f. 58.60 and 10.0 kcal mol^{-1}, respectively in **42**] but slightly less than complex **48** [*E*(2) values: 70.17 and 13.80 kcal mol^{-1}, respectively]. However, the syndetic donation is significantly larger in **49** compared to **42** [C^7–C^8π to the Pd–Cl_{trans}σ* and Pd–Cl_{cis}σ* orbitals: 41.92 and 16.0 kcal mol^{-1}for **49**, respectively; 20.33 and 6.48 kcal mol^{-1} for **42**, respectively**]**. For the back-donation from Pd LP's to the C–Hσ* orbital, there is a decrease in donation in **49** compared to **42** [*E*(2) values for donations from LP(3) and LP(4) Pd to the C–Hσ* orbital: 2.53 and 2.70 kcal mol^{-1}, respectively in **49**; 2.85 and 4.87 kcal mol^{-1}, respectively in **42**]. Interestingly, below the coordination plane, a slightly shorter distance between Cl···HO is observed [distance in **49** and **42**: 2.073 and 2.092 Å, respectively]; there is a small increase in donation from Cl to O–Hσ* [*E*(2) values: 17.80 and 16.63 kcal mol^{-1}, respectively].

Moving further to π-electron donating S^- substituted complex **50**, the Pd····H^8 distance lengthens [2.180 Å; c.f. 1.819 Å in **42**] and Pd···C^8 becomes shorter, from 2.240 Å in **42** to 2.146 Å in **50** (Figure 6.8, Table 6.2). The shorter Pd···C^8 distance now lies within the range of η^1-complexes of palladium.[139] These changes are associated with the variations in angles and torsions as the N=C^1–C^{8a}–C^8 dihedral angle becomes larger [18.5; c.f. 15.1° in **42**], the C^1–C^{8a}–C^8–H^8 becomes significantly larger [57.0°; c.f. 38.2° for **42**] and the C–H deformation angle, H^7–C^7–C^8–H^8 also becomes larger [–43.7; c.f. –27.2° in **42]**. However, the plane angle is slightly decreased from 34.5° in **42** to 33.6° in **47**, and the Cl–Pd–N=C torsion angle is barely affected at –24.9° from –25.2° (**42**). Regarding the separation angles, the Pd···C–H angle increases to 76.8° [c.f. 54.0° in **42**] and the Pd···H–C^8 angle decreases to 73.4 from 95.2° (**42**). Below the coordination plane, the Cl^2···HO distance is slightly decreased to 2.010 Å from 2.092 Å (**42**), however, the angle Cl^2···HO becomes slightly more linear at 152.5 c.f. 146.9° (**42**). Looking at the spectroscopic data, there is a smaller decrease in ^1JC–H on ligand complexation and a smaller reduction in the C–H stretching frequency with respect to the free ligand compared to that which occured for **42** [Δ^1JC–H and ΔυC–H values for **50**: 18.5 Hz and 248.5 cm^{-1}, respectively; c.f. 36.2 Hz and 670.6 cm^{-1}, respectively for **42**].

The QTAIM properties for **50** indicate a bcp for Pd···C^8 (Figure 6.9) with greater electron density than in **49** (σ-electron donating substituent, $B(OH)_3^-$) [ρ(bcp) value in **50** and **49**: 0.0969 and 0.0844 *e*/$Bohr^3$, respectively] (Table 6.3). The ellipticity value is now significantly less than **49** [0.1174 and 1.0045, respectively] indicating a stronger Pd···C^8 interaction in the former. Inspection of C–H^8 bcp properties, the decrease on complex formation for both the electron density and the Laplacian of the electron density is reduced in magnitude [Δρ(bcp) and $\Delta\nabla^2$ρ(bcp) values: 0.0208 *e/*$Bohr^3$ and –0.1422 *e*/$Bohr^5$ in **50**, respectively; 0.0386 *e*/$Bohr^3$ and –0.2602 *e*/$Bohr^5$ in **49**, respectively; 0.0477 *e/*$Bohr^3$ and –0.3910 *e*/$Bohr^5$ in **42**, respectively] and a smaller increase in the ellipticity values in the complex compared to the ligand [ε(bcp): 0.0413; 0.0898 and 0.0933 in **49** and **42**, respectively]. The QTAIM charges for **50** indicate an increase in both the C^8 and H^8 charges where the C^8 charge becomes more negative and that for H^8 becomes more positive with respect to the values in the ligand, but these changes are slightly less than were seen in complex **49** (σ-electron donating substituent $B(OH)_3^-$) [change in the C^8 charge: –0.049 and –0.077 *e*, respectively; change in the H^8 charge: 0.048 and 0.052 *e*, respectively]. Here, it is noted that the H^8 hydrogen charge in the free ligand of **50** is slightly negative, but in the complex it becomes positive, indicating a change in the overall electronic environment [$q(H^8)$: –0.003 *e* for the free ligand; 0.051 *e* for complex **50**]. The QTAIM charges also reveal a significant decrease in the metal charge which is now reduced to 0.570 *e* compared to **42** (OH) [*q*(Pd) in **42**: 0.641 *e*]. This decrease is accompanied by delocalisation of the electron density onto the metal as a result of the stronger π-electron donating effect by $B(OH)_3^-$. However, the overall QTAIM data indicate a weakening in the agostic interaction.

It is noted that the Laplacian of the electron density at the Pd···C^8 bcp is significantly decreased in the case of the electron donating substituents [$B(OH)_3^-$ and S^- in **49** and **50** respectively] compared to other complexes studied so far (Table 6.3). This decrease in the

Laplacian is depicted in the contour plot (Figure 6.10) where comparatively greater accumulation of the charge density between C^8 carbon and the Pd is indicated.

The NBO analysis for **50** indicates a substantial decrease in the donation from the C–Hσ to the Pd–Cl_{trans}σ* and Pd–Cl_{cis}σ*orbitals [*E*(2) value: 0.0 and 3.10 kcal mol^{-1} in **48**, respectively; c.f. 64.0 and 13.81 kcal mol^{-1} for **49**, respectively; and 58.60 and 10.00 kcal mol^{-1}, respectively in **42**] (Table 6.4a). However, the NBO analysis now shows a covalent bond between Pd and C^8 with a Wiberg bond index of 0.3858 [0.2770 and 0.2281 in **49** and **42**, respectively]. This bond is involved in several donor-acceptor interactions [e.g. the largest donation as Pd–C donor found for Pd–C^8 to Pd–Cl_{cis}σ*, *E*(2) value: 56.60 kcal mol^{-1}; as acceptor LP(4) Cl to Pd–C^8σ*, *E*(2) value: 100.63 kcal mol^{-1}]. In **50**, the significant donations into Pd···C^8 seem responsible for the decrease of the palladium charge [*q*(Pd) for **50**, **49** and **42** are 0.570, 0.616 and 0.641 *e*, respectively]. Thus, comparing the σ-electron donating $B(OH)_3^-$ and π-electron donating S^- substituents, it is seen that the agostic and syndetic donations become higher in the case of the former substituent while the later significantly reduces these donations and instead favours stronger Pd to C^8 covalency.

Finally, to see the maximum of the electron donating effect in the (N)–OH series, two S^- were placed at *ortho* C^7 and *para* C^5 positions on the aromatic ring, complex **51** (Figure 6.11a). The structural features (Table 6.2) indicate a significant increase in the Pd····H^8 separation [2.356 Å; c.f. 2.180 and 1.819 Å in **50** and **42**, respectively], however, the Pd···C^8 distance is only slightly increased in comparison to **50** [values: 2.172 and 2.146 Å in **51** and **50**, respectively; c.f. 2.240 Å in **42**]. These changes are accompanied by the planes angle (aromatic ring plane/metal coordination plane) becoming larger by almost 10° compared to **50** [values: 43.5 and 33.6° in **51** and **50**, respectively]; C^1–C^{8a}–C^8–H^8 torsion becoming smaller by 4.6° [values in **51** and **50**: 52.4 and 57.0°, respectively] and the N=C^1–C^{8a}–C^8 torsion increasing to 23.8° from 18.5° (**50**). The separation angles indicate an increase in the Pd···C^8–H^8 angle and a decrease in the Pd···H–C angle [Pd····C–H values for **51** and **50**: 85.4 and 76.8°, respectively; Pd····H–C values for **51** and **50**: 66.8 and 73.4°, respectively].

The spectroscopic properties for **51** (Table 6.2) indicate a decrease of 14.4 Hz in ^1JC–H (from respective ligands) compared to **50** where the decrease was found to be 18.5 Hz. The C–H stretching vibration shift to lower energy on complex formation is substantially less than in **50** [difference of 156.7 cm^{-1}; c.f. 248.5 and 670.6 cm^{-1} in **50** and **42**, respectively]. Both these spectroscopic properties indicate a weakening of the agostic interaction. The QTAIM analysis indicates a bond path between Pd···C^8 (Figure 6.11b) the properties of which are almost identical to **50** (Table 6.3). The most noticeable change in the QTAIM analysis is a further decrease in the metal charge [0.534 and 0.570 *e* in **51** and **50**, respectively; c.f. 0.641 *e* in **42**]. The Laplacian contour plot for **51** (Figure 6.11c) shows an accumulation of charge density indicating an attractive interaction between the Pd and C^8. Here, again, the NBO analysis shows an even smaller agostic donation from the C–Hσ to the $Pd–Cl_{cis}σ^*$ orbital [$E(2)$ values for **51** and **50**: 2.70 and 3.10 kcal mol^{-1}, respectively]. Also, there is a similar kind of $Pd–C^8$ covalency with a significantly greater Wiberg bond index value for **51** compared to that found in **50** [Wiberg bond index value for $Pd\cdots C^8$ in **51**, **50** and **42**: 0.4555, 0.3858 and 0.2281, respectively].

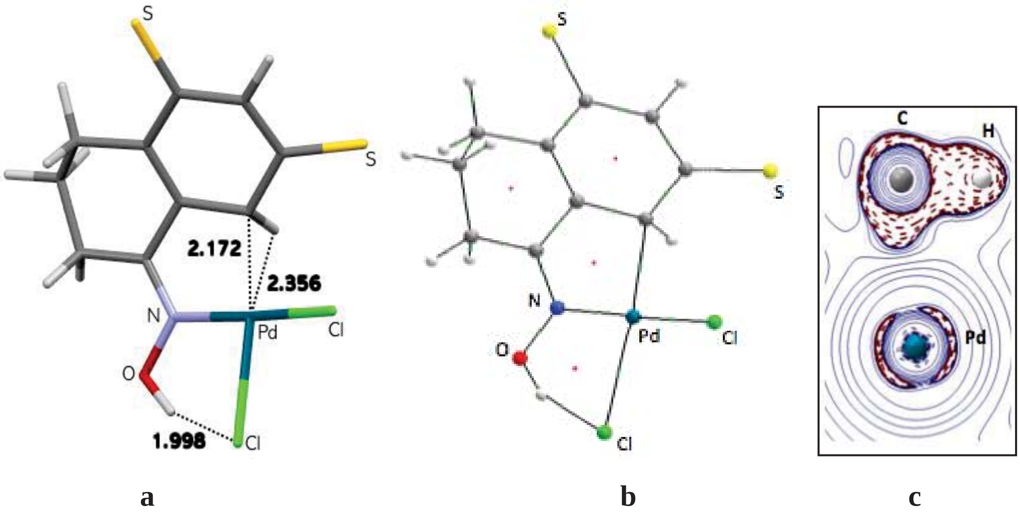

Figure 6.11 a) Optimised geometry and important separations (Å); b) QTAIM olecular graph showing bond paths for the $C^8\cdots Pd$ separation; c) 2D contour plot of the Laplacian of the electron density for the $C–H^8$ and metal interaction in complex **51**.

6.4.4 Steric Effects on the Aromatic Ring at the C^7 Position, Complexes 52–54

Earlier synthetic studies indicated that the cyclopalladation reaction was halted when the sterically hindering group was increased in size at the C^7 position of the aromatic ring of the 1-tetralone oxime ligand.[124] Therefore, it was of particular interest to place alkyl groups of increasing size at the C^7 position to see the steric influences on the agostic interaction.

The structural features in Table 6.2 indicates that in going from H (**42)**, Me (**52**), isopropyl (**53**) to *tert*-butyl (**54**), there is little effect of steric size on the Pd–N bond length, with only a small decrease seen in the case of the *tert*-butyl group [Pd–N bond length in **52–54**: 2.011, 2.011 and 2.006 Å, respectively; 2.015 Å for **42**]. In a similar way, there is little decrease in the $OH\cdots Cl^2$ distance below the coordination plane, which shows that the hydrogen bonding component holds the (N)–OH group at a fixed position [$Cl\cdots HO$ distance in **52**–**54**: 2.069, 2.067 and 2.076 Å, respectively; c.f. 2.092 Å in **42**] (Figure

6.12). However, there are significant changes seen in the Pd···H^8 and Pd···C^8 separations as the ligands rotate downwards with the increasing steric size from methyl to *tert*-butyl substituents. The trend is that both the separations become longer from methyl to *tert*-butyl, i.e. the Pd···H^8 separations in **52**–**54** are 1.894, 1.899 and 2.128 Å, respectively; c.f. 1.819 Å in **42**, and the Pd···C^8 separations in **52**–**54** are 2.321, 2.345 and 2.457 Å respectively; c.f. 2.240 Å in **42**, however, it is noted that in the case of the *tert*-butyl group the changes are more pronounced.

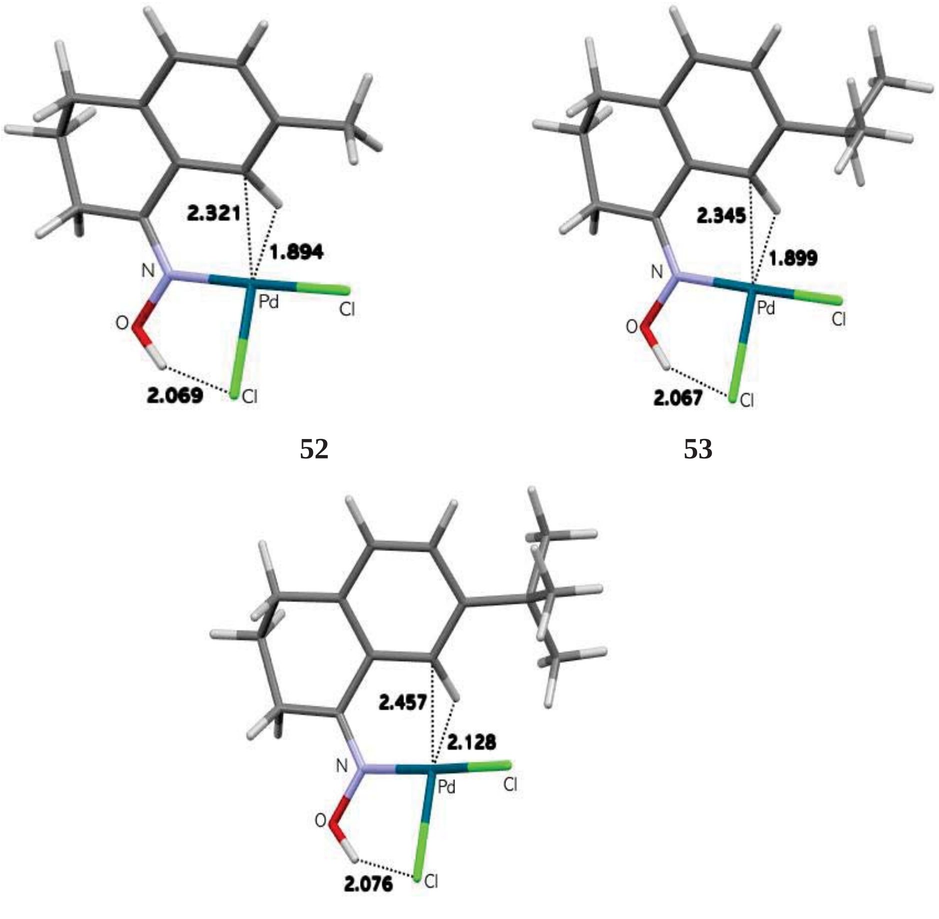

52

53

54

Figure 6.12 Optimised geometries with important separations (Å) for complexes **52**–**54**.

These separation changes occur when the C–H^8 deformation angle decreases from Me to *tert*-butyl (**52**–**54**) [values: –21.6, –18.0 and –8.1°, respectively; c.f. –27.2° for **42**], the plane angle increases from **52** to **54** [values: 35.5, 35.8 and 46.5°, respectively; c.f. 34.5° for **42**] and in a similar way the N=C–C–C^8 also increases from **52**–**54** [values: 18.2, 18.4 and 26.8, respectively; 15.1 in **42**]. Regarding the separation angles, the Pd···C–H^8 angle slightly increases slightly in **54** while remaining almost unchanged in **52** and **53** compared to **42** [values for **52**–**54**: 54.2, 53.3 and 59.8°, respectively; 54.0° in **42**]. In the case of the

Pd···H–C^8 angle, there is an increase in **52** and **53** but a decrease in **54** compared to **42** [Pd···H–C angle values in **52**–**54**: 96.7, 98.0 and 93.4°, respectively; c.f. 95.2° in **42**].

Computed IR and NMR spectroscopic properties for **52**–**54** show a decrease in the move to highfield for the chemical shift in the ^{1}H NMR spectrum as the steric size increases, with the value for the CMe$_3$ ligand recording a small downfield shift compared to the free ligand value [Δδ: 0.65 ppm] (Table 6.2). More importantly, the changes in the ^1JC–H coupling constants show a gradual decrease when compared to the free ligands [Δ^1JC–H values of 30.1, 29.7 and 16.9 Hz in **52**–**54**, respectively; c.f. 36.2 for **42**]. The calculated C–H stretching frequencies also show a similar trend of a decrease in the complexes compared to the ligands, becoming dramatically closer to the free ligand value for CMe$_3$ (**54)** [Δ νC–H: 517.2, 516.8 and 261.8 cm^{-1} for **52**–**54**, respectively; c.f. 670.6 cm^{-1} for **42**]

The QTAIM data (Table 6.3) indicate that the bond paths for the Pd····H^8 separations in **52** and **53** are similar to **42**, but the bond path switches to the Pd···C^8 separation in the case of **54**. This occurs even though the Pd···H^8 and Pd···C^8 distances both increase in **54**. Analysing the QTAIM properties, it is seen that for both the Pd···H^8 bcps in **52** and **53**, the electron density, the Laplacian of the electron density and the energy density values decrease compared to **42** [ρ(bcp), ∇^2ρ(bcp) and *H*(bcp) in **52**: 0.0694 *e/*Bohr^3, 0.2256 e/Bohr^5 and –0.0141 Hartree/Bohr^3, respectively; ρ(bcp), ∇^2ρ(bcp) and *H*(bcp) in **53**: 0.0676 *e*/Bohr^3, 0.2201 *e*/Bohr^5 and –0.0134 Hartree/Bohr^3, respectively; c.f. 0.0820 *e*/Bohr^3, 0.2631 *e*/Bohr^5, –0.0210 Hartree/Bohr^3, respectively in **42**]. For the Pd···C^8 bcp in **54**, the electron density, the Laplacian of the electron density and the energy density values are much less than in **42** [ρ(bcp), ∇^2ρ(bcp) and *H*(bcp) for **54**: 0.0478 *e*/Bohr^3, 0.1402 *e*/Bohr^5 and –0.0069 Hartree/Bohr^3, respectively]. Comparing the Laplacian contours for **52–54** (Figure 6.14), it is seen that the accumulation of the charge density between the C–H and the metal is substantially decreased in **54** compared to **52** and **53**.

The QTAIM properties for the C–H^8 bcp (Figure 6.13; Table 6.3), in comparison to the corresponding ligands, show a similar magnitude decrease in the change in electron density for **52** and **53** but for **54**, the difference is significantly less [decrease in **52**–**54**: 0.0379, 0.0380 and 0.0207 *e*/Bohr^3, respectively; c.f. 0.0477 *e*/Bohr^3 in **42**]. The change in the Laplacian of the electron density and the ellipticity change also become smaller in going from **52** to **54** compared to **42**. There is a decrease of only –0.1385 *e*/Bohr^5 in the Laplacian of the electron density and an increase of 0.0404 in the ellipticity value in **54** compared to **42.** It is therefore seen that the agostic bond becomes weaker as the size of the steric group increases at the C^7 position (*ortho* to the C^8–H bond).

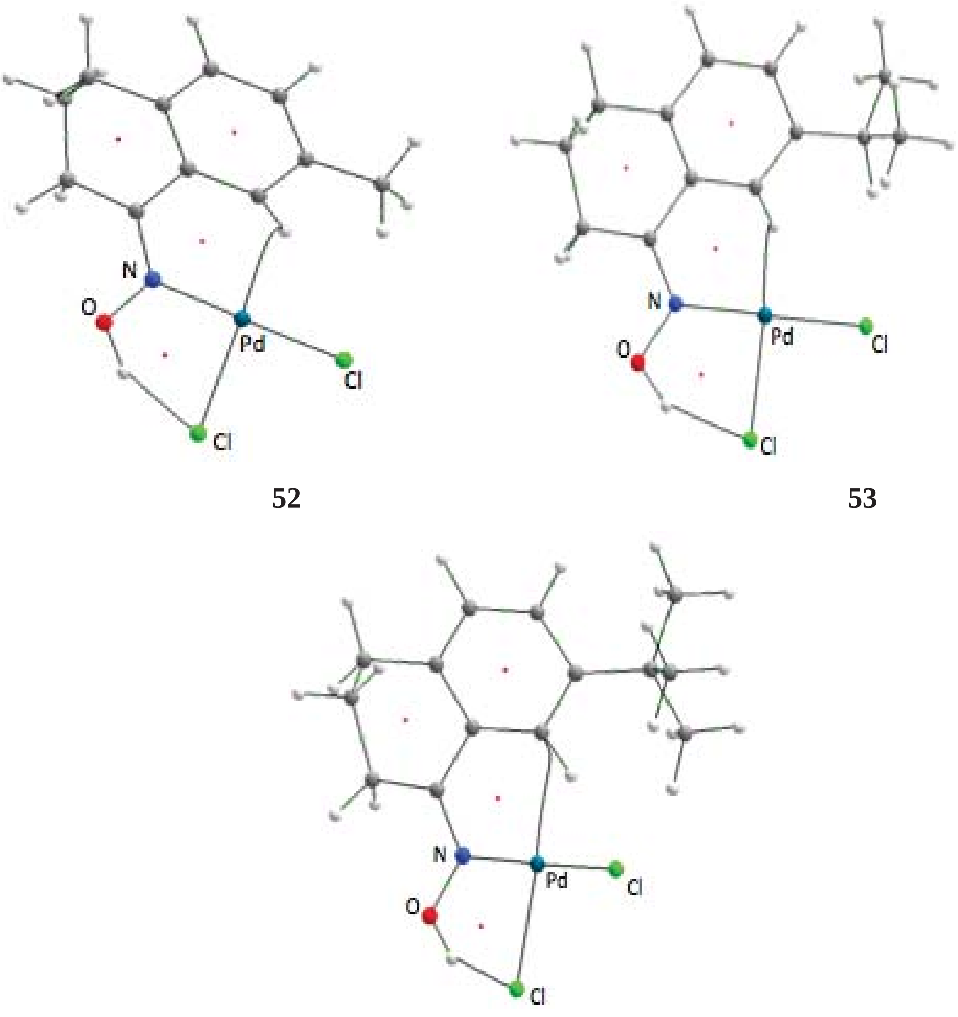

52 **53**

54

Figure 6.13 QTAIM molecular graphs showing the bond paths for Pd···H^8, Pd···C^8 and OH–Cl^2 separations for **52**–**54**.

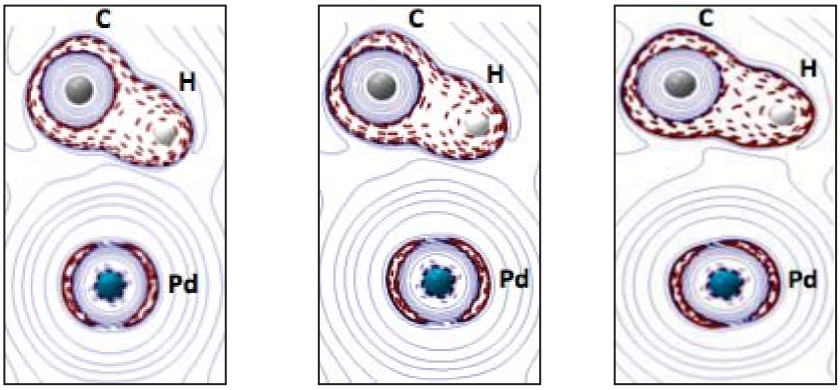

52 **53** **54**

Figure 6.14 2D contour plots of the Laplacian of the electron density for the C–H^8 and Pd interaction in **52**–**54**.

The NBO data (Table 6.4a,b) also indicate a significant decrease in the agostic donations from the C–Hσ to the Pd–Cl$_{trans}$σ* and Pd–Cl$_{cis}$σ*orbitals, on going from **42** (where the *E*(2) values for the C–Hσ to Pd–Cl$_{trans}$σ* and Pd–C$_{cis}$σ*donations were 58.60 and 10.0 kcal mol^{-1}, respectively) to **52** [comparable *E*(2) values: 44.46 and 8.66 kcal mol^{-1}, respectively]. In **53** these are even smaller, [*E*(2) values: 41.51 and 8.14 kcal mol^{-1}, respectively) and then a dramatic decrease for **54** where the values become substantially smaller, at 19.76 and 5.07 kcal mol^{-1}, respectively consistent with the spectroscopic and QTAIM analyses where the change between the C–H^8 in the complex was insignificant from the ligand.

However, for the syndetic donations, there is almost no change in going from Me (**52**) to CHMe$_2$ (**53**) and a small change from CHMe$_2$ (**53**) to CMe$_3$ (**54**) [*E*(2) values for the donation from C^7–C^8**π** to the Pd–Cl$_{trans}$σ* and Pd–Cl$_{cis}$σ* orbitals: 18.34 and 5.88 kcal mol^{-1} in **52**, respectively; 17.78 and 5.89 kcal mol^{-1} in **53**, respectively; 15.01 and 4.25 kcal mol^{-1} in **54**, respectively; 20.33 and 6.48 kcal mol^{-1} in **42**, respectively]. Thus, it is noted that the increasing steric effects at the C^7 position decreases the agostic donation but only slightly affects the syndetic donations. The decrease in the agostic donation is correlated with the decrease in the overlap matrix values: i.e. the overlap matrix value associated with the C–Hσ to Pd–Cl$_{trans}$σ* donation is 0.3404 compared to **42** which has a value of 0.4488 (refer to Table 6.7 in Appendix D.2). Thus, the steric effect of the bulky *tert*-butyl group at the *ortho* position prevents a constructive spatial overlap between the C–H and the metal···Clσ* NBOs. For the back bonding Pd to C–Hσ* donation, there is also a significant decrease in going from Me to CMe$_3$ and, similarly to the other donations, in the case of CMe$_3$, the decrease was more significant [*E*(2) values from LP(3) and LP(4) Pd to C–Hσ* donations: 2.97 and 2.66 kcal mol^{-1} in **52**, respectively; 3.31 and 2.44 kcalmol^{-1} in **53**, respectively; 0.99 and 0.47 kcalmol^{-1} in **54**, respectively; c.f. 2.85 and 4.87 kcal mol^{-1} in **42**, respectively]. Regarding the below-plane hydrogen bonding, there is only a small increase for all the complexes, **52**–**54** compared to **42** [*E*(2) values for the Cl to O–Hσ* donation: 17.82, 17.91 and 17.22 kcal mol^{-1} for **52**–**54**, respectively; c.f. 16.63 kcal mol^{-1} in **42**].

6.4.5 Electronic Effects for the (N)–OMe Ligand, Complexes 55–58

It was seen with the (N)–OH series that the electronic effects on the aromatic ring affect the strength of the agostic interaction. However, there was a (N)–OH···Cl hydrogen bonding component present which was strong enough to 'lock' the (N)–OH and Cl groups. Therefore, it was of interest to ascertain the electronic effects by 'unlocking' the (N)–

OH···Cl component by using (N)–OMe ligand. As for the (N)–OH ligands, electron withdrawing substituents (σ and π-electron withdrawal SO_2Cl and $N{=}NPO(OEt)_2$, respectively) and electron donating substituents $B(OH)_3^-$ and S^-, respectively were placed at the C^5–H position (Scheme 5.1). In the (N)–OMe ligand, complex **43**, it is seen that the ligand is shifted upwards and the C–H^8 bond is positioned over the metal coordination plane. In general, in the case of the (N)–OMe ligand, the structural features show almost no change in the Pd–N bond length in the case of electron withdrawing substituents, however, there is a small decrease for the electron donating substituents. In addition, there are some significant changes seen in the Pd–Cl bond length for the case of the electron donating substituents.

As observed earlier for **43**, by changing (N)–OH to (N)–OMe, the Pd···H^8 separation becomes longer at 1.841 Å than the 1.819 Å in (**42**) (Figure 6.1a; 6.4a), however, the Pd···C^8 separation becomes slightly shorter [2.224 and 2.240 Å in **43** and **42**, respectively]. Replacing the C^5–H atom in **43** with the σ-electron withdrawing SO_2Cl group (complex **55**), both the Pd···H^8 and Pd···C^8 separations become slightly smaller [Pd···H^8 values in **55** and **43**: 1.833 and 1.841 Å, respectivley; Pd···C^8 values in **55** and **43**: 2.205 and 2.224 Å, respectively] (Table 6.2; Figure 6.15). The changes in torsion angles are similar to those found in the (N)–OH complexes. There is a similar increase in the C–H bond length as was found for the analogous complexes of the (N)–OH series.

The spectroscopic data (Table 6.2) show that there is a small increase in agostic donation. The coupling constant becomes slightly smaller [difference from ligands for **55** and **43**: 35.1 Hz and 33.6 Hz, respectivley]; the calculated C–H stretch shifts to lower energy by 698.3 cm^{-1} [c.f. 659.9 cm^{-1} for **43**]. Similar spectral changes were observed for (N)–OH complexes **42** and **47** [$\Delta^1 J$C–H values for (N)–OH (**42**) and (N)–OH with SO_2Cl (**47**): 36.2 and 38.2 Hz, respectively; C–H stretching shifts for (N)–OH **(42)** and (N)–OH with SO_2Cl (**47**): 670.6 and 725.2 cm^{-1}, respectively]. The small spectral differences thus indicate a small substituent effect when substituting the (N)–OH to the (N)–OMe ligand.

Looking at the QTAIM analysis (Table 6.3), there is a bcp for the Pd···C^8 separation (Figure 6.16) with slightly increased electron density and energy density values for **55** compared to **43** [ρ(bcp) and *H*(bcp) values: 0.0851 *e*/Bohr^3 and –0.0273 Hartree/Bohr^3, respectively; c.f. 0.0820 *e*/Bohr^3 and –0.0244 Hartree/Bohr^3, respectively for **43**]. The Pd····C^8 bcp properties for **55** are slightly different to the Pd···H^8 bcp properties for the (N)–OH analogue complex **47** [ρ(bcp) and *H*(bcp) values for **47** ((N)–OH with SO_2Cl at C^5): 0.0841 *e*/Bohr^3 and –0.0225 Hartree/Bohr^3, respectively]. The C–H^8 bond critical point properties show a small decrease in the electron density ρ(bcp) in complex **55** as compared to the free ligand [decrease in ρ(bcp) for **55** and **43**: 0.0491 and 0.0464 *e*/Bohr^3, respectivley] which is similar to that seen in (N)–OH complexes **42** and **47** [decrease in ρ for **47** and **42**: 0.0510 and 0.0479 *e*/Bohr^3, respectively]. The changes in the Laplacian of the electron density and ellipticity values for the C^8–H bcp in the (N)–OMe complexes are also similar to those found for the (N)–OH complexes [decrease in the negative value for the Laplacian of electron density for **55** and **47**: 0.3432 and 0.3310 *e*/Bohr^5, respectively; an increase in the ellipticity value for **55** and **47**: 0.0907 and 0.0979, respectively].

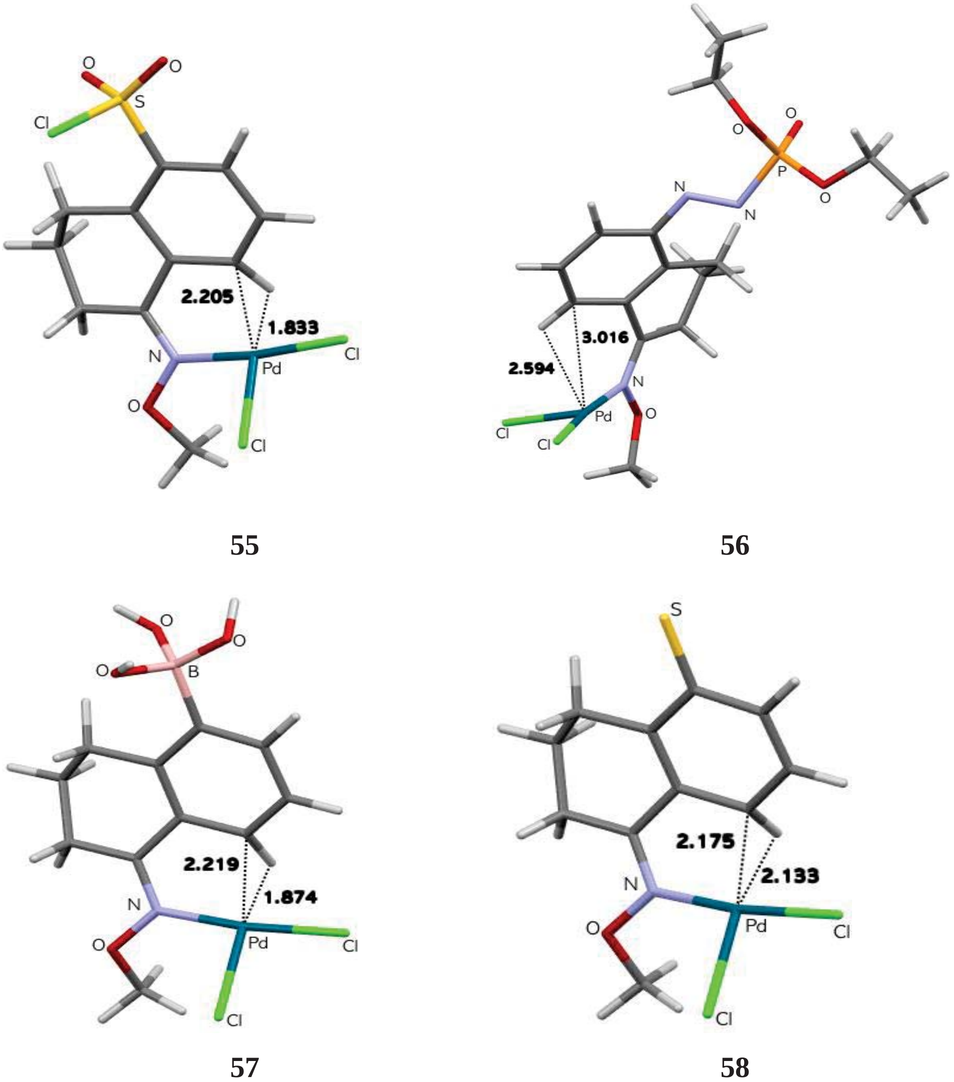

55 **56**

57 **58**

Figure 6.15 Optimised geometries with important separations (Å) for **55**–**58**.

The NBO analysis for **55** (Table 6.4) shows significant increases in both the agostic donations [*E*(2) values for the C–Hσ to Pd–Cl$_{trans}$σ* and Pd–Cl$_{cis}$σ* donations: 72.11 and 13.80 kcal mol^{-1} in **55**, respectively; c.f. 57.68 and 9.45 kcal mol^{-1} in **43** respectively] and in the syndetic donation [*E*(2) values for the C^7–C^{8}π to Pd–Cl$_{trans}$σ* and Pd–Cl$_{cis}$σ* donations: 26.73 and 10.26 kcal mol^{-1} in **55**, respectively; c.f. 18.94 and 5.95 kcal mol^{-1} in

43, respectively]. These increases in the agostic donations were also seen in (N)–OH complex **47** [*E*(2) values: 75.57 and 14.98 kcal mol^{-1}, respectively] but both of these values are slightly greater in **47**, and this would appear to be the only effect of the rotation allowed by removal of the (N–)OH···Cl hydrogen bonding, with the syndetic donation essentially unchanged [*E*(2) values for the C^7–$C^8\pi$ to Pd–$Cl_{trans}\sigma^*$ and Pd–$Cl_{cis}\sigma^*$ donations in **47**: 27.55 and 10.47 kcal mol^{-1}, respectively].

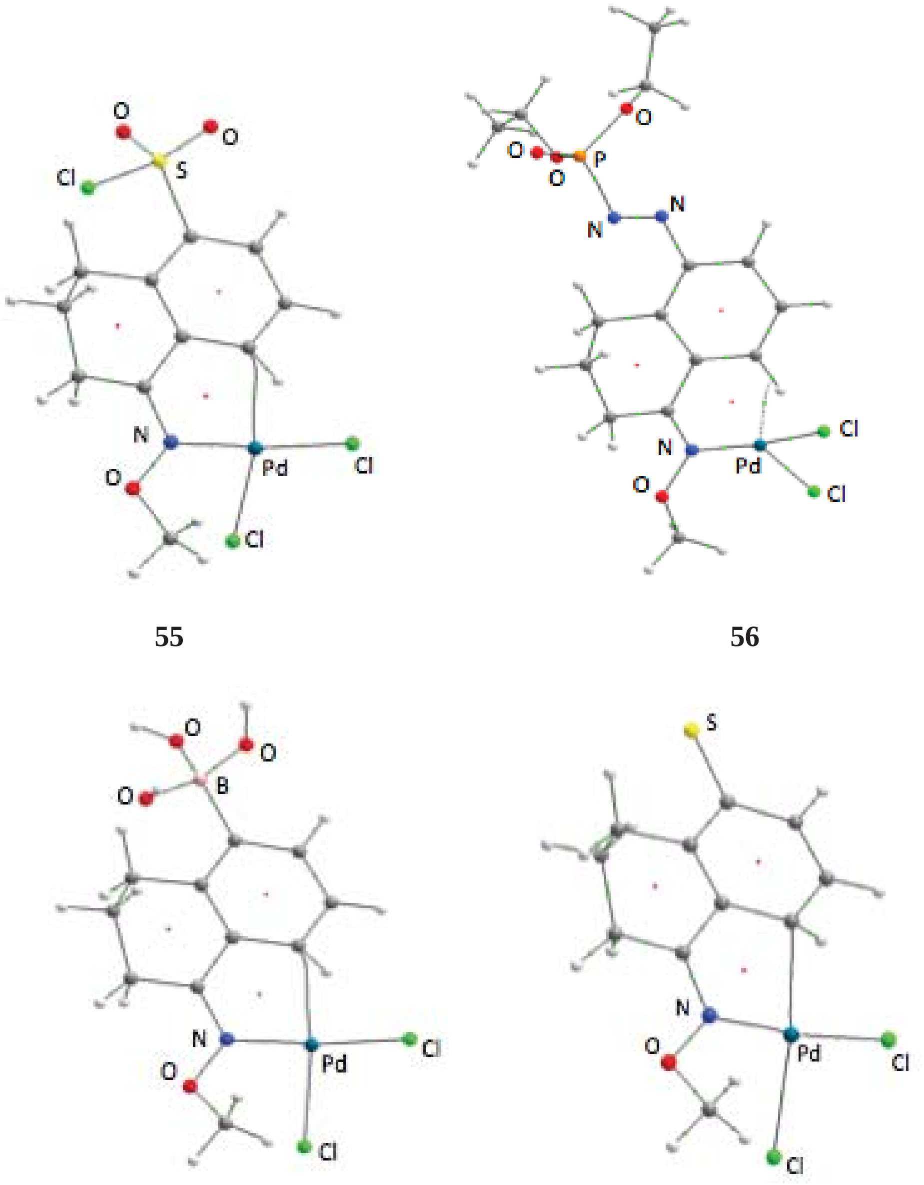

55 **56**

57 **58**

Figure 6.16 QTAIM molecular graphs showing the bond paths for C^8····Pd separation in **55–58**.

Placing the π-electron withdrawing N=NPO(OEt)$_2$ substituent on the ligand, complex **56**, causes a dramatic change in the structure on changing from the (N)–OH to the (N)–

OMe group. In complex **56**, the (N)–OMe ligand swings under the coordination plane and the aromatic ring above it (Figure 6.15). The aromatic ring now lies directly above the Pd centre with the C^8–H bond pointing towards Cl^2. This new orientation for the ligand and the associated Pd···H^8 and Pd···C^8 distances of 2.594 and 3.016 Å, respectively, suggest the formation of an anagostic interaction (Table 6.2).[126]

The spectroscopic properties for **56** (Table 6.2) indicate a slightly larger ^1JC–H for the complex [144.3 Hz; c.f. 140.9 Hz for ligand] and a larger downfield chemical shift for H^8 [$\Delta\delta$: 2.90 ppm]. These NMR characteristics are typical of anagostic interactions which are retained in the solution. Also, the IR stretching frequency is decreased by only 16 cm^{-1}, similar to the other anagostic structures (Chapter 3).[126]

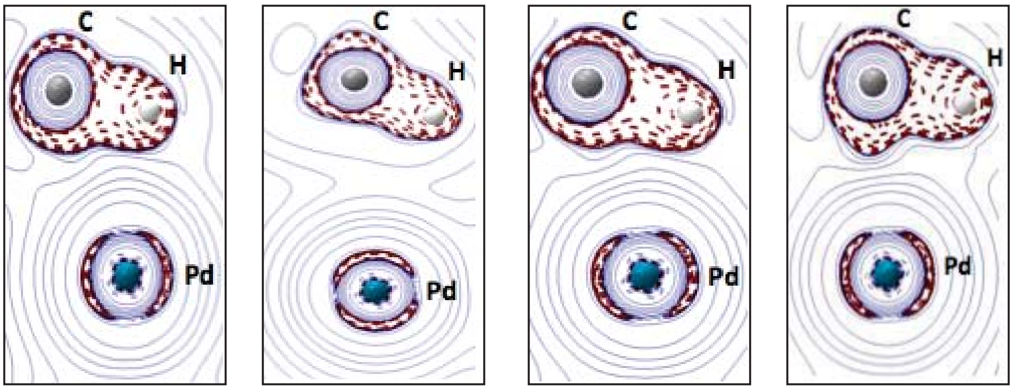

55 **56** **57** **58**

Figure 6.17 2D contour plots of the Laplacian of the electron density for the C–H^8 and Pd interaction in **55–58**.

The QTAIM characteristics (Table 6.3) indicate a Pd···H^8 bcp (Figure 6.17) with unsurprisingly less electron density [0.0185 e/Bohr^3]. The positive values for both the Laplacian of the electron density and the energy density [values: 0.0524 e/Bohr^3 and 0.0004 Hartree/Bohr^3, respectively] indicate no covalency is involved. The C^8–H bcp properties also indicate no noticeable changes in the electron density, Laplacian of the electron density, and the ellipticity values; all these features are again indicative of anagostic interactions.[126] The NBO analysis shows very small donations for both agostic and syndetic interactions as the $E(2)$ values for the C–Hσ to Pd–$Cl_{trans}\sigma^*$ and Pd–$Cl_{cis}\sigma^*$ donations are 1.15 and 1.03 kcal mol^{-1}, respectively and for the C^7–$C^8\pi$ to Pd–$Cl_{trans}\sigma^*$ and Pd–$Cl_{cis}\sigma^*$ donations: 0.76 and 0.43 kcal mol^{-1}, respectively. These smaller donations also resemble those found for other calculated anagostic structures.[126]

Turning to the σ-electron donating $B(OH)_3^-$ substituent, complex **57**, the ligand straightens upwards (Figure 6.15) in comparison to the (N)–OH complex **49** with the *para* substituted $B(OH)_3^-$ group **49**, which makes the Pd···C^8 separation smaller but the

Pd····H^8 separation longer [Pd···C^8 distance in **57** and **43**: 2.219 and 2.224 Å, respectively; Pd···H^8 distance in **57** and **43**: 1.874 and 1.841 Å, respectively; c.f. Pd···C^8 distance for **49** [(N)–OH with $B(OH)_3^-$] and **42** (OH): 2.208 and 2.240 Å, respectively; Pd···H^8 distance for **49** and **42**: 1.901 and 1.874 Å, respectively]. The associated separation angles Pd····H^8–C and Pd···C–H^8 also change a little [Pd····H^8–C^8 angles: 117.7 and 116.7° in **57** and **43**, respectively; Pd····C–H^8 angles: 57.6 and 55.7° in **57** and **43**, respectively] and the angle between aromatic ring and metal coordination planes is decreased by 6° in comparison to **43** which is a slightly greater decrease compared with the analogous (N)–OH complex **49**, where the plane angle was only decreased by 1°.

The calculated spectroscopic data indicate a small decrease in ^1JC–H for the complex in comparison to the free ligand value [decrease of 30.7 and 33.6 Hz for **57** and **43**, respectively] and also a decrease in the C–H stretching shift to lower energy [553.4 cm^{-1} and 659.9 cm^{-1} for **57** and **43** respectively]. In comparing the $B(OH)_3^-$ substituent (**57**) for (N)–OH (**42**) and (N)–OMe (**43**), the agostic interaction appears stronger with (N)–OMe as compared to the free ligand, the decrease in ^1JC–H, and the C–H frequency shift to lower energy are more significant [differences: Δ^1JC–H is 31.0 Hz for **57**; c.f. 40.4 Hz for **49** and the ΔυC–H is 553.4 cm^{-1} for **57**; c.f. 494.9 cm^{-1} in **49**].

The QTAIM characteristics for **57** (Table 6.3) indicate that the Pd···C^8 bcp (Figure 6.16) is similar to **43**, showing analogous changes in properties as were found in the case of OH-$B(OH)_3^-$ complex **49**. The change in the electron density at the Pd···C^8 bcp in **57** is slightly less compared to the (N)–OH case [a difference between $B(OH)_3^-$ substituted and unsubstituted complexes for OMe (**57** and **43**) and OH (**49** and **42**) ligands: 0.0007 *e*/$Bohr^3$ and 0.0024 *e*/$Bohr^3$, respectively,]. The Laplacian of the electron density and the energy density values also change slightly in the case of the (N)–OH complex. The C–H^8 bond critical point properties show a slightly greater decrease in the electron density in the OMe-$B(OH)_3^-$ complex **57** as compared with the free ligand, compared to the change for OH-$B(OH)_3^-$ complex **49** [a decrease of 0.0433 and 0.0386 *e*/$Bohr^3$, respectively]. This slightly larger decrease in the C–H^8 electron density points to increased agostic donation to the metal. The QTAIM charges show similar magnitude of changes as seen in **49**.

For the NBO analysis of **57**, it is seen that agostic donations (Table 6.4) become slightly greater in comparison to the H substituent [*E*(2) values for the donation from the C–Hσ to Pd–Cl_{trans}σ* and Pd–Cl_{cis}σ* orbitals: 66.48 and 14.02 kcal mol^{-1}, respectively; c.f. 57.68 and 9.45 kcal mol^{-1} in **43**, respectively] but less than the σ-electron withdrawing substituent SO_2Cl (**55**) which has *E*(2) values of 72.11 and 13.80 kcal mol^{-1}, respectively. However, the syndetic donation significantly increases in **57** [*E*(2) values for the C^7–C^8π to Pd–Cl_{trans}σ* and Pd–Cl_{cis}σ* donations in **57** and **55**: 34.41 and 13.47 (**57**), respectively;

26.73 and 10.26 kcal mol^{-1} (**55**), respectively; c.f. 18.94 and 5.95 kcal mol^{-1} in **43**, respectively]. A similar increase was also found in the (N)–OH complex with the $B(OH)_3^-$ group (**49**) [*E*(2) values: 27.55 and 10.47 kcal mol^{-1}, respectively; c.f. 20.33 and 6.48 kcal mol^{-1} for **43**, respectively]. Overall, in comparing the σ-electron withdrawing, SO_2Cl and σ-electron donating, $B(OH)_3^-$ substituents, the agostic donation becomes larger in the former whereas the syndetic donations become larger for the latter.

Placing the π-electron donating S^- group at the C^5-position of the (N)–OMe complex **43** causes the Pd···C^8 separation to become shorter [2.175 and 2.224 Å for **58** and **43**, respectively] and the Pd····H^8 separation to become longer [2.133 and 1.841 Å for **58** and **43**, respectively] (Figure 6.15). The shorter Pd···C^8 distance of 2.175 Å is now again well within the range of η^1-complexes of palladium[139] but is slightly longer than found for (N)–OH complex **50** [distance:2.146 Å]. However, the Pd···H^8 separation in **58** is significantly shorter than was seen in **50** [values: 2.133 and 2.180 Å, respectively] which might indicate a different bonding situation (Table 6.4). There is also a significant decrease in the C–H bond length, which is now 1.114 Å, compared to 1.151 Å in **43**, whereas this decrease was a bit larger in the case of (N)–OH complex **50** [a decrease of 0.1 Å in [(N)–OH with S^-] compared to **42**]. Looking at bond angles and torsions, there is a large increase in the C–H deformation angle which is increased by almost 12° compared to **43** and a slight decrease in the plane angle by 3° than in **43**. In comparing these angles with (N)–OH with S^- complex **50**, the C–H deformation angle decreased by almost 16°. However, there was just 1° decrease in the angle between aromatic ring and metal coordination planes in the case of **50**.

The calculated spectroscopic data (Table 6.2) show a difference between complex **58** and the free ligand of 261.7 cm^{-1} (to lower energy), which is significantly less than in **43** [a difference of 660 cm^{-1}]. However, the C–H stretching to lower energy in **58** is just a bit higher than was found in complex **50** where the difference between complex and ligand was 248.5 cm^{-1}. These spectroscopic values show a similar kind of effect for the S^- substituent in both OH and OMe ligands.

The QTAIM analysis shows a bond path between Pd and C^8 (Figure 6.16) with slightly larger values for the electron density and the energy density indicating a stronger interaction [ρ(bcp) for **58** and **43**: 0.0898 and 0.0820 *e*/Bohr^3, respectively; *H*(bcp) for **58** and **43**: –0.0344 and –0.0244 Hartree/Bohr^3, respectively]. The Pd···C^8 bcp electron density and energy density values in **58** are insignificantly smaller than were found in **50** (Table 6.3).

Here again, the QTAIM charges for hydrogen H^8, carbon C^8, and Rh are changed with similar magnitudes as were found in **50** (OH complex with S^-). Analogous to the (N)–OH series with the S^{-} substituent (complexes **50** and **51**), the Laplacian of the electron density for complex **58** also shows the accumulation of charge density between carbon C^8 and palladium in an attractive situation (Figure 6.17).

Interestingly, the NBO analysis shows a well formed Pd–C bond with corresponding donations LP C^8 to the Pd–$Cl_{trans}\sigma^*$ and to the Pd–$Cl_{cis}\sigma^*$ [$E(2)$ values: 113.6 and 32.3 kcal mol^{-1}, respectively] (Table 6.4) contrary to (N)–OH series complex **50** which has a more delocalised Pd···C^8 interaction. In addition, there is a donation from C–H to the Pd–$Cl_{trans}\sigma^*$ and the Pd–$Cl_{cis}\sigma^*$ [$E(2)$ values in **58**: 24.11 and 3.94 kcal mol^{-1}, respectively; 0.0 and 3.10 kcal mol^{-1} in **50**, respectively]. Thus in **58**, there is both a Pd–C^8 bond present as well as an agostic interaction.

6.4.6 Steric and Electronic Effects on the (N)–CMe_3 ligand, Complexes 59–63

Based on the complexes studied so far, the electronic and steric effects on the aromatic ring were studied along with substituents attached to N that provide little steric strain to the system. During the analysis, it was seen that SO_2Cl at the C^5 position increases the agostic as well as syndetic donations, (complexes **47** and **55**), whereas S^{-} at C^5 favours Pd–C covalency and substantially decreases the agostic donations, (complexes **50** and **58**). It was also seen that by increasing the steric size to CMe_3 at the N atom, the Pd–N rotation reduces, resulting in a decrease in the Pd···C^8 separation [2.177 Å (N)–CMe_3 (**44**); c.f. 2.240 Å in (N)–OH (**42**)] and a small increase in the Pd···H^8 distance [1.884 Å; c.f. 1.819 Å in **42**].

The NBO donations indicated a noticeable increase in Pd to C^7–$C^8\pi^*$ donation which went up to 3.04 kcal mol^{-1} in the case of (N)–CMe_3 (**44**) from 1.60 kcal mol^{-1} in the (N)–OH case (**42**) (Table 6.4). There was also a small decrease seen in the back-bonding donation from the Pd to C–$H\sigma^*$ donation [$E(2)$ values: 7.72 and 6.20 kcal $mol^{-1}$for (N)–CMe_3 and (N)–OH, respectively]. The steric influence of CMe_3 at the *ortho* position of the aromatic ring along with (N)–OH group (**54**) was also seen where the agostic donations were drastically reduced [$E(2)$ values for the C–$H\sigma$ to Pd–$Cl_{trans}\sigma^*$ and Pd–$Cl_{cis}\sigma^*$ donations: 19.76 and 5.07 kcal mol^{-1}, respectively; c.f. 58.60 and 10.0 kcal mol^{-1}, respectively in **42**]. There were also small decreases in the syndetic donations in complex **54** [$E(2)$ values for the C^7–$C^8\pi$ to Pd–$Cl_{trans}\sigma^*$ and Pd–$Cl_{cis}\sigma^*$ donations: 15.01 and 4.25 kcal mol^{-1}, respectively; c.f. 20.33 and 6.48 kcal mol^{-1} in **42**, respectively].

By considering all the above observations obtained by placing the *tert*-butyl group on the N, it was of interest to maximise the steric influence on the ligand and see whether any changes in the agostic or syndetic donations occur (Scheme 6.1). Looking at complex **59** with C^7–CMe_3 and (N)–CMe_3 substituents, the ligand is rotated downwards in such a way that one methyl group of the *tert*-butyl substituent lies above and one below, the metal coordination plane (Figure 6.18). In this orientation, both the Pd···H^8 and Pd···C^8 separations become significantly longer compared to **44** [Pd···H^8 in **59** and **44**: 2.534 and 1.884 Å, respectively; c.f. Pd···C^8 separations in **59** and **44**: 2.264 and 2.177 Å, respectively]. This arises when the Rh–N=C angle reduces to 96.5 from 112.1° in **44**; the N=C^1–C^{8a}–C^8 angle becomes significantly larger by almost 23° in comparison to **44**; and the C^1–C^{8a}–C^8–H^8 torsion reduces by 15.5° from that in **44**. The angle between the aromatic ring and coordination planes also increases to 75.5 from 68.9° in **44**. The C–H bond length substantially decreases to 1.091 from 1.148 Å in **44**. The separation angles indicate an increase in the Pd···C–H angle [91.2 and 59.9° for **59** and **44**, respectively] and a decrease in the Pd···H–C angle [values: 63.3 and 88.3°, respectively].

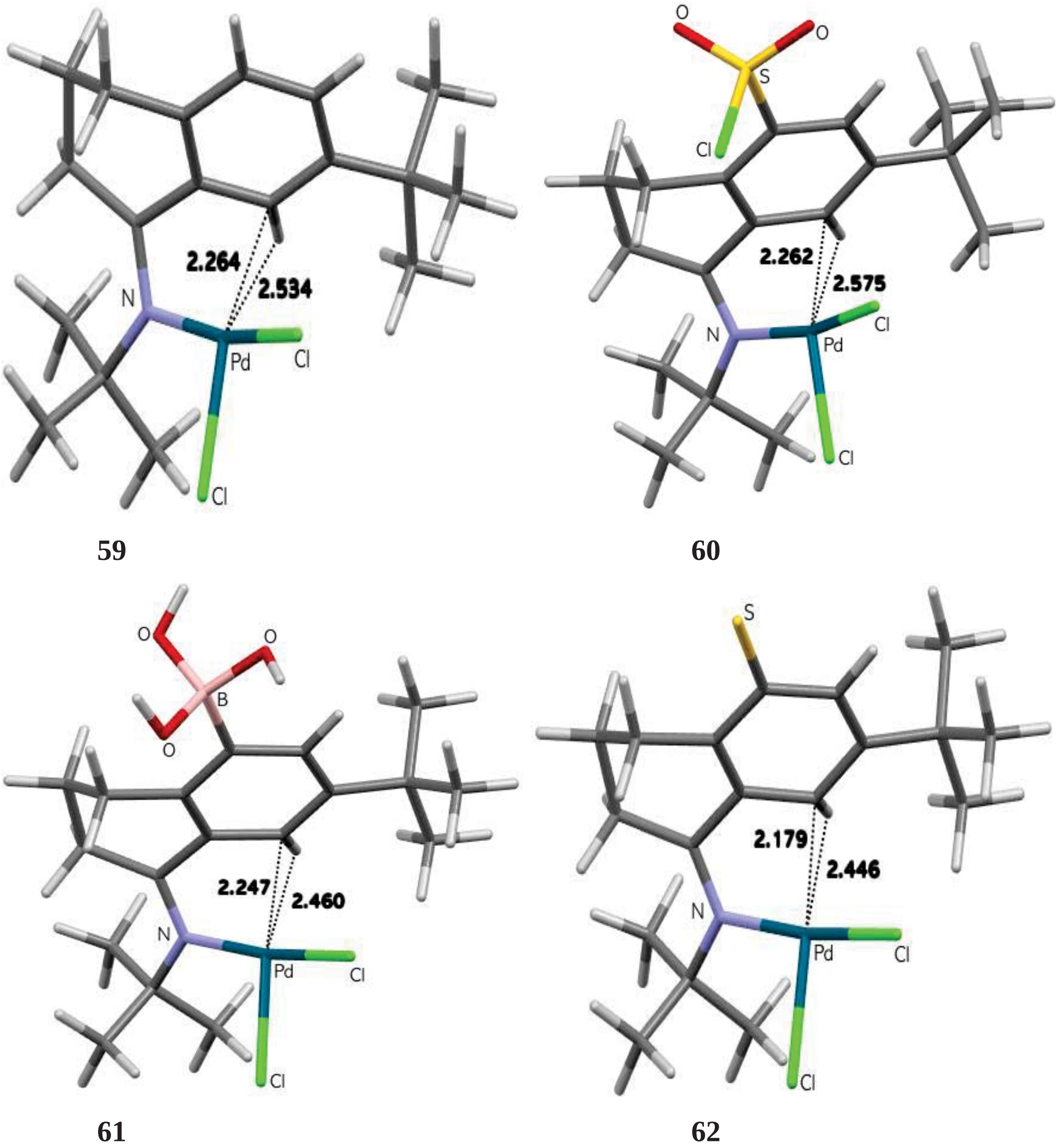

59 **60**

61 **62**

Figure 6.18 Optimised geometries with important separations (Å) for complexes **59–62**.

The calculated spectroscopic data for **59** (Table 6.2) indicate that there is a large decrease in the strength of the agostic interaction, as there is almost no change in ^1JC–H in the complex in comparoson to the ligand value [values for the complex and free ligand are 138.9 and 138.6 Hz, respectively], and only a decrease of 33.2 cm^{-1} in the C–H stretching frequency for the complex. The QTAIM analysis now indicates bcps for Pd···C^8 and Pd···C^{8a} (Figure 6.19) as expected from the closer separations [2.264 and 2.282 Å, respectively]. The bcp properties vary slightly in both, the former interaction being slightly stronger.

Inspection of the NBO analysis for **59** (Table 6.4) shows that there is now a significant increase in the syndetic donation with *E*(2) values for the C^8–C^{8a}π to Pd–Cl$_{trans}$σ* and Pd–Cl$_{cis}$σ* donations: 59.62 and 15.67 kcal mol^{-1}, respectively [c.f. 20.03 and 6.63 kcal mol^{-1} in **44**, respectively]. However, there is now a substantial decrease in the agostic donation, as is also evidenced by the spectroscopic data, the *E*(2) values for the C–Hσ to Pd–Cl$_{trans}$σ* and Pd–Cl$_{cis}$σ* orbitals are 7.51 and 3.66 kcal mol^{-1}, respectively; c.f. 57.07 and 11.64 kcal mol^{-1} in **44**, respectively. Thus, it now appears that by increasing the steric influence by adding the CMe$_3$ at C^7 on the ligand, the syndetic donations become stronger. This might influence the ligand to not go onto the cyclometallation step. The driving force for the increase in the syndetic donations is the spatial overlap which is now significant compared to complex **44** [(N)–CMe$_3$ ligand]. For example, the overlap matrix value for the C^7–C^{8}π to Pd–Cl$_{trans}$σ* donation is 0.4307 compared to **44** where the value was 0.1801 (refer to Table 6.7 in Appendix D.1 for overlap matrix values).

To further manipulate the syndetic and agostic donations on complex **59**, electronic groups were placed at the C^5 position. For this purpose, σ-electron withdrawal substituent SO$_2$Cl (**60**), σ-electron donating B(OH)$_3^-$ substituent (**61**) and π-electron donating group S$^-$ (**62**) were employed (Scheme 6.1). In this series, the N=NPO(OEt)$_2$ was not included because of its bulky tail effect and also this group was not seen previously to influence the syndetic donations.

The structural features of complexes **60–62** indicate a relative decrease in the Pd····C^8 separation compared with **59**, but the decrease is more significant in complex **62** with the S$^-$ substituent [distance: 2.262, 2.247 and 2.179 Å for **60–62**, respectively; c.f. 2.264 Å in **59**] (Figure 6.18). A similar trend is seen in the case of the Pd···H^8 separation where it increases in the case of SO$_2$Cl and subsequently decreases for both the B(OH)$_3^-$ and S$^-$ complexes [values for **60**–**62**: 2.575, 2.460 and 2.446 Å, respectively; c.f. 2.534 Å in case of **59**] (Table 6.2) , whereas, the Pd···C^{8a} separation decreases in **60** but increases substantially in **61** and **62** [values: 2.243, 2.429 and 2.554 Å, respectively; c.f. 2.282 Å in **59**]. The angle and torsional changes also have a similar trend to the separations. For instance, the Pd–N=C angle decreases in SO_2Cl substituted complex **60** but increases in both **61** and **62**. Here, again, the larger increase is seen in complex **62** [95.8, 100.4 and 104.0° in **60**, **61** and **62**, respectively; c.f. 96.5° in **59**], but the plane angle increases in the SO_2Cl case (complex **60**) and decreases for S^-(complex **62**) [values: 76.2, 73.7 and 73.3 in **60**, **61** and **62**, respectively; c.f. 75.5° in **59**] (Table 6.2).

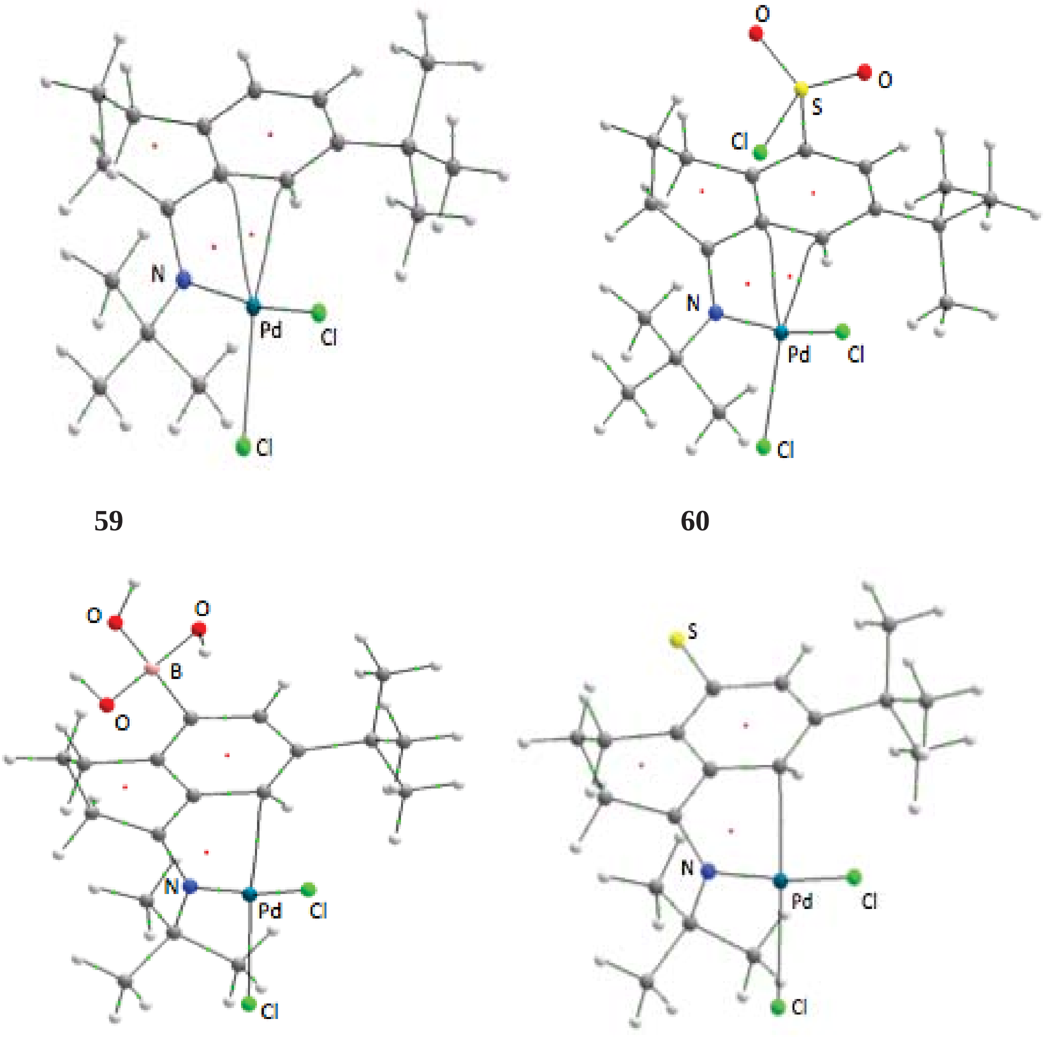

59 **60**

61 **62**

Figure 6.19 QTAIM molecular graphs showing the bond paths for the Pd···C^8 separation in **59–62**.

The spectroscopic properties for the C–H bond (Table 6.2) indicate almost no changes with respect to the free ligands, which again shows that there is no agostic interaction present. Similar to complex **59**, the QTAIM calculations also show two bcps in **60** (Figure 6.19): one for Pd····C^8 separation [(ρ(bcp), $\nabla^2\rho$(bcp) and H(bcp): 0.0735 *e*/Bohr^3; 0.1719 *e*/Bohr^5 and –0.0203 Hartree/Bohr^3, respectively; c.f. 0.0720 *e*/Bohr^3, 0.1607 *e*/Bohr^5 and –0.0203 Hartree/Bohr^3 in **59**, respectively]; and one for Pd···C^{8a} separation in complex **60** [ρ(bcp), ∇^2ρ(bcp) and H(bcp) in **60**: 0.0757 e/Bohr^3, 0.1662 e/Bohr^3 and –0.0226 Hartree/Bohr^3, respectively c.f. 0.0706 e/Bohr^3, 0.1689 e/Bohr^5 and –0.0185 Hartree/Bohr^3, respectively in **59**] as it also has a close approach with C^{8a}, whereas in complexes **61** and **62**, only the Pd···C^8 bcp was seen [ρ(bcp) in **61** and **62**: 0.0732 and 0.0876 e/Bohr^3, respectively; ∇^2ρ(bcp): 0.1379 and 0.1237 e/Bohr^5, respectively; and H(bcp): –0.0228 and –0.0332 Hartree/Bohr^3, respectively]. As the properties of all the Pd–C^8 bcps (Table 6.3) in **60–62** are essentially unchanged from values seen in complex **59**, the nature of the interaction is still in the category of a transit-closed shell interaction.[99] The Laplacian contours for **59–62** (Figure 6.20) show accumulation of the charge density density from the C–H bond towards the metal, but in correlation with the less positive Laplacian values, accumulation of charge density is slightly less in **61** and **62**. Of these, in **62** the accumulation of charge density between C^8 and the metal is significant which again shows development of an attractive situation between C^8 and Pd. As a major component in the agostic interaction comes from the orbital interaction, the use of the NBO analysis becomes more crucial in this case.

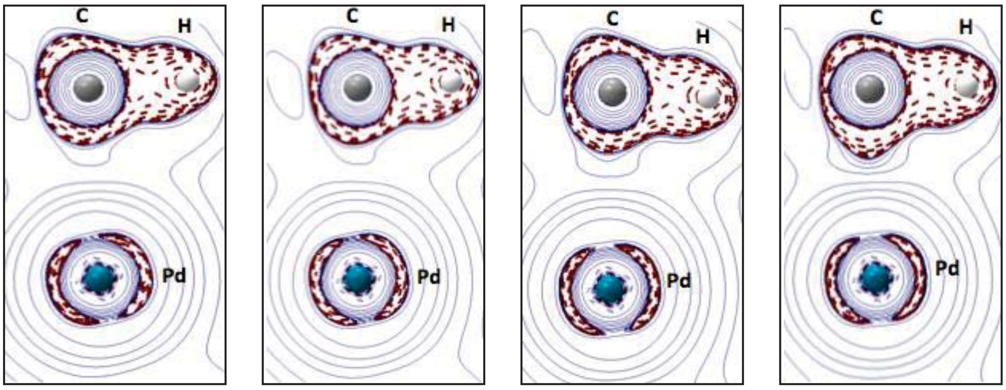

59 **60** **61** **62**

Figure 6.20 2D contour plots of the Laplacian of the electron density for the C–H^8 and Pd interaction in **59**–**62**.

The NBO analysis (Table 6.4) again shows a larger syndetic donation in complex **60** with E(2) values for C^8–C^{8a}π to Pd–Cl$_{trans}$σ* and Pd–Cl$_{cis}$σ*: 57.85 and 13.83 kcal mol^{-1}, respectively [c.f. 59.62 and 15.67 kcal mol^{-1}, respectively in **59**], whereas in both σ- and π-electron donating substituted complexes, the syndetic donation is very small [E(2) values: 2.80 and 0.71 kcal mol^{-1}, respectively in **61**; 4.55 and 3.19 kcal mol^{-1}, respectively in **62**]. Both **61** and **62** now have stronger donations from C^8 to Pd–Cl$_{trans}$σ* with E(2) values: 66.60 and 100.17 kcal mol^{-1}, respectively. Here again the increase in the electron density in the aromatic ring favours Pd–C^8 covalency. Regarding the agostic donations, there is a slight decrease in **60** [E(2) values: 6.33 and 3.37 kcal mol^{-1}, respectively; c.f. 7.51 and 3.66

kcal mol^{-1}, respectively in **59**], whereas in both complexes **61** and **62**, there is comparatively an increase in the agostic donation [*E*(2) values for the C–Hσ to Pd–Cl$_{trans}$σ* and Pd–Cl$_{cis}$σ*donations in **61**: 10.62 and 4.29 kcal mol^{-1}, respectively; and 12.81 and 4.31 kcal mol^{-1}, respectively in **62**].

Thus, from the NBO analyses for the series of complexes with CMe$_3$ at C^7 and (N)–CMe$_3$, **58–62**, it appears that the agostic donation decreases due to the steric influence of the CMe$_3$ at C^7 position and although the stronger electron-donating groups slightly increase these donations the steric influence dominates. However, the electronic effects can change the syndetic donations as it was seen that the electron-withdrawing group favours the syndetic donations but by placing a stronger σ- or π-substituent, a stronger Pd–C^8 covalency appears and the syndetic donations disappear.

To further manipulate the electronic effects, the *tert*-butyl group at C^7–H position in complex **62** was replaced by an S$^-$ group (complex **63)**. The structural features indicate a similar kind of orientation for C–H^8 (Figure 6.21) as was found in **62**, however, the Pd···C^8 distance becomes shorter to 2.142 Å [c.f. 2.179 Å in **62**] (Table 6.2). The QTAIM analysis shows an increased negative energy density for the Pd···C^8 bcp (Figure 6.21b) [*H*(bcp): –0.0402 and –0.0332 Hartree/Bohr^3 in **63** and **62** respectively] (Table 6.3). The calculated spectroscopic data (Table 6.2) are indicative of a decrease in the electron density for the C–H bond as a larger decrease on complex formation in the coupling constant is seen in **63** compared to **62** [decrease in ^1JC–H from the ligand: 11.0 and 8.0 Hz for **63** and **62**, respectively] and the C–H stretching frequency shifts to lower energy by 123.8 and 106.7 cm^{-1}, respectively. These observations all suggest that the agostic interaction is now slightly stronger.

However, the NBO analysis (Table 6.4) reveals that there is a decrease in the agostic donations as the *E*(2) values are only 0.0 and 2.75 kcal mol^{-1} for the donation from the C–Hσ to the Pd–Cl$_{trans}$σ* and Pd–Cl$_{cis}$σ* orbitals, respectively, compared with **62** where agostic donations were large [values: 12.8 and 4.3 kcal mol^{-1}, respectively]. Surprisingly, no donation was found for LP C^8 to Pd–Cl$_{cis}$σ* donation to indicate the origins of the effects driving the changes in the Pd····C^8 separation but interestingly, the NBO analysis shows a stronger Pd···C^8 bond with covalency of 1.6254 electrons and a larger Wiberg bond index value of 0.4115 (refer to Table 6.6 in Appendix D.1). Thus, here again, similar to the other complexes with S$^-$, the NBO analysis indicate covalency for the Pd–C^8 bond. Thus, pumping large amounts of electron density into the aromatic system facilitates Pd–C^8 bond formation and negates the development of agostic interactions.

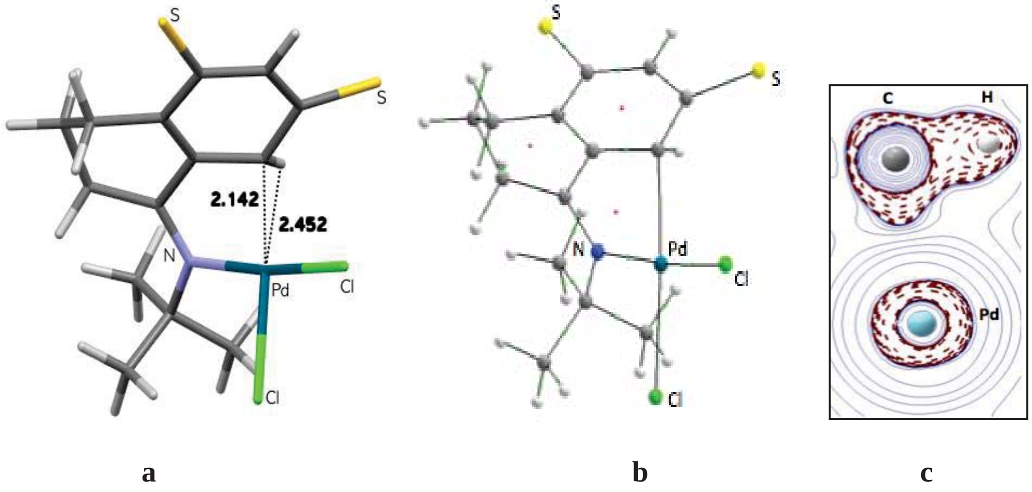

Figure 6.21 a) Optimised geometry and important separations; b) QTAIM molecular graph showing bond paths between $C^8\cdots$Pd; c) 2D contour plot of the Laplacian of the electron density for the $C–H^8$ and metal interaction for complex **63**.

6.4.7 [$PdCl_2$(8-Methylquinoline)], Complex 64

In addition to aromatic sp^2 C–H functionalisations, aliphatic sp^3 C–H functionalisations are also crucial for cyclometallation reactions.[9b,10] To explore the agostic interaction in aliphatic sp^3 C–H groups, the 8-methylquinoline ligand which is a commonly used for cyclometallation reactions, was used.[140] The expected agostic structure [$Pd(Cl)_2$(8-methylquinoline)] for the cyclometallation reaction of 8-methylquinoline with $PdCl_4^{2-}$ was computed in the same way as the other complexes above.[126]

In this case, two sp^3 CH_3 hydrogens form close approaches to the metal with one significantly closer than the other [Pd··· H separations of 1.888 and 2.187 Å; Pd····C separation: 2.352 Å] (Figure 6.22a). The rotation of the C–C bond involving the benzylic position is such that the C–H electron density of the upper hydrogen forms the stronger agostic interaction, as shown by the length of the C–H bonds [1.144 and 1.112 Å for the C–H bond pointing away from the metal] (Table 6.5).

The NBO donations show that the upper agostic interaction has C–Hσ to $Pd–Cl_{trans}$ σ* and $Pd–Cl_{cis}$σ* donations [$E(2)$ values of 43.98 and 9.05 kcal mol^{-1}, respectively] and the lower one has $E(2)$ values of 16.63 and 3.71 kcal mol^{-1}, respectively compared with the third non-interacting hydrogen [values: 1.46 and 0.40 kcal mol^{-1}, respectively] (Table 6.5). The similarity to the [$PdCl_2$(1-tetralone oxime)] complexes and complex **64** is that the donations are into the same Pd–Cl antibonding orbitals. The C–H occupancy is decreased by 0.1028 *e* from the ligand value (Table 6.5) correlating with the donations for the agostic interaction.[41,133]

The QTAIM analysis indicates a bond path between Pd and upper hydrogen H^{19} (Figure 6.22b) which has bcp properties slightly less than the 1-tetralone ligands [Pd···H bcp properties in **64**: ρ(bcp), $\nabla^2\rho$(bcp) and H(bcp) are 0.0669 e/Bohr^3, 0.2115 e/Bohr^5 and –0.0157 Hartree/Bohr^3, respectively; c.f. 0.0820 e/Bohr^3, 0.2631 e/Bohr^5 and –0.0210 Hartree/Bohr^5, respectively for complex **42**] (Table 6.5). As the Laplacian of the electron density ($\nabla^2\rho$) and the energy density (H) are positive and negative, respectively, and the ratio of the absolute potential energy density and kinetic energy density is more than 1, therefore, the nature of the interaction lies in the category of a 'transit-closed shell interaction', meaning a closed shell interaction with some covalency involved.[97] The nature of the interaction in **23** is similar to that seen in the 1-tetralone ligands. The Laplacian contours in Figure 6.22c show a accumulation of the charge density between C–H^{19} moiety and metal as was seen for **42**.

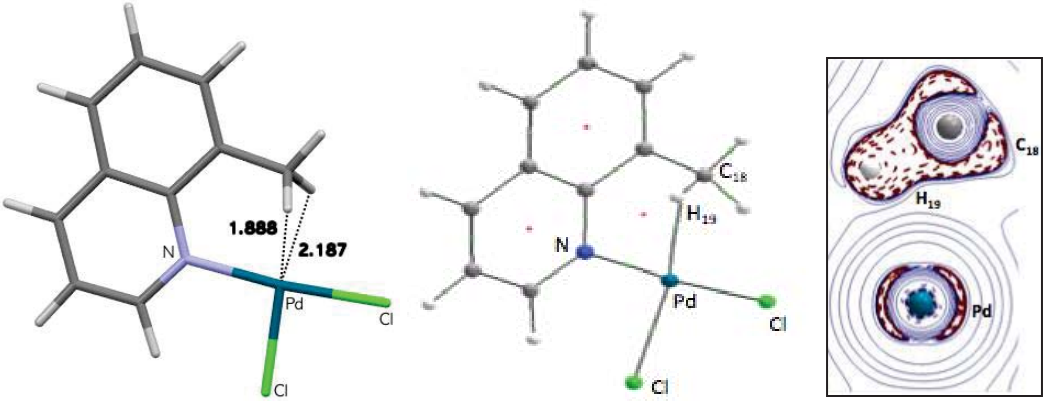

a **b** **c**

Figure 6.22 a) Optimised geometry and important separations; b) QTAIM molecular graph showing bond paths for H^{19}···Pd; c) 2D contour plot of the Laplacian of the electron density for the C–H^{19} and metal interaction for complex **64**.

Table 6.5 Selected parameters for complex **64**.

Structural parameters:	
Distance (Å)	
Pd$\cdots$H^{19}	1.888
Pd$\cdots$C^{18}	2.352
C^{18}–H^{19}	1.144
(Ligand)	1.099
Angles (^{o})	
Pd–H^{19}–C^{18}	98.7
Pd–C^{18}–H^{19}	52.5
QTAIM Analysis:	
ρ [e/Bohr^{3}]	0.0669
$\nabla^{2}\rho$(bcp) [*e*/Bohr^{5}]	0.2115
H(bcp) [Hartree/Bohr^{3}]	-0.0157
–V/G	1.2287
q(H^{19}) (*e*)	0.054
q(C^{18}) (*e*)	-0.141
q(Pd) (*e*)	0.624
NBO analysis:	
C^{18}–H^{19}σ bond	
Occupancy (n)	1.8841
(Ligand)	**1.9869**
Energy (a.u.)	-0.4434
(Ligand)	**-0.4095**
Pd–Cl$_{cis}$σ*	
Occupancy (n)	0.2461
Energy (a.u.)	0.2929
Pd–Cl$_{trans}$σ*	
Occupancy	0.3633
Energy (a.u.)	0.2408
Donor-acceptor interactions:	
E(2) value for C^{18}–H^{19} to Pd–Cl$_{trans}$σ* (kcal mol^{-1})	43.98
E(2) value for C^{18}–H^{19} to Pd–Cl$_{cis}$σ* (kcal mol^{-1})	9.05
Spectroscopic analysis:	
^{1}JC^{18}–H^{19} (Complex) (Hz)	84.3
(Ligand)	**108.0**
νC^{18}–H10 (Complex) (cm^{-1})	2522.4
(Ligand)	**3026.5**
Chemical shift (δ) of H^{19} (ppm)	3.04
(Ligand)	**3.09**

6.5 Conclusion

In this Chapter, it has been shown that the agostic interaction can be manipulated by increasing or decreasing the electron density in the aromatic ring. It is seen for the first time that along with agostic donations, there are some other donations involved from the C–Cπ bond to antibonding metal centred orbitals which have been termed ‘syndetic.' It is seen that the change in electronic effects influences the NBO energies of the donor-acceptor NBOs in the agostic interaction and subsequently affects the strength of the interactions. On the other hand, steric effects from the ligand support the syndetic interaction and reduce the strength of the agostic interaction. The driving force for the syndetic interaction comes from the spatial overlap between the C–Cπ and palladium centred orbitals.

The electronic influence of the sigma electron donating substituent $B(OH)_3^-$ with (N)–OH (complex **49**) or (N)–OMe (complex **57**) at the *para* position C^5 of the aromatic ring significantly enhances the syndetic donation by increasing the electron density in the aromatic system. However, the sigma electron withdrawing substituent SO_2Cl with (N)-OH (complex **47)** or (N)–OMe (complex **55**) at the *para* position of the aromatic ring increases both the agostic and syndetic donations.

The electron-withdrawing substituent $N_2PO(OEt)_2$ at the C^5 position along with the (N)–OH ligand (complex **48**) enhances both the agostic and syndetic donations, but with the (N)–OMe ligand (complex **56**) both the agostic and syndetic donations turn off.

The π-electron donating substituent S^- at the C^5 position or in combination with a C^7 position with (N)–OH (complexes **50** and **55**) or having only S^- with the (N)–OMe ligand (complex **58**) increases the electron density into the π-system which leads to a carbon-metal bond with significant covalency.

An increase in steric effects at the coordinating N atom (complex **42–44**) does not influence the agostic or syndetic donations. However, an increase in steric influence at the C^7 position (complexes **52–54**) (along with the (N)–OH ligand) minimises the agostic donations but only slightly affects the syndetic donations. Moreover, a combined influences at C^7 and the coordinating N atom by the *tert*-butyl group (complex **59**) leads to a significant increase in syndetic donations.

A steric and electron withdrawing combination where *tert*-butyl is placed at C^7 and at the coordinating N atom, and SO_2Cl at C^5 (complex **60**) decreases the agostic interaction but does not affect the syndetic interaction. However, a combination of sterics (CMe_3 at N and the C^7 position) and electron donating substituents $B(OH)_3^-$ and S^- (at the C^5 position) (complex **61** and **62**) almost switches off both the agostic and syndetic donations. Finally, a combined electronic (S^- at C^5 and C^7) and steric (N)–CMe_3 effect (complex **63**) completely switches off both interactions and instead develops an interaction between carbon C^8 and the palladium metal centre. Small increases in agostic and syndetic donations were seen by changing the coordinating atom from N to O (complex **46**), or by replacing the alicyclic ring by CH_3 (complex **45**).

Chapter 7

Summary and Perspective

7.1 Thesis Summary

This thesis addresses a variety of important steric and electronic factors which are crucial for cyclometallation reactions. It is previously known that the cyclometallated product is formed as a result of different kinds of carbon–hydrogen···metal (C–H···M) interactions. This includes the electrostatic dominating anagostic, electrostatic but also back-bonding character preagostic and finally the agostic interaction,[28] which is partially covalent interaction where a covalency is involved when the C–H bond donates electron density to the metal centre. Despite a significant amount of research and available literature on C–H···M interactions which addresses the structural and bonding properties of these interactions, there is a lack of in-depth studies addressing the role of steric and electronic factors on C–H···M interactions.[28–30,34,35,41,104] Therefore, the current work in this thesis has been carried out with the motivation of how the steric and electronic factors influence the nature of C–H···M interactions.

Regarding the anagostic interactions in the Rh-tetralone complexes (Chapter 3), it has been shown that both steric and electronic effects influence the nature of the interactions. The larger steric influence at the coordinating N atom flattens the tetralone aromatic ring which brings the carbon of C–H anagostic group closer to the metal. This effect was even larger when a combination of strong steric and electronic substituents was used. It has been shown that the electron-donating group S^{-} at the aromatic ring *para* position to the C–H bond, significantly increases the negative charge on the carbon and which results in an attractive interaction (C-anagostic interaction) between the carbon and metal. Although the C-anagostic interaction was reported recently with other pincer type ligands,[66] the work in this thesis has shown that the C-anagostic situation can be achieved with the flexible tetralone ligands as well. It is found that the large differences in NBO energies between C–H and the metal is the main obstacle in driving covalency between them. In Chapter 4, the metal centre and precursors were changed, and Pd (II) complexes were computed for a comparison with Rh (I) complexes. It was found that for the $[PdCl_3(\text{1-tetralone ligand})]^-$ anions, no C-anagostic interaction formed but instead agostic covalency was achieved when the strongest electronic and steric influences were used. This agostic covalency was facilitated by the weak C–H···Cl (ancillary ligand) bonding. This aspect is also seen for the first time in this work that the agostic-like donations are possible to achieve with the anagostic square planar geometries.

Furthermore it was seen that the 1-tetralone ligands were incapable of keeping the hydrogen right over the metal and only longer anagostic approaches can be achieved. Therefore, another ligand type was required to study the role of steric and electronic factors on short anagostic approaches which ensure the distance of less than 2.5 Å between metal and hydrogen.[34] For this purpose, an inflexible *iso*-quinoline ligand was used (Chapter 5). This ligand was widely used previously in cyclometallation reactions.[127] It was shown that the electronic influence was not very strong but the steric effect at the *ortho* position to the coordinating N atom pushes the anagostic hydrogen towards the metal and as a result, the shortest approach of 2.180 Å was seen. Furthermore, it was shown that the nature of the short anagostic approach was not purely electrostatic and there was some covalency component involved in some of the complexes. It was also seen that with the closest approach of 2.180 Å, there was significant back-bonding involved which is a feature of preagostic interactions.

Regarding the agostic interaction (Chapter 6), the role of the sterics and electronics was studied with the palladium (II)-tetralone complexes. It is shown for the first time that with the tetralone ligand, there is donation from the C–C π bond system close to the agostic carbon, to palladium centred orbitals. This donation has not been reported in the literature before. This new donation is given the term ‘syndetic’ donation. It was observed that combined influences of bulky steric groups such as a *tert*-butyl group *ortho* to the agostic C–H group and at the ligating N atom, can switch off the agostic donations and significantly enhance the ‘syndetic’ donations. It was also seen that the electronic factors affect the donor-acceptor NBOs energies and the steric affects influence the spatial overlap between them.

7.2 Perspective

For the closer anagostic metal···H approaches, the neutral inflexible ligands were used. However, there are other known cationic complexes in experimental studies which can give closer approaches. Therefore, it would be interesting to study the metal···H interactions by changing the overall charge of the metal complexes. As with the inflexible *iso*-quinoline ligand, only neutral complexes of rhodium (I) were studied, therefore it would also be interesting to use other metals by changing the metal precursors, then both the electrostatics and the covalency could be influenced.

Regarding the agostic interactions, as new ‘syndetic’ donations were evident with the flexible tetralone ligand where the C–C bond donated electron density into the metal orbitals, therefore it would be interesting to study an inflexible ligand and other ligand systems where the aromatic ring can freely rotate in order to bring the C=C bond over the metal centre.

Solvent effects on the various types of carbon–hydrogen···metal interactions could be studied and could then be analysed for the influence on the overall cyclometallation process. Full mechanistic studies based on locating transition states and intermediates in the overall cyclometallation process could also be studied.

7.3 Applications

The present thesis work was an attempt to address the metal····hydrogen–carbon (M····H–C) interactions in context to cyclometallation reactions. It has been shown that steric and electronic factors associated with the ligands can switch on and off the agostic interaction. The entry of a C-anagostic interaction can have a significant effect on the cyclometallation reaction as the metal–carbon bond has a covalent type character which might not go to an agostic intermediate. It was also seen that the inflexible ligands ensure a close metal···hydrogen separation, but they have covalency components involved which may be helpful in the formation of the agostic intermediate. Finally, the role of syndetic interactions in agostic interaction mediated cyclometallations seems important as it can switch off and on the agostic interaction.

References

---

[1] X. Ribas, *C–H and C–X Bond Functionalisation: Transition Metal Mediation*, RSC Catalysis Series No.11, 2013.

[2] G. Dyker, *Handbook in Organic Synthesis*, WILEY-VCH GmbH & Co. KgaA, Weinheim, 2005.

[3] J. A. Labinger, J. E. Bercaw, *Nature*, 2002, **417**, 507

[4] A. S. Goldman, K. I. Goldberg, *ACS Symposium 885*, *Activation and Functionalisation of C–H Bonds*, 2004.

[5] (*a*) R. Grant, C. Grant, I. W. Hackh, *Grant and Hackh's Chemical* Dictionary, McGraw-Hill, New York, 5th *ed.*,1987; (*b*) A. D. McNaught, A. Wilkinson, *Compendium of Chemical Terminology*, *IUPAC Recommendations*, TSC, Cambridge, UK, 2nd ed., 1997.

[6] S. Trofimenko, S. *Inorg. Chem.*, 1973, **12**, 1215–1221.

[7] M. I. Bruce. *Angew. Chem. Int. Ed.*, 1977, **16**, 73–86.

[8] I. Omae, *Coord. Chem. Rev.*, 2004, **248**, 995–1023.

[9] a) I. Omae, *Coord. Chem. Rev.*, 2011, **255**, 139–160; (b) I. Omae, *J. Organomet. Chem.*, 2011, **696**, 1128–1145.

[10] M. Albrecht, *Chem. Rev.*, 2010, **110**, 576–623.

[11] S. S. Stahl, J. A. Labinger, J. E. Bercaw, *Angew, Chem. Int. Ed.*, 1998, **37**, 2180–2192.

[12] M. Lersch, M. Tilset, *Chem. Rev.*, 2005, **105**, 2471–2526.

[13] R. G. Pearson, *Chemical Hardness*, Wiley-VCH: Weinheim, Germany, 1997.

[14] R. F. Jordan, A. S. Guram, *Organometallics*, 1990, **9**, 2116–2123.

[15] J.-M. Valk, F. Maassarani, P. van der Sluis, A. L. Spek, J. Boersma, G. van Koten, *Organometallics*, 1994, **13**, 2320–2329.

[16] G. van Koten, *Pure Appl. Chem.*, 1989, **61**, 1681–1694.

[17] R. G. Goel, R. Montemayor, *Inorg. Chem.*, 1977, **16**, 2183–2186.

[18] K. M. Engle, T.-M. Mei, M. Wasa, J.-Q. Yu, *Theor. Chem. Acc.*, 2012, **45**, 788–802.

[19] (*a*) Y. Liu, Y. Bai, J. Zhang, Y. Li, J. Jiao, X. Qi, *Eur. J. Org. Chem.*, 2007, 6084–6088; (*b*) X. Guo, H. Rao, H. Fu, Y. Jiang, Y. Zhao, *Adv. Synth. Catal.*, 2006, **348**, 2197–2202; (*c*) R. A. Altman, K. W. Anderson and S. L. Buchwald, *J. Org. Chem.*, 2008, **73**, 5167–5169; (*d*) H. Rao, Y. Jin, H. Fu, Y. Jiang and Y. Zhao, *Chem. Eur. J.*, 2006, **12**, 3636–3646

[20] J. T. Markiewicz, O. Wiest, P. Helquist, *J. Org. Chem.*, 2010, **75**, 4887–4890.

[21] (*a*) J. Dupont, M. Pfeffer, *Eds. Palladacycles*; Wiley-VCH: Weinheim, Germany, 2008; (*b*) M. Gomez, G. Muller, M. Rocamora, *Coord. Chem. Rev.*, 1999, **769**, 193–195; (*c*) J. Dupont, C. S. Consorti, J. Spencer, *Chem. Rev.*, 2005, **105**, 2527–2571; (d) J. Albert, J. Granell, G. Muller, *J. Organomet. Chem.*, 2006, **691**, 2101–2106; (*e*) J.-P. Djukic, J.-B. Sortais, L. Barloy, M. Pfeffer, *Eur. J. Inorg. Chem.*, 2009, 817–853.

[22] I. P. Rothwell, *Acc. Chem. Res.*, 1988, **21**, 153–159.

[23] D. L. Davies, S. M. A. Donald, O. Al-Duaij, S. A. Macgregor, M. Pölleth, *J. Am. Soc.*, 2006, **128**, 4210–4211.

[24] (*a*) G. W. Parshall, *Acc. Chem. Res.*, 1970, **3**, 139–144; (*b*) A. D. Ryabov, *Chem. Rev.*, 1990, **90**, 403–424.

[25] (*a*) R. N. Perutz, S. Sabo-Etienne, *Angew. Chem. Int. Ed.*, 2007, **46**, 2578–2592; (*b*) Z. Liu, *Coord. Chem. Rev.*, 2007, **251**, 2280–2291.

[26] D. L. Davies, S. M. A. Donald, S. A. Macgregor, *J. Am. Chem. Soc.*, 2005, **127**, 13754–13755.

[27] T. G. P. Harper, P. J. Desrosiers, T. C. Flood, *Organometallics*, 1990, **9**, 2523–2528.

[28] M. Brookhart, M. L. H. Green, G. Perkin, *PNAS*, 2007, **104**, 6908–6914.

[29] M. Brookhart, M. L. H. Green, *J. Organomet. Chem.*, 1983, **250**, 395–408.

[30] M. Brookhart, M. L. H. Green, L.-L. Wong, *Adv. Organomet. Chem.*, 1988, **36**, 1–115.

[31] W. I. Sundquist, D. P. Bancroft, S.J. Lippard, *J. Am. Chem. Soc.*, 1990, **112,** 1590–1596.

[32] D. Braga, F. Grepioni, E. Tedesco, K. Biradha, G.R. Desiraju, *Organometallics*, 1997, **16**, 1846–1856

[33] M. Bortolin, U. E. Bucher, H. Ruegger, L. M. Venanzi, A. Albinati, F. Lianza, S. Trofimenko, *Organometallics*, 1992, **11**, 2514–2521.

---

[34] Y. Zhang, J. C. Lewis, R. G. Bergman, J. A. Ellman, E. Oldfield, *Organometallics*, 2006, **25**, 3515–3519

[35] M. Lein, *Coord. Chem. Rev.*, 2009, **253**, 625–634.

[36] (*a*) D. M. Roe, P.M. Bailey, K. Moseley, P. M. Maitlis, *J. Chem. Soc. Chem. Commun*., 1972, 1273–1274; (*b*) A. Albinati, C. G. Anklin, F. Ganazzoli, H. Ruegg, P. S. Pregosin, *Inorg. Chem*., 1987, **26**, 503–508; (*c*) W. Yao, O. Eisenstein, R. H. Crabtree, *Inorg. Chim. Acta*, 1997, **254**, 105–111.

[37] W. Scherer, G. S. McGrady, *Angew. Chem. Int. Ed*., 2004, **43**, 1782–1806.

[38] R. J. Goddard, R. Hoffmann, E. D. Jemmis, *J. Am. Chem. Soc*., 1980, **102**, 7667–7676.

[39] O. Eisenstein, Y. Jean, *J. Am. Chem. Soc*., 1985, **107**, 1177–1186.

[40] W. Scherer, T. Priermeier, A. Haaland, H. V. Volden, G. S. McGrady, A. J. Downs, R. Boese, D. Blaser, *Organometallics*, 1998, **17**, 4406–4412.

[41] T. S. Thakur, G. R. Desiraju, *Mol Struct: Theochem*., 2007, **810**, 143–154.

[42] A. Haaland, W. Scherer, K. Ruud, G. S. McGrady, A. J. Downs, O. Swang, *J. Am. Chem. Soc*., 1998, **120**, 3762–3772.

[43] J. M. Boncella, M. L. Cajigal, K. A. Abboud, *Organometallics*, 1996, **15**, 1905–1912.

[44] E. Clot, O. Eisenstein, *Structure and Bonding*, Springer-Verlag Berlin Heidelberg, 2004, **113**, 1–36.

[45] Y Han, L. Deng, T. Ziegler, *J. Am. Chem. Soc*., 1997, **119**, 5939–5945.

[46] A. C. Cooper, E. Clot, J. C. Huffman, W. E. Streib, F. Maseras, O. Eisenstein, K. G. Caulton, *J. Am. Chem. Soc*., 1999, **121**, 97–106.

[47] M. E. van der Boom, M. A. Iron, O. Atasoylu, L. J. W. Shimon, H. Rozenberg, Y. Ben-David, L. Konstantinovski, J. M. L. Martin, D. Milstein, *Inorg. Chim. Acta*, 2004, **357**, 1854–1864.

[48] W. Barrata, C. Mealli, E. Herdtweck, A. Lenco. S. A. Mason, P. Rigo, *J. Am. Chem. Soc.*, 2004, **126**, 5549–5562.

[49] E. F. van der Eide, P. Yang, R. M. Bullock, *Angew. Chem. Int. Ed*., 2013, **52**, 10190–10194.

[50] M. A. Ortuño, P. Vidossich, G. Ujaque, S. Conejero, A. Lledós, *Dalton Trans.*, 2013, **42**, 12165–12172.

[51] R. F. W. Bader, *Atoms in Molecules–A Quantum Theory*, Oxford University press, Oxford, **1990**

[52] P. L. A. Popelier, G. Logothetis, *J. Organomet. Chem.*, 1998, **555**, 101–111.

[53] W. Scherer, W. Hieringer, M. Spiegler, P. Sirsch, G. S. McGrady, A. J. Downs, A. Haaland, B. Pedersen, *Chem. Commun.*, 1998, 2471–2472.

[54] M. Lein, J. A. Harrison, A. J. Nielson, *Dalton Trans.*, 2013, **42**, 10939–10951.

[55] (*a*) H. V. Hunyh, L. R. Wong, P.S. Ng, *Organometallics*, 2008, **27**, 2231–2237; (*b*) M. Montag, I. Efremenko, R. Cohen, G. Leitus, L. J. W. Shimon, Y. Diskin-Posner, Y. Ben-David, J. M. L. Martin, D. Milstein, *Chem. Eur. J*., 2008, **14**, 8183–8194; (*c*) J. Ruiz, J. Lorenzo, C. Vicente, G. López, J. M. López-de-Luzuriaga, M. Monge, F. X. Aviléd, D. Bautista, V. Moreno, A. Laguna, *Inorg. Chem*., 2008, **47**, 6990–7001; (*d*) J. Pérez, A. Espinosa, J. M. Galiana, E. Pérez, J. L. Serrano, M. A. G. Aranda, M. Insausti, *Dalton Trans*., 2009, 9625–9636; (*e*) A. John, M. M. Shaikh, R. J. Butcher, P. Ghosh, *Dalton Trans*., 2010, **39**, 7353–7363; (*f*) A. T. Çolak, O. Z. Yeşilel, O. Büyükgüngör, *J. Mol. Struct*., 2011, **991**, 68–72; (*g*) B. G. Cooper, C. M. Fafard, B. M. Foxman, C. M. Thomas, *Organometallics*, 2010, **29**, 5179–5186; (*h*) M. S. Khalaf, S. H. Oakley, M. P. Coles, P. B. Hitchcock, *Dalton Trans*., 2010, **39**, 1635–1642; (*i*) R. Angamuthu, L. L. Gelauff, M. A. Siegler, A. L. Spek, E. Bouwman, *Chem. Commun.*, 2009, 2700–2702; (*j*) E. S. Tabei, H. Samouei, M. Rashidi, *Dalton Trans.*, 2011, **40**, 11385–11388; (*k*) M. G. D. Holaday, G. Tarafdar, A. Kumar, M. L. P. Reddy, A. Srinivasan, *Dalton Trans*., 2014, **43**, 7699–7703.

[56] G. Zheng, S. Li, *Inorg. Chem*., 2011, **50**, 10572–10580.

[57] M. Bortoluzzi, G. Paolucci, B. Pitteri, A. Vavasori, V. Bertolasi, *Organometallics*, 2009, **28**, 3247–3255.

[58] M. Teci, E. Brenner, S. Matt, L. Toupet, *Eur. J. Inorg. Chem*., 2013, 2841–2848.

[59] S. Kolay, M. Kumar, A. Wadawale, D. Das, V. K. Jain, *J. Organomet. Chem*., 2015, **794**, 40–47.

[60] N. Singh, A. J. Elias, *Dalton Trans*., 2011, **40**, 4882–4891.

---

[61] J. C. Lewis, J. Wu, R. G. Bergman, J. A. Ellman, *Organometallics*, 2005, **24**, 5737–5746.

[62] Scifinder, 2015; Chemical Abstracts Service: Columbus, OH, 2015; (accessed 20 December 2015)

[63] A.G. Jarvis, P. E. Sehnal, S. E. Bajwa, A. C. Whitwood, X. Zhang, M. S. Cheung, Z. lin, I. J. S. Fairlamb, *Chem. Eur. J.*, 2013, **19**, 6034–6043.

[64] S. Schöler, M. H. Wahl, N. I. C. Wurster, A. Puls, C. Hättig, G. Dyker, *Chem. Commun.*, 2014, **50**, 5909–5911.

[65] W. Scherer, A. C. Dunbar, J. E. Barquera-Lozada, D. Schmitz, G. Eickerling, D. Kratzert, D. Stalke, A. Lanza, P. Macchi, N. P. M. Casati, J. Ebad-Allah, C. Kuntscher, *Angew. Chem. Int. Ed.*, 2015, **54**, 2505–2509.

[66] C. Lepetit, J. Poater, M. E. Alikhani, B. Silvi, Y. Canac, J. Contreas-García, M. Solà, R. Chauvin, *Inorg. Chem.*, 2015, **54**, 2960–2969.

[67] A. R. Leach, *Molecular Modelling: Principles and Applications*, Pearson education Ltd, England, 2nd ed., 2001.

[68] F. Jensen, *Introduction to Computational Chemistry*, John Wiley & Sons Ltd., England, 2003.

[69] C. J. Cramer, *Essentials of Computational Chemistry: Theories and Models;* 2nd ed.; John Wiley & Sons, Ltd.: West Sussex, England, 2004.

[70] W. J. Hehre, *A guide to Molecular Mechanics and Quantum Chemical Calculations*, Wavefunction Inc., USA, 2003

[71] (*a*) A. D. Becke, *Phys. Rev. A*, 1988, **38**, 3098–3100; (*b*) C. Lee, W. Yang, R. G. Parr, *Phys. Rev. B*, 1988, **37**, 785–789.

[72] (*a*) J. P. Perdew, *Phys. Rev. B,* 1986, **34**, 7406; (*b*) J. P. Perdew, *Phys. Rev. B,* 1986, **33**, 8822–8824.

[73] (*a*) A. D. Becke, *J. Chem. Phys.*, 1993, **98**, 5648–5652; (*b*) A. D. Becke, *J. Comput. Chem.*, 1999, **20**, 63–69.

[74] C. Adamo, V. Barone, *J. Chem. Phys.*, 1999, **110**, 6158–6170.

[75] E. Lewars, *Computational Chemistry: Introduction to the theory and Applications of the Molecular and Quantum Mechanis*, Kluwer Academic Publishers, USA, 2004.

[76] S. Grimme, J. Antony, S. Ehlrich, H. Krieg, *J. Chem. Phys.*, 2010, **132**, 154104–54118.

[77] J. P. Perdew, K. Burke, M. Ernzerhof, *Phys. Rev. Lett.*, 1996, **77**, 3865–3868.

[78] S. Grimme, *J. Comput. Chem.*, 2006, **27**, 1787–1789.

[79] S. F. Sousa, P. A. Fernandes, M. J. Ramos, *J. Phys. Chem. A,* 2007, **111**, 10439–10452.

[80] T. Sperger, I. A. Sanhueza, I. Kalvet, F. Schoenebeck, *Chem. Rev.*, 2015, **115**, 9532–9586.

[81] J. D. Chai, M. Hed-Gordon, *Phys. Chem. Chem. Phys.*, 2008, **10**, 6615–6620.

[82] K. Raghavachari, G. W. Trucks, *Chem. Phys. Lett.*, 1989, **157**, 479–483.

[83] K. E. Riley, M. Pitoňák, P. Jurečka, P. Hobza, *Chem. Rev.*, 2010, **110**, 5023–5063.

[84] M. Bühl, C. Reimann, D. A. Pantazis, T. Bredow, F. Neese, *J. Chem. Theory Comput.*, 2008, **4**, 1449–1459.

[85] M. P. Waller, H. Braun, N. Hojdis, M. Bühl, *J. Chem. Theory Comput.*, 2007, **3**, 2234–2242.

[86] M. J. Calhorda, P. S. Pregosin, L. F. Veiros, *J. Chem. Theory Comput.*, 2007, **3**, 665–670.

[87] H. Jacobsen, *J. Chem. Theory Comput.*, 2011, **7**, 3019–3025.

[88] J. Moellmann, S. Grimme, *Organometallics*, 2013, **32**, 3784–3787.

[89] Y. Minenkov, A. Singstad, G. Occhipinti, V. R. Jensen, *Dalton Trans.*, 2012, **41**, 5526–5541.

[90] (*a*) W. R. Wadt, P. J. Hay, *J. Chem. Phys.*, 1985, **82**, 299–310; (*b*) P. J. Hay, W. R. Wadt, *J. Chem. Phys.*, 1985, 82, 270–283; (*c*) W. R. Wadt, P. J. Hay, *J. Chem. Phys.*, 1985, **82**, 284–298.

[91] M. Dolg, U. Wedig, H. Stoll, H. Preuss, *J. Chem. Phys.*, 1987, **86**, 866–872.

[92] A. B. Chaplin, J. A. Harrison, A. J. Nielson, C. Shen, J. M. Waters, *Dalton Trans.*, 2004, **17**, 2643–2648.

[93] M. Steinmetz, S. Grimme, *ChemistryOpen*, 2013, **2**, 115–124.

[94] Y. Zhao and D. G. Truhlar, *J. Phys. Chem. A*, 2005, **109**, 5656–5667.

[95] T. H. Dunning Jr., *J. Chem. Phys.*, 1989, **90**, 1007–1023.

---

[96] C. F. Matta, R. J. Boyd, *The Quantum Theory of Atoms in Molecules*, WILEY-VCH Verlag GmbH & Co. KgaA, Weinheim, 2007.

[97] E. Espinosa, I. Alkorta, J. Elguero, E. Molins, *J. Chem. Phys.*, 2002, **117**, 5529–5542.

[98] F. Weinhold, F.; Landis, C. *Valency and Bonding: A Natural Bond Orbital Donor–Acceptor Perspective, Cambridge University Press, Cambridge, UK*, 2005.

[99] (*a*) E. R. Johnson, S. Keinan, P. Mori-Sánchez, J. Contreas-García, A. J. Cohen, W. Yang, *J. Am. Chem. Soc*., 2010, **132**, 6498–6506; (*b*) J. Contreas-García, R. A. Boto, F. Izquierdo-Ruiz, I. Reva, T. Woller, Mercedes Alonso, *Theor. Chem. Acc.*, 2016, **135**, 242–256.

[100] (*a*) E. M. Beck, M. J. Gaunt, *Topics in Current Chemistry*: *C–H Activation*, (Eds: J. Q. Yu, Z. J. Shi), Springer, Berlin/Heidelberg, Germany, 2010, pp 85–121; (*b*) J. Yamaguchi, A. D. Yamaguchi, K. Itami, *Angew. Chem. Int. Ed.*, 2012, **51**, 8960–9009; (*c*) J. Wencel-Delord, T. Dröge, F. Liu, F. Glorius, *Chem. Soc. Rev.*, 2011, **40**, 4740–4761.

[101] (*a*) M. Pfeffer, *Pure Appl. Chem.*, 1992, **64**, 335–342; (*b*) A. D. Ryabov, *Synthesis*, 1985, **3**, 233–252; (*c*) J. Dupont, M. Pfeffer and J. Spencer, *Eur. J. Inorg. Chem*., 2001, 1917–1927.; (*d*) R. B. Bedford, *Chem. Commun.*, 2003, 1787–1796.; (*e*) L. Cuesta, E. P. Urriolabeitia, *Comments Inorg. Chem*., 2012, **33**, 55–85.

[102] J. Saßmannshausen, *Dalton Trans*., 2012, **41**, 1919–1923.

[103] N. Ding, J. Zhang and T. S. A. Hor, *Dalton Trans*., 2009, 1853–1858.

[104] (*a*) C. A. Johnson, A. J. Nielson, *Polyhedron*, 1982, **1**, 501–502; (*b*) T. C. Jones, A. J. Nielson and C. E. F. Rickard, *Aust. J. Chem*., 1984, **37**, 2179–2192; (*c*) M. Curic, D. Babic, Z. Marinic, L Pasa-Tolic, V. Butkovic, J. Plavec and L. Tusek-Bozic, *J. Organomet. Chem*., 2003, **687**, 85–99.

[105] (*a*) A. C. Cope, E. C. Friedrich, *J. Am. Chem. Soc.*, 1968, **90**, 909–913; (*b*) A. J. Cheney, B. L. Shaw, *J. Chem. Soc., Dalton Trans.*, 1972, 754–763.

[106] C. Hansch, A. Leo, R. W. Taft, *Chem. Rev.*, 1991, **91**, 165–195.

[107] M. B. Smith, *March's Advanced Organic Chemistry: Reactions, Mechanism and Structure, 7th Ed.*,Wiley, New York, 2013

[108] M. J. Frisch, G. W. Trucks, H. B. Schlegel, G. E. Scuseria, M. A. Robb, J. R. Cheeseman, G. Scalmani, V. Barone, B. Mennucci, G. A. Petersson, H. Nak- atsuji, M. Caricato, X. Li, H. P. Hratchian, A. F. Izmaylov, J. Bloino, G. Zheng, J. L. Sonnenberg, M. Hada, M. Ehara, K. Toyota, R. Fukuda, J. Hasegawa, M. Ishida, T. Nakajima, Y. Honda, O. Kitao, H. Nakai, T. Vreven, J. A. Mont- gomery Jr., J. E. Peralta, F. Ogliaro, M. Bearpark, J. J. Heyd, E. Brothers, K. N. Kudin, V. N. Staroverov, R. Kobayashi, J. Normand, K. Raghavachari, A. Rendell, J. C. Burant, S. S. Iyengar, J. Tomasi, M. Cossi, N. Rega, J. M. Millam, M. Klene, J. E. Knox, J. B. Cross, V. Bakken, C. Adamo, J. Jaramillo, R. Gomperts, R. E. Stratmann, O. Yazyev, A. J. Austin, R. Cammi, C. Pomelli, J. W. Ochterski, R. L. Martin, K. Morokuma, V. G. Zakrzewski, G. A. Voth, P. Salvador, J. J. Dannenberg, S. Dapprich, A. D. Daniels, Ö. Farkas, J. B. Foresman, J. V. Ortiz, J. Cioslowski, D. J. Fox, Gaussian *09*, revision D.01, Gaussian, Inc., Wallingford CT, 2009

[109] T. Yanai, D. P. Tew, N. C. Handy, *Chem. Phys. Lett.*, 2004, **393**, 51–57.

[110] Y. Sun, L. Hu, H. Chen, *J. Chem. Theory Comput.*, 2015, **11**, 1428–1438.

[111] K. A. Peterson, D. Figgen, M. Dolg, H. Stoll, *J. Chem. Phys.*, 2007, **126**, 124101–24112.

[112] Todd A. Keith, *AIMAll*, version 14.11.23, TK Gristmill Software, Overland Park KS, USA, 2014, http://aim.tkgristmill.com.

[113] E. D. Glendening, J. K. Badenhoop, A. E. Reed, J. E. Carpenter, J. A. Bohm-ann, C. M. Morales, C. R. Landis, F. Weinhold, *NBO*, version 6.0, Theoretical Chemistry Institute, University of Wisconsin, Madison, WI, 2013; http:// nbo6.chem.wisc.edu/.

[114] W. Humphery, A. Dalke, K. Schulten, *J. Mol. Graphics*, 1996, **14**, 33–38.

[115] A. Bondi, *J. Chem. Phys*., 1964, **68**, 441–451.

[116] (*a*) G. Aullon, D. Bellamy, L. Brammer, E. A. Bruton, A. G. Orpen, *Chem. Commun.*, 1998, 653–654; (*b*) L. Brammer, *Dalton Trans.*, 2003, 3145–3157.

[117] D. Steele, P. F. M. Verhoeven, *Vib. Spectrosc.*, 2001, **25**, 29–39.

[118] B. T. Heaton, C. Jacob, J. T. Sampanthar, *J. Chem. Soc., Dalton Trans.*, 1998, 1403–1410.

[119] A. H. Pakiari, K. Eskandari, *J. Mol. Struct. Theochem*., 2007, **806**, 1–7.

---

[120] J. Contreras-García, W. Yang, E. R. Johnson, *J. Phys. Chem. A*, 2011, **115**, 12983–12990.

[121] J. E. Barquera-Lozada, A. Obenhuber, C. Hauf, W. Scherer, *J. Phys. Chem. A*, 2013, **117**, 4304–4315.

[122] G. R. Runtz, R. F. W. Bader, R. R. Messer, *Can. J. Chem.*, 1977, **55**, 3040–3045.

[123] R. L. Bennett, M. L. Bruce, B. L. Goodall, M. Z. Iqbal, F. G. A. Stone, *J. Chem. Soc., Dalton Trans.*, 1972, 1787–1791.

[124] A. J. Nielson, *J. Chem. Soc., Dalton Trans.*, 1981, 205–211.

[125] B. V. Pandivan, P. Deepa, P. Kolandival, *Phys. Chem. Chem. Phys.*, 2015, **17**, 27496–27508.

[126] J. A. Harrison, A. J. Nielson, M. A. Sajjad, G. C. Saunders, P. Schwerdtfeger, *Eur. J. Inorg. Chem.*, 2016, 64–77.

[127] A. J. Deeming, I. P. Rothwell, *J. C. S. Dalton*, 1980, 1259–1264.

[128] A. Albinati, P. S. Pregosin, F. Wombacher, *Inorg. Chem.*, 1990, **29**, 1812–1817.

[129] (*a*) X. Chen, K. M. Engle, D.-H. Wang, J.-Q. Yu, *Angew. Chem., Int. Ed.*, 2009, **48**, 5094–5115; (*b*) T. W. Lyons, M. S. Sanford, *Chem. Rev.*, 2010, **110**, 1147–1169; (*c*) O. Baudoin, *Chem. Soc. Rev.*, 2011, **40**, 4902–4911; (*d*) A. F. M. Noisier, M. A. Brimble, *Chem. Rev.*, 2014, **114**, 8775–8806; (*e*) D. E. Stephens, J. Lakey-Beitia, A. C. Atesin, T. A. Atesin, G. Chavez, H. D. Arman, O. V. Larlonov, *ACS Catal.*, 2015, **5**, 167–175.

[130] (*a*) G. Rouquet, N. Chatani, *Angew. Chem., Int. Ed.*, 2013, **52**, 11726–11743; (*b*) I. P. Beletskaya, A. V. Cheprakov, *J. Organomet. Chem.*, 2004, **689**, 4055–4082.

[131] B. Vabre, F. Deschamps, D. Zargarian, *Organometallics*, 2014, **33**, 6623–6632.

[132] A. Vigalok, O. Uzan, L. J. W. Shimon, Y. Ben-David, J. M. L. Martin, D. Milstein, *J. Am. Chem. Soc.*, 1998, **120**, 12539–12544.

[133] M. Lein, J. A. Harrison, A. J. Nielson, *Dalton Trans.*, 2011, **40**, 10731–10741.

[134] D. A. Pantazis, J. E. McGrady, F. Maseras, M. J. Etienne, *Chem. Theory Comput.*, 2007, **3**, 1329–1336.

[135] S. Murugesan, B. Stöger, E. Pittenauer, G. Allmaier, L. F. Veiros, K. Kirchner, *Angew. Chem. Int. Ed.*, 2016, **55**, 3045–3048.

[136] (*a)* R. G. Miller, R. D. Stauffer, D. R. Fahey, I. R. Parnell, *J. Am. Chem.* Soc., 1970, **92**, 1511–1521; (*b*) J. F. Van Baar, K. Vrieze, P. J. Stufkens, *J. Organomet. Chem.*, 1975, **85**, 249–263.

[137] (*a*) I. Rozas, I. Alkorta, J. Elguero, *J. Am. Chem. Soc.*, 2000, **122**, 11154–11161; (*b*) W. Koch, G. Frenking, J. Guass, D. Cremer, J. R. Collins, *J. Am. Chem. Soc.*, 1987, **109**, 5917–5934.

[138] D. A. Colby, A. S. Tsai, R. G. Bergman, J. A. Ellman, *Acc. Chem. Res.*, 2012, **45**, 814–825.

[139] (*a*) D. Saha, R. Verma, D. Kumar, S. Pathak, S. Bhunya, A. Sarkar, *Organometallics*, 2014, **33**, 3243–3246; (*b*) P. Kočovsky, S. Vyskočil, I. Cisařová, J. Sejbal, I. Tislerova, M. Smrcina, G. C. Lloyd-Jones, S. C. Stephen, C. P. Butts, M/ Murrey, V. Langers, *J. Am. Chem. Soc.*, 1999, **121**, 7714–7715.

[140] D. W. Evans, G. R. Baker and G. R. Newkome, *Coord. Chem. Rev.*, 1989, **93**, 155–183.